

Finite element modelling of transport and non-hydrostatic flow in environmental fluid mechanics

Eindige elementen modellering van
transport en niet-hydrostatische stroming
in de waterloopkunde

**Finite element modelling
of transport and non-hydrostatic flow
in environmental fluid mechanics**

Proefschrift

ter verkrijging van de graad van doctor
aan de Technische Universiteit Delft,
op gezag van de Rector Magnificus prof. dr. ir. J.T. Fokkema,
voorzitter van het College voor Promoties,
in het openbaar te verdedigen op vrijdag 26 juni 2009 om 14.00 uur

door

Robert Jan LABEUR
civiel ingenieur
geboren te Zaandam.

Dit proefschrift is goedgekeurd door de promotor:

Prof. dr. ir. G.S. Stelling

Samenstelling promotiecommissie:

Rector Magnificus	voorzitter
Prof. dr. ir. G.S. Stelling	Technische Universiteit Delft, promotor
Prof. dr. ir. C. van Rhee	Technische Universiteit Delft
Prof. dr. ir. L.J. Sluys	Technische Universiteit Delft
Prof. dr. ir. J.J.W. van der Vegt	Technische Universiteit Twente
Prof. dr. A.E.P. Veldman	Rijksuniversiteit Groningen
Prof. dr. ir. C. Vuik	Technische Universiteit Delft
Dr. G.N. Wells	University of Cambridge
Prof. dr. ir. M.J.F. Stive	Technische Universiteit Delft, reservelid

ISBN 978-90-8559-528-1

©2009 R.J. Labeur

All rights reserved. No part of this publication may be reproduced, stored in a retrieval system or transmitted in any other form or by any means, without the prior written permission of the author, or when appropriate, of the publishers of the publications.

Printed by Optima Grafische Communicatie, Rotterdam.

Financial support by Svašek Hydraulics B.V., Rotterdam, for the printing of this thesis is gratefully acknowledged.

Preface

The studies and model developments described in this thesis were performed in the Environmental Fluid Mechanics Section of the Civil Engineering and Geosciences Faculty, Delft University of Technology, under the supervision of G.S. Stelling, Professor of Environmental Fluid Mechanics, and with contributions from G.N. Wells, Ph.D., University of Cambridge, and J.D. Pietrzak, Ph.D., Delft University of Technology. B.A. Wols and J.C.C. van Nieuwkoop, Master students Civil Engineering, provided useful data from experiments in the Fluid Mechanics Laboratory which were conducted under the guidance of W.S.J. Uijttewaal, Professor of Experimental Hydraulics, Delft University of Technology.

The work is a continuation of earlier model development at Svašek Hydraulics B.V., Rotterdam. Their support by making the code publically available and by providing project data, including some mesh schematizations, is much appreciated.

*Als met water zelf, met de gedachte
spelen dat je ooit en eindelijk
zult weten wat het is.*

*Het is regen geweest, een rivier, een zee,
hier was het, hier heb ik het gezien
en zie ik water en weet niet wat het is.*

RUTGER KOPLAND

*Voor de artsen en verpleegkundigen van
Intensive Care Chirurgie,
Sophia Kinderziekenhuis, Rotterdam.*

Contents

1	General introduction	1
1.1	Numerical hydraulics	1
1.1.1	A short history	1
1.1.2	Model equations	3
1.1.3	Discretization principles	6
1.2	Present research	9
1.2.1	Scientific objective	9
1.2.2	Practical relevance	11
1.2.3	Scope of this thesis	12
2	Finite element computing	13
2.1	Mathematical preliminaries	14
2.1.1	Function spaces	14
2.1.2	Variational formulations	17
2.2	Galerkin methods	19
2.2.1	Continuous Galerkin method	19
2.2.2	Discontinuous Galerkin method	21
2.2.3	Galerkin interface stabilization method	23
2.3	The discrete problem	25
2.3.1	Mesh partitioning	25
2.3.2	Time stepping	27
2.3.3	Matrix form	30
2.4	The algebraic problem	31
2.4.1	Sparse matrices	31
2.4.2	Solution algorithms	32
2.4.3	Computational aspects	34
2.5	Numerical examples	35
2.5.1	Flow in an outlet	35
2.5.2	Standing wave	38
2.6	Conclusion	39

3	Scalar transport	41
3.1	The model problem	41
3.1.1	Governing equations	41
3.1.2	Variational formulation	43
3.1.3	Solution characteristics	44
3.2	Continuous and discontinuous methods	46
3.2.1	Continuous Galerkin method	46
3.2.2	Discontinuous Galerkin method	50
3.2.3	Discussion: CG or DG?	52
3.3	Galerkin interface stabilization method	54
3.3.1	General formulation	54
3.3.2	Interface flux	56
3.3.3	Properties	58
3.4	Implementation	60
3.4.1	Time stepping	60
3.4.2	Solution procedure	61
3.4.3	Stabilization mechanism	63
3.4.4	Fourier analysis	64
3.5	Numerical examples	66
3.5.1	Advection-diffusion with source	66
3.5.2	Boundary layers	67
3.5.3	Anisotropic diffusion	71
3.5.4	Simple waves	72
3.5.5	Practical application: sediment transport North Sea	77
3.6	Conclusion	79
4	Incompressible flow	81
4.1	Mathematical formulation	81
4.1.1	Governing equations	81
4.1.2	Variational formulation	83
4.1.3	Dimensional scaling	84
4.2	Galerkin interface stabilization method	85
4.2.1	Introduction	85
4.2.2	General formulation	87
4.2.3	Interface flux	89
4.2.4	Properties	91
4.3	Implementation	94
4.3.1	Time stepping	94
4.3.2	$P^1 - P^1$ discretization	95
4.3.3	Solution procedure	98
4.3.4	Stabilization mechanism	101
4.4	Numerical examples	102
4.4.1	Stokes flow	103
4.4.2	Burgers' equation	105

4.4.3	Driven cavity flow	109
4.4.4	Borda mouthpiece	109
4.4.5	Internal waves	113
4.4.6	Practical application: current load on VLCC	117
4.5	Conclusion	119
5	Free-surface flow	121
5.1	Moving domains	121
5.1.1	Kinematics	121
5.1.2	Transport theorem	124
5.1.3	Construction of mappings	126
5.2	Incompressible flow on moving domains	126
5.2.1	General formulation	127
5.2.2	Geophysical free-surface flows	128
5.2.3	Dimensional scaling	129
5.3	Galerkin interface stabilization method	131
5.3.1	General formulation	131
5.3.2	Interface flux	133
5.3.3	Properties	135
5.4	The fully-discrete problem	139
5.4.1	Fractional-step formulation	139
5.4.2	Discrete conservation	142
5.4.3	Implementation for geophysical flows	144
5.4.4	Normal mode analysis	149
5.5	Numerical examples	151
5.5.1	Linear waves	152
5.5.2	Large amplitudes	155
5.5.3	Wave propagation over a submerged bar	159
5.5.4	Undulating flow downstream of a weir	160
5.5.5	Sub-marine landslide	163
5.5.6	Practical application: storm surge barrier	168
5.6	Conclusion	170
6	General discussion and outlook	173
6.1	General discussion	173
6.2	Outlook	177
7	Summary/samenvatting	181
7.1	Summary	181
7.2	Samenvatting in het Nederlands	185

Appendices	191
A Internal flow	193
A.1 Boussinesq approximation	193
A.2 Solution algorithm	194
B Turbulence modelling	195
B.1 Wall-friction coefficient	195
B.2 Turbulence viscosity	196
C Shallow-water equations	199
C.1 Governing equations	199
C.2 Variational formulation	200
Bibliography	203
List of figures	213
List of tables	219
Notation	221
Curriculum Vitae	225

Chapter 1

General introduction

1.1 Numerical hydraulics

1.1.1 A short history

Numerical fluid mechanics was virtually initiated by Blaise Pascal (1623-1662), who founded hydrostatics and developed a mechanical calculator. In the ‘Age of Reason’ Newton (1643-1727) formulated the fundamental laws of motion which were specialized later to the case of inviscid fluid flow by Euler (1707-1783). The extension to laminar flow of viscous fluids is due to Navier (1785-1836) with the correct derivation and basic solutions being given by Stokes (1819-1903). Their Navier-Stokes equations (1822) are now generally accepted as the mathematical starting point for fluid flow problems, although it remains to be proven that these equations possess unique solutions in three dimensions¹.

While theoretical fluid mechanics attained a high level of sophistication, its purely mathematical results found limited application in engineering, mainly due to the natural role of turbulence which was not very well understood until Prandtl (1875-1953). More relevant in practice were the results of Torricelli (1608-1647), who studied the motion of fluids through apertures, the energy conservation law formulated by Bernoulli (1700-1782) and the expressions derived by de Borda (1733-1799) to calculate the energy losses in contractions and mouthpieces. To describe flows in one-dimensional open channels de Saint-Venant (1797-1886), assuming hydrostatic pressure, derived the shallow-water equations (SWE) while de Chézy (1718-1798) and Darcy (1803-1858) established empirical relations for the energy loss by bottom friction. Supported with these empirical results, the scientific method gradually gained importance in the design of drainage, irrigation systems [22] and flood defence².

¹The existence and smoothness of the Navier-Stokes problem is one of the seven Millennium Problems posed by The Clay Mathematics Institute.

²Some artists of the ‘Romantic Era’ also criticized the scientific approach. In the novel



Figure 1.1: *Zuiderzee flood, 1916, the Netherlands: (a) inundation of the island of Marken and (b) computational network for tidal predictions as employed by Lorentz [58].*

One of the first numerical models applied in civil engineering hydraulics is the *harmonic method*, conceived by Lorentz [58] in the aftermath of the Zuiderzee flood in 1916, which was developed to calculate tidal-wave propagation in a network of one-dimensional tidal channels, see Figure 1.1. Interestingly, this approach would nowadays be classified as a ‘residual free’ sub-grid method as the underlying linearized SWE are solved exactly on each element of the network and coupled via a continuity condition in the nodes. During 1930-1950 the harmonic method was extended and refined by Dronkers [20] but computations were still performed manually. To relieve this computational effort van Veen [91] exploited the equivalence of the linearized SWE with the ‘telegraph equation’ by using alternating currents in electrical circuits to simulate tidal flow problems. This ultimately resulted in the DELTAR [96], an electrical analogon which provided tidal forecasts for the Dutch delta region between 1964 and 1982.

On the digital front, the first computer models became operational during the 1950’s and are thriving nowadays’s engineering practice. The developments started with one-dimensional network models which permitted to abandon the linearization procedures needed in the analytical methods, see Dronkers [20]. With increasing computer capacity, the 1960’s saw the first practical two-dimensional shallow-water flow models which successfully used the alternating direction implicit method (ADI) where the shallow-water equations are solved sequentially in the x - and in the y -direction. In computational hydraulics this method was introduced by Leendertse [53] and refined later by Stelling [83]. The underlying Cartesian grids are generally inconvenient to capture complicated geometries which motivated the

Der Schimmelreiter by Theodor Storm [85] the rational dike warden Hauke Haijen opposes the superstition of his neighbours which leads to a catastrophic flood.

development of methods using boundary fitted, curvi-linear grids or unstructured grids [70]. Modelling the vertical structure of the flow in stratified estuaries was introduced by Vreugdenhil [94]. The extension to truly three-dimensional hydrostatic models followed in the 1990's [27] where the unstructured models mainly adopted the philosophy of being unstructured in the horizontal but structured in the vertical [12, 59].

More recently, it became feasible to include non-hydrostatic effects as well, which are neglected in the shallow-water approach, to model short waves, buoyant flows or small-scale flows around hydraulic structures. Many of these models somehow employ an approximation to the non-hydrostatic equations, splitting the solution procedure into a hydrostatic and a non-hydrostatic part [43, 82]. In a similar vein, finite element models can be extended with non-hydrostatic components using a vertical stack of prisms [41]. This approach is however problematic if intrinsically three-dimensional problems are to be considered. An early, fully three-dimensional flow model was developed by Versteegh [92], using a Cartesian grid and artificial compressibility in combination with the ADI method to by-pass the continuity constraint, where the pressure is treated in an equal manner in all three directions. In Tezduyar [87] a non-hydrostatic finite element flow model on arbitrary grids is presented taking into account free-surface deformation.

From these historical notes, one can only speculate about future directions of numerical model development in environmental fluid mechanics. This thesis continues by considering a fully unstructured, finite element model for transport and incompressible flow problems in environmental fluid mechanics without *a priori* assumptions concerning the pressure distribution nor the geometrical orientation of the flow. The main reasons for pursuing this approach is that it allows intrinsically three-dimensional objects to be accurately resolved while it would also enable the modelling of domains having a partial free surface.

1.1.2 Model equations

The motion of water and the associated transport of dissolved or suspended matter in systems that hydraulic engineers have to deal with are basically governed by conservation laws. To this end the water is modelled by its velocity $\mathbf{u}(\mathbf{x}, t)$ and its density $\rho(\mathbf{x}, t)$ at the point \mathbf{x} and time t . Letting $\Omega \subset \mathbb{R}^3$ denote the domain of interest and $I = (t_0, t_N)$ the considered time interval, the flow problem is solved if we know all relevant variables in $\Omega \times I$ to a sufficient degree of accuracy³. To this end, an Eulerian control volume $V \subset \Omega$ is considered having a boundary ∂V to which \mathbf{n} is the unit outward normal vector, see Figure 1.2.

³From an engineering point of view this means that the model results allow to discriminate between different management strategies or design options [95].

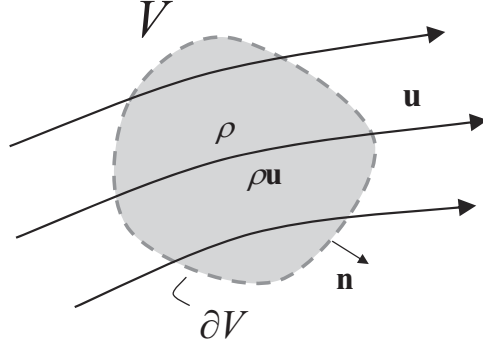


Figure 1.2: *Schematic of Eulerian control volume V .*

Conservation of mass requires that the change of the total mass contained in V equals the net inward transport of mass through the boundary ∂V during a time interval I ,

$$\int_V \Delta \rho = - \int_I \int_{\partial V} \rho \mathbf{u} \cdot \mathbf{n}, \quad (1.1)$$

where $\Delta \rho$ denotes the increment of the density ρ in the time interval I and \mathbf{n} is the unit outward normal vector on ∂V . For differentiable \mathbf{u} and ρ , applying Green's divergence theorem leads to the *continuity equation*

$$\frac{\partial \rho}{\partial t} + \nabla \cdot (\rho \mathbf{u}) = 0, \quad (1.2)$$

in which $\partial \rho / \partial t$ denotes the time derivative of the density and ∇ denotes the spatial gradient operator. Using the chain rule Equation (1.2) may also be written as

$$\frac{\partial \rho}{\partial t} + \mathbf{u} \cdot \nabla \rho \equiv \frac{D \rho}{D t} = -\rho \nabla \cdot \mathbf{u}. \quad (1.3)$$

The left hand side constitutes the total or material derivative giving the density variations of a moving fluid particle caused by changing pressure, temperature and salinity. In environmental water systems these density variations are usually considered negligible with respect to the reference density (Boussinesq-approximation). This reduces Equation (1.3) to the *incompressibility condition*

$$\nabla \cdot \mathbf{u} = 0, \quad (1.4)$$

which can be regarded as a constraint for the flow velocity field.

Considering conservation of linear momentum in V leads to

$$\int_V \Delta (\rho \mathbf{u}) = \int_I \int_V \mathbf{f} - \int_I \int_{\partial V} (p \mathbf{n} - \boldsymbol{\sigma} \mathbf{n}), \quad (1.5)$$

in which \mathbf{f} are the external forces acting on the fluid per unit volume (such as gravity), p is the fluid pressure and $\boldsymbol{\sigma}$ is the flux tensor resulting from the advective and viscous momentum transfer. The advective part of this tensor is given by the dyadic product $\rho\mathbf{u} \otimes \mathbf{u}$, where $(\mathbf{u} \otimes \mathbf{u})_{ij} = u_i u_j$. The diffusive part is related to the deformation rate of the fluid. For Newtonian, incompressible fluids the diffusive flux is given by $-2\mu\nabla^s\mathbf{u}$, where μ is the fluid viscosity and $\nabla^s = \frac{1}{2}\nabla(\cdot) + \frac{1}{2}\nabla(\cdot)^T$ is the symmetric gradient operator. Applying the divergence theorem, and combining the previous expressions for the flux $\boldsymbol{\sigma}$, leads to the *momentum equation*

$$\frac{\partial(\rho\mathbf{u})}{\partial t} + \nabla \cdot (\rho\mathbf{u} \otimes \mathbf{u}) + \nabla p - \nabla \cdot (2\mu\nabla^s\mathbf{u}) = \mathbf{f}. \quad (1.6)$$

The pressure is directly related to the density by an equation of state but as the fluid has been assumed incompressible the pressure is in this case implicitly determined by Equation (1.4) instead. The molecular viscosity of water is only small ($\mu \approx 10^{-3}$ kg/ms) and can be neglected at the time and length scales typically encountered in civil engineering hydraulics. At the same time this small viscosity renders the water motion turbulent in most of these cases.

Turbulent fluctuations of velocities and pressure are usually not fully resolved in a computational model and Equation (1.6) has to be averaged in some way to describe the resulting net fluid motion in terms of the modelled average velocities. The averaging procedure introduces additional transport terms representing the mean turbulent advection of momentum by the unresolved velocity fluctuations. These turbulent 'stresses' are usually modelled in terms of the gradient of the resolved velocities, analogous to the representation of viscous stresses. In this way the averaged equation for the resolved velocity becomes essentially similar to Equation (1.6) with μ being replaced by a turbulence viscosity μ_t which has to be calculated by a turbulence closure model [68].

Finally, the transport of dissolved or suspended matter (such as salinity or sediment) is considered. As the mass of each transported constituent is conserved, the mass balance equation also holds individually for the density ρ_i of component i . When the concentration of a transported substance is described in terms of its mass fraction $\phi_i = \rho_i/\rho$ the divergence theorem gives, after elimination of the incompressibility constraint Equation (1.4) the following *transport equation* for ϕ_i

$$\frac{\partial\phi_i}{\partial t} + \mathbf{u} \cdot \nabla\phi_i - \nabla \cdot (\kappa_t\nabla\phi_i) = f_i, \quad (1.7)$$

where f_i is the densimetric source term of constituent i and κ_t is the turbulence diffusivity whose magnitude may differ from the turbulent kinematic viscosity $\nu_t = \mu_t/\rho$. If the transport of matter involves changes in density the flow and the advected density field will interact. Density changes

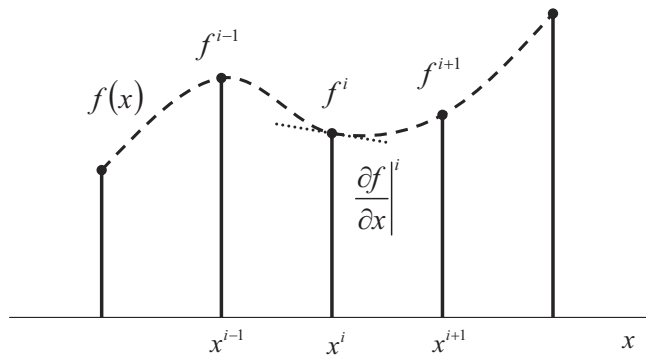
caused by natural variations of salinity and temperature are usually small enough to use the Boussinesq- approximation and the flow virtually remains incompressible as expressed by Equation (1.4). However, even small density variations can have a huge impact on the flow field. This is modelled by coupling the momentum equation to the transport equation through the volumetric forcing term \mathbf{f} which will amongst others depend on the local density.

In all cases, the interaction with flow and transport processes outside the domain of interest is imposed by supplying boundary conditions on the boundary of Ω . In time dependent cases also the initial condition at time $t = 0$ must be provided.

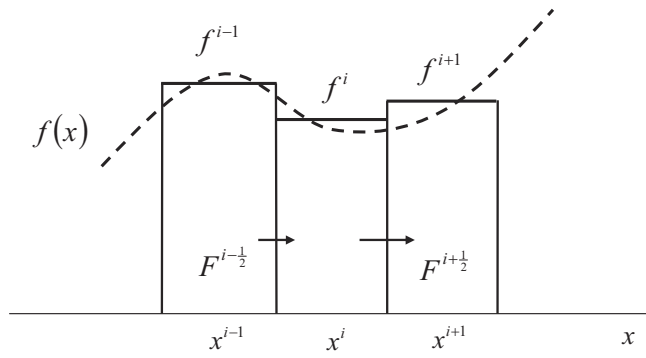
1.1.3 Discretization principles

Model discretization comprises the transformation of the continuous problems given by Equations (1.4), (1.6) and (1.7) into an algebraic system of equations that can be solved by a computer. Firstly, this involves the representation of the continuous flow field in terms of a discrete set of numbers. Secondly, the governing differential equations must be approximated in some way to give the evolution of the discrete variables in time. A myriad of discretization techniques has been devised while new methods are continuously being developed. Apparently, the ultimate method has not yet been found. Without trying to be complete, some well-known classes are briefly described here to mark some distinguishing features of the finite element method as compared to other modelling principles. A schematic of these principles is depicted in Figure 1.3.

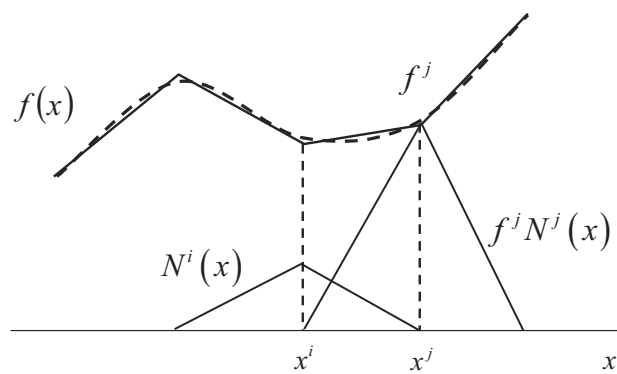
- *Finite difference methods* use a mapping of the flow domain onto a regular grid of discrete points. The flow variables are represented by point-wise values f^i on an associated set of grid points \mathbf{x}^i while the differential equations that determine the time evolution of these variables are approximated from Taylor-series expansions between the discrete data points.
- *Finite volume methods* are based on a partitioning of the flow domain into a number of control volumes or cells each representing a local flow state. Balance equations are used to determine the rate of change of the flow state within each volume. This requires the determination of fluxes $\mathbf{F}^{i \pm \frac{1}{2}}$ between control volumes from the cell based data.
- *Spectral methods* use a set of analytical global basis functions covering the entire domain to represent the flow variables. Traditionally, goniometric or polynomial functions are used for this purpose. Substitution into the differential equations directly yields analytical expressions from which the evolution of the flow field is evaluated. In case of



(a) finite difference method



(b) finite volume method



(c) finite element method

Figure 1.3: Schematic illustration of discretization principles.

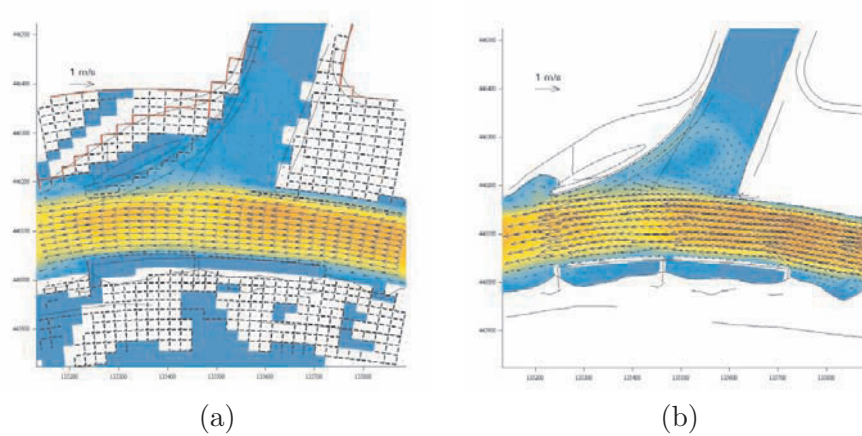


Figure 1.4: *Example river optimization study (Lek - the Netherlands): finite difference shallow-water flow model (a) and finite element model (b) used to compute the horizontal circulation in modified lay-out of junction [55].*

non-linear problems this procedure requires an orthogonal projection of the analytical solution onto the basis functions.

- *Finite element methods* finally, also use a set of basis functions to represent the flow field. However, the basis functions $N^i(\mathbf{x})$ are not defined globally but locally using partitions of the domain called elements. The governing equations are approximated using weak formulations. This only requires square integrability of functions and their derivatives which allows rather simple classes of basis functions and elements of more or less arbitrary size and shape.

Each of the previous methods may have its own merits but, in general, there are no objective reasons to prefer one method over the other. Moreover, for most standard problems exactly the same algebraic equations result if the same configuration of grid points is used, the only difference being the way the problem is visualized in the modellers mind. More decisive for choosing a certain method is therefore the type of grid structure that can be employed.

A *structured* ordering of data, commonly applied for finite difference and finite volume methods, may be exploited to give highly efficient numerical algorithms. This is especially useful when storing and manipulating large amounts of data but it also means less flexibility when designing the layout of a computational grid. An *unstructured*, tailor made mesh as typically employed by finite element methods may in this respect offer the modeller some more freedom when dealing with irregular topography or complicated layouts, see Figure 1.4, although this comes at the expense of reduced computational performance in terms of data processing.

For these reasons a finite element model is perhaps more appreciated in an engineering environment, as it enables a quick assessment of design alternatives, while structured models could be a more appropriate choice for large water management and warning systems containing a vast amount of variables. To accommodate the first group of applications, the coupled solution of the set of Equations (1.4), (1.6) and (1.7) by the finite element method in the context of small-scale civil engineering flow problems is the main focus of this thesis.

1.2 Present research

1.2.1 Scientific objective

The principal challenge of numerical flow modelling is to control, in a consistent way, two types of instabilities that may occur: (1) instabilities associated with the advection terms and (2) instabilities due to the incompressibility constraint. In methods employing structured grids the problem is readily solved by applying a staggered scheme where pressure and velocity unknowns are located in alternate grid points and advection terms are stabilized via upwind differencing [92]. The finite element approach is less straightforward in the sense that different basis functions have to be chosen for the pressure and velocity fields where the latter generally requires a higher order approximation, see for instance Gunzburger [30] for possible combinations. This however leads to an even more complex data structure requiring different topologies for velocity and pressure unknowns.

More convenient in this respect are continuous basis functions where velocity and pressure unknowns are stored in the same nodes. These equal-order elements require additional stabilization which is generally achieved by modifying the interpolated velocity field between nodal values. This may be effected through the addition of element-wise velocity unknowns, bubble methods [8]; the reconstruction of element velocities from nodal values, streamline upwind Petrov-Galerkin (SUPG) method [10]; or by the addition of residual-based terms, Galerkin least-squares (GLS) method [38]. While computationally attractive, ensuring sufficient stability without introducing excessive dissipation can be problematic. Low-order bubble methods for instance are not optimally stable [81] while SUPG and GLS methods involve a problem-dependent stabilization parameter which must be chosen judiciously [87].

Recently, discontinuous Galerkin (DG) methods have been re-discovered as an attractive alternative. The advected field is approximated by locally discontinuous functions which involves the definition of fluxes at element interfaces. The fluxes are obtained from the flow states in neighbouring elements for which a wealth of flux splitting schemes is available [33, 56]. Upwinding is thus easily incorporated leading to good stability properties and,

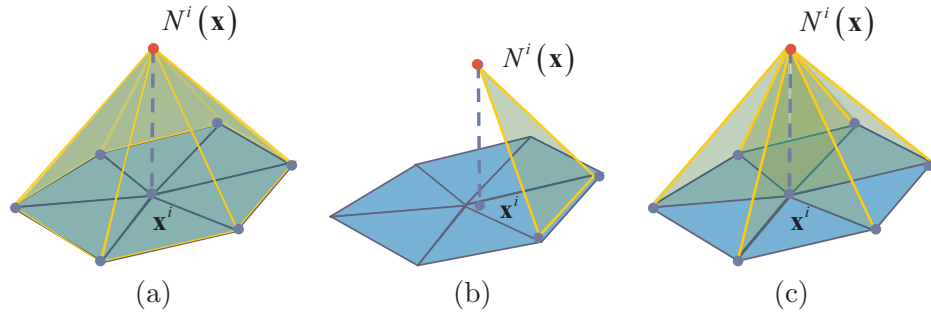


Figure 1.5: *Linear two-dimensional basis functions: (a) continuous, (b) discontinuous, (c) global interface function.*

in combination with continuous pressure functions, the velocity-pressure compatibility problem is completely avoided. These benefits however come at the price of an increased number of degrees of freedom compared to a continuous Galerkin (CG) method on the same mesh. Also, the complexity of the scheme increases when diffusive terms are introduced [1]. Recently, for the advection-diffusion problem, a number of researchers have tried to circumvent these complications by coupling the discontinuous field to a global continuous field, see Sangalli [77], Hughes et al. [35] and Buffa et al. [11]. In the framework of the incompressible Stokes equations Cockburn and Gopalakrishnan [16] have introduced hybrid methods where locally discontinuous solutions on elements are coupled through the use of global Lagrange multipliers enforcing weak continuity of the pressure and tangential velocity on element interfaces. These novel techniques may be exploited to reduce the underlying system of equations to a global algebraic problem.

This research explores similar concepts by using interface functions which are global, continuous functions defined on the interfaces between elements, see Figure 1.5. The problem of interest is posed element-wise using weakly imposed Dirichlet boundary conditions on each element which are given as a function of the interface field. The interface field is then determined such that the resulting flux between elements is weakly continuous. This approach allows the natural incorporation of upwinding at element boundaries, which is typical of DG methods, while retaining the number of degrees of freedom as for a CG method. As the stabilizing term is inherited from the formulation of the interface flux, it automatically adapts to the flow conditions avoiding the need for a problem dependent stabilization parameter. Moreover, conservation is guaranteed with a minimum amount of artificial dissipation. Interestingly, the approach may be applied to stabilize incompressible flow problems using equal-order interpolations [51].

The discretization technique, coined Galerkin Interface Stabilization (GIS) method, is developed for the transport equation and the incompressible

Navier-Stokes equations, in the context of small-scale environmental fluid mechanics problems. These flow phenomena feature non-hydrostatic pressures while the advection and diffusion of momentum are dominant processes. In some cases, the deformation of the free surface may be appreciable which raises moving domain issues and also leads to non-trivial free-surface boundary conditions. In an estuarine environment, the coupling between the flow and an advected density field introduces compatibility problems [65] which requires special consideration. To accurately resolve intrinsic three-dimensional geometries the mesh may be constructed from tetrahedrons (or triangles in two dimensions) having an arbitrary orientation, that is without a principal or ‘preferred’ direction in the mesh. As the development of the model is motivated by practical problems, its implementation is tested using a range of examples obtained from engineering practice.

1.2.2 Practical relevance

The flow model is intended to be used for the practical computation of water motion through or around hydraulic structures in civil engineering systems such as weirs, barriers, shipping locks (see Figure 1.6), harbour dams or outfalls. The correct modelling of these flows may contribute to optimizing the design of such structures and the adjoint management of water systems, thus gaining functionality and cost effectiveness. Practical situations often involve complex geometries while most project environments demand a quick assessment of modified or alternative designs.

Given these considerations, the finite element method is particularly suited as a basis for such a design supportive modelling tool. It allows a relatively high degree of mesh flexibility and the variational format facilitates a consistent treatment of all relevant terms. To be able to fully exploit these qualities however, the unstructured data arrangement that comes along with finite element models may not lead to excessive computational effort. The present work has resulted in a finite element model, coined FINLAB, performing reasonably efficient with the interface functions playing a crucial role in this respect. The stabilized method is cast into a general variational framework which would also allow the extension to other technical disciplines.

It has still to be kept in mind that in a design optimization process or when supporting the development of management strategies the experience of the modeller is far more important than the class of numerical method that is actually being used. In the hands of an experienced modeller any method may give reliable results in terms of supporting the decisions to be made. The quality of the results is therefore less dependent on the specific choice of the method than on the personal expertise and experience of the modeller.

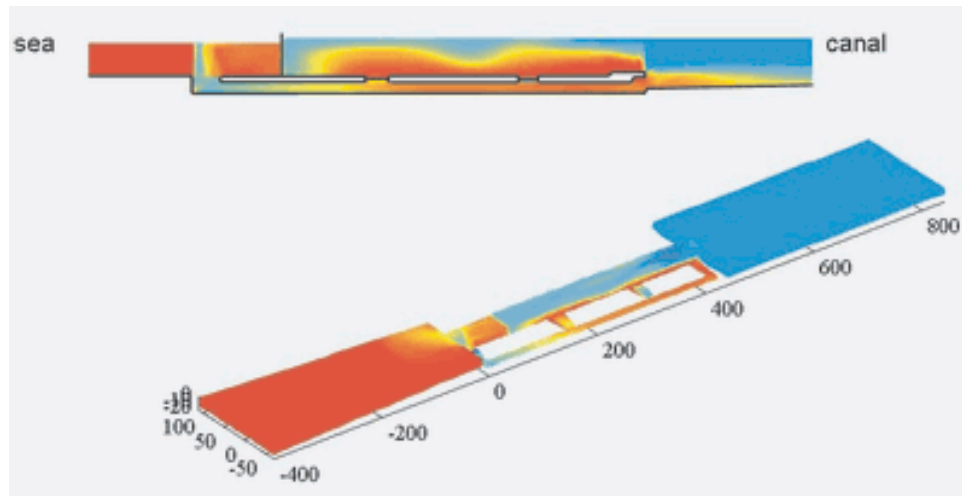


Figure 1.6: *Example model application (Terneuzen - the Netherlands): exchange of salt water (red) and fresh water (blue) in shipping lock, distances in m [47].*

1.2.3 Scope of this thesis

This thesis is organized as follows. Chapter 2 introduces finite element notation and practical issues associated with the use of CG and DG methods are identified. A combination of both methods is pursued in Chapter 3 for the advection-diffusion problem to develop a general stabilization technique which hinges on the use of interface functions. In Chapter 4, the analysis continues towards a stabilized variational form of the incompressible Navier-Stokes equations on a fixed domain. Chapter 5 extends the resulting flow model to the general case of advection-dominated flows with a free surface. Throughout the exposition, the numerical code is tested using numerous examples involving analytical solutions, experimental data and practical applications. In Chapter 6, general conclusions are drawn and directions for further research are suggested. Summaries in English and Dutch are finally provided in Chapter 7.

Chapter 2

Finite element computing

This chapter introduces basic concepts to transform the flow of water into a finite element computer model amenable to practical computation. In a nutshell, some common discretization techniques are given anticipating the developments in the upcoming chapters. Most of the theory presented in this chapter can be found in general finite element textbooks of which Zienkiewicz and Taylor [99], Johnson [42], Gresho et al. [28], Gunzburger [30] and Pironneau [68] are particularly relevant.

To demonstrate finite element discretization the potential flow problem, which arises in the study of irrotational flows, is used as an example. For a domain $\Omega \subset \mathbb{R}^d$ with smooth boundary $\Gamma = \partial\Omega$ on which \mathbf{n} is the outward normal unit vector, this problem reads: given a source term¹ $f : \Omega \rightarrow \mathbb{R}^d$, the Dirichlet boundary condition $g : \Gamma_g \rightarrow \mathbb{R}$ and the Neumann boundary condition $h : \Gamma_h \rightarrow \mathbb{R}$, find $\mathbf{u} : \Omega \rightarrow \mathbb{R}^d$ and $\phi : \Omega \rightarrow \mathbb{R}$ such that

$$\mathbf{u} = \nabla\phi \quad \text{in } \Omega, \quad (2.1)$$

$$\nabla \cdot \mathbf{u} = f \quad \text{in } \Omega, \quad (2.2)$$

$$\phi = g \quad \text{on } \Gamma_g, \quad (2.3)$$

$$\mathbf{u} \cdot \mathbf{n} = h \quad \text{on } \Gamma_h, \quad (2.4)$$

where d is the number of spatial dimensions and the boundary Γ has been partitioned into Γ_g and Γ_h such that $\Gamma_g \cup \Gamma_h = \Gamma$ and $\Gamma_g \cap \Gamma_h = \emptyset$. It will be assumed throughout that the source term and the boundary conditions possess sufficient regularity such that a solution is admitted. Note that the potential flow problem has been expressed as a system of two first-order equations, with a view to later manipulations. Despite its simplicity, potential flow theory covers an important class of flow problems, notably the flow towards hydraulic structures [62] and the propagation of surface waves [60]. Although primarily used here as an example, any numerical flow

¹While for incompressible flows $f = 0$, the general case $f \neq 0$ is given here as this form is frequently used in incompressible flow solvers.

model should therefore be able to reproduce the corresponding irrotational flow features.

2.1 Mathematical preliminaries

The discretization of flow problems, such as the potential flow example given by Equations (2.1) to (2.4), comprises two subsequent steps. Firstly, the flow variables in Ω must be represented by a finite set of discrete numbers for which finite element methods employ function spaces having specific properties. Secondly, a procedure is needed to represent the flow and transport problems in terms of the discretized variables for which finite element techniques use variational formulations of the problem. These two topics are the subject of this section.

2.1.1 Function spaces

Exact solutions of continuous problems having derivatives up to order m generally belong to the class $C^m(\Omega)$ of continuous functions possessing up to order m continuous derivatives. In contrast, finite element approximations only require square integrability of functions and their derivatives thus admitting larger solution spaces. Generally, finite element solutions are defined in $L^2(\Omega)$, the space of square integrable functions on Ω . This space has an inner product

$$(u, v) = \int_{\Omega} uv \, d\Omega, \quad (2.5)$$

which defines the \mathcal{L}^2 norm

$$\|u\|_2 = (u, u)^{1/2}, \quad (2.6)$$

where u and v are functions belonging to $L^2(\Omega)$. In quite a few cases, functions $u \in L^2$ are considered having a prescribed value on a partition Γ_g of the boundary Γ , which is denoted by

$$L_g^2(\Omega, \Gamma_g) = \{u \in L^2(\Omega) : u = g \text{ on } \Gamma_g \subset \partial\Omega\}. \quad (2.7)$$

where g is the value u takes on Γ_g .

For second order problems finite element solutions involve the Hilbert space $H^1(\Omega) \subset L^2(\Omega)$ of functions whose first partial derivatives are also square integrable

$$H^1(\Omega) = \{u \in L^2(\Omega) : \partial_i u \in L^2(\Omega), 1 \leq i \leq d\}, \quad (2.8)$$

where ∂_i denotes the partial derivative in the Cartesian direction i . Functions $u \in H^1(\Omega)$ are C^0 continuous and have an additional \mathcal{H}^1 norm given by

$$\|u\|_1 = \{(u, u) + (\partial u_i, \partial u_i)\}^{1/2}, \quad (2.9)$$

and a \mathcal{H}^1 semi-norm given by

$$|u|_1 = (\partial_i u, \partial_i u)^{1/2}, \quad (2.10)$$

using the summation convention.

The previously defined function spaces are also used for vector valued functions $\mathbf{u} = (u_1, \dots, u_d)^T \in \mathbb{R}^d$, which will be denoted using boldface type. For instance, the space of square integrable vector valued functions is defined by

$$\mathbf{L}^2(\Omega) = \{\mathbf{u} \mid \mathbf{u} \in [L^2(\Omega)]^d\}. \quad (2.11)$$

For functions $\mathbf{u}, \mathbf{v} \in \mathbf{L}^2(\Omega)$ the inner product is naturally defined as

$$(\mathbf{u}, \mathbf{v}) = \int_{\Omega} \mathbf{u} \cdot \mathbf{v} \, d\Omega, \quad (2.12)$$

which defines an associated \mathcal{L}^2 norm

$$\|\mathbf{u}\|_2 = (\mathbf{u}, \mathbf{u})^{1/2}. \quad (2.13)$$

These definitions are easily extended to Hilbert spaces $\mathbf{H}^1(\Omega)$ of vector valued functions and associated norms.

Finite element discretization typically employs a partitioning of the spatial domain Ω into disjoint, open subdomains Ω_e (elements) each having a boundary $\partial\Omega_e$ on which \mathbf{n} is the outward normal unit vector, see Figure 2.1. In the interior of the domain Ω elements intersect pairwise in common interfaces. The partitioning defines the following unions

$$\tilde{\Omega} = \bigcup_e \Omega_e \quad (2.14)$$

$$\tilde{\Gamma} = \bigcup_e \partial\Omega_e = \bigcup_i \Gamma_i, \quad (2.15)$$

where $\tilde{\Omega}$ is the union of all element interiors, $\tilde{\Gamma}$ is the union of all element boundaries and Γ_i are element interfaces. On a partitioned domain, a space $V(\tilde{\Omega}) \subset L^2(\Omega)$ can be defined containing functions that are piecewise continuous on elements but discontinuous across element boundaries. These so-called broken function spaces are formally defined by

$$V(\tilde{\Omega}) = \left\{ v \in L^2(\tilde{\Omega}) : v \in H^1(\Omega_e) \, \forall e \right\}. \quad (2.16)$$

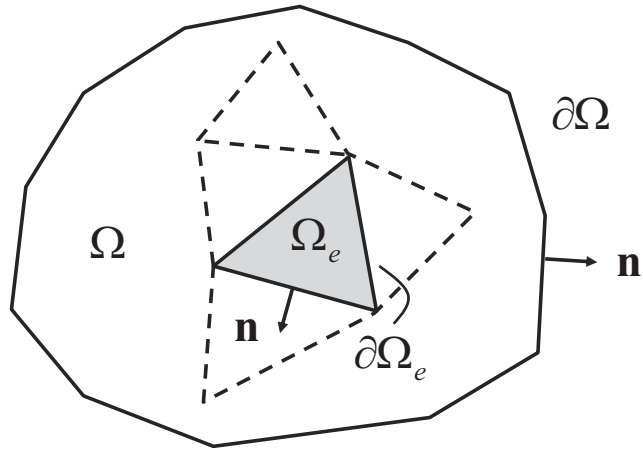


Figure 2.1: Schematic of finite element partitioning.

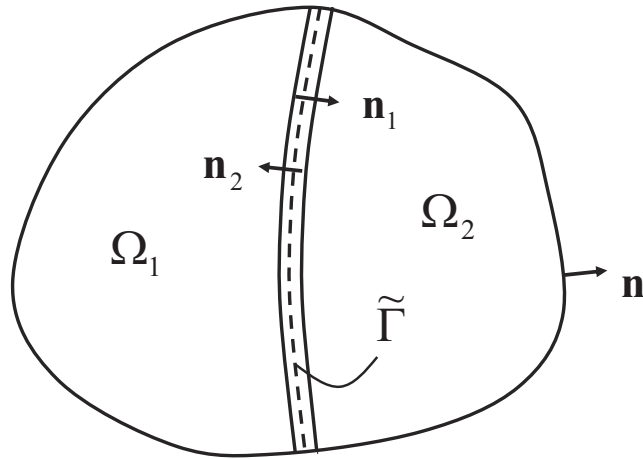


Figure 2.2: Schematic of broken (discontinuous) function space.

On an element boundary functions $v \in V(\tilde{\Omega})$ are left undefined, but traces v^- and v^+ are given by

$$v^\pm = \lim_{\epsilon \downarrow 0} v(\mathbf{x} \pm \epsilon \mathbf{n}) \quad \text{for } \mathbf{x} \in \partial\Omega_e. \quad (2.17)$$

On an exterior boundary Γ the trace v^+ is not defined but simply set to $v^+ = v^-$, for convenience. Using the above trace definitions, the average and jump of functions v on an element boundary $\partial\Omega_e$ are defined as, respectively,

$$\{v\} = \frac{1}{2}(v^+ + v^-), \quad (2.18)$$

and

$$[[v]] = (v^- - v^+) \mathbf{n}, \quad (2.19)$$

where the definition of v^+ on exterior boundaries implies that $[[v]] = 0$ on Γ . Note that, unlike the average $\{v\}$, the jump $[[v]]$ is a vector quantity. For vector valued functions $\mathbf{v} \in \mathbf{V}(\tilde{\Omega})$ the jump involves the vector product of \mathbf{v} with \mathbf{n} .

Frequently, spaces will be considered containing functions defined on $\tilde{\Gamma}$ having a unique value on element interfaces. For example, $L^2(\tilde{\Gamma})$ denotes the space of square integrable functions on $\tilde{\Gamma}$. A subspace concerns the trace of the Hilbert space $H^1(\Omega)$ on $\tilde{\Gamma}$ which is denoted by

$$\bar{U}(\tilde{\Gamma}) = \left\{ \bar{u} \in H^{1/2}(\tilde{\Gamma}) : \bar{u} \in L^2(\Gamma_i) \quad \forall i \right\}, \quad (2.20)$$

where the space $H^{1/2}$ is a fractional Hilbert space. In the sequel, a bar will be used to denote functions defined on interfaces. Functions $\bar{u} \in \bar{U}$ are C^0 continuous in the sense that

$$\lim_{\epsilon \rightarrow 0} \bar{u}(\mathbf{x} + \epsilon \mathbf{t}) = \bar{u}(\mathbf{x}) \quad \text{for } \mathbf{x} \in \tilde{\Gamma}, \quad (2.21)$$

where \mathbf{t} is any unit vector tangent to $\partial\Omega_e$ in that $\mathbf{t} \cdot \mathbf{n} = 0$. These trace spaces will play a prominent role in this thesis.

2.1.2 Variational formulations

The next step of the discretization process involves the representation of the underlying mathematical equations in terms of discrete functions, which is in fact a fundamental issue in finite element approximation. Many problems in physics may be formulated in terms of a variational principle, and classical finite element methods exploit this property to construct approximate solutions. In this respect, it is noteworthy to mention that all flow problems

encountered in geophysical fluid dynamics can be stated as a variational principle, see for instance Salmon [76].

Potential flow, for instance, is a minimizer of the total kinetic energy in the domain Ω [14]. The potential flow problem, Equations (2.1) and (2.2), is therefore expressed alternatively as a minimization problem

$$\min_{\mathbf{u}, \phi} J = \int_{\Omega} \frac{1}{2} \mathbf{u} \cdot \mathbf{u} \, d\Omega + \int_{\Omega} \phi (\nabla \cdot \mathbf{u} - f) \, d\Omega - \int_{\Gamma_h} \phi (\mathbf{u} \cdot \mathbf{n} - h) \, d\Gamma, \quad (2.22)$$

where \mathbf{u} and ϕ belong to the general solution spaces \mathbf{C}^{∞} and C^{∞} , respectively, and the functional J constitutes the total kinetic energy in Ω with the continuity constraint Equation (2.2) and the Neumann boundary condition Equation (2.4) enforced through a Lagrange multiplier ϕ . The functional J attains its minimum where the variation δJ is zero for arbitrary but small variations $\delta \mathbf{u}$ and $\delta \phi$. Taking the variation of J and using partial integration, this gives the following condition for the minimum

$$\begin{aligned} \delta J = \int_{\Omega} (\mathbf{u} - \nabla \phi) \cdot \delta \mathbf{u} \, d\Omega + \int_{\Omega} (\nabla \cdot \mathbf{u} - f) \delta \phi \, d\Omega \\ - \int_{\Gamma_h} (\mathbf{u} \cdot \mathbf{n} - h) \delta \phi \, d\Gamma = 0. \end{aligned} \quad (2.23)$$

For $\phi = g$ and $\delta \phi = 0$ on Γ_g , the variational form Equation (2.23) is fully equivalent with Equations (2.1) to (2.4) with the potential function ϕ being identified as the Lagrange multiplier enforcing continuity and the Neumann boundary condition.

Variational formulations may be used to bypass the exact solution of a problem by satisfying the model equations in a weak sense only. While giving identical results for the exact solution space, variational formulations also allow spaces having less stringent continuity requirements. For instance, the functional (2.22) is formally defined for any $\mathbf{u} \in \mathbf{H}^1(\Omega)$ and $\phi \in L^2(\Omega)$ which can be exploited to construct approximate solutions. Supposing that \mathbf{u} and ϕ are approximated in finite dimensional spaces $\mathbf{V} \subset \mathbf{H}^1(\Omega)$ and $Q \subset L^2(\Omega)$, respectively, Equation (2.23) may be restated as: find $\mathbf{u} \in \mathbf{V}$ and $\phi \in Q$ such that

$$\begin{aligned} \int_{\Omega} (\mathbf{u} - \nabla \phi) \cdot \mathbf{v} \, d\Omega + \int_{\Omega} (\nabla \cdot \mathbf{u} - f) q \, d\Omega \\ - \int_{\Gamma_h} (\mathbf{u} \cdot \mathbf{n} - h) q \, d\Gamma = 0 \quad \forall \mathbf{v} \in \mathbf{V} \quad \forall q \in Q, \end{aligned} \quad (2.24)$$

where it has been assumed that ϕ satisfies the Dirichlet boundary condition and functions q vanish on Γ_g . Obviously, Equation (2.24) is consistent with the strong form of the problem as it is also satisfied by the exact solution

(\mathbf{u}_e, ϕ_e) . This implies Galerkin orthogonality of the discrete error

$$\int_{\Omega} (\mathbf{e}_u - \nabla e_\phi) \cdot \mathbf{v} \, d\Omega = 0 \quad \forall \mathbf{v} \in \mathbf{V}, \quad (2.25)$$

$$\int_{\Omega} \nabla \cdot \mathbf{e}_u q \, d\Omega - \int_{\Gamma_h} \mathbf{e}_u \cdot \mathbf{n} q \, d\Gamma = 0 \quad \forall q \in Q, \quad (2.26)$$

where $\mathbf{e}_u = \mathbf{u} - \mathbf{u}_e$ and $e_\phi = \phi - \phi_e$ are the discrete errors of the velocity and the potential function, respectively. Letting \mathbf{V} and Q approach the exact solution spaces, these errors can be made arbitrary small provided that the Ladyshenskaya-Babuška-Brezzi (LBB) condition is satisfied [8]. This condition reads: there exists a mesh-independent constant $\gamma > 0$ such that

$$\sup_{\mathbf{v} \in \mathbf{V}} \frac{(\nabla q, \mathbf{v})}{\|\mathbf{v}\|_2} \geq \gamma \|\nabla q\|_2 \quad \forall q \in Q. \quad (2.27)$$

Satisfaction of the LBB condition requires that the gradient ∇q is not orthogonal to the velocity space \mathbf{V} for non-trivial functions $q \in Q$ [30]. For a proper choice of \mathbf{V} and Q , such that the inequality given in Equation (2.27) holds, the approximate solution will converge to the exact solution if the solution spaces are refined². Variational formulations are therefore the natural starting point for finite element discretization.

2.2 Galerkin methods

Equation (2.24) is a mixed variational form as it contains both \mathbf{u} and ϕ as dependent variables. A further reduction of the problem is possible by expressing \mathbf{u} in terms of ϕ directly in which case the mixed form becomes *irreducible*. Of particular interest in this thesis are continuous and discontinuous Galerkin methods which are discussed next.

2.2.1 Continuous Galerkin method

A continuous Galerkin (CG) method for the potential flow problem is obtained by setting $\mathbf{u} = \nabla \phi$ in Equation (2.24) directly which is effected by choosing $\mathbf{V} = \nabla Q$. Consider therefore continuous function spaces Q and Q_g defined by, respectively,

$$Q = \left\{ q \in H^1(\tilde{\Omega}) : q \in P(\Omega_e) \, \forall e \right\}, \quad (2.28)$$

$$Q_g = \left\{ q \in H^1(\tilde{\Omega}) : q \in P(\Omega_e) \, \forall e, \, q = g \text{ on } \Gamma_g \right\}, \quad (2.29)$$

where $P(\Omega_e)$ is a set of finite element basis functions defined on subdomains Ω_e . The space Q_g only differs from Q in that the Dirichlet boundary

²In practice this means that the resolution of the computational mesh will be increased.

conditions are satisfied. The variational problem becomes: find $\phi \in Q_g$ such that

$$\int_{\tilde{\Omega}} (\nabla^2 \phi - f) q d\Omega - \int_{\Gamma_h} (\nabla \phi \cdot \mathbf{n} - h) q d\Gamma = 0 \quad \forall q \in Q. \quad (2.30)$$

As functions ϕ are only C^0 continuous the second derivative term can, in general, not be evaluated directly. Integration by parts of this term leads to

$$\int_{\tilde{\Omega}} \nabla^2 \phi q d\Omega = \sum_e \int_{\partial\Omega_e} \nabla \phi \cdot \mathbf{n} q d\Gamma - \int_{\tilde{\Omega}} \nabla \phi \cdot \nabla q d\Omega, \quad (2.31)$$

where \sum_e denotes summation over all elements. As a crucial step, the resulting gradient terms on element boundaries are assumed weakly continuous which requires that

$$\sum_e \int_{\partial\Omega_e} \nabla \phi \cdot \mathbf{n} q d\Gamma = \int_{\Gamma_h} \nabla \phi \cdot \mathbf{n} q d\Gamma \quad \forall q \in Q. \quad (2.32)$$

Using Equations (2.31) and (2.32), Equation (2.30) can be recast into: find $\phi \in Q_g$ such that

$$\int_{\tilde{\Omega}} \nabla \phi \cdot \nabla q d\Omega + \int_{\tilde{\Omega}} f q d\Omega = \int_{\Gamma_h} h q d\Gamma \quad \forall q \in Q. \quad (2.33)$$

As the general Equation (2.23), this variational form is consistent with the strong form of the problem which implies Galerkin orthogonality of the error

$$\int_{\tilde{\Omega}} \nabla e \cdot \nabla q d\Omega = 0 \quad \forall q \in Q, \quad (2.34)$$

where the error $e = \phi - \phi_e$.

The CG method has a number of properties marking its ability to construct approximate solutions. To highlight just one important property, it is noted that Equation (2.33) is also obtained from the following minimization problem

$$\min_{\phi \in Q_g} J = \int_{\tilde{\Omega}} \frac{1}{2} \nabla \phi \cdot \nabla \phi d\Omega + \int_{\tilde{\Omega}} f \phi d\Omega - \int_{\Gamma_h} h \phi d\Gamma, \quad (2.35)$$

By straightforward algebra it can be shown that the difference between functionals J of the discrete solution and the exact solution is given by

$$J(\phi) - J(\phi_e) = \int_{\tilde{\Omega}} \frac{1}{2} \nabla e \cdot \nabla e d\Omega, \quad (2.36)$$

which implies that $J(\phi) \geq J(\phi_e)$. As a consequence, discrete solutions satisfying Equation (2.33) are optimal in the sense that for a given finite element space Q the error measured in the \mathcal{H}^1 semi-norm is minimum

$$\|\nabla e\| = \min_{\phi \in Q_g} \|\nabla(\phi - \phi_e)\|. \quad (2.37)$$

A priori estimates for the error can be obtained from local Taylor-series expansions of the solution leading to the general result

$$\|e\|_m \leq Ch_e^{k+1-m} \|\phi\|_{k+1}, \quad (2.38)$$

where $h_e = \text{diam}(\Omega_e)$ is a measure of the element size, C is a constant depending on the element shape and m addresses the type of norm being considered [42]. For linear polynomials $k = 1$ the \mathcal{L}^2 norm of the error converges quadratically with the element size

$$\|e\|_2 \leq Ch_e^2 \|\nabla^2 \phi\|_2, \quad (2.39)$$

while the corresponding \mathcal{H}^1 semi-norm of the error converges linearly,

$$|e|_1 \leq Ch_e \|\nabla^2 \phi\|_2. \quad (2.40)$$

These convergence rates are considered sufficient for general environmental fluid mechanics applications.

2.2.2 Discontinuous Galerkin method

A discontinuous Galerkin (DG) method for the potential flow problem is obtained by approximating the potential function ϕ in a broken function space. For certain problems, notably the advection-diffusion equation of the next chapter, the weaker continuity requirements pose some advantages that may be exploited to obtain improved solutions. To this end spaces Q and Q_g are defined as, respectively,

$$Q = \left\{ q \in L^2(\tilde{\Omega}) : q \in P(\Omega_e) \ \forall e \right\}, \quad (2.41)$$

$$Q_g = \left\{ q \in L^2(\tilde{\Omega}) : q \in P(\Omega_e) \ \forall e, \ q = g \text{ on } \Gamma_g \right\}, \quad (2.42)$$

where $P(\Omega_e)$ is a set of finite element basis functions defined on elements. Introducing auxiliary interface terms $\bar{\phi} : \tilde{\Gamma} \rightarrow \mathbb{R}$ and $\bar{\mathbf{u}} : \tilde{\Gamma} \rightarrow \mathbb{R}^d$, Equation (2.24) may be integrated by parts giving the following variational problem: given a source term f , find $\phi \in Q_g$ and $\mathbf{u} \in \mathbf{V} = \mathbf{L}^2(\tilde{\Omega})$ such that

$$\begin{aligned} \int_{\tilde{\Omega}} \mathbf{u} \cdot \mathbf{v} \, d\Omega + \int_{\tilde{\Omega}} \phi \nabla \cdot \mathbf{v} \, d\Omega - \sum_e \int_{\partial\Omega_e} \bar{\phi} \mathbf{n} \cdot \mathbf{v} \, d\Gamma - \int_{\tilde{\Omega}} \mathbf{u} \cdot \nabla q \, d\Omega \\ + \sum_e \int_{\partial\Omega_e} \bar{\mathbf{u}} \cdot \mathbf{n} q \, d\Gamma - \int_{\tilde{\Omega}} f q \, d\Omega = 0 \quad \forall q \in Q, \quad \forall \mathbf{v} \in \mathbf{V}, \end{aligned} \quad (2.43)$$

where it has been assumed that $\bar{\phi}$ and $\bar{\mathbf{u}}$ satisfy the respective boundary conditions. Setting $\mathbf{v} = \nabla q$ for all $q \in Q$ and partial integration yields the

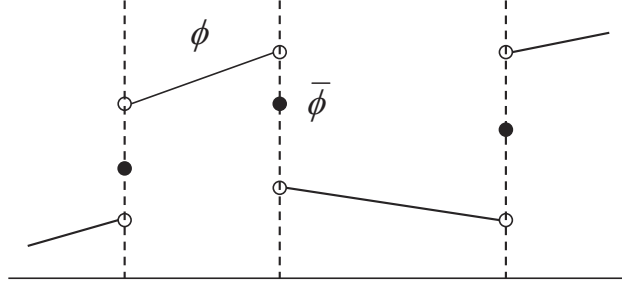


Figure 2.3: The discontinuous field ϕ and the interface function $\bar{\phi}$.

primal form of the DG method: given f , find $\phi \in Q_g$ such that

$$\int_{\tilde{\Omega}} \nabla \phi \cdot \nabla q \, d\Omega + \sum_e \int_{\partial\Omega_e} (\bar{\phi} - \phi) \mathbf{n} \cdot \nabla q \, d\Gamma - \sum_e \int_{\partial\Omega_e} \bar{\mathbf{u}} \cdot \mathbf{n} q \, d\Gamma + \int_{\tilde{\Omega}} f q \, d\Omega = 0 \quad \forall q \in Q. \quad (2.44)$$

The above formulation closely resembles that in Arnold et al. [1] although the format of Equation (2.44) is slightly different, with a view to later elaborations.

To complete the DG formulation, the interface variables $\bar{\phi}$ and $\bar{\mathbf{u}}$ have to be expressed in terms of the function ϕ in neighbouring elements, see Figure 2.3. For consistency, $\bar{\phi}$ and $\bar{\mathbf{u}}$ have to approach the exact solution in the continuous limit. Conservation requires that jumps $[[\bar{\phi}]]$ and $[[\bar{\mathbf{u}}]]$ are zero. An example of a conservative and consistent method is the interior penalty (IP) method which has the following definitions for the interface terms

$$\bar{\phi} = \{\phi\}, \quad (2.45)$$

$$\bar{\mathbf{u}} = \{\nabla \phi\} - \frac{\alpha}{h_e} [[\phi]], \quad (2.46)$$

where $h_e = \text{diam}(\Omega_e)$ is a measure of the local element size and α is a suitably chosen $\mathcal{O}(1)$ penalty parameter which is required for stability. The resulting weak formulation is similar to that of the CG method except for the inclusion of the interface terms. For continuous function spaces these terms vanish reducing Equation (2.44) to the CG method.

As can be shown by straightforward algebra, the DG-IP method minimizes the following error functional

$$\min_{\phi \in Q_g} \int_{\tilde{\Omega}} \frac{1}{2} \nabla e \cdot \nabla e \, d\Omega - \int_{\tilde{\Gamma}} [[e]] \cdot \{\nabla e\} \, d\Gamma + \int_{\tilde{\Gamma}} \frac{1}{2} \frac{\alpha}{h_e} [[e]] \cdot [[e]] \, d\Gamma, \quad (2.47)$$

where the discrete error is denoted $e = \phi - \phi_e$. This implies that the solution is optimal in the sense that for a given function space the above

error functional is minimum. The error functional highlights the need for the penalty term α as, due to the second term, the functional may become negative in which case it does not give a norm. Provided that the stability constant α is not too large, a priori error estimates for the DG-IP method basically share the general convergence result of the CG method given by Equation (2.38), although the derivation is far more complicated [1].

2.2.3 Galerkin interface stabilization method

A practical issue with the use of DG methods is the proliferation of the number of degrees of freedom for a given number of elements relative to the CG method. If a variational problem involves the solution of implicit systems, the DG method will be outperformed by the corresponding CG method on the same mesh. In this thesis, reduced DG formulations will be pursued having the number of unknowns of a CG method while preserving the attractive properties of discontinuous methods. The ensuing method is coined Galerkin interface stabilization (GIS) method.

The starting point for the GIS method is the DG formulation given by Equation (2.44) in which the interface state $\bar{\phi}$ is an independent, global variable that belongs to a trace space \bar{Q} defined by

$$\bar{Q} = \left\{ \bar{q} \in H^{1/2}(\tilde{\Gamma}) : \bar{q} \in P(\Gamma_i) \forall i \right\}, \quad (2.48)$$

where $P(\Gamma_i)$ is a set of finite element basis functions defined on element interfaces. In addition, a related space \bar{Q}_g is used which only differs from \bar{Q} in the sense that the boundary conditions on Γ_g are satisfied. According to the above definitions, the interface state $\bar{\phi}$ is unique on element interfaces.

The interface flux $\bar{\mathbf{u}}$ is left undefined, other than that it must be expressed in terms of $\bar{\phi}$ and quantities belonging to an element. It may not depend on quantities from a neighbouring element, the reason for which will become apparent shortly. This definition renders $\bar{\mathbf{u}}$ discontinuous across element interfaces. A constraint for the interface field $\bar{\phi}$ is obtained by requiring weak continuity of the flux and weak satisfaction of the Neumann boundary condition, which is expressed as

$$\sum_e \int_{\partial\Omega_e} \bar{\mathbf{u}} \cdot \mathbf{n} \bar{q} d\Gamma = \int_{\Gamma_h} h \bar{q} d\Gamma \quad \forall \bar{q} \in \bar{Q}. \quad (2.49)$$

Combination of Equations (2.44) and (2.49) gives the following variational problem: given the source term f and the boundary condition h , find $\phi \in Q$ and $\bar{\phi} \in \bar{Q}_g$ such that

$$\begin{aligned} \int_{\tilde{\Omega}} \nabla \phi \cdot \nabla q d\Omega + \sum_e \int_{\partial\Omega_e} (\bar{\phi} - \phi) \mathbf{n} \cdot \nabla q d\Gamma + \sum_e \int_{\partial\Omega_e} \bar{\mathbf{u}} \cdot \mathbf{n} (\bar{q} - q) d\Gamma \\ + \int_{\tilde{\Omega}} f q d\Omega = \int_{\Gamma_h} h \bar{q} d\Gamma \quad \forall q \in Q, \quad \forall \bar{q} \in \bar{Q}_g. \end{aligned} \quad (2.50)$$

Obviously, the number of unknowns has increased compared to the standard DG method due to the introduction of the interface function $\bar{\phi}$ in addition to the discontinuous field ϕ . However, as the flux $\bar{\mathbf{u}}$ only depends on the interface term $\bar{\phi}$ and terms particular to an element, ϕ can be eliminated from Equation (2.50) in favour of the global variable $\bar{\phi}$.

To demonstrate this reduction procedure consider a flux, reminiscent of the IP method, which has the required property

$$\bar{\mathbf{u}} = \nabla\phi + \frac{\alpha}{h_e} (\bar{\phi} - \phi) \mathbf{n} \quad \text{on } \partial\Omega_e. \quad (2.51)$$

Inserting this expression in Equation (2.50) yields: given the source term f and boundary condition h , find $\phi \in Q$ and $\bar{\phi} \in \bar{Q}_g$ such that

$$\begin{aligned} \int_{\tilde{\Omega}} \nabla\phi \cdot \nabla q \, d\Omega + \sum_e \int_{\partial\Omega_e} (\bar{\phi} - \phi) \mathbf{n} \cdot \nabla q \, d\Gamma \\ + \sum_e \int_{\partial\Omega_e} \nabla\phi \cdot \mathbf{n} (\bar{q} - q) \, d\Gamma + \sum_e \int_{\partial\Omega_e} \frac{\alpha}{h_e} (\bar{\phi} - \phi) (\bar{q} - q) \, d\Gamma \\ + \int_{\tilde{\Omega}} f q \, d\Omega = \int_{\Gamma_h} h \bar{q} \, d\Gamma \quad \forall q \in Q, \quad \forall \bar{q} \in \bar{Q}. \end{aligned} \quad (2.52)$$

Setting $\bar{q} = 0$ yields a set of local problems on each element Ω_e with weakly imposed Dirichlet boundary conditions $\bar{\phi}$. These local problems can be solved to express ϕ in terms of $\bar{\phi}$. Next, setting $q = 0$ and substituting the local expressions for ϕ (static condensation), yields a global system of equations for $\bar{\phi}$ which has the same structure as that of the associated CG method. After solution of the global problem, the field ϕ is found by local back substitution. Equation 2.52 is equivalent to the following minimization problem,

$$\begin{aligned} \min_{\phi \in Q, \bar{\phi} \in \bar{Q}_g} J = \int_{\tilde{\Omega}} \frac{1}{2} \nabla\phi \cdot \nabla\phi \, d\Omega + \sum_e \int_{\partial\Omega_e} (\bar{\phi} - \phi) \mathbf{n} \cdot \nabla\phi \, d\Gamma \\ + \sum_e \int_{\partial\Omega_e} \frac{1}{2} \frac{\alpha}{h_e} (\bar{\phi} - \phi)^2 \, d\Gamma + \int_{\tilde{\Omega}} f \phi \, d\Omega - \int_{\Gamma_h} h \bar{\phi} \, d\Gamma, \end{aligned} \quad (2.53)$$

which clearly shows the variational structure of the GIS method.

In the context of the potential flow example, the above procedure may seem tedious as the corresponding CG formulation, Equation (2.33), is already stable. However, the procedure may be exploited to stabilize advection dominated flow and transport problems while inheriting the favourable properties of DG methods. Moreover, for an appropriate choice of the interface flux, the LBB condition for mixed problems given in Equation (2.27) may be circumvented. The reduction of DG formulations using interface functions will therefore be a recurring theme in the next chapters.

2.3 The discrete problem

For practical computing variational problems have to be transformed into algebraic systems that can be solved on a computer. In this section an overview of basic finite element spatial discretization and time integration methods is given with particular emphasis on those methods that will be used in the next chapters.

2.3.1 Mesh partitioning

In order to define the appropriate discrete subspaces the domain of interest must be partitioned into elements first. A finite element mesh commonly consists of triangles and quadrilaterals in \mathbb{R}^2 or tetrahedrons, prisms and hexahedrons in \mathbb{R}^3 . The construction of a mesh is performed by a mesh generator, which partitions the domain Ω into elements Ω_e satisfying specified criteria. This thesis uses a mesh generator developed by Segal and Praagman [80] of which an example triangular mesh is shown in Figure 2.4. To a certain extent, the size and shape of the elements may be chosen freely. This enables the user to accurately resolve complex geometrical features such as coastlines, irregular sea bed topography or man-made structures (breakwaters, barriers). Moreover, the resolution of the mesh may be increased in regions of specific interest or in parts of the domain where sharp gradients of the solution are expected. For a thorough discussion on this topic see Gresho et al. [28]. Advanced codes employ adaptive mesh refinement where, driven by the discrete error, the element density increases automatically in regions giving the largest contribution to the global error (h -refinement). Another adaptive strategy is to move the nodes, while preserving the mesh topology, in such a way as to minimize the discrete error [3]. These adaptive techniques are however left out of consideration here.

Following the construction of a mesh, a discrete finite dimensional solution space is defined by assigning to each element a set $P(\Omega_e)$ of elementary basis functions. The combination of the shape of an element and the set of basis functions defines the element type. The set of Lagrange polynomial basis functions $P^k(\Omega_e)$ is an obvious choice where the polynomial order k may be chosen a priori or may depend adaptively on the solution (p -refinement). Although finite element methods are not restricted to using polynomials [28], it is certainly the most appropriate choice for common applications. One advantage of using polynomials is their compact support, i.e. the basis functions have a value of one in the associated node of the underlying mesh and a value of zero in all other nodes. This restricts the connectivity of a node to its immediate neighbour nodes. Figures 2.5 and 2.6 list some common two- and three-dimensional polynomial elements, showing the nodal locations of the associated basis functions.

For the mixed problem of Section 2.1.2 the function spaces representing

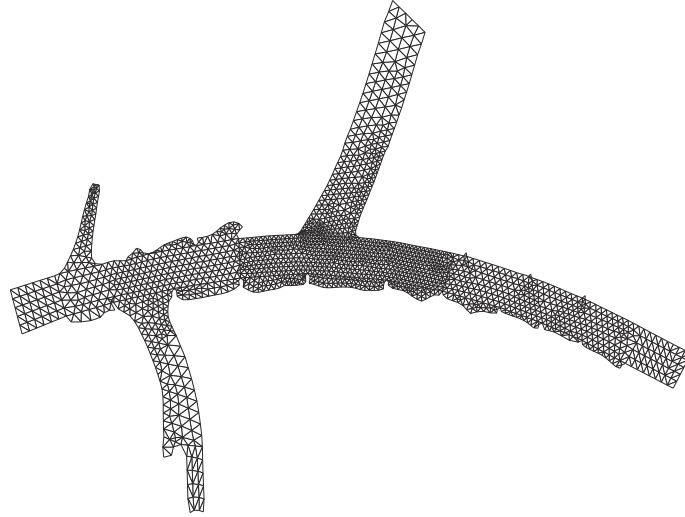


Figure 2.4: *Example of finite element mesh: section of the river Lek, The Netherlands.*

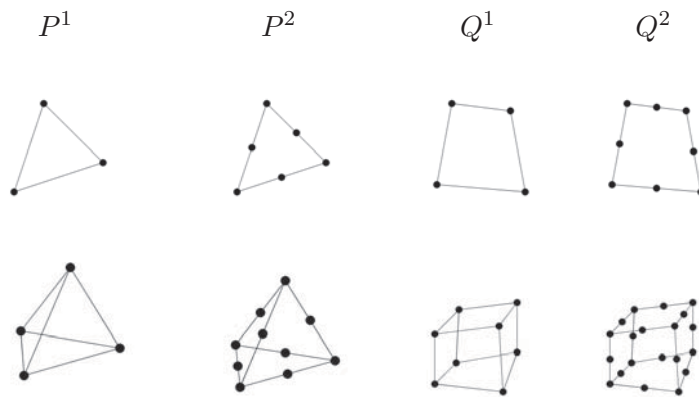


Figure 2.5: *Linear and quadratic two- and three-dimensional continuous elements.*

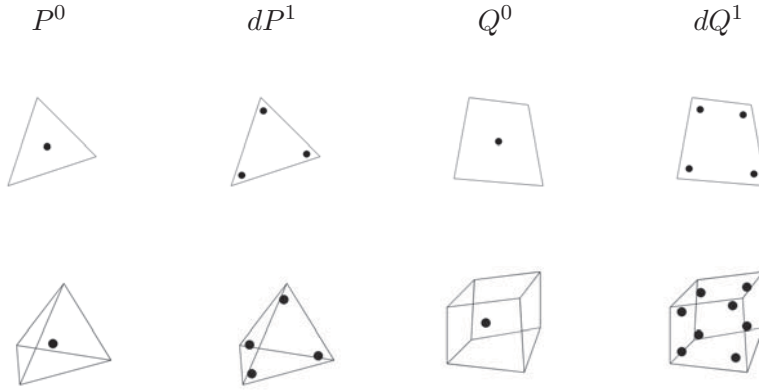


Figure 2.6: *Linear and quadratic two- and three-dimensional discontinuous elements.*

\mathbf{u} and ϕ may not be chosen independently due to the LBB stability condition. Practically, this implies that the discrete velocity space \mathbf{V} used in Equation (2.24) should be taken sufficiently large compared to the space Q for the potential function. The approximation of the velocity \mathbf{u} and the potential ϕ in equal order polynomial function spaces is generally unstable. Some simple, yet stable mixed element pairs are shown in Figure 2.7. The $P^1 - P^0$ element on simplexes has a continuous piecewise linear velocity potential ϕ and piecewise constant velocity \mathbf{u} . For this element $\mathbf{u} = \nabla\phi$ exactly which renders the associated variational form irreducible. Another stable mixed finite element pair is the MINI element [8], which has continuous piecewise linear \mathbf{u} and ϕ where \mathbf{u} is enriched with piecewise linear or cubic functions having a value of one in the element barycenter and a value of zero on element boundaries, also referred to as ‘bubble’-functions. The bubble degrees of freedom may be eliminated from the variational problem yielding a system of equations for (\mathbf{u}, ϕ) for the global degrees of freedom only [81]. In the sequel, this idea will be extended to DG methods where the reduction of the problem using interface variables, as in section 2.2.3, yields a similar stabilizing effect.

2.3.2 Time stepping

Frequently, time dependent model equations will be considered where the solution evolves in time. Also the geometry of the domain or the position of the boundary may vary in time, for instance in case of flooding and drying or free-surface motion. To demonstrate some principles, the following abstract time dependent problem is considered on a fixed domain Ω : at time t , find $\phi \in U$ such that

$$\int_{\Omega} \frac{\partial \phi}{\partial t} u \, d\Omega = \mathcal{B}(\phi, u) \quad \forall u \in U, \quad (2.54)$$

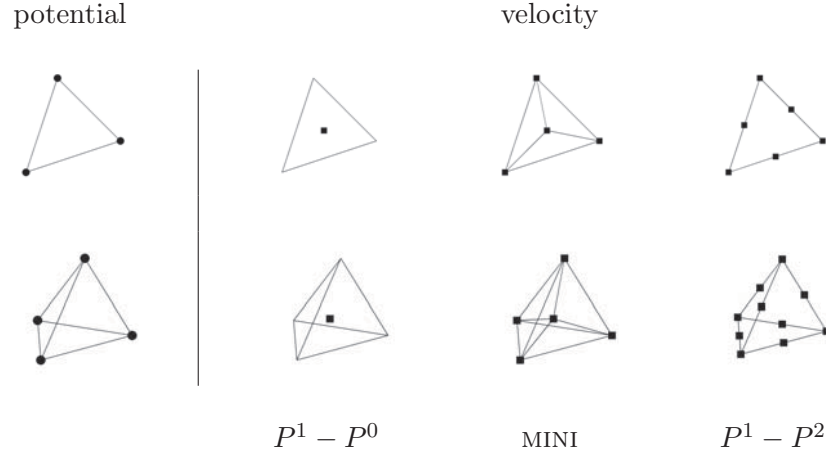


Figure 2.7: Some stable two- and three-dimensional mixed-element combinations for the potential (●) and velocity (■) degrees of freedom.

where U is an appropriate finite element function space defined on $\tilde{\Omega}$ and \mathcal{B} is a given bi-linear form including the necessary boundary conditions. The solution ϕ has to be determined on the time interval $I = (t_0, t_N)$ using the initial condition $\phi(t_0) = \phi_0$.

A time discrete weak form of Equation (2.54) may be obtained by partitioning the time interval I into N sub-intervals using a sequence of discrete time levels: $I = (t_0, t_1, \dots, t_{N-1}, t_N)$. Letting I_n denote the sub-interval (t_n, t_{n+1}) and V a function space defined on the space-time ‘slab’ $\Omega \times I_n$ the discrete weak formulation becomes [87]: given ϕ_n^- , find $\phi \in V$ such that

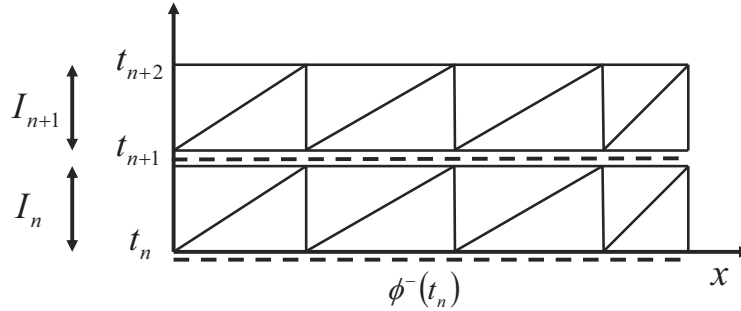
$$\int_{I_n} \int_{\Omega} \frac{\partial \phi}{\partial t} v \, d\Omega \, dt + \int_{\Omega} (\phi_n - \phi_n^-) v \, d\Omega = \int_{I_n} \mathcal{B}(\phi, v) \, dt \quad \forall v \in V, \quad (2.55)$$

where ϕ_n^- is the solution at time t_n obtained from the previous substep, see Figure 2.8. The ‘initial’ condition ϕ_n^- is not imposed by constraining the function space V but enforced weakly by terms containing the jump discontinuity at the time level $t = t_n$. A practical issue with the above space-time formulation is that it adds an extra dimension to the discrete function space which increases the computational effort, except when using basis functions that are piecewise constant in time.

A more practical approach is therefore to discretize Equation (2.54) first in time and then in space. Using for instance the θ -method to step in time, the discrete weak formulation becomes: given ϕ_n , find $\phi_{n+1} \in U$ such that

$$\int_{\Omega} \frac{\phi_{n+1} - \phi_n}{\Delta t} u \, d\Omega = \mathcal{B}(\phi_{n+\theta}, u) \quad \forall u \in U, \quad (2.56)$$

where the time step Δt is the size of the interval I_n , the time integration parameter $\theta \in [0; 1]$ and $\phi_{n+1} = (1 - \theta) \phi_n + \theta \phi_{n+1}$. The scheme may be

Figure 2.8: *Example of a space-time mesh.*

written more compactly as: given ϕ_n , find $\phi_{n+\theta} \in U$ such that

$$\int_{\Omega} \frac{\phi_{n+\theta} - \phi_n}{\theta \Delta t} u \, d\Omega = \mathcal{B}(\phi_{n+\theta}, u) \quad \forall u \in U, \quad (2.57)$$

after which the solution at time level $n + 1$ is found by extrapolation

$$\phi_{n+1} = \phi_n + (\phi_{n+\theta} - \phi_n) / \theta. \quad (2.58)$$

Equation (2.57) has the advantage that all unknowns are expressed at the same time level $n + \theta$. Note that this scheme has a similar form as the space-time formulation Equation (2.55) if the latter uses basis functions that are piecewise constant in time. The cases $\theta = 0$ and $\theta = 1$ yield the forward and backward Euler schemes, respectively, which are both first-order accurate. The forward Euler scheme is conditionally stable only while the backward Euler scheme is strongly stable, smoothing rough initial data. Second order accuracy is obtained for $\theta = \frac{1}{2}$ (Crank-Nicolson scheme) but the method will only be weakly stable (small perturbations are not smoothed).

A time integration scheme combining second-order accuracy and strong stability is the fractional-step (FS) method of Bristeau et al. [9]. Originally developed to deal with operator splitting, this scheme has proven useful as a pure time stepping method, see Rannacher [72]. On a sequence of three sub-steps $t_n \rightarrow t_{n+\alpha} \rightarrow t_{n+1-\alpha} \rightarrow t_{n+1}$ the one step θ -method is applied using a time integration parameter θ in the first and last steps and a parameter $\theta' = 1 - \theta$ in the middle step. For $\alpha = 1 - 1/\sqrt{2}$ the resulting scheme is second order accurate for any $\theta \in [\frac{1}{2}; 1]$. The choice $\theta = (1 - 2\alpha) / (1 - \alpha)$ has the convenient property that $\alpha\theta = (1 - 2\alpha)\theta'$. The scheme is then easily implemented by using the θ -method of Equation (2.57) with a fixed value of $\theta\Delta t$ while switching to the current θ or θ' during the update, Equation (2.58).

In this thesis the FS method is preferred for time dependent problems requiring a high degree of accuracy. If the time stepping scheme is solely used to obtain stationary solutions, the backward Euler method is selected as its strong damping properties will accelerate convergence towards a steady state.

2.3.3 Matrix form

The discrete function space obtained from the finite element discretization is spanned by N polynomial basis functions $N^i(\mathbf{x})$ having a value of one on the associated node i and zero on any other node $j \neq i$. In this way a discrete function $\phi(\mathbf{x})$ may be represented by a vector $\boldsymbol{\phi} = [\phi^1, \dots, \phi^N]^T$ of nodal values

$$\phi(\mathbf{x}) = \sum_{i=1}^N \phi^i N^i(\mathbf{x}). \quad (2.59)$$

Using this discrete representation, the variational form of Equation (2.33) for instance results in the following matrix system

$$\mathbf{A}(\boldsymbol{\phi}) = \mathbf{b}, \quad (2.60)$$

where the global matrix \mathbf{A} and the right hand side vector \mathbf{b} are given by, respectively,

$$A^{ij} = \int_{\tilde{\Omega}} \nabla N^i \cdot \nabla N^j \, d\Omega, \quad (2.61)$$

$$b^i = - \int_{\tilde{\Omega}} f N^i \, d\Omega + \int_{\Gamma_h} h N^i \, d\Gamma. \quad (2.62)$$

In a practical code the contributions to \mathbf{A} and \mathbf{b} are computed element by element and assembled into a global matrix system by looping over all elements.

The computation of \mathbf{A} and \mathbf{b} involves the integration of functions and derivatives of functions over an element. To this end, the element is mapped onto a standard element defined in reference co-ordinates $\boldsymbol{\chi}$, see Figure 2.9. Expressing the spatial coordinate \mathbf{x} as

$$\mathbf{x}(\boldsymbol{\chi}) = \sum_{i=1}^N \mathbf{x}^i N^i(\boldsymbol{\chi}), \quad (2.63)$$

the derivatives and integrals, appearing in Equation (2.60), are calculated using transformation rules. Analytical integration of functions over the standard element is usually avoided by reverting to discrete integration formulas (Gauss-integration) where the integral of a function $f(\mathbf{x})$ on the element Ω_e is approximated by a summation over discrete integration points \mathbf{x}^j having weights w^j

$$\int_{\Omega_e} f(\mathbf{x}) \, d\Omega \approx \sum_{j=1}^{n_w} w^j f(\mathbf{x}^j) \, \Delta_e, \quad (2.64)$$

where n_w is the number of integration points and Δ_e is the measure of the element. Clearly, the order of the approximation increases with increasing n_w and for a wide range of standard elements formulas have been derived

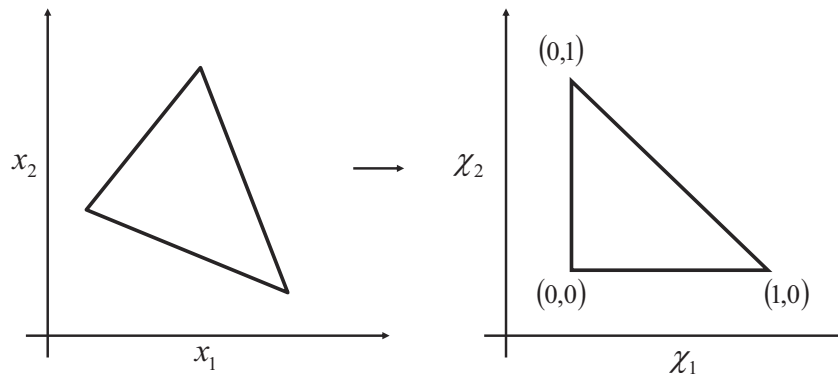


Figure 2.9: Mapping a triangular element (left) onto a standard triangle (right).

giving highly accurate or even exact results for a proper choice of integration points and associated weights. For a range of element types and polynomial orders values for the abscissa \boldsymbol{x}^j and weights w^j are tabulated in Zienkiewicz and Taylor [99].

2.4 The algebraic problem

The solution of algebraic problems resulting from finite element discretization, such as Equation (2.60), involves the inversion of a large system of equations. This part of the solution process is computationally demanding and is largely effected by the chosen type of element. This section considers these aspects in more detail, with particular emphasis on the role of the underlying spatial discretization.

2.4.1 Sparse matrices

Commonly, finite element basis functions have compact support. The nodal basis functions N^i only differ from zero within elements connected to the associated node, and the $N \times N$ global matrix has relatively few non-zero entries. An example of a typical sparsity pattern is given in Figure 2.10. The ‘sparsity’ can be exploited to efficiently store and solve the algebraic system [69]. For example, a matrix \mathbf{A} with a general sparsity pattern as for instance

$$\mathbf{A} = \begin{pmatrix} a_{11} & 0 & a_{13} & 0 \\ 0 & a_{22} & 0 & a_{24} \\ 0 & a_{32} & a_{33} & 0 \\ a_{41} & 0 & a_{43} & a_{44} \end{pmatrix}$$

may be stored in three one-dimensional arrays row , col and beg as

$$\begin{aligned} row &= \{a_{11}, a_{13}, a_{22}, a_{24}, a_{32}, a_{33}, a_{41}, a_{43}, a_{44}\}, \\ col &= \{1, 3, 2, 4, 2, 3, 1, 3, 4\}, \\ beg &= \{1, 3, 5, 7, 10\}, \end{aligned}$$

where row contains all matrix elements of \mathbf{A} in row-order with col pointing to the corresponding column number and beg pointing to the first position of each new row in the array row . The last element of beg is added in order to be able to find the last element of the last row. When solving sparse matrix systems, operations only involving the upper or lower triangular part of a matrix are frequently needed, which requires the position of the diagonal elements in \mathbf{A} . This information is stored in an additional pointer array di containing the positions of the diagonal elements in row . For the above example di is given by

$$di = \{1, 3, 6, 9\}.$$

The above storage scheme, also referred to as compressed sparse row (CSR) format, can be used for matrices with an arbitrary sparsity pattern. For a symmetric matrix the storage requirements may be reduced even further by a factor of about two storing the upper triangular part only. Although the sparsity pattern of matrices resulting from a finite element flow model is generally symmetric, the matrix entries are typically non-symmetric. Techniques to deal efficiently with symmetric matrices are therefore not discussed further here.

With the CSR storage scheme, and for a typical finite element discretization, the matrix-vector multiplication $\mathbf{y} = \mathbf{A}(\mathbf{x})$ can be performed in $\mathcal{O}(N)$ multiplications, with N being the number of unknowns. In an equally efficient way the upper and lower triangular parts of a matrix can be inverted in $\mathcal{O}(N)$ operations without requiring additional storage space. For algorithms performing matrix-vector multiplication and lower-upper inversion a reference is made to van der Ploeg [69].

2.4.2 Solution algorithms

Direct solution of large sparse systems by Gaussian elimination is complicated by the fact that the factorization process causes fill-in of the sparsity structure which progressively increases the computer demands during the elimination. The problem may be alleviated by reordering the variables in such a way that the resulting matrix has a minimum bandwidth (profiling) or leads to a minimum amount of fill in during the elimination (minimum degree). Alternatively, iterative solution techniques may be used where an estimate of the solution is systematically improved using a sequence of matrix-vector multiplications. This not only preserves the original sparse

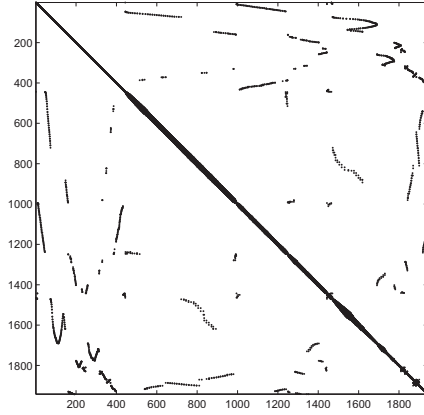


Figure 2.10: *Sparsity pattern of the nodal structure underlying the mesh of the river Lek from Figure 2.4; $N_{\text{node}} = 1942$, $N_{\text{sparse}} = 12700$.*

matrix structure but also enables to quit the solution process as soon as the estimate of the solution has become sufficiently accurate. Originally developed for symmetric and positive definite matrices, iterative methods have been successfully extended to non-symmetric systems during the 1990's. A particularly useful method in the context of flow and transport modelling is the stabilized bi-conjugate gradient method (BICGSTAB) of van der Vorst [93].

The iteration may be stopped as soon as some norm of the residual vector $\mathbf{r} = \mathbf{b} - \mathbf{A}(\phi)$ drops below a prescribed minimum. The type of norm to be used and the corresponding minimum value requires some numerical experimentation. In this thesis the quadratic norm $\|\mathbf{r}\|_2$ is used which has to be a factor ϵ smaller than the initial error norm

$$\|\mathbf{r}\|_2 \leq \epsilon \|\mathbf{b} - \mathbf{A}(\phi_0)\|_2, \quad (2.65)$$

where ϕ_0 is the initial guess of the solution vector. The precise value of the parameter ϵ may depend on the application. In time dependent flow and transport simulations $\epsilon \approx 10^{-4}$ is generally sufficient while direct iteration towards steady state solutions requires a smaller value $\epsilon \approx 10^{-10}$. Depending on the application other norms or stopping criteria may be used.

For a prescribed value of ϵ the number of required iteration steps is determined by the convergence rate which is defined as the relative decrease of the error norm after one iteration step. The convergence rate is related to the spectral condition number of the matrix \mathbf{A} which depends on its eigenvalue distribution. Matrices resulting from the discretization of flow and transport problems are generally ill-conditioned which may lead to low convergence rates or even stagnation of the iterative process. The convergence behaviour may be improved by solving the modified system

$$\mathbf{P} \mathbf{A}(\phi) = \mathbf{P}(\mathbf{b}), \quad (2.66)$$

instead of solving the original Equation (2.60), where the preconditioner \mathbf{P} is an approximation of \mathbf{A}^{-1} with the same storage requirements as \mathbf{A} and whose construction and inversion take at most $\mathcal{O}(N)$ floating point operations. To construct \mathbf{P} an incomplete lower-upper (ILU) decomposition may be performed using the conventional LU factorization process on \mathbf{A} while ignoring the fill-in additional to the initial sparse matrix structure. Compared to other (cheaper) preconditioning techniques, for instance diagonal scaling or Gauss-Seidel iteration, the performance of ILU preconditioning in terms of improved convergence and robustness is generally considered superior [69].

Sparse matrix algorithms may also be applied to solve algebraic systems arising from constrained mixed formulations, for instance Equation (2.24). However, due to the LBB condition, the solution process will be more complicated. Firstly, the coupled variables \mathbf{u} and ϕ need to be approximated in different solution spaces leading to multiple sets of sparsity patterns. This renders the sparse matrix operations less efficient, notably the construction of preconditioners. Secondly, the algebraic structure of constrained (saddle-point) problems leads to an implicit expression for the Lagrange multiplier ϕ in terms of the constrained variable \mathbf{u} . The corresponding diagonal blocks of the matrix system become zero which requires non-standard preconditioning techniques [57]. In this respect, stabilized equal order element pairs offer the advantage that one sparsity pattern serves both variables. Moreover, the stabilization in itself by-passes the saddle-point problem and improves the condition number of the preconditioned system. These advantages are the main motivation for pursuing these type of elements in the next chapters.

2.4.3 Computational aspects

The computational efficiency of a finite element model is determined by the size of the resulting sparse matrix, relative to the number of nodes, and by the convergence rate of the iterative solution process. The number of non-zero sparse matrix entries N_{sparse} determines the number of floating point operations N_{flop} per matrix-vector multiplication. In optimally converging cases, the required number of iterations depends on the number of degrees of freedom N_{dof} according to $\log N_{\text{dof}}$. The number of floating point operations to obtain a solution is therefore proportional to

$$N_{\text{flop}} \sim N_{\text{sparse}} \log N_{\text{dof}}, \quad (2.67)$$

which will determine the total CPU-time needed to obtain the solution. Using this relation, the computer demands to solve the potential flow problem are estimated for the elements listed in Figures 2.5 to 2.7. Given a mesh of N nodes, the corresponding values of N_{dof} and N_{sparse} are listed in Table 2.1. The estimates are based on a regular configuration of elements. It is noted that the interface element (Section 2.2.3) has the same nodal configuration as

	element	P^0	Q^0	P^1	Q^1	dP^1	dQ^1	MINI
2-d	N_{dof}	$2 N$	N	N	N	$6 N$	$4 N$	$5 N$
	N_{sparse}	$8 N$	$5 N$	$7 N$	$9 N$	$24 N$	$20 N$	$49 N$
3-d	N_{dof}	$6 N$	N	N	N	$24 N$	$8 N$	$4 N$
	N_{sparse}	$30 N$	$7 N$	$12 N$	$27 N$	$120 N$	$56 N$	$120 N$

Table 2.1: *Element comparison for the potential flow problem on a mesh of N nodes.*

the corresponding P^1 element. If N is sufficiently large, the factor $\log N_{\text{dof}}$ is almost independent of the element type, and the relative amount of work is indicated by the respective values of N_{sparse} . Depending on the application however, the matrix assembly may also contribute significantly to the total required CPU-time.

Table 2.1 shows that Q^0 elements, which involve the same computational structure as that of finite volume methods, result in a relatively small size of the associated sparse matrix. Continuous P^1 elements are however a good alternative in this respect. Less efficient are the P^0 elements although the relative size of the sparse matrix is still acceptable in two dimensions. On the other hand, the discontinuous dP^1 and dQ^1 elements both lead to a significant increase in the size of the algebraic system rendering these elements impractical for solving implicit equations. However, when used in an explicit time stepping mode, the locally invertible element matrices will offer an advantage compared to continuous elements, which require the inversion of a global matrix. The MINI element is the most uneconomical element of the elements listed in this comparison. However, the inclusion of the velocity space additional to the potential function is indispensable for the Stokes and Navier-Stokes problems rather than for the relatively simple potential flow problem considered here.

2.5 Numerical examples

This section demonstrates some practical aspects of finite element discretization in the context of the potential flow problem. The examples address the convergence rates of several methods in relation to the computational effort.

2.5.1 Flow in an outlet

The first example concerns the plane irrotational flow in an outlet by Thijsse [88]. Figure 2.11 shows the outlet which has a nozzle to minimize energy

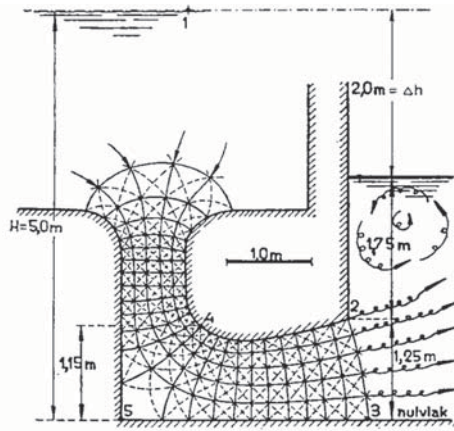


Figure 2.11: *Outlet and corresponding orthonormal flow net, from Thijsse [88].*

losses. The same figure also shows the corresponding flow net which was used to solve potential flow problems in former times.

The computations are performed for the linear CG method, the linear DG method and a mixed method using the MINI element. In this particular case the source term f equals zero and the GIS method is fully equivalent to the CG method. A successive range of meshes is employed where the element size h_e is halved in each step of the refinement. Figure 2.12a shows the mesh for a mesh size of 2 m. The boundary conditions specify a zero velocity potential on the outflow boundary (right), an inward normal velocity of 1 m/s on the inflow boundary (left) and a zero normal velocity on the side-walls and the surface (upper boundary). The interface fluxes for the DG method are computed from Equations (2.46) using a penalty parameter $\alpha = 6$. The resulting sparse matrix systems are solved using the BICGSTAB method in combination with ILU preconditioning setting the stopping criterion to $\epsilon = 10^{-10}$.

Figure 2.12b shows the corresponding CG solution in terms of the streamlines and equi-potential lines. The streamlines are computed in a post-processing step. The plotting intervals are chosen such that an orthonormal flow net results. Qualitatively, the computed solution is similar to the graphical solution shown in Figure 2.11. The required numbers of iteration steps are listed in Table 2.2 and also presented graphically in Figure 2.13. Roughly, the number of iteration steps doubles if the element size is halved which implies that $N_{\text{iter}} \sim N_{\text{dof}}^{1/2}$. The total number of floating point operations is therefore proportional to $N_{\text{flop}} \sim N_{\text{dof}}^{3/2}$ which, compared to Equation (2.67), is sub-optimal. Next, the convergence orders are considered by calculating the energy functionals of the corresponding minimization problems, Equation (2.35) for the CG method and Equation (2.22) for the

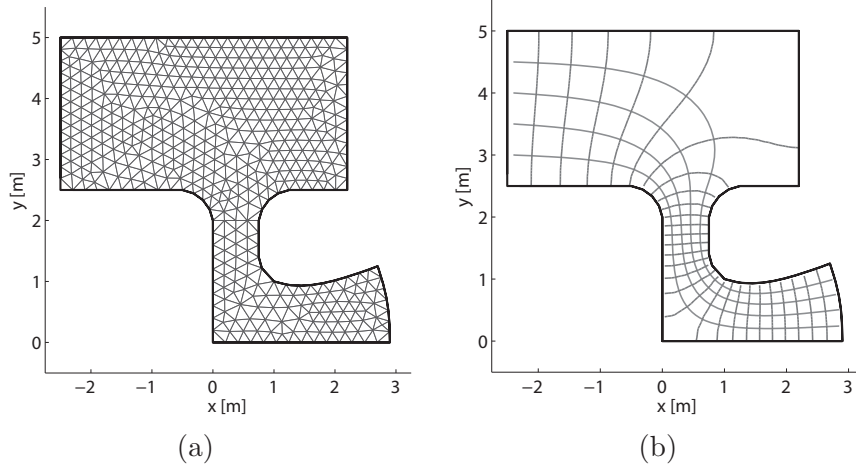


Figure 2.12: *Flow in an outlet: finite element mesh (a) and computed orthogonal flow net for the MINI element (b).*

element	$N = 142$	$N = 512$	$N = 1963$	$N = 7417$	$N = 29505$
CG/GIS (P^1)	16	31	63	124	246
DG-IP (dP^1)	38	71	180	532	stagnation
mixed (MINI)	17	32	68	162	stagnation

Table 2.2: *Flow in an outlet: number of required BICGSTAB iterations.*

mixed method. For all considered methods a suitable error-norm of the solution can be defined by

$$|||e||| = (J - J_e)^{1/2}, \quad (2.68)$$

where J and J_e are the energy functionals corresponding to the numerical solution and the exact solution, respectively, see for instance Equation (2.36). The functional J_e is unknown but the convergence order p of the error $|||e|||$ can be estimated from J since

$$J = J_e + |||e|||^2 \approx J_e + Ch_e^{2p}, \quad (2.69)$$

where C is a mesh dependent constant. Figure 2.13 shows that for the considered methods J is inversely proportional to the number of nodes. As for a two-dimensional mesh the number of nodes is inversely proportional to h_e^2 it follows that for all methods $p = 1$ and $|||e|||$ has $\mathcal{O}(h_e)$ convergence which is in accordance with theoretical error estimates.

Concluding, having the same order of convergence, the linear CG method requires the least computational effort per degree of freedom. The MINI

element and the DG method are about three times slower due to the increased size of the sparse matrix system that has to be solved. In this example, the latter two methods are also less robust leading to stagnation of the iterative solution process on the finest mesh.

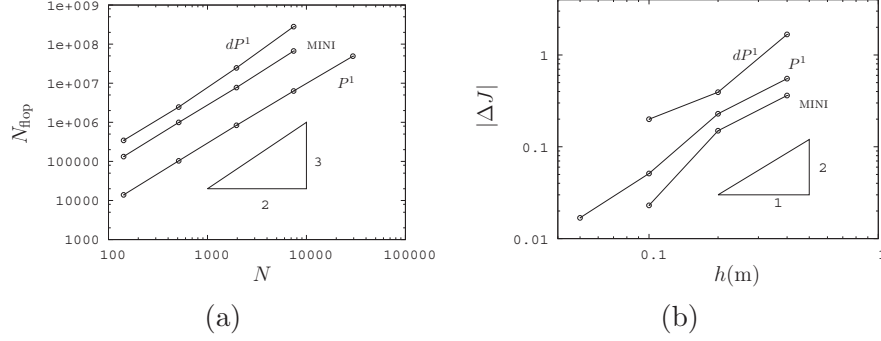


Figure 2.13: *Flow in an outlet: number of floating point operations (a) and increments of the energy functional ΔJ relative to the finest mesh solution (b).*

2.5.2 Standing wave

This example considers the accuracy of the GIS method relative to the CG method for the Helmholtz equation

$$\nabla^2 \tilde{\phi} + k^2 \tilde{\phi} = 0 \quad \text{on } \Omega \subset \mathbb{R}^2, \quad (2.70)$$

where $\tilde{\phi}$ denotes the complex amplitude of the potential function and k^2 is a separation factor. The Helmholtz equation arises in the study of wave diffraction and is obtained by integrating the potential flow equation over the water depth, using a linearized free-surface boundary condition [6]. The corresponding CG and GIS weak formulations are obtained through the replacement of f with $k^2 \tilde{\phi}$ in Equations (2.33) and (2.50), respectively.

The computational domain is the rectangle $(x, y) = (0; 3\pi) \times (0; \pi)$. On the boundary $x = 0$ a Dirichlet boundary condition $\tilde{\phi} = \cos y$ is prescribed while on all other boundaries a homogeneous Neumann boundary condition is imposed. For $k^2 = 2$, the exact solution to this problem is given by

$$\tilde{\phi}_e = \cos x \cos y. \quad (2.71)$$

The computations are performed on a successive range of triangular meshes with decreasing element size. The GIS penalty parameter appearing in the interface flux term is set to $\alpha = 6$. The solution procedure involves ILU preconditioned BICGSTAB iteration, using a stopping criterion $\epsilon = 10^{-10}$.

The resulting error $e = \tilde{\phi} - \tilde{\phi}_e$, measured in the \mathcal{L}^2 norms and the \mathcal{H}^1 semi-norm, is shown in Figure 2.14. The observed convergence rates are of

order two in the \mathcal{L}^2 norm and of order one in the \mathcal{H}^1 semi-norm, respectively. For both methods this result is in agreement with the general error estimate given by Equation (2.38).

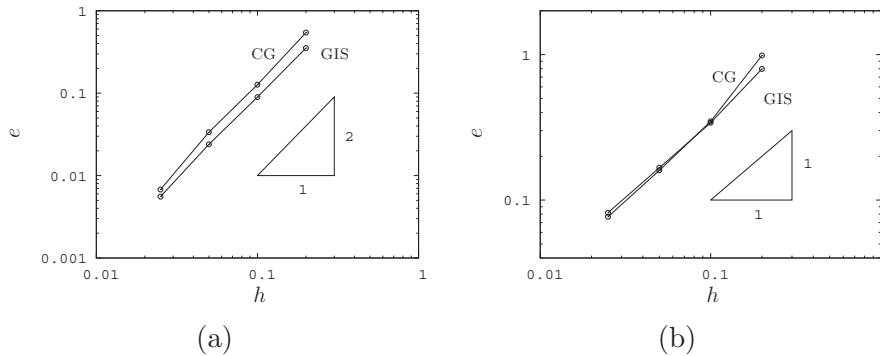


Figure 2.14: *Standing wave: errors for the linear CG and GIS methods in the \mathcal{L}^2 norm (a) and in the \mathcal{H}^1 semi-norm (b).*

2.6 Conclusion

The solution of algebraic problems obtained from finite element discretization involves the storage and manipulation of systems of equations having an arbitrary ordering of unknowns. The ordering is inherited from the underlying weak formulation of the problem, and is of crucial importance when considering the computational efficiency of a method. In this respect, the continuous Galerkin method offers a relatively simple arrangement of unknowns and therefore requires relatively few floating point operations per degree of freedom to obtain a solution. The discontinuous Galerkin method is an inefficient choice if implicit systems have to be solved but, having a local mass matrix, may prove useful when solving explicit systems.

Blending continuous and discontinuous methods, an alternative approach has been formulated having the same order of accuracy. By introducing global interface functions, the favourable properties of discontinuous methods are retained while the size of the system that has to be solved is reduced to that of a continuous method. This approach is not strictly necessary for the potential flow problem of this chapter, but will be fully exploited for the advection-diffusion and incompressible Navier-Stokes equations to by-pass advective instabilities and instabilities due to the incompressibility constraint.

Chapter 3

Scalar transport

Transport of dissolved or suspended matter is an important phenomenon in many hydraulic engineering problems such as sediment transport and morphology or the dispersal of pollutants. If the transport of matter involves changes in density, as for example in estuaries or near cooling water outfalls, the advected concentration field interacts with the flow through buoyancy forces. The transport equation also constitutes an important sub problem of the flow equations. This chapter introduces a new finite element method for the advection-diffusion equation. The method is also intended as a building block for incompressible Navier-Stokes solvers¹.

3.1 The model problem

3.1.1 Governing equations

Consider a domain $\Omega \in \mathbb{R}^d$, where $d = 1, 2, 3$, is the number of spatial dimensions, which has a boundary $\Gamma = \partial\Omega$. It is assumed that the boundary is sufficiently smooth and the outward normal vector on Γ is denoted \mathbf{n} . The transport of scalar quantities in Ω is considered on the time interval $I = (t_0, t_N)$. Formulated as a coupled system of first order equations, the transport problem reads: given an advective velocity $\mathbf{a} : \Omega \times I \rightarrow \mathbb{R}^d$, a densimetric source term $f : \Omega \times I \rightarrow \mathbb{R}$ and (turbulence) diffusivity κ , find $\phi : \Omega \times I \rightarrow \mathbb{R}$ such that

$$\frac{\partial \phi}{\partial t} + \nabla \cdot \boldsymbol{\sigma} = f \quad \text{in } \Omega \times I, \quad (3.1)$$

$$\boldsymbol{\sigma} = \mathbf{a}\phi - \kappa \nabla \phi \quad \text{in } \Omega \times I, \quad (3.2)$$

where ϕ is the mass fraction of the transported constituent and $\boldsymbol{\sigma} : \Omega \times I \rightarrow \mathbb{R}^d$ is the associated flux vector. The solution of Equations (3.1) and (3.2)

¹This chapter is partly based on: ‘A Galerkin interface stabilisation method for the advection-diffusion and Navier-Stokes equations’, Robert Jan Labeur and Garth N. Wells. In: *Computer Methods in Applied Mechanics and Engineering*, **196**, 4985-5000, 2007.

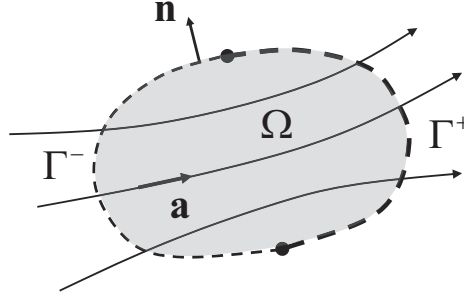


Figure 3.1: *Schematic of inflow and outflow boundaries.*

requires initial conditions $\phi_0 = \phi(\mathbf{x}, t_0)$ on Ω and boundary conditions on $\Gamma \subset \partial\Omega$ for all $t \in I$. Denoting the Dirichlet boundary Γ_g and the Neumann boundary Γ_h , where $\Gamma_g \cup \Gamma_h = \partial\Omega$ and $\Gamma_g \cap \Gamma_h = \emptyset$, the boundary conditions are given by

$$\phi = g \quad \text{on} \quad \Gamma_g \times I, \quad (3.3)$$

$$\boldsymbol{\sigma} \cdot \mathbf{n} = h \quad \text{on} \quad \Gamma_h \times I. \quad (3.4)$$

In case of pure advection ($\kappa = 0$) boundary conditions can only be imposed on the inflow part of the boundary, denoted Γ^- , where the advective velocity \mathbf{a} is directed into the domain, i.e. $\mathbf{a} \cdot \mathbf{n} \leq 0$. On outflow boundaries, denoted Γ^+ , the velocity $\mathbf{a} \cdot \mathbf{n} > 0$ and the advective flux is implicitly determined by the trace of ϕ on Γ , see Figure 3.1. A more precise formulation of the Neumann boundary condition is therefore given by

$$\boldsymbol{\sigma} \cdot \mathbf{n} - (1 - \gamma) \mathbf{a} \cdot \mathbf{n} \phi = h \quad \text{on} \quad \Gamma_h \times I, \quad (3.5)$$

where $\gamma = 1$ on inflow boundaries and $\gamma = 0$ on outflow boundaries. On inflow boundaries h specifies the total normal flux and on inflow boundaries h prescribes the normal diffusive flux, see Hughes and Wells [37].

The continuous first order system may be written as a single second-order equation for the scalar variable ϕ by substituting Equation (3.2) for the flux into transport Equation (3.1), which leads to

$$\frac{\partial \phi}{\partial t} + \nabla \cdot (\mathbf{a}\phi - \kappa \nabla \phi) = f \quad \text{on} \quad \Omega \times I. \quad (3.6)$$

The first order system is however more general in the sense that it admits a much wider class of function spaces in which solutions can be defined. It is therefore the general starting point for the finite element discretization of the transport equation considered in this chapter.

3.1.2 Variational formulation

Consider a partitioning of the domain Ω into open, disjoint sub domains Ω_e (elements), each having a boundary $\partial\Omega_e$ on which \mathbf{n} is the outward normal vector. The partitioning defines the following unions

$$\tilde{\Omega} = \bigcup_e \Omega_e \quad (3.7)$$

$$\tilde{\Gamma} = \bigcup_e \partial\Omega_e = \bigcup_i \Gamma_i, \quad (3.8)$$

where $\tilde{\Omega}$ is the union of all element interiors, $\tilde{\Gamma}$ is the union of all element boundaries and Γ_i are element interfaces.

A general variational form for the transport problem, including all discrete approximations treated in this chapter, is obtained by approximating ϕ in a broken Hilbert-space V defined by

$$V = \{v \in L^2(\Omega) : v \in H^1(\Omega_e) \ \forall e\}. \quad (3.9)$$

Functions $v \in V$ have square-integrable first derivatives in every element Ω_e but may be discontinuous across element interfaces Γ_i . Likewise, the flux $\boldsymbol{\sigma}$ is approximated in a space \mathbf{W} of square integrable, discontinuous vector valued functions \mathbf{w} defined by

$$\mathbf{W} = \{\mathbf{w} \in \mathbf{L}^2(\Omega) : \mathbf{w} \in \mathbf{H}^1(\Omega_e) \ \forall e\}, \quad (3.10)$$

Functions $v \in V$ and $\mathbf{w} \in \mathbf{W}$ are undefined on element interfaces, and the state and flux on $\tilde{\Gamma}$ are given by auxiliary functions $\bar{\phi} : \tilde{\Gamma} \times I \rightarrow \mathbb{R}$ and $\bar{\boldsymbol{\sigma}} : \tilde{\Gamma} \times I \rightarrow \mathbb{R}^d$, respectively.

The derivation of the variational form of Equations (3.1) and (3.2) is similar to that of the potential flow problem in Section 2.2.2, leading to the following mixed problem: at given time t , given a source term $f \in L^2(\Omega)$, find $\phi \in V$ and $\boldsymbol{\sigma} \in \mathbf{W}$ such that

$$\begin{aligned} & \int_{\tilde{\Omega}} \frac{\partial \phi}{\partial t} v \, d\Omega - \int_{\tilde{\Omega}} \boldsymbol{\sigma} \cdot \nabla v \, d\Omega + \sum_e \int_{\partial\Omega_e} \bar{\boldsymbol{\sigma}} \cdot \mathbf{n} v \, d\Gamma + \int_{\tilde{\Omega}} (\boldsymbol{\sigma} - \mathbf{a}\phi + \kappa \nabla \phi) \cdot \mathbf{w} \, d\Omega \\ & + \sum_e \int_{\partial\Omega_e} \kappa (\bar{\phi} - \phi) \mathbf{n} \cdot \mathbf{w} \, d\Gamma = \int_{\tilde{\Omega}} f v \, d\Omega \quad \forall v \in V, \quad \forall \mathbf{w} \in \mathbf{W}, \end{aligned} \quad (3.11)$$

where \sum_e denotes summation over elements, see also Arnold et al. [1] for details of the derivation. In deriving Equation (3.11) the first derivative terms have been integrated by parts leading to the element boundary integrals containing the auxiliary functions $\bar{\phi}$ and $\bar{\boldsymbol{\sigma}}$. These quantities are to be expressed in terms of ϕ and $\boldsymbol{\sigma}$ on either side of the element interface. For the moment $\bar{\phi}$ and $\bar{\boldsymbol{\sigma}}$ are left undefined, although it is assumed that they satisfy the boundary conditions.

Equation (3.11) may be reduced to the conventional second-order form by taking $\mathbf{W} = \nabla V$ which gives: at time t , given f , find $\phi \in V$ such that

$$\begin{aligned} \int_{\tilde{\Omega}} \frac{\partial \phi}{\partial t} v \, d\Omega - \int_{\tilde{\Omega}} \mathbf{a} \phi \cdot \nabla v \, d\Omega + \int_{\tilde{\Omega}} \kappa \nabla \phi \cdot \nabla v \, d\Omega + \sum_e \int_{\partial\Omega_e} \bar{\boldsymbol{\sigma}} \cdot \mathbf{n} v \, d\Gamma \\ + \sum_e \int_{\partial\Omega_e} \kappa (\bar{\phi} - \phi) \mathbf{n} \cdot \nabla v \, d\Gamma = \int_{\tilde{\Omega}} f v \, d\Omega \quad \forall v \in V. \end{aligned} \quad (3.12)$$

Provided that the proper choices for V , $\bar{\phi}$ and $\bar{\boldsymbol{\sigma}}$ are made, Equation (3.12) is consistent with the strong form of the transport problem [51]. Before giving possible choices, a few elementary properties of the transport equation are briefly discussed as these should be reflected in the ensuing numerical method, at least to some approximate degree.

3.1.3 Solution characteristics

In order to describe the general behaviour of solutions of the transport equation, the second-order Equation (3.6) is simplified assuming an incompressible velocity field $\nabla \cdot \mathbf{a} = 0$ and a uniform, isotropic diffusivity κ while neglecting the source function f , which leads to

$$\frac{\partial \phi}{\partial t} + \mathbf{a} \cdot \nabla \phi = \kappa \nabla^2 \phi. \quad (3.13)$$

The left hand side constitutes the advection term, or material derivative, while the right hand side is the diffusion term. The physical and numerical behaviour of solutions is determined by the dimensionless Reynolds number and the Péclet number, respectively.

3.1.3.1 The Reynolds number

The Reynolds number is defined by $Re = |\mathbf{a}|L_{\text{ref}}/\kappa$ where L_{ref} is a reference length scale of the problem, for instance the size of a cloud of tracer or the water depth. The limiting behaviour of solutions for small and large values of Re , respectively, is depicted in Figure 3.2.

For $Re \ll 1$ the diffusive terms dominate and a cloud of dissolved material spreads evenly where its size is proportional to $\sqrt{\kappa t}$. In the absence of source terms, the total mass in the cloud remains constant (conservation property). The boundary conditions have to be imposed along the entire boundary of the domain. By virtue of the maximum principle the maximum value of ϕ is either assumed initially in Ω or along the boundary $\partial\Omega$ [86].

For $Re \gg 1$ advection dominates and in the absence of source terms ϕ will be constant along characteristic curves in the (\mathbf{x}, t) -plane given by the equation $d\mathbf{x}/dt = \mathbf{a}$. On each characteristic curve the corresponding value of ϕ is determined either by its intersection with the plane $t = 0$ (initial condition) or by its intersection with the lateral boundaries (boundary

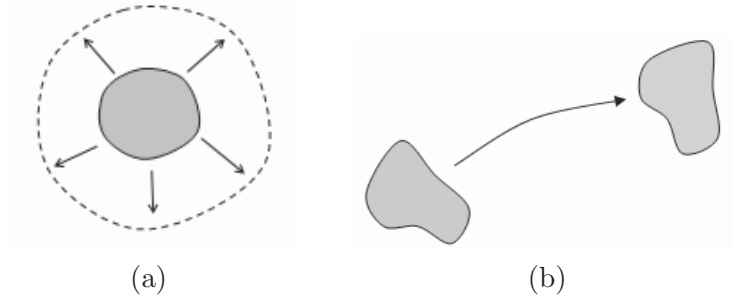


Figure 3.2: *The Reynolds number: (a) dominant diffusion ($Re \ll 1$) and (b) dominant advection ($Re \gg 1$).*

condition). Total mass is conserved while along characteristics ϕ can not exceed the value assumed initially or imposed along the boundary (maximum principle). For pure advection, boundary conditions can only be prescribed on the inflow boundary Γ^- . Boundary conditions imposed on Γ^+ are only effective when $\kappa \neq 0$. The resulting outflow boundary layer has a width of order $\kappa/|\mathbf{a}|$ over which the solution gradually attains the imposed value at the boundary.

3.1.3.2 The Péclet number

The Péclet number, defined by $Pe = \frac{1}{2}|\mathbf{a}|h_e/\kappa$, may be regarded as a Reynolds number using a length scale of half the element size h_e . For an outflow boundary layer, the limiting behaviour of solutions for large and small values of Pe is shown in Figure 3.3.

For dominant advection ($Pe > 1$) numerical solutions tend to exhibit oscillations. To avoid this unphysical behaviour, artificial diffusion can be added in streamwise direction such that $Pe \leq 1$ (upwinding). While this effectively suppresses the spurious modes it will also obscure the true physics of the problem. Pure advection schemes, the (semi-) Lagrangian methods [68] or the second moment method [26], do a better job in this respect but also require considerable effort to implement the diffusion terms correctly. The biggest challenge in numerical modelling of transport is in fact the construction of an algorithm that performs well for arbitrary, possibly non-uniform Péclet numbers.

In this respect many numerical techniques have been developed over the years, most prominently in the realm of finite difference and finite volume methods. The ordered data arrangement enables a judicious manipulation of the fluxes, usually by means of limiters, such that the resulting method preserves monotonicity with a minimum of artificial side effects [54]. Initially, the developments in finite elements lagged somewhat behind until the introduction of the SUPG method by Brooks and Hughes [10] and characteristic Galerkin methods [68, 100] which are both based on C^0 -continuous

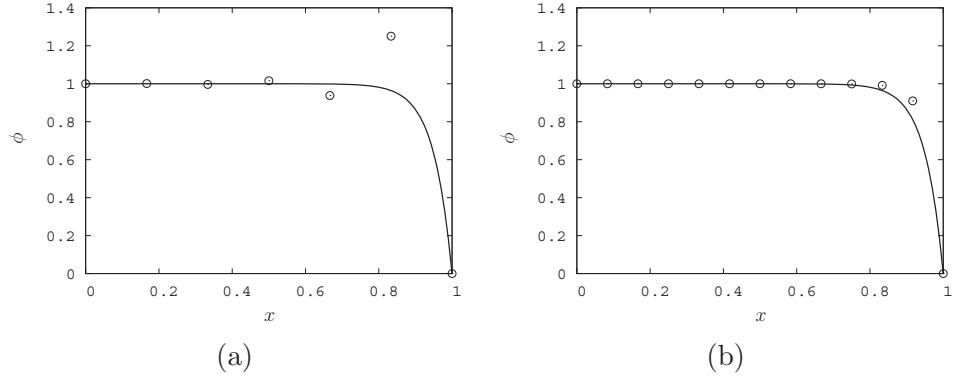


Figure 3.3: *The Péclet number: outflow boundary layer for $Pe > 1$ (a) and for $Pe < 1$ (b); analytical solution (solid) and numerical solution (circles).*

basis functions. Currently, there is a renewed interest in discontinuous Galerkin methods, already conceived by Reed and Hill [73], as a robust yet accurate method to solve hyperbolic problems [4].

3.2 Continuous and discontinuous methods

This section presents a short overview of standard finite element methods for the advection-diffusion problem, providing a background for the Galerkin Interface Stabilization method, introduced later on, which blends various features of continuous and discontinuous Galerkin methods.

3.2.1 Continuous Galerkin method

The continuous Galerkin (CG) method is obtained from the general variational form of the scalar transport problem Equation (3.12) by considering continuous function spaces U and U_g defined by

$$U = \left\{ u \in H^1(\tilde{\Omega}) : u \in P^k(\Omega_e) \forall e \right\}, \quad (3.14)$$

$$U_g = \left\{ u \in H^1(\tilde{\Omega}) : u \in P^k(\Omega_e) \forall e, u = g \text{ on } \Gamma_g \right\}, \quad (3.15)$$

where P^k is a set of element wise polynomial basis functions of order $\leq k$ and functions in $U_g \subset U$ satisfy the Dirichlet boundary condition on Γ_g . Functions $u \in U$ are unique on element interfaces and setting $\bar{\phi} = \phi$ on $\tilde{\Gamma}$ in Equation (3.12) gives the following variational form: at time t , find $\phi \in U_g$ such that

$$\int_{\tilde{\Omega}} \frac{\partial \phi}{\partial t} u \, d\Omega - \int_{\tilde{\Omega}} \boldsymbol{\sigma} \cdot \nabla u \, d\Omega + \sum_e \int_{\partial\Omega_e} \bar{\boldsymbol{\sigma}} \cdot \mathbf{n} u \, d\Gamma = \int_{\tilde{\Omega}} f u \, d\Omega \quad \forall u \in U. \quad (3.16)$$

where the element flux $\boldsymbol{\sigma} = \mathbf{a}\phi - \kappa\nabla\phi$. As a crucial step the interface fluxes $\bar{\boldsymbol{\sigma}}$ are assumed weakly continuous across interior element interfaces while satisfying the Neumann boundary condition on Γ_h , which is stated as

$$\sum_e \int_{\partial\Omega_e} \bar{\boldsymbol{\sigma}} \cdot \mathbf{n} u \, d\Gamma = \int_{\Gamma_h} (1 - \gamma) \mathbf{a} \cdot \mathbf{n} \phi u \, d\Gamma + \int_{\Gamma_h} hu \, d\Gamma \quad \forall u \in U. \quad (3.17)$$

The first term on the right hand side is the advective flux on outflow Neumann boundaries, where $\gamma = 0$, with h specifying the normal diffusive flux. On inflow boundaries $\gamma = 1$ and h specifies the total normal flux. Substituting Equation (3.17) in Equation (3.16) yields the following problem: at time t , find $\phi \in U_g$ such that

$$\begin{aligned} \int_{\tilde{\Omega}} \frac{\partial\phi}{\partial t} u \, d\Omega - \int_{\tilde{\Omega}} \boldsymbol{\sigma} \cdot \nabla u \, d\Omega + \int_{\Gamma_h} (1 - \gamma) \mathbf{a} \cdot \mathbf{n} \phi u \, d\Gamma \\ = \int_{\tilde{\Omega}} fu \, d\Omega - \int_{\Gamma_h} hu \, d\Gamma \quad \forall u \in U. \end{aligned} \quad (3.18)$$

Variational Equation (3.18) has a number of desirable properties. Consistency with the strong form of the transport problem can be proven while the formulation is also conservative, both globally and locally, see Hughes et al. [34]. For the \mathcal{L}^2 error norm the convergence rates are $\mathcal{O}(h_e^{k+1})$ and $\mathcal{O}(h_e^{k+1/2})$ in the diffusive and the advection limits, respectively, see Johnson [42]. Stability on the other hand may become problematic in advection dominated cases. Monotonicity is only preserved conditionally for κ sufficiently large. If the Péclet number is larger than one the advection terms may give rise to ‘wiggles’ in the numerical solution near sharp gradients, outflow boundary layers and discontinuities, see Figure 3.3.

Apparently, the determination of the element flux $\boldsymbol{\sigma}$ in Equation (3.18) directly from ϕ is not adequate in case of dominant advection. Although some authors advocate never to suppress the wiggles in favour of good looking solutions², some stabilization may be necessary to keep solutions monotone. The CG method can be stabilized in a consistent way, by manipulating the advective fluxes, without affecting the overall accuracy of the solution. A well known stabilization technique is the Streamline Upwind Petrov-Galerkin (SUPG) method of Brooks and Hughes [10]. In each element the associated numerical flux $\boldsymbol{\sigma}$ is replaced with a modified flux $\tilde{\boldsymbol{\sigma}}$ according to

$$\tilde{\boldsymbol{\sigma}} = \boldsymbol{\sigma} - \tau_e \mathbf{a} \underbrace{\left(\frac{\partial\phi}{\partial t} + \nabla \cdot \boldsymbol{\sigma} - f \right)}_{\text{element wise residual}}. \quad (3.19)$$

²The ‘wiggle-signal’ generally indicates a poor quality of the way the underlying equation is discretized requiring mesh refinement in the respective part of the domain, see Gresho et al. [28].

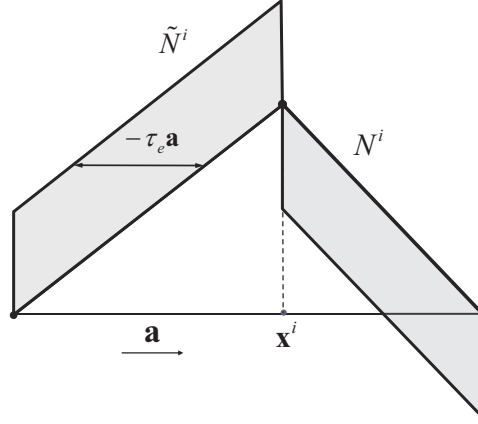


Figure 3.4: SUPG method: regular weighting function N^i and modified weighting function \tilde{N}^i .

The additional terms are proportional to the element wise residual using a stabilization parameter τ_e which has the dimension of time. The modified weak formulation becomes: find $\phi \in U_g$ such that

$$\begin{aligned} \int_{\tilde{\Omega}} \frac{\partial \phi}{\partial t} u \, d\Omega - \int_{\tilde{\Omega}} \tilde{\boldsymbol{\sigma}} \cdot \nabla u \, d\Omega + \sum_e \int_{\partial\Omega_e} (1 - \gamma) \mathbf{a} \cdot \mathbf{n} \phi u \, d\Gamma \\ = \int_{\tilde{\Omega}} f u \, d\Omega - \int_{\Gamma_h} h u \, d\Gamma \quad \forall u \in U. \end{aligned} \quad (3.20)$$

The procedure effectively increases the diffusivity in streamwise direction and for a proper choice of τ_e nearly monotone solutions will be obtained. Equation (3.20) is consistent with the strong form of the problem as in the continuous limit the element residuals tend to zero and $\tilde{\boldsymbol{\sigma}} \rightarrow \boldsymbol{\sigma}$. As can be shown by straightforward algebra, Equation (3.20) is also obtained by shifting the weighting functions u over a distance $-\tau_e \mathbf{a}$ along the streamlines in a direction opposite to the advective velocity thereby increasing the influence of the elements on the upstream side of a particular node, see Figure 3.4.

The parameter τ_e should have the order of h_e^2/κ for diffusion dominated problems and the order of $h_e/|\mathbf{a}|$ in case of dominant advection [36]. For stationary, one-dimensional cases an optimal expression for τ_e can be derived yielding nodally exact solutions for every Péclet number. In two and three dimensions this is not possible although the performance of the SUPG method is not critically dependent on a very precise choice for τ_e either which explains the variety of alternative formulations for $\tilde{\boldsymbol{\sigma}}$ found in literature [81].

Provided that τ_e is approximated in a reasonable way, $\mathcal{O}(h_e^{k+1})$ and $\mathcal{O}(h_e^{k+1/2})$ convergence rates for the \mathcal{L}^2 error norm are obtained for the diffusive and advective limit cases respectively, the proof of which is given

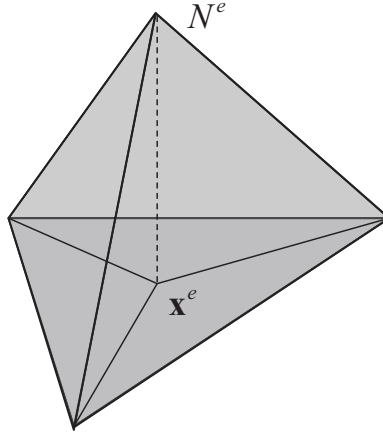


Figure 3.5: *Bubble function N^e of the MINI element.*

in Johnson [42]. Being formulated in flux form, the SUPG method is conservative, provided that the modified flux $\tilde{\sigma}$ is used for the evaluation of the fluxes [37]. Although oscillations are effectively controlled, SUPG solutions are not strictly monotone which in the vicinity of shocks and boundary layers may result in some under- or overshoot. If this should be prevented non-linear ‘discontinuity capturing’ may be used by shifting the weighting functions u in the direction of the gradient of the solution as well [36].

A different stabilization concept utilizes local functions on elements, also referred to as ‘bubble functions’, in order to increase the accuracy of the advective fluxes. The degrees of freedom associated with the bubble functions can be eliminated during the matrix assembly process after which a global system of equations results for the nodal degrees of freedom only, a procedure referred to as ‘static condensation’. After solution of the nodal degrees of freedom, the bubble degrees of freedom are retained in a back-substitution step which does not require the inversion of a large system of equations. For a general treatment of this concept see France et al. [25]. An example of this approach is the MINI element which uses a space of continuous P^1 basis functions combined with element wise basis functions N^e that have a value of one in the barycenter and vanish on the element boundaries, see Figure 3.5. The variational form after static condensation is fully equivalent to that obtained from the SUPG method, with a modified expression for the stability parameter τ_e [8]. In the high Péclet number range the MINI element leads to non-optimal stabilization which may be bypassed by scaling the bubble function with a Péclet -number dependent parameter, see Simo et al. [81].

An advantage of using local ‘bubbles’ instead of SUPG -type weighting functions is that the fluxes remain directly dependent on the nodal data. Stability is provided by the geometrical definition of the element and the as-

sociated function space without artificial manipulation of the element fluxes. This also avoids the computation of additional stability parameters, which may be a critical issue if the computational problem involves different flow regimes. However, the example of the MINI element shows that the bubble functions need to be chosen with care as not every choice automatically leads to sufficient stabilization. A theoretical framework to construct optimal bubble functions is provided by the residual-free bubble (RFB) method of Russo [75]. The resulting basis functions are however too complex to implement in general flow and transport models.

3.2.2 Discontinuous Galerkin method

The observation that solutions of the advection problem admit discontinuities naturally leads to considering discontinuous spaces in variational form Equation (3.12). For purely hyperbolic problems the ensuing discontinuous Galerkin (DG) method was already proposed in Reed and Hill [73] and extended to elliptic problems by Arnold [2]. Consider therefore function spaces V and V_g defined by, respectively,

$$V = \left\{ v \in L^2(\tilde{\Omega}) : v \in P^k(\Omega_e) \forall e \right\}, \quad (3.21)$$

$$V_g = \left\{ v \in L^2(\tilde{\Omega}) : v \in P^k(\Omega_e) \forall e, v = g \text{ on } \Gamma_g \right\}, \quad (3.22)$$

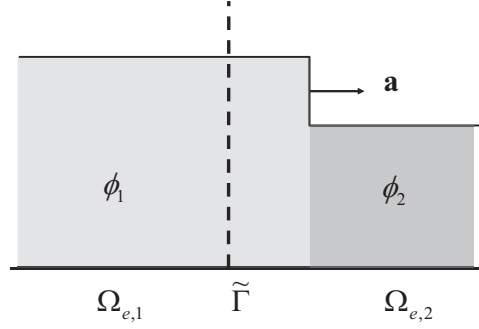
where P^k , with $k \geq 0$, is a set of polynomial basis functions defined on elements and V_g contains all functions in V that satisfy the Dirichlet boundary conditions. The DG formulation is obtained by supplementing Equation (3.12) with the Neumann boundary condition given in Equation (3.4), which leads to the following variational problem: at time t , given the source term f and the boundary condition h , find $\phi \in V_g$ such that

$$\begin{aligned} \int_{\tilde{\Omega}} \frac{\partial \phi}{\partial t} v \, d\Omega - \int_{\tilde{\Omega}} \boldsymbol{\sigma} \cdot \nabla v \, d\Omega + \sum_e \int_{\partial\Omega_e} \bar{\boldsymbol{\sigma}} \cdot \mathbf{n} v \, d\Gamma + \sum_e \int_{\partial\Omega_e} \kappa (\bar{\phi} - \phi) \cdot \mathbf{n} \nabla v \, d\Gamma \\ + \int_{\Gamma_h} (1 - \gamma) \mathbf{a} \mathbf{n} \cdot \phi v \, d\Gamma = \int_{\tilde{\Omega}} f v \, d\Omega - \int_{\Gamma_h} h v \, d\Gamma \quad \forall v \in V, \end{aligned} \quad (3.23)$$

in which $\bar{\phi}$ and $\bar{\boldsymbol{\sigma}}$ are yet unknown functions which are constructed from the fields ϕ in the two elements sharing an interface.

Assuming that the interface flux may be decomposed additively into an advective part and a diffusive part, the advective flux $\bar{\boldsymbol{\sigma}}^a$ may be computed using a flux splitting procedure taking into account the characteristic direction of the transport velocity, see Figure 3.6. This is accomplished by solving a local Riemann problem which yields

$$\bar{\boldsymbol{\sigma}}^a = \{\mathbf{a}\phi\} + \frac{1}{2} |\tilde{\mathbf{a}} \cdot \mathbf{n}| \llbracket \phi \rrbracket, \quad (3.24)$$

Figure 3.6: *The local Riemann problem.*

where $\tilde{\mathbf{a}}$ is the advective velocity at the interface. This formulation gives an upwind bias to the flux. Note that the advection terms in Equation (3.23) do not involve the interface state $\bar{\phi}$. Flux splitting methods described in literature mainly differ in the definition of the interface advective velocity $\tilde{\mathbf{a}}$, see for instance the classical paper by Harten et al. [33]. For non-linear problems a proper expression for $\tilde{\mathbf{a}}$ is crucial to obtain a correct behaviour of solutions at shocks, by satisfying the entropy condition, for which a general approach is outlined in LeVeque [56]. The diffusive part of the interface flux $\bar{\sigma}^d$ and the associated state $\bar{\phi}$ may be taken as averages of the respective values on both sides of an interface augmented with terms containing the jumps of σ and ϕ . A systematic overview of existing methods is presented in Arnold et al. [1]. As an example, in the interior penalty (IP) method the interface state and the diffusive interface flux are formulated as, respectively,

$$\bar{\phi} = \{\phi\}, \quad (3.25)$$

$$\bar{\sigma}^d = -\{\kappa \nabla \phi\} + \frac{\alpha}{h_e} \kappa \llbracket \phi \rrbracket, \quad (3.26)$$

where h_e is the element width normal to the interface and α is a dimensionless $\mathcal{O}(1)$ penalty parameter which is necessary for stability of DG methods. The similar form of the advection flux given by Equation (3.24) and the diffusive flux of Equation (3.26) allows to write the total interface flux $\bar{\sigma} = \bar{\sigma}^a + \bar{\sigma}^d$ compactly as

$$\bar{\sigma} = \{\sigma\} + \beta \llbracket \phi \rrbracket, \quad (3.27)$$

where

$$\beta = \frac{1}{2} |\tilde{\mathbf{a}} \cdot \mathbf{n}| + \frac{\alpha}{h_e} \kappa. \quad (3.28)$$

The substitution of Equation (3.25) for the interface state $\bar{\phi}$ and Equation (3.27) for the interface flux $\bar{\sigma}$ into variational Equation (3.23) yields a formulation in terms of the unknown field ϕ only.

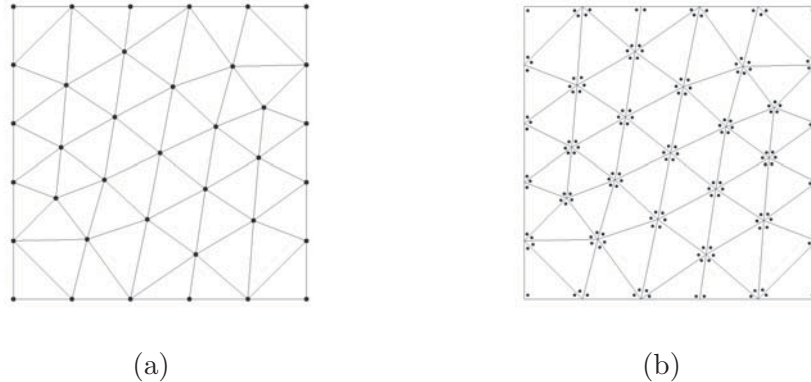


Figure 3.7: *Nodal degrees of freedom for the linear CG method (a) and the DG method (b).*

The resulting DG-IP method is consistent and locally conservative since $\bar{\phi}$ and $\bar{\sigma}$ are unique on element interfaces while the corresponding expressions approach the continuous limit if the element size h_e tends to zero [1]. The method is also optimally accurate in the sense that the \mathcal{L}^2 error norm has $\mathcal{O}(h_e^{k+1/2})$ and $\mathcal{O}(h_e^{k+1})$ convergence rates in the advective and diffusive limits, respectively [1, 42]. Linear monotone advection schemes can be first order accurate at most and linear DG solutions involving steep gradients are not completely wiggle free. Slope limiters or artificial dissipation may be applied to suppress artificial wiggles, respecting the conservation and consistency properties [44, 90].

3.2.3 Discussion: CG or DG?

While having attractive properties, a practical impediment of DG methods is the increased number of degrees of freedom relative to a continuous Galerkin method on the same mesh. Considering the increase of the number of non-zero entries in the associated sparse matrix system the situation is even worse, see also Table 2.1. For systems involving the inversion of a global sparse matrix discontinuous methods are likely to be outperformed by methods employing continuous basis functions. As the DG mass matrix is locally invertible, application of DG methods is particularly useful for, but also more or less restricted to, explicit problems not requiring the inversion of a global matrix.

Stabilized continuous Galerkin methods are more economical, both with respect to data storage requirements and computational efficiency of sparse matrix operations. The required stabilization by SUPG or GLS methods is easy to implement and leads to near optimal convergence. Although these properties are attractive some drawbacks persist. This mainly concerns the

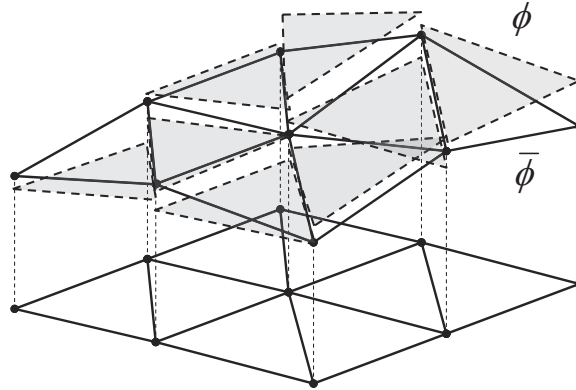


Figure 3.8: *Discontinuous functions connected by a continuous interface 'frame'.*

stabilization parameter which must be judiciously chosen, the determination of which relies on numerical tests. Ensuring sufficient stability without the introduction of excessive dissipation can thus become problematic. Furthermore, the direct correspondence between nodal data and the fluxes is lost, although this can be circumvented by using a modified advective velocity, see Hughes and Wells [37]. While these drawbacks may still be acceptable in scalar transport modelling, the application in flow solvers can become more problematic especially when different flow regimes reign within the same domain. This may amongst others lead to dissipation of (internal) waves, as demonstrated in Labeur and Pietrzak [49].

A better approach is therefore using bubble functions. Static condensation eliminates the bubble degrees of freedom, which reduces the system to the nodal degrees of freedom only and effectively stabilizes the problem. A clear advantage of this approach is that the bubbles retain the direct dependency of the fluxes on the data. However, it is not easy in general to construct bubbles that perform well in situations involving a wide range of Péclet numbers. The MINI element for example has non-optimal or even insufficient stabilization in the high Péclet number range [81]. Although optimal bubbles may be constructed dependent on the Péclet number, the intended elegance and simplicity of the approach is somewhat lost if the bubble functions change during the solution process, as in time dependent or non-linear cases, which severely complicates its implementation.

At this stage of the discussion the DG method, which is optimally stable and also conservative, may be reconsidered. The major drawback of this method, namely the massive data processing when solving implicit systems, would be alleviated if the DG sparse matrix structure could be reduced to a much smaller size. To achieve this, piecewise discontinuous functions may be considered that are in some way 'coupled' to global functions associated

with the nodes of the mesh. Elimination of the discontinuous part of the solution by means of static condensation would then reduce the sparse matrix structure to a size comparable to that of the CG method on the same mesh. Recently, a number of researchers have explored these concepts. In Sangalli [77] discontinuous bubbles are used to stabilize the continuous weak form of the stationary advection problem. In the multi-scale discontinuous Galerkin (MDG) method introduced in Hughes et al. [35] and analyzed further in Buffa et al. [11] the discontinuous solution ϕ is split into a continuous coarse-scale part $\bar{\phi}$ and a discontinuous fine-scale part $\phi' = \phi - \bar{\phi}$ which is solved by a local problem on elements with the boundary conditions obtained from the coarse scale solution.

In this thesis a different approach is pursued. Starting from a general DG formulation, a variational problem on each element is posed which is subject to weak Dirichlet boundary conditions. The boundary conditions are given by a function which is defined on element interfaces. This leaves two unknown fields, a field ϕ on elements and an interface field $\bar{\phi}$ on the interfaces, see Figure 3.8. The element field can be eliminated locally, and the interface field is solved for globally by requiring weak continuity of the numerical flux across element boundaries. Upwinding of this flux provides the necessary dose of stabilization from which the method is coined Galerkin Interface Stabilization (GIS) method. As will be shown the GIS method leads to a SUPG type stabilization term in the global equations while the element fluxes are retained by the local functions. As the interface functions may also be regarded as continuous ‘frames’ connecting local element functions the GIS method bears some similarity to Trefftz-type elements [99].

3.3 Galerkin interface stabilization method

In this section a modification of the DG method is proposed having the same global structure as the CG method while preserving the local upwinding and conservation properties of a DG method. The resulting method, coined Galerkin Interface Stabilization (GIS) method, is also described in Labeur and Wells [51].

3.3.1 General formulation

The starting point for the GIS method is the general variational form given by Equation (3.12) in which the interface state $\bar{\phi}$ is an independent variable which will be defined on the union of interior element interfaces $\tilde{\Gamma}$. Consider therefore a function space \bar{V} and a related space \bar{V}_g defined by, respectively,

$$\bar{V} = \left\{ \bar{v} \in H^{1/2}(\tilde{\Gamma}) : \bar{v} \in P^l(\tilde{\Gamma}_i) \quad \forall i \right\}, \quad (3.29)$$

$$\bar{V}_g = \left\{ \bar{v} \in H^{1/2}(\tilde{\Gamma}) : \bar{v} \in P^l(\tilde{\Gamma}_i) \quad \forall i, \bar{v} = g \text{ on } \Gamma_g \right\}, \quad (3.30)$$

where the fractional space $H^{1/2}$ is the trace of $H^1(\Omega)$ on $\tilde{\Gamma}$ and P^l , with $l \geq 1$, is a set of polynomial basis functions defined on element interfaces. Note that the function $\bar{\phi}$ is single-valued on element boundaries, and that functions in \bar{V}_g satisfy the Dirichlet boundary conditions. The numerical interface flux $\bar{\sigma}$ in Equation (3.12) is still undefined, other than to say that it is not single-valued on element boundaries and that it is expressed in terms of quantities belonging to an element and the interface function $\bar{\phi}$ only. It may not depend on quantities from neighbouring elements.

An equation for $\bar{\phi}$ may be formulated by imposing weak continuity of the normal component of the numerical flux across element boundaries and weak satisfaction of the Neumann boundary conditions, which requires that

$$\sum_e \int_{\partial\Omega_e} \bar{\sigma} \cdot \mathbf{n} \bar{v} \, d\Gamma = \int_{\Gamma_h} (1 - \gamma) \mathbf{a} \cdot \mathbf{n} \bar{\phi} \bar{v} \, d\Gamma + \int_{\Gamma_h} h \bar{v} \, d\Gamma \quad \forall \bar{v} \in \bar{V}. \quad (3.31)$$

The above expression has been constructed such that only the diffusive flux is imposed at outflow Neumann boundaries. Since $\bar{\sigma}$ is dependent on ϕ and $\bar{\phi}$, Equation (3.31) provides a constraint between ϕ and $\bar{\phi}$. In general DG methods, $\bar{\sigma}$ is constructed such that its jump is point-wise zero on interior element boundaries, whereas Equation (3.31) enforces this condition in a weak sense. The interface variable $\bar{\phi}$ may thus be regarded as a Lagrange multiplier enforcing the normal flux continuity constraint across element boundaries. Unlike in Hughes et al. [35], weak continuity of the flux is imposed directly, which leads naturally to an expression for determining $\bar{\phi}$. It is noteworthy to mention that the forcing term f appears in the local equation only.

By combining Equations (3.12) and (3.31), the following mixed problem is obtained: at time t , given the source term f and the boundary condition h , find $\phi \in V$ and $\bar{\phi} \in \bar{V}_g$ such that

$$\begin{aligned} \int_{\tilde{\Omega}} \frac{\partial \phi}{\partial t} v \, d\Omega - \int_{\tilde{\Omega}} \sigma \cdot \nabla v \, d\Omega - \sum_e \int_{\partial\Omega_e} \bar{\sigma} \cdot \mathbf{n} (\bar{v} - v) \, d\Gamma \\ + \sum_e \int_{\partial\Omega_e} \kappa (\bar{\phi} - \phi) \mathbf{n} \cdot \nabla v \, d\Gamma + \int_{\Gamma_h} (1 - \gamma) \mathbf{a} \cdot \mathbf{n} \bar{\phi} \bar{v} \, d\Gamma \\ = \int_{\tilde{\Omega}} f v \, d\Omega - \int_{\Gamma_h} h \bar{v} \, d\Gamma \quad \forall v \in V, \quad \forall \bar{v} \in \bar{V}. \end{aligned} \quad (3.32)$$

Setting $\bar{v} = 0$ in the above equation leads to a set of local equations and can be used to express ϕ in terms of $\bar{\phi}$ element wise. This is possible since $\bar{\sigma}$ depends on quantities local to an element and the interface function $\bar{\phi}$ only. Setting then $v = 0$, ϕ can be eliminated locally and the global equation can be solved to yield $\bar{\phi}$. The process is essentially the same as the static condensation of bubble functions. The major difference introduced here is the choice of discontinuous ‘bubbles’ within an element together with the

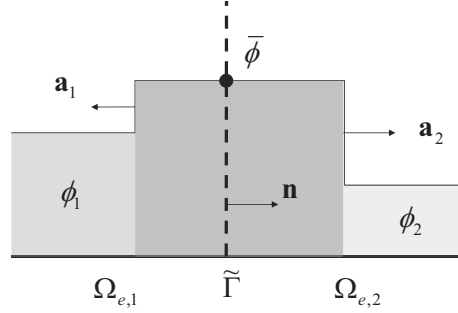


Figure 3.9: Construction of the advective flux from the local Riemann problem.

corresponding formulations involving the jump discontinuities across the element interfaces and the upwinding of the associated fluxes.

3.3.2 Interface flux

To solve Equation (3.32) it remains to construct an expression for the interface flux $\bar{\sigma}$ having the required properties. To this end it is assumed that $\bar{\sigma}$ can be decomposed additively into an advective part $\bar{\sigma}^a$ and a diffusive part $\bar{\sigma}^d$, the determination of which requires a different approach.

For the advective (hyperbolic) part, the local Riemann problem at the interface has to be considered. Generally, the solution of the Riemann problem consists of left and right travelling discontinuities separated by an intermediate state, see Figure 3.9. The numerical flux is then determined by the intermediate state $\bar{\phi}$ if the discontinuity travels into an element while the flux is determined by the element state ϕ if the propagation direction is outward. This principle can be used to construct the following expression for the advective flux

$$\bar{\sigma}^a = \mathbf{a}\phi + \gamma\tilde{\mathbf{a}}(\bar{\phi} - \phi), \quad (3.33)$$

where $\tilde{\mathbf{a}}$ is the transport velocity at the interface, $\gamma = 1$ where $\tilde{\mathbf{a}} \cdot \mathbf{n} \leq 0$ (inflow) and $\gamma = 0$ where $\tilde{\mathbf{a}} \cdot \mathbf{n} > 0$ (outflow). The transport velocity $\tilde{\mathbf{a}}$ generally depends on the traces of \mathbf{a} on the respective interface, see Harten et al. [33] or LeVeque [56] for possible definitions of $\tilde{\mathbf{a}}$. The following choice is made here

$$\tilde{\mathbf{a}} = \min(\mathbf{a}^+ \cdot \mathbf{n}, \mathbf{a}^- \cdot \mathbf{n}) \mathbf{n}, \quad (3.34)$$

where \mathbf{a}^+ and \mathbf{a}^- are the traces of \mathbf{a} on the element boundary $\partial\Omega_e$. This expression for $\tilde{\mathbf{a}}$ prevents $\bar{\phi}$ from becoming undefined in the cases of source or sink interfaces, i.e. where $\mathbf{a}^+ \cdot \mathbf{n}$ and $\mathbf{a}^- \cdot \mathbf{n}$ have a different sign.

For the diffusive part of the interface flux, the elliptic nature of the associated diffusion problem must be taken into account. This naturally leads to a formulation in which the element flux at the interface is augmented

with terms proportional to the jump $\bar{\phi} - \phi$. Out of many possibilities [1] a formulation is chosen which is reminiscent of the IP method

$$\bar{\sigma}^d = -\kappa \nabla \phi - \frac{\alpha}{h_e} \kappa (\bar{\phi} - \phi) \mathbf{n}, \quad (3.35)$$

where α is a dimensionless penalty parameter which is required for stability of DG methods, and h_e is a measure of the element size. Also for anisotropic diffusion, when κ is a symmetric tensor, Equation (3.35) is a consistent formulation for the diffusive interface flux.

As the expressions for $\bar{\sigma}^a$ and $\bar{\sigma}^d$ given by the respective Equations (3.33) and (3.35) have a similar format, the total interface flux $\bar{\sigma} = \bar{\sigma}^a + \bar{\sigma}^d$ can be written compactly as

$$\bar{\sigma} = \sigma + \beta (\bar{\phi} - \phi) \mathbf{n}, \quad (3.36)$$

where the term β is given by

$$\beta = \gamma \tilde{\mathbf{a}} \cdot \mathbf{n} - \frac{\alpha}{h_e} \kappa, \quad (3.37)$$

which, owing to its definition, is always a negative quantity.

Using Equations (3.2) and (3.36) for the numerical element and interface fluxes, respectively, Equation (3.32) leads to the following local problem: at time t , given the source term f , find $\phi \in V$ such that

$$\begin{aligned} \int_{\tilde{\Omega}} \frac{\partial \phi}{\partial t} v \, d\Omega + \int_{\tilde{\Omega}} \nabla \cdot (\mathbf{a}\phi - \kappa \nabla \phi) v \, d\Omega + \sum_e \int_{\partial\Omega_e} \beta (\bar{\phi} - \phi) v \, d\Gamma \\ + \sum_e \int_{\partial\Omega_e} \kappa (\bar{\phi} - \phi) \mathbf{n} \cdot \nabla v \, d\Gamma = \int_{\tilde{\Omega}} f v \, d\Omega \quad \forall v \in V, \end{aligned} \quad (3.38)$$

in which the regular part of the flux has been integrated by parts. The above local problem solves the advection-diffusion problem on each element with weakly imposed Dirichlet boundary conditions $\bar{\phi}$ on the element boundary $\partial\Omega_e$. From Equation (3.31) the global problem becomes: at time t , given the boundary condition h , find $\bar{v} \in \bar{V}_g$ such that

$$\begin{aligned} \sum_e \int_{\partial\Omega_e} (\mathbf{a}\phi - \kappa \nabla \phi) \cdot \mathbf{n} \bar{v} \, d\Gamma + \sum_e \int_{\partial\Omega_e} \beta (\bar{\phi} - \phi) \bar{v} \, d\Gamma \\ - \int_{\Gamma_h} (1 - \gamma) \mathbf{a} \cdot \mathbf{n} \bar{\phi} \bar{v} \, d\Gamma = \int_{\Gamma_h} h \bar{v} \, d\Gamma \quad \forall \bar{v} \in \bar{V}. \end{aligned} \quad (3.39)$$

Equation (3.38) can be used to express ϕ locally in terms of $\bar{\phi}$, which can then be substituted in Equation (3.39) to obtain a global equation for the nodal degrees of freedom $\bar{\phi}$. After solving for $\bar{\phi}$, the local equation is used to obtain the element degrees of freedom ϕ in a back-substitution step.

3.3.3 Properties

Before discussing a particular choice for the function spaces V and \bar{V} some general properties of the variational form given by Equation (3.32) with the fluxes given by Equation (3.36) are considered in some more detail.

3.3.3.1 Consistency

For sufficiently smooth functions ϕ and continuous advective velocity, the local problem given by Equation (3.38) leads to

$$\begin{aligned} \int_{\tilde{\Omega}} \left(\frac{\partial \phi}{\partial t} + \nabla \cdot \boldsymbol{\sigma} - f \right) v \, d\Omega + \sum_e \int_{\partial\Omega_e} \beta (\bar{\phi} - \phi) v \, d\Gamma \\ + \sum_e \int_{\partial\Omega_e} \kappa (\bar{\phi} - \phi) \mathbf{n} \cdot \nabla v \, d\Gamma = 0 \quad \forall v \in V, \end{aligned} \quad (3.40)$$

which demonstrates consistency with the strong form of the transport problem, given by Equations (3.1) and (3.2), and the enforcement of $\bar{\phi} = \phi$ on $\tilde{\Gamma}$. Using $\bar{\phi} = \phi$ on $\tilde{\Gamma}$, the global problem given by Equation (3.39) leads to

$$\begin{aligned} \sum_e \int_{\partial\Omega_e \setminus \Gamma_h} \boldsymbol{\sigma} \cdot \mathbf{n} \bar{v} \, d\Gamma + \int_{\Gamma_h} (\gamma \mathbf{a} \phi - \kappa \nabla \phi) \cdot \mathbf{n} \bar{v} \, d\Gamma \\ = \int_{\Gamma_h} h \bar{v} \, d\Gamma \quad \forall \bar{v} \in \bar{V}_g, \end{aligned} \quad (3.41)$$

which implies continuity of the flux and satisfaction of the modified Neumann boundary condition given by Equation (3.5).

3.3.3.2 Linear conservation

For a pure Neumann problem, $\Gamma_g = \emptyset$, setting $v = \bar{v} = 1$ in Equation (3.32) yields

$$\int_{\Omega} \frac{\partial \phi}{\partial t} \, d\Omega = \int_{\Omega} f \, d\Omega - \int_{\partial\Omega} (1 - \gamma) \mathbf{a} \cdot \mathbf{n} \bar{\phi} \, d\Gamma - \int_{\partial\Omega} h \, d\Gamma, \quad (3.42)$$

which proves linear conservation since the total increase of ϕ in $\tilde{\Omega}$ equals the total production plus the net inward flux over the boundary $\partial\Omega$. For Dirichlet boundary conditions the proof is more subtle as it is not possible to set $\bar{v} = 1$ on the entire domain then. Global conservation can still be demonstrated however by defining an auxiliary flux on Γ_g , see Hughes and Wells [37] for details of the approach. Setting $\bar{v} = 0$ on $\tilde{\Omega}$, $v = 0$ on $\Omega \setminus \Omega_e$ and $v = 1$ on Ω_e in Equation (3.32) gives

$$\int_{\Omega_e} \frac{\partial \phi}{\partial t} \, d\Omega = \int_{\Omega_e} f \, d\Omega - \int_{\partial\Omega_e} \bar{\boldsymbol{\sigma}} \cdot \mathbf{n} \, d\Gamma, \quad (3.43)$$

which proves local conservation in terms of the numerical flux, as is typical for DG methods. Unlike common DG methods the jump in $\bar{\sigma}$ is not point-wise zero on element interfaces, but the flux is weakly continuous in \bar{V} only.

3.3.3.3 Quadratic conservation

For the advective limit ($\kappa = 0$), setting $v = \phi$ and $\bar{v} = \bar{\phi}$ in Equation (3.32) and using homogeneous boundary conditions and zero source term gives

$$\begin{aligned} \int_{\tilde{\Omega}} \frac{\partial \phi}{\partial t} \phi \, d\Omega - \int_{\tilde{\Omega}} \phi \mathbf{a} \cdot \nabla \phi \, d\Omega + \sum_e \int_{\partial\Omega_e} \mathbf{a} \cdot \mathbf{n} \phi (\phi - \bar{\phi}) \, d\Gamma \\ - \sum_e \int_{\partial\Omega_e} \gamma \tilde{\mathbf{a}} \cdot \mathbf{n} (\phi - \bar{\phi})^2 \, d\Gamma + \int_{\Gamma_h} (1 - \gamma) \mathbf{a} \cdot \mathbf{n} \bar{\phi}^2 \, d\Gamma = 0. \end{aligned} \quad (3.44)$$

For a solenoidal vector field, $\nabla \cdot \mathbf{a} = 0$ in $\tilde{\Omega}$ and $[\![\mathbf{a}]\!] = 0$ on $\tilde{\Gamma}$, integration by parts of the regular flux term gives, after rearrangement,

$$\begin{aligned} \frac{d}{dt} \int_{\tilde{\Omega}} \frac{1}{2} \phi^2 \, d\Omega + \sum_e \int_{\partial\Omega_e} \frac{1}{2} |\mathbf{a} \cdot \mathbf{n}| (\phi - \bar{\phi})^2 \, d\Gamma \\ + \int_{\Gamma_h} \frac{1}{2} |\mathbf{a} \cdot \mathbf{n}| \bar{\phi}^2 \, d\Gamma = 0. \end{aligned} \quad (3.45)$$

This demonstrates that for the considered case the \mathcal{L}^2 norm of ϕ will not increase. For the diffusive limit case, a similar exercise yields

$$\begin{aligned} \frac{d}{dt} \int_{\tilde{\Omega}} \frac{1}{2} \phi^2 \, d\Omega + \int_{\tilde{\Omega}} \kappa \nabla \phi \cdot \nabla \phi \, d\Omega + \sum_e \int_{\partial\Omega_e} \frac{\alpha}{h_e} \kappa (\phi - \bar{\phi})^2 \, d\Gamma \\ + 2 \sum_e \int_{\partial\Omega_e} \kappa (\bar{\phi} - \phi) \mathbf{n} \cdot \nabla \phi \, d\Gamma = 0, \end{aligned} \quad (3.46)$$

implying that in the diffusive limit the \mathcal{L}^2 norm of ϕ may increase due to the fourth term on the left hand side which may become negative for function spaces V with polynomial orders $k > 0$. This non-physical behaviour can be avoided by choosing the penalty parameter α sufficiently large or by discarding the fourth left hand side term altogether, as in the skew-symmetric IP method [1, 35].

3.3.3.4 Stability

A non-increasing \mathcal{L}^2 norm does not yet prove stability as this requires coercivity of the variational form, implying that the rate of change of the \mathcal{L}^2 norm is also bounded from below for any non-trivial ϕ and $\bar{\phi}$. In the diffusive case this may be accomplished by choosing α sufficiently large or by reverting to the skew-symmetric IP formulation. The advective case is

more problematic as for $\phi = \bar{\phi}$ on $\tilde{\Gamma}$ and $\mathbf{a} \cdot \mathbf{n} = 0$ on Γ_h the respective terms in the left hand side of Equation (3.44) are already zero. This does not yet mean that the GIS method is unstable. The difficulty is inherent in the structure of the mixed formulation, which requires the satisfaction of an inf – sup condition in order to be stable. Demonstration of this is non-trivial and is not pursued here. It will be shown however that for the P^1 element a stabilizing mechanism is present which is closely related to that of the SUPG method. Furthermore, numerical examples have revealed remarkable stability properties, as will be demonstrated in Section 3.5.

3.4 Implementation

In this section the numerical implementation of the GIS method will be elaborated for P^1 elements by setting the polynomial orders $k = l = 1$ for the discontinuous space V and the space of interface functions \bar{V} , respectively. In this particular case the resulting formulation becomes relatively simple with most terms resembling those present in the linear CG method.

3.4.1 Time stepping

For P^1 basis functions all second derivative terms in Equations (3.38) and (3.39) vanish. For piecewise constant κ and using the θ -method to step in time the resulting discrete problem reads: given ϕ_n , the source term $f_{n+\theta}$ and boundary condition $h_{n+\theta}$, find $\phi_{n+\theta} \in V$ and $\bar{\phi}_{n+\theta} \in \bar{V}_g$ such that

$$\begin{aligned} \int_{\tilde{\Omega}} \frac{\phi_{n+\theta} - \phi_n}{\theta \Delta t} v \, d\Omega + \int_{\tilde{\Omega}} \nabla \cdot (\mathbf{a} \phi_{n+\theta}) v \, d\Omega + \sum_e \int_{\partial\Omega_e} \beta (\bar{\phi}_{n+\theta} - \phi_{n+\theta}) v \, d\Gamma \\ + \sum_e \int_{\partial\Omega_e} \kappa (\bar{\phi}_{n+\theta} - \phi_{n+\theta}) \mathbf{n} \cdot \nabla v \, d\Gamma = \int_{\tilde{\Omega}} f_{n+\theta} v \, d\Omega \quad \forall v \in V, \end{aligned} \quad (3.47)$$

and

$$\begin{aligned} \sum_e \int_{\partial\Omega_e} (\mathbf{a} \phi_{n+\theta} - \kappa \nabla \phi_{n+\theta}) \cdot \mathbf{n} \bar{v} \, d\Gamma + \sum_e \int_{\partial\Omega_e} \beta (\bar{\phi}_{n+\theta} - \phi_{n+\theta}) \bar{v} \, d\Gamma \\ - \int_{\Gamma_h} (1 - \gamma) \mathbf{a} \cdot \mathbf{n} \bar{\phi}_{n+\theta} \bar{v} \, d\Gamma = \int_{\Gamma_h} h_{n+\theta} \bar{v} \, d\Gamma \quad \forall \bar{v} \in \bar{V}, \end{aligned} \quad (3.48)$$

where Δt is the time step size, $\theta \in [0; 1]$ is a numerical parameter and $n + \theta$ denotes the intermediate time level $t_n + \theta \Delta t$, see also Section 2.3.2. The solution at the new time level $n + 1$ is obtained by extrapolation: $\phi_{n+1} = \phi_n + (\phi_{n+\theta} - \phi_n) / \theta$. The remainder of this section addresses the above fully-discrete formulations.

3.4.2 Solution procedure

The functions ϕ_n and $\bar{\phi}_n$ at time level t_n are expressed in terms of P^1 finite element basis functions and nodal values as

$$\phi_n(\mathbf{x}) = \sum_i N^i(\mathbf{x}) \phi_n^i, \quad (3.49)$$

$$\bar{\phi}_n(\mathbf{x}) = \sum_j \bar{N}^j(\mathbf{x}) \bar{\phi}_n^j, \quad (3.50)$$

where N^i and \bar{N}^j are finite element basis functions consistent with the definitions in Section 3.3.1 and ϕ_n^i and $\bar{\phi}_n^j$ are nodal degrees of freedom. For the case considered here, in which $k = l = 1$, the distinction between N^i and \bar{N}^j may be dropped on element boundaries which permits to set $N^i = \bar{N}^j$ on $\partial\Omega_e$ whenever $i = j$. The local problem (3.47) now leads to the algebraic equation

$$\frac{1}{\theta\Delta t} \mathbf{M}(\phi_{n+\theta} - \phi_n) + \mathbf{A}\phi_{n+\theta} + (\mathbf{K} + \mathbf{Q})(\bar{\phi}_{n+\theta} - \phi_{n+\theta}) = \mathbf{f}_{n+\theta}, \quad (3.51)$$

where ϕ_n^i is a vector containing the local unknowns of ϕ at time t_n , the element matrices \mathbf{M} , \mathbf{A} , \mathbf{K} and \mathbf{Q} are given by, in respective order,

$$M^{ij} = \int_{\Omega_e} N^i N^j d\Omega, \quad (3.52)$$

$$A^{ij} = \int_{\Omega_e} N^i \nabla \cdot (\mathbf{a} N^j) d\Omega, \quad (3.53)$$

$$K^{ij} = \int_{\partial\Omega_e} N^j (\kappa \mathbf{n}) \cdot \nabla N^i d\Gamma, \quad (3.54)$$

$$Q^{ij} = \int_{\partial\Omega_e} \beta N^i N^j d\Gamma, \quad (3.55)$$

and the element vector $\mathbf{f}_{n+\theta}$ is given by

$$f_{n+\theta}^i = \int_{\Omega_e} N^i f_{n+\theta} d\Omega. \quad (3.56)$$

As can be shown by partial integration, the matrix \mathbf{K} is algebraically equivalent to the standard element diffusion matrix of the linear CG method, for κ piecewise constant. The global problem given by Equation (3.48) has the following matrix format

$$\sum_e \left[(\tilde{\mathbf{A}} - \mathbf{K}^T) \phi_{n+\theta} + \mathbf{Q}(\bar{\phi}_{n+\theta} - \phi_{n+\theta}) - \mathbf{P}\bar{\phi}_{n+\theta} \right] = \sum_e \mathbf{h}_{n+\theta}, \quad (3.57)$$

where the matrices $\tilde{\mathbf{A}}$ and \mathbf{P} are given by, respectively,

$$\tilde{A}^{ij} = \int_{\partial\Omega_e} (\mathbf{a} \cdot \mathbf{n}) N^i N^j d\Gamma, \quad (3.58)$$

$$P^{ij} = \int_{\partial\Omega_e \cap \Gamma_h} (1 - \gamma) (\mathbf{a} \cdot \mathbf{n}) N^i N^j d\Gamma, \quad (3.59)$$

the right hand side vector $\mathbf{h}_{n+\theta}$ is given by

$$h_{n+\theta}^i = \int_{\partial\Omega_e \cap \Gamma_h} N^i h_{n+\theta} d\Gamma, \quad (3.60)$$

and \sum_e represents assembly of the element matrices into a global matrix. Note that for P^1 elements and piecewise constant κ the matrix \mathbf{K}^T equals the matrix \mathbf{K} in Equation (3.54). For a solenoidal velocity field $\tilde{\mathbf{A}} = \mathbf{A} + \mathbf{A}^T$.

By algebraic manipulation, Equation (3.57) can be expressed entirely in terms of the global unknowns $\bar{\phi}_{n+\theta}$ and the known local degrees of freedom ϕ_n . Subtracting Equation (3.57) from Equation (3.51) in an element wise fashion yields

$$\begin{aligned} \sum_e \left[\left(\frac{1}{\theta\Delta t} \mathbf{M} + \mathbf{A} - \tilde{\mathbf{A}} \right) \phi_{n+\theta} + (\mathbf{K} + \mathbf{P}) \bar{\phi}_{n+\theta} \right] \\ = \sum_e \left(\frac{1}{\theta\Delta t} \mathbf{M} \phi_n + \mathbf{f}_{n+\theta} - \mathbf{h}_{n+\theta} \right). \end{aligned} \quad (3.61)$$

In order to eliminate $\phi_{n+\theta}$ the local Equation (3.51) is rewritten as

$$\phi_{n+\theta} = \bar{\phi}_{n+\theta} - \mathbf{T} \left[\frac{1}{\theta\Delta t} \mathbf{M} (\bar{\phi}_{n+\theta} - \phi_n) + \mathbf{A} \bar{\phi}_{n+\theta} - \mathbf{f}_{n+\theta} \right], \quad (3.62)$$

where

$$\mathbf{T} = \left(\frac{1}{\theta\Delta t} \mathbf{M} + \mathbf{A} - \mathbf{K} - \mathbf{Q} \right)^{-1}. \quad (3.63)$$

Substitution of Equation (3.62) into Equation (3.61) and re-arrangement results in the following global equation

$$\begin{aligned} \sum_e \mathbf{W} \left[\frac{1}{\theta\Delta t} \mathbf{M} (\bar{\phi}_{n+\theta} - \phi_n) + \mathbf{A} \bar{\phi}_{n+\theta} - \mathbf{f}_{n+\theta} \right] \\ + \sum_e \left(\mathbf{K} + \mathbf{P} - \tilde{\mathbf{A}} \right) \bar{\phi}_{n+\theta} + \sum_e \mathbf{h}_{n+\theta} = 0, \end{aligned} \quad (3.64)$$

where the element ‘weighting matrix’ \mathbf{W} is given by

$$\mathbf{W} = \mathbf{I} - \left(\frac{1}{\theta\Delta t} \mathbf{M} + \mathbf{A} - \tilde{\mathbf{A}} \right) \mathbf{T}. \quad (3.65)$$

Besides being compact, this form of the matrix equations is particularly convenient in practice as it only involves the multiplication of standard CG matrices with the weighting matrix \mathbf{W} , in an element wise fashion. The only non-standard element matrices that must be computed to obtain \mathbf{W} are the element boundary matrices \mathbf{Q} and $\tilde{\mathbf{A}}$ given by Equations (3.55) and (3.58), respectively. Importantly, for elements where $\mathbf{a} = \mathbf{0}$ and $\kappa = 0$ the expression for \mathbf{W} remains non-singular. For $\mathbf{T} = \mathbf{0}$ the interface stabilization

terms vanish, and the conventional CG method is recovered. Reversely, a linear CG computer code is easily converted into a linear GIS code with the use of Equation (3.64).

The elimination of the ϕ degrees of freedom at the element level results in an efficient algorithm, as global Equation (3.64) has the number of un-knowns of the associated CG method. The resulting sparse matrix system may be solved efficiently using iterative techniques as for instance the BICGSTAB algorithm combined with ILU preconditioning [69, 93]. In time stepping problems, the element degrees of freedom ϕ need to be stored in memory. After solving the global system, their values are updated in a simple back-substitution procedure, using local Equation (3.62) and subsequent extrapolation to the next time level t_{n+1} .

3.4.3 Stabilization mechanism

For a stationary problem, with solenoidal advective field \mathbf{a} and homogeneous Dirichlet boundary conditions, the global problem from Equation (3.64) reads, after using $\tilde{\mathbf{A}} = \mathbf{A} + \mathbf{A}^T$ and re-ordering,

$$\underbrace{\sum_e (-\mathbf{A}^T + \mathbf{K}) \bar{\phi} - \sum_e \mathbf{f}}_{\text{standard CG terms}} + \underbrace{\sum_e \mathbf{A}^T \mathbf{T} (\mathbf{A} \bar{\phi} - \mathbf{f})}_{\text{additional terms}} = \mathbf{0}. \quad (3.66)$$

Compared to the standard linear continuous Galerkin method Equation (3.66) has additional terms containing element wise ‘residual’ vectors $\mathbf{A} \bar{\phi} - \mathbf{f}$ from the advection and source terms. For higher order elements, the element wise residuals would also contain the diffusive part of the flux, but in this case of linear elements all second derivatives in Equation (3.47) have vanished and the diffusive part is not present in the element residual.

For the SUPG method, assuming piecewise linear velocity \mathbf{a} and a linear source function f , global Equation (3.20) has the following matrix form [36]

$$\underbrace{\sum_e (-\mathbf{A}^T + \mathbf{K}) \bar{\phi} - \sum_e \mathbf{f}}_{\text{standard CG terms}} + \underbrace{\sum_e \mathbf{A}^T \tau_e \mathbf{M}^{-1} (\mathbf{A} \bar{\phi} - \mathbf{f})}_{\text{SUPG stabilization term}} = \mathbf{0}, \quad (3.67)$$

where τ_e is a stabilization parameter, assumed piecewise constant, which is given by

$$\tau_e = \frac{1}{2} \frac{h_e}{|\mathbf{a}'|} \xi, \quad (3.68)$$

where h_e is the streamwise length of the element, \mathbf{a}' is a measure of the advective velocity within an element and ξ is a function of the Péclet number [87]. The SUPG stabilization term closely resembles that of the interface stabilization method, with the matrix $\tau_e \mathbf{M}^{-1}$ replacing the matrix \mathbf{T} of the latter. If all terms in the ‘residual’ vector $\mathbf{A} \bar{\phi} - \mathbf{f}$ are equal (element

wise), the methods are algebraically equivalent as the matrix \mathbf{T} can then be replaced by a matrix $\tau'_e \mathbf{M}^{-1}$ with the parameter τ'_e given by

$$\tau'_e = \frac{\sum_{i,j} \mathbf{T}}{\sum_{i,j} \mathbf{M}^{-1}}, \quad (3.69)$$

where $\sum_{i,j}$ denotes summation over all matrix entries.

To show the correspondence between τ'_e and τ_e , consider a one-dimensional case with piecewise constant velocity a for which the matrix \mathbf{T} is given by

$$\mathbf{T} = \begin{pmatrix} \frac{1}{2}|a| + \frac{(\alpha-1)\kappa}{h_e} & \frac{1}{2}a + \frac{\kappa}{h_e} \\ -\frac{1}{2}a + \frac{\kappa}{h_e} & \frac{1}{2}|a| + \frac{(\alpha-1)\kappa}{h_e} \end{pmatrix}^{-1}. \quad (3.70)$$

From Equation (3.69), and using Equation (3.70), τ'_e can be expressed as

$$\tau'_e = \frac{1}{2} \frac{h_e}{|a|} \xi', \quad (3.71)$$

where ξ' is a Péclet -number dependent function given by

$$\xi' = \frac{1 + (\alpha - 2) Pe^{-1}}{1 + (\alpha - 1) Pe^{-1} + \frac{1}{2} \alpha (\alpha - 2) Pe^{-2}}. \quad (3.72)$$

Comparison of τ'_e with the expression for τ_e given by Equation (3.68) shows that in this example the interface stabilization method is equivalent to the SUPG method with ξ' replacing ξ .

Figure 3.10 shows the term ξ' for penalty values $\alpha = 4$ and $\alpha = 6$. Also shown are functions ξ for which SUPG stabilization is optimally accurate and functions for which stabilization is critical in the sense that solutions are just monotone, see Simo et al. [81]. For any penalty value α , the function ξ' approaches the optimal value of one in the advective limit. In the diffusive case, $\alpha = 6$ leads to the optimal limit behaviour $\xi' = \frac{1}{3} Pe$ as $Pe \downarrow 0$, but the corresponding ξ' is too small in the high Péclet number range. Taking $\alpha = 4$ improves this behaviour at the price of a slight deviation from the optimal value of ξ in the diffusive limit. Importantly, with a fixed α , the model adapts automatically to the flow conditions, removing the ambiguity in selecting a Péclet-number dependent stabilization term.

3.4.4 Fourier analysis

Next, a Fourier analysis is performed for the one-dimensional case with uniform advective velocity a and diffusivity κ by imposing periodic solutions of the following form

$$\phi = \tilde{\phi} e^{(i\omega - \mu)t} e^{-ikx}, \quad (3.73)$$

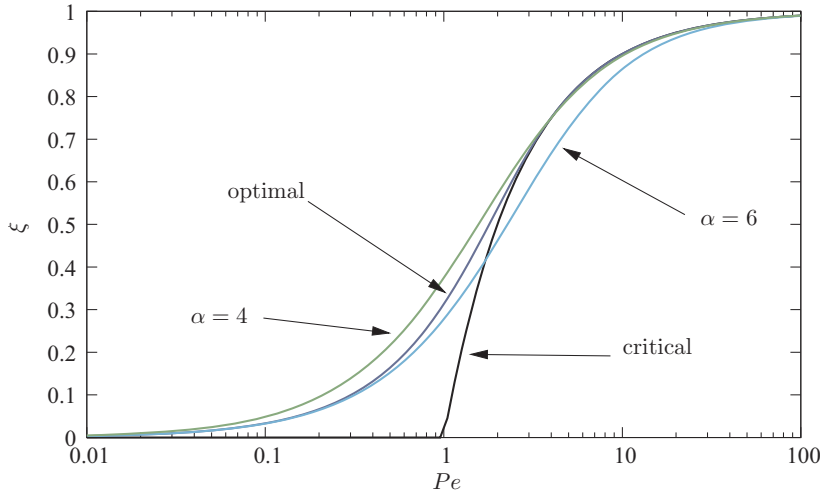


Figure 3.10: *Optimal ξ (dark blue) and critical ξ (black) for the SUPG method and ξ' for the GIS method with $\alpha = 4$ (green) and $\alpha = 6$ (light blue).*

where $\tilde{\phi}$ is a constant complex amplitude, k is the spatial wave number, ω is the radian frequency, μ is the damping rate and $i = \sqrt{-1}$ is the imaginary unit. For each wave number, the corresponding frequency and damping rate can be determined by solving the generalized eigenvalue problem which is obtained after inserting the periodic solution into the semi-discrete Equations (3.38) and (3.39).

The eigenvalue problem has two roots which, together with the exact root, are given in Figure 3.11 as functions of the dimensionless wave number kh_e/π . Note that for the advective case ω and μ are scaled with a factor $h_e/|a|$ while for the diffusive case the scaling factor is h_e^2/κ , in order to obtain dimensionless quantities. In the advection dominated case the frequency of the physical mode, shown in frame (a) is close to the exact frequency $\omega = ka$ while the negative frequency of the non-physical mode indicates propagation in the opposite direction. As shown in frame (b) the non-physical mode is strongly damped and will quickly disappear from the solution. For wave numbers $kh_e < 0.4\pi$, which involves more than 15 elements per wavelength, the damping rate of the physical root is close to the exact solution $\mu = 0$. Note that the frequency of the physical mode is a monotone function of the wave number. The group velocity $c_g = \partial\omega/\partial k$ is therefore positive which avoids the upstream propagation of energy and the associated accumulation of spurious wiggles. Frame (c) shows that in the diffusive case the physical and the non-physical modes have the exact frequency $\omega = 0$. As shown in frame (d), the non-physical root of the diffusive case is strongly damped leaving the physical root as the dominant part of the solution. For a stability parameter $\alpha = 6$ the damping rate of the physical mode is close to the exact solution $\mu = \kappa k^2$ if the wave number $kh_e < 0.8\pi$, which requires more than

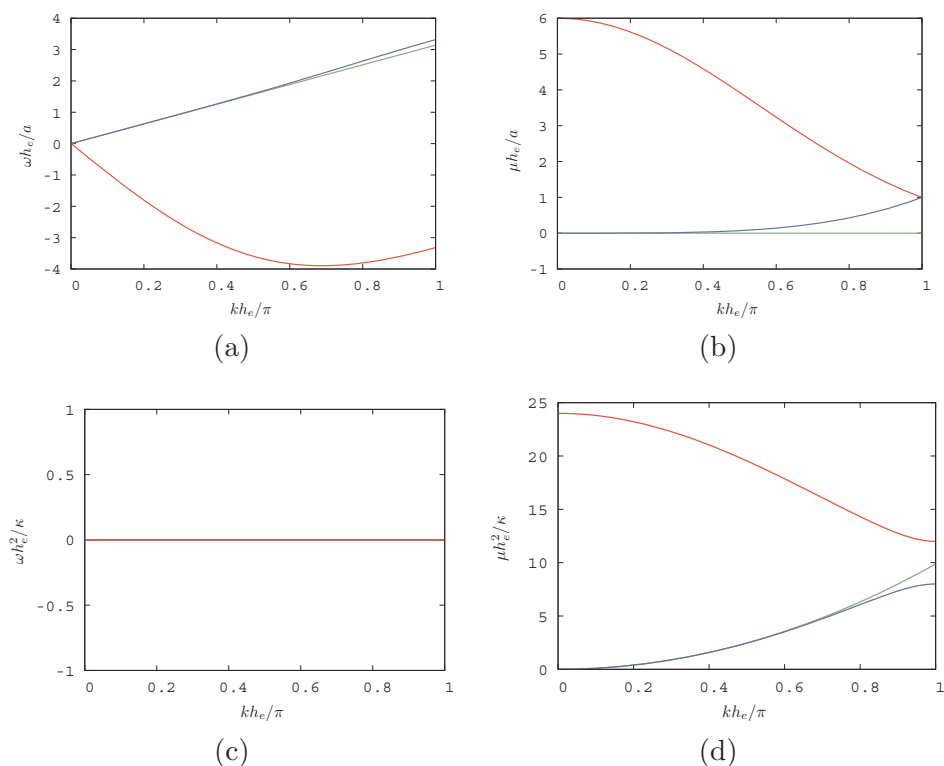


Figure 3.11: *Fourier analysis: advection, (a) dispersion and (b) damping; diffusion ($\alpha = 6$), dispersion (c) and damping (d); physical roots (blue), non-physical roots (red) and exact solutions (green).*

8 elements per wavelength.

3.5 Numerical examples

In this section the linear interface stabilization method is demonstrated for a range of numerical examples. Unless stated otherwise all examples use a stability constant $\alpha = 4$. For the one-dimensional cases a direct linear solver is used while two- and three-dimensional cases use the BICGSTAB method in combination with straightforward ILU preconditioning.

3.5.1 Advection-diffusion with source

Because of its resemblance with SUPG-type stabilization it is anticipated that the linear interface stabilization method also has $\mathcal{O}(h_e^2)$ and $\mathcal{O}(h_e^{3/2})$ convergence rates in the \mathcal{L}^2 error norm for the diffusive and the advective limit cases, respectively. In order to confirm these convergence rates the

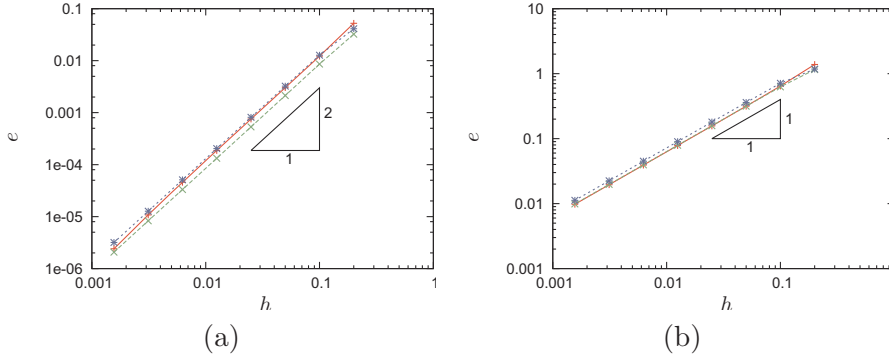


Figure 3.12: *Advection-diffusion with source: error in the \mathcal{L}^2 norm (a) and in the \mathcal{H}^1 semi-norm (b) for $Pe = 100$ (blue), $Pe = 1$ (green) and $Pe = 0.01$ (red).*

following one-dimensional smooth test problem is considered

$$Pe \frac{\partial \phi}{\partial x} - \frac{\partial^2 \phi}{\partial x^2} = 50 (1 - Pe x - 50x^2) \exp(-25x^2), \quad (3.74)$$

on the domain $\Omega = (-1, 1)$ with $\phi = 0$ at $x = \pm 1$. For every Péclet number, the exact solution ϕ_e to this problem is given by

$$\phi_e = \exp(-25x^2). \quad (3.75)$$

The computations are performed using uniform meshes with element sizes h_e ranging from $1/1000$ to $1/10$. The value of κ is adjusted in order to obtain Péclet numbers of 0.01 , 1 and 100 , respectively.

The resulting error $e = \phi_e - \phi$, measured in the \mathcal{L}^2 norm and in the \mathcal{H}^1 semi-norm, is shown in Figure 3.12. In the advective and diffusive limits, the observed convergence rate is of order two in the \mathcal{L}^2 norm and of order one in the \mathcal{H}^1 semi-norm. For the advective case, this result is slightly better than generally predicted for stabilized linear finite element methods.

3.5.2 Boundary layers

Consider the stationary advection-diffusion equation

$$\mathbf{a} \cdot \nabla \phi - \kappa \nabla^2 \phi = 0 \quad \text{on } \Omega \subset \mathbb{R}^d, \quad (3.76)$$

in which $\mathbf{a} \in \mathbb{R}^d$ is a uniform advective velocity and κ is a uniform diffusivity. The numerical behaviour of solutions is determined by the way the boundary conditions are enforced, the orientation of \mathbf{a} with respect to the mesh and the element Péclet number. The following examples address these issues.

3.5.2.1 Outflow boundary

Consider the domain $\Omega = (0, 1)$ with Dirichlet boundary conditions $g = 1$ at $x = 0$ and $g = 0$ at $x = 1$. The exact solution to Equation (3.76) for this case is given by

$$\phi_e = \frac{\exp(ax/\kappa) - \exp(a/\kappa)}{1 - \exp(a/\kappa)}, \quad (3.77)$$

which involves an outflow boundary layer having a width of order κ/a . For large Péclet numbers, the boundary layer is thin with respect to the element size h_e and the numerical solution may become oscillatory.

Figure 3.13 shows the computed solutions for $h_e = 1/20$ and Péclet numbers ranging from 0.01 to 10. In general, the agreement between the exact solution and the numerical solution is good. For $Pe = 10$, the solution for ϕ shows some overshoot near the outflow boundary, but this remains localized. In terms of $\bar{\phi}$ there is no overshoot. The effect of weakly imposed boundary conditions on ϕ can be observed in Figure 3.13 for the case $Pe = 10$. At the outflow boundary, there is a significant difference between ϕ and $\bar{\phi}$. This demonstrates an advantage of using weak Dirichlet boundary conditions in regions with steep gradients.

The interpolated values of the interface variable $\bar{\phi}$ provide a good representation of the discontinuous field ϕ and may be used for post processing purposes instead of the latter. Especially in higher dimensions this will be convenient as the vector of the nodal degrees of freedom $\bar{\phi}$ requires considerably less storage space than the vector ϕ containing the local unknowns.

3.5.2.2 Characteristic boundary layer

Consider the unit square $\Omega : (0, 1) \times (0, 1)$ with Dirichlet boundary conditions $g = 1$ on $y = 0$, $g = 0$ on $x = 0$ and homogeneous Neumann boundary conditions elsewhere. The computational domain is partitioned by regular triangular elements with uniform element size $h_e = 1/30$. The transport velocity in Equation (3.76) is set to $\mathbf{a} = (\cos \varphi, \sin \varphi)^T$ using characteristic directions φ of 15° , 30° , 45° and 60° , respectively. The diffusivity κ is set to 10^{-6} . The exact solution to this problem involves a discontinuity which is aligned with the characteristic direction and the test will reveal the ability of the model to resolve the associated steep gradients [42, 81].

Figure 3.14 shows that for all directions φ the characteristic boundary layer is adequately resolved. The jump discontinuities are captured in about five elements. The under- and overshoot on either side of the boundary layer remains localized. Table 3.1 summarizes maximum and minimum values of ϕ and $\bar{\phi}$ across the boundary layer showing variations of $\pm 15\%$ and $\pm 10\%$ of the theoretical jump, respectively. These results demonstrate that the weak enforcement of the interelement continuity constraint reduces the amount of under- and overshoot in the global solution $\bar{\phi}$.

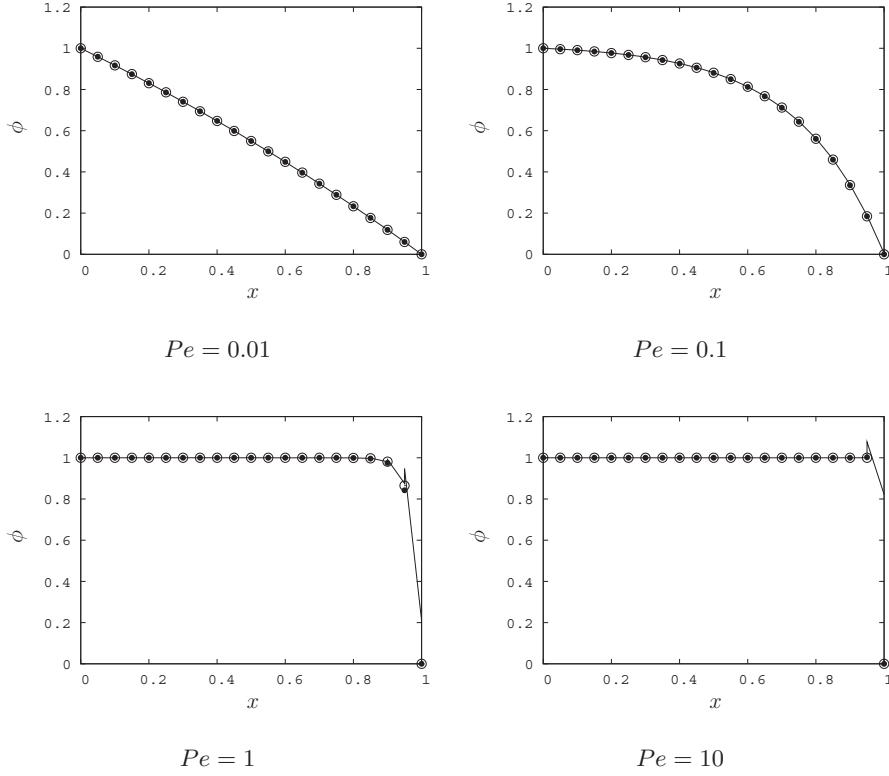


Figure 3.13: Outflow boundary layer for various Péclet numbers; $\bar{\phi}$ (dots), ϕ (solid) and exact solution (circles).

3.5.2.3 Advection in a box

This example considers the influence of the Péclet number on the behaviour of three-dimensional boundary layers. In two or three dimensions the Péclet number is ambiguous and following definition is used here

$$Pe = \frac{\int_{\Omega_e} |\mathbf{a} \cdot \nabla N^j| N^j d\Omega}{\int_{\Omega_e} \kappa \nabla N^j \cdot \nabla N^j d\Omega}, \quad (3.78)$$

using the summation convention. The above expression is the ratio of the traces of the modulus of the element advection and diffusion matrices.

The computational domain is the unit cube $\Omega : (0, 1) \times (0, 1) \times (0, 1)$. The three-dimensional mesh of the cube is constructed by expanding a two-dimensional mesh of triangles in z -direction using 20 layers of tetrahedrons. The resulting mesh has 10227 nodes and an element size $h_e = 1/20$. The advective velocity in Equation (3.76) is set to $\mathbf{a} = (1, 1, 1)^T$ and the diffusivity κ is adjusted in order to obtain Péclet numbers of 0.01, 0.1, 1 and 10, respectively. Dirichlet boundary conditions are imposed on each face of the cube setting $g = 1$ on the inflow boundary given by the plane $x = 0$

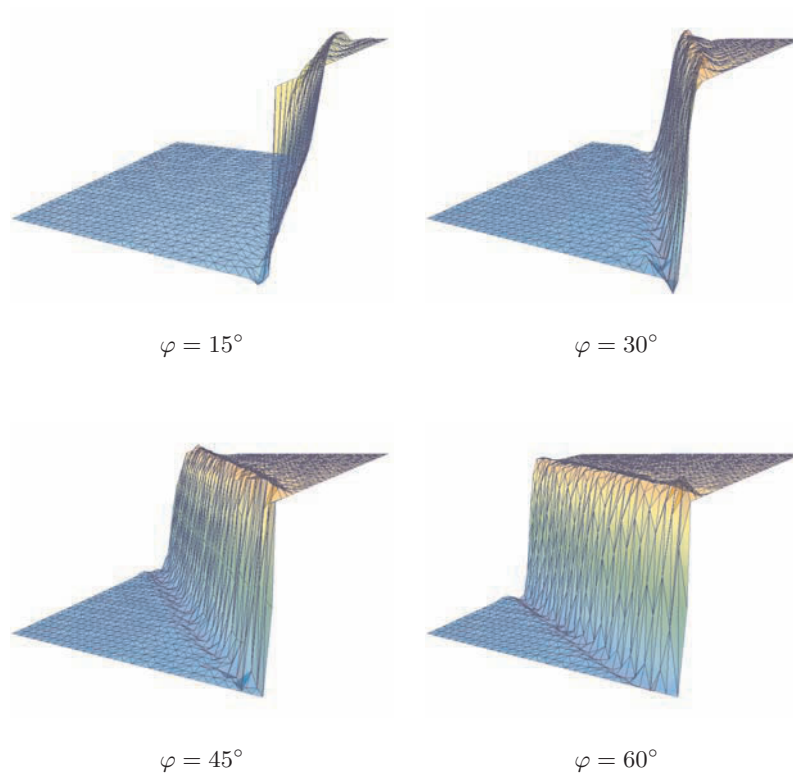


Figure 3.14: *Characteristic boundary layer: numerical solution $\bar{\phi}$ for various characteristic directions.*

$\varphi :$	15°	30°	45°	60°
ϕ_{\max}	1.146	1.136	1.157	1.166
$\bar{\phi}_{\max}$	1.067	1.082	1.094	1.110
ϕ_{\min}	-0.104	-0.179	-0.155	-0.129
$\bar{\phi}_{\min}$	-0.068	-0.122	-0.081	-0.087

Table 3.1: *Characteristic boundary layer: minimum and maximum values of computed ϕ and $\bar{\phi}$.*

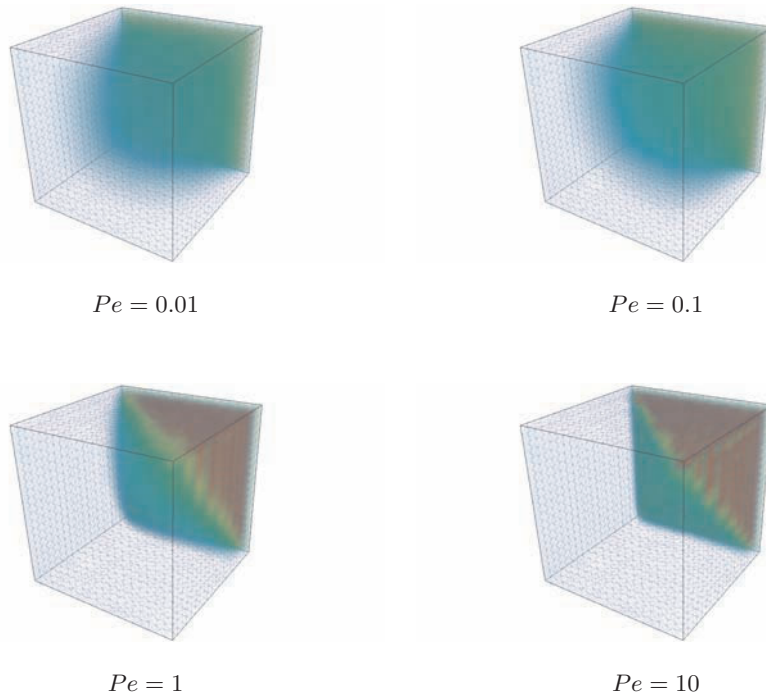


Figure 3.15: *Advection in a box: numerical solution $\bar{\phi}$ (interpolated) for different Péclet numbers, view is in upstream direction; red indicates $\bar{\phi} > 1$.*

and setting $g = 0$ elsewhere. To by-pass the singularities at the edges of the cube, the Dirichlet condition is imposed via a penalty formulation using a penalty parameter 10^6 . The solution involves outflow boundary layers at the planes $x = 1$, $y = 1$ and $z = 1$, respectively, and a characteristic boundary layer centered around the plane $x = \min(y, z)$.

Figure 3.15 shows the numerical solution $\bar{\phi}$. The numerical solution is smooth for $Pe \leq 0.1$ but for $Pe \geq 1$ the outflow boundary layer exhibits significant overshoot, see also Table 3.2. The overshoot remains confined to a small neighbourhood of the outflow boundary and does not spoil the solution in upstream direction. The overshoot is caused by the Dirichlet boundary condition for $\bar{\phi}$ which affects the inter-element boundary condition in all elements connected to the outflow boundary, irrespective of the direction of the tangential velocity at element interfaces. In all cases, the characteristic boundary layers are nicely resolved with a maximum over- and undershoot of $\bar{\phi}$ of about 15% of the theoretical jump in the $Pe = 10$ case.

3.5.3 Anisotropic diffusion

Anisotropic diffusive transport is particularly relevant in environmental water systems since the intensities of the horizontal and vertical mixing processes may differ considerably, the physics of which is explained in Fischer

	$Pe = 0.01$	$Pe = 0.1$	$Pe = 1$	$Pe = 10$
$\bar{\phi}_{\max}$	1.000	1.000	1.754	2.611
$\bar{\phi}_{\min}$	0.000	0.000	-0.013	-0.162

Table 3.2: *Advection in a box: minimum and maximum values of $\bar{\phi}$.*

[24]. In shallow water the dispersion coefficients in streamwise and cross stream directions, respectively, may differ by a factor of ten to twenty.

The formulation of the diffusive interface flux from Equation (3.35) should take anisotropy into account, which is tested by solving the two-dimensional diffusion equation obtained trivially from Equation (3.6) by setting $\mathbf{a} = \mathbf{0}$. The initial condition is a Gaussian hat with unit concentration in the center $(x, y) = (0, 0)$ and standard deviation $\sigma_0 = 1$. For the boundary condition $\phi \rightarrow 0$ if $|\mathbf{x}| \rightarrow \infty$, the exact solution ϕ_e to this problem reads

$$\phi_e = \frac{1}{\sigma_s \sigma_n} \exp\left(-\frac{s^2}{2\sigma_s^2} - \frac{n^2}{2\sigma_n^2}\right), \quad (3.79)$$

where (s, n) are coordinates with respect to the principal axis of the diffusion tensor, $\sigma_{s,n}^2 = \sigma_0^2 + 2\kappa_{s,n}t$ are the corresponding standard deviations in which $\kappa_{s,n}$ are the transformed diffusivities.

The computational domain is the square $\Omega : (-12, 12) \times (-12, 12)$ which is partitioned using thirty elements along each side of the square giving an element size $h_e = 0.8$. The diffusivities are set to $\kappa_s = 10$ and $\kappa_n = 1$. The principal axis of the diffusion tensor κ has angles φ of 0° , 45° , 90° and 135° with the x -axis, respectively. The computation proceeds until $t = 1$ for which $\sigma_s^2 = 21$ and $\sigma_n^2 = 3$. The domain is chosen large enough to avoid interference of the solution with the boundaries which permits to set $\bar{\phi} = 0$ on $\partial\Omega$. For time stepping, the FS scheme is used with an average time step size $\Delta t = 1/30$.

The numerical solutions are shown in Figure 3.16 together with the exact fields. The correspondence between the numerical and the exact solutions is good. For $\varphi = 45^\circ$ a slight deviation from the exact solution may be observed, which is probably caused by the bias in the orientation of the mesh, from lower left to upper right. The results confirm that the proposed approximation of the interface flux by Equation (3.35) is appropriate in the case of anisotropic diffusion.

3.5.4 Simple waves

The next series of examples concerns the time dependent advection problem

$$\frac{\partial \phi}{\partial t} + \mathbf{a} \cdot \nabla \phi = 0 \quad \text{on } \Omega \subset \mathbb{R}^d, \quad (3.80)$$

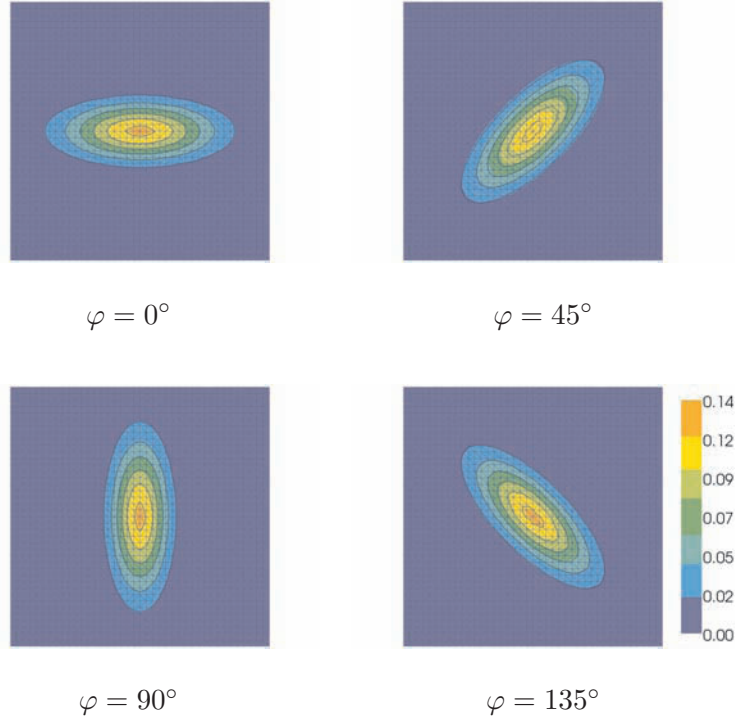


Figure 3.16: *Anisotropic diffusion: numerical solution $\bar{\phi}$ (colour) and exact solution (isolines) for different orientations of the principal axis of the diffusion tensor; contour intervals 0.02.*

where the solenoidal advective velocity $\mathbf{a} : \Omega \rightarrow \mathbb{R}^d$. For the initial condition $\phi(\mathbf{x}, t_0) = \phi_0$ the exact solution to this problem is given by

$$\phi_e(\mathbf{x}(\boldsymbol{\chi}, t)) = \phi_0(\boldsymbol{\chi}), \quad (3.81)$$

where $\boldsymbol{\chi}$ is a label co-ordinate attached to material points moving with the velocity \mathbf{a} and which is chosen such that $\boldsymbol{\chi} = \mathbf{x}$ at $t = t_0$. For a uniform velocity \mathbf{a} the above solution corresponds to a rigid body translation.

The numerical behaviour of solutions is to a large extent determined by the Courant-Friedrich-Lewis (*CFL*) number, the definition of which is ambiguous in two - and three dimensions. The following expression is used here

$$CFL = \frac{\int_{\Omega_e} |\mathbf{a} \cdot \nabla N^j| N^j d\Omega}{\int_{\Omega_e} \Delta t^{-1} N^j N^j d\Omega}, \quad (3.82)$$

which is the ratio of the traces of the modulus of the element advection and mass matrices. The examples investigate the influence of the Courant number on the quality of numerical solution for the FS time stepping scheme.

	case	$CFL = 0.2$	$CFL = 0.4$	$CFL = 0.8$	$CFL = 1.6$
$\bar{\phi}_{\max}$	1-d	0.9532	0.9511	0.9142	0.8505
	2-d	0.9353	0.9252	0.9195	0.8544
	3-d	0.8899	0.8889	0.8833	0.7873
$\bar{\phi}_{\min}$	1-d	-0.0034	-0.0065	-0.0329	-0.1651
	2-d	-0.0059	-0.0055	-0.0392	-0.1674
	3-d	-0.0071	-0.0068	-0.0477	-0.1916
rel. celerity	1-d	0.9993	0.9993	0.9994	1.0010
	2-d	0.9954	0.9950	0.9925	0.9833
	3-d	0.9983	0.9982	0.9976	0.9954

Table 3.3: *Summary simple-wave tests: minimum and maximum concentrations and relative celerity; initial distributions are Gaussian with standard deviation $2h_e$; theoretical total displacements $15h_e$.*

3.5.4.1 Travelling hill

The one-dimensional domain $\Omega = (0, 1)$ is partitioned by thirty uniform elements. The initial condition is a Gaussian hill with unit height, center position $x = 0.2$ and standard deviation $\sigma_x = 2h_e$. Setting the advective velocity $a = 1$, the time step size Δt is varied in order to obtain Courant numbers of 0.2, 0.4, 0.6 and 1.8, respectively. The computation proceeds until the theoretical translation of the hill equals $15h_e$.

The numerical results are shown in Figure 3.17. Regarding the small initial size of the hill with respect to the element size, the numerical results are in good agreement with the theoretical solution. For $CFL < 0.8$ the position of the center of the hill is reproduced correctly while the peak height has decreased to about 0.95, see also Table 3.3. For $CFL \geq 0.8$ the relative celerity remains close to one but high frequency dispersion causes some distortion and undershoot on the upstream side of the hill. This could be suppressed by using the backward Euler time stepping scheme which will however increase artificial diffusion. In all cases the total mass remained constant, which confirms the theoretical result given by Equation (3.42).

3.5.4.2 Rotating cone

On the unit circle $\Omega = \{(x, y) | x^2 + y^2 < 1\}$ a rotational velocity field is given by $(a_x, a_y) = (-y, x)$. The initial condition ϕ_0 is a Gaussian hat with unit height, center position $(x, y) = (\frac{1}{2}, 0)$ and standard deviations $\sigma_x = \sigma_y = 2h_e$. The domain is partitioned by equilateral elements with element size $h_e \approx 1/10$. The time step size Δt is adjusted in order to obtain

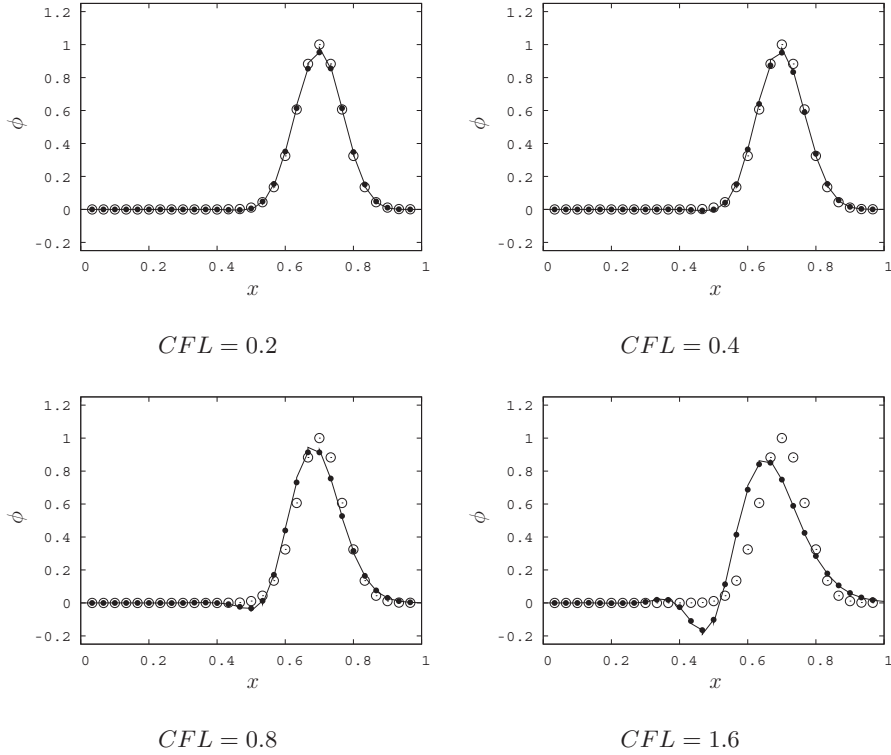


Figure 3.17: Translation of a Gaussian hill for various Courant numbers showing ϕ (solid), $\bar{\phi}$ (dots) and exact solution (circles).

Courant numbers of 0.2, 0.4, 0.8 and 1.6, respectively, measured at the center of the cone. The total simulation time yields a theoretical rotation through π radians, implying a total displacement of the cone center of about $15 h_e$.

The computational results are shown in Figure 3.18. For Courant numbers of 0.4 and 0.8 the results are in good agreement with the theoretical solutions, giving the correct position of the center of the cone while keeping the peak value close to one, see also Table 3.3. For Courant numbers 0.8 and 1.6, high frequency dispersion causes some distortion and negative concentrations on the upstream side of the cone. Computations confirm that the total mass remains constant. The accuracy of the results is comparable to that of the one-dimensional test.

3.5.4.3 Spiralling blob

On the cylindrical domain $\Omega = \{(x, y, z) : y^2 + z^2 < 1, 0 < x < 3\}$ the flow field $\mathbf{a} = (\frac{1}{2}, z, -y)^T$ describes a helical motion around the axis of the cylinder. The initial condition ϕ_0 is a Gaussian blob with unit height, centered at the point $(x, y, z) = (\frac{1}{2}, \frac{1}{2}, 0)$ and with standard deviations $\sigma_x = \sigma_y = \sigma_z = 2 h_e$. The simulation proceeds until a theoretical rotation

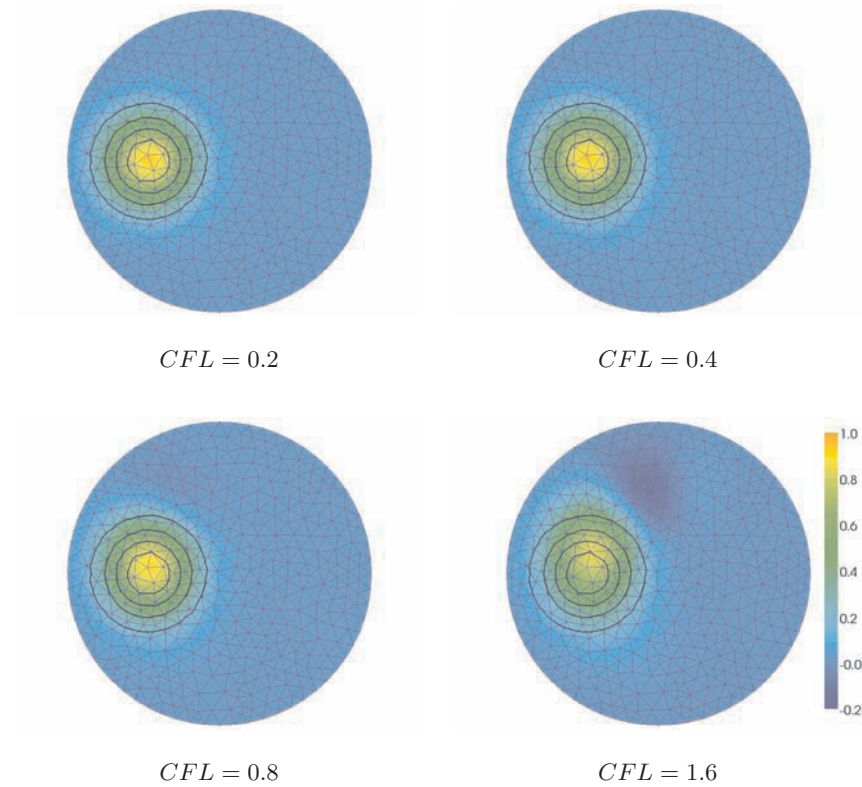


Figure 3.18: Numerical solution $\bar{\phi}$ (colour) and exact solution (isolines) of the rotating cone problem for various Courant numbers; values isolines: 0.2, 0.4, 0.6 and 0.8.

through $\pi/\sqrt{2}$ radians giving a total displacement along streamlines of $15 h_e$. The mesh is constructed from the two-dimensional circular mesh of the rotating cone test by ‘inflating’ the mesh in x -direction with thirty layers of tetrahedral elements giving an element size $h_e \approx 1/10$. Different time step sizes are used in order to obtain Courant numbers of 0.2, 0.4, 0.8 and 1.6, respectively, measured at the center of the blob.

The results of the computations are shown in Figure 3.19 and summarized in Table 3.3. For Courant numbers of 0.2 and 0.4 the numerical solution is close to the exact solution with peak values of 0.89 and minimum values of about -0.007 , respectively. The relative celerity is close to one for these cases. For $CFL \geq 0.8$ the celerity error hardly increases but in terms of peak height reduction and undershoot the results are less accurate than for the smaller Courant numbers. Some distortion of the blob in streamline direction can be observed leading to negative concentrations on the upstream side of the blob. Given the small size of the initial blob with respect to the element size the results are still satisfactory, although in the corresponding one- and two-dimensional situations the shape of the advected cloud is

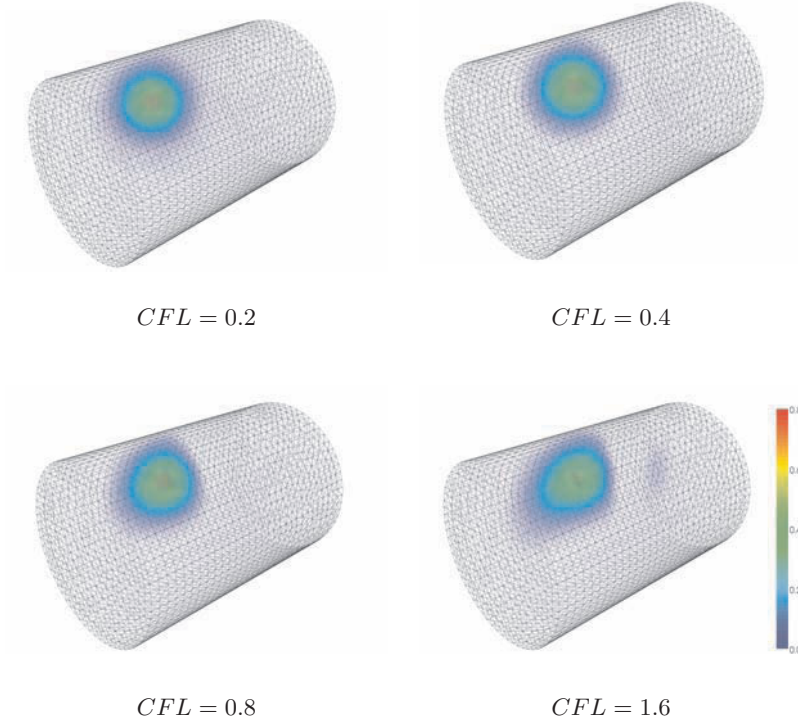


Figure 3.19: *Spiralling blob: numerical solution $\bar{\phi}$ (colour) for different Courant numbers, helical flow is from right to left.*

generally preserved better.

3.5.5 Practical application: sediment transport North Sea

This example concerns the two-dimensional depth averaged transport of suspended sediment in the North Sea by tidal currents. The source term is non-zero due to deposition and erosion of sediment at the seabed. The transport equation for this case is given by

$$d \frac{\partial \phi}{\partial t} + d \mathbf{u} \cdot \nabla (\alpha \phi) - \nabla \cdot (d \kappa \nabla \phi) = w_s (\phi_{eq} - \phi) \quad (3.83)$$

where ϕ is the depth averaged sediment concentration, \mathbf{u} is the depth averaged flow velocity (obtained from a shallow water flow model), d is the water depth, α is a shape factor accounting for vertical variations of the sediment concentration, w_s is the effective sediment settling velocity and ϕ_{eq} is the equilibrium sediment concentration, i.e. the depth averaged concentration for which erosion and sedimentation at the seabed are in equilibrium. Formulations for α , w_s and ϕ_{eq} follow from the specific type of sediment transport model that is actually used. Details of the specific choices made here can be found in van Prooijen et al. [71].

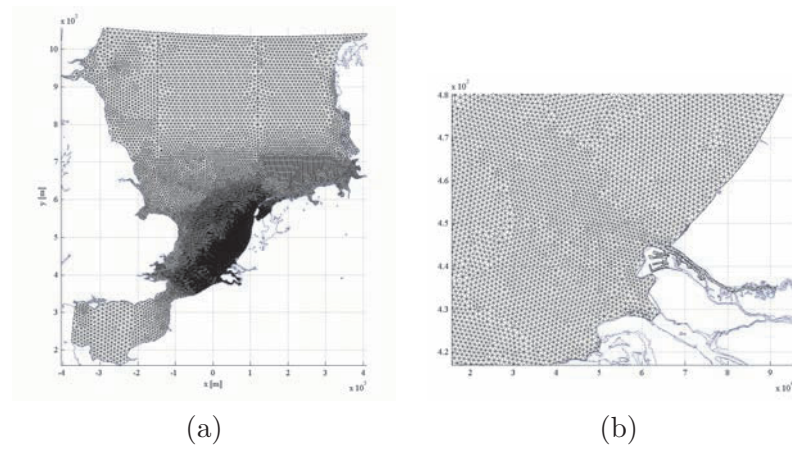


Figure 3.20: *Finite element mesh of the North Sea (a) and detail of the area around the Port of Rotterdam (b), source: van Prooijen et al. [71].*

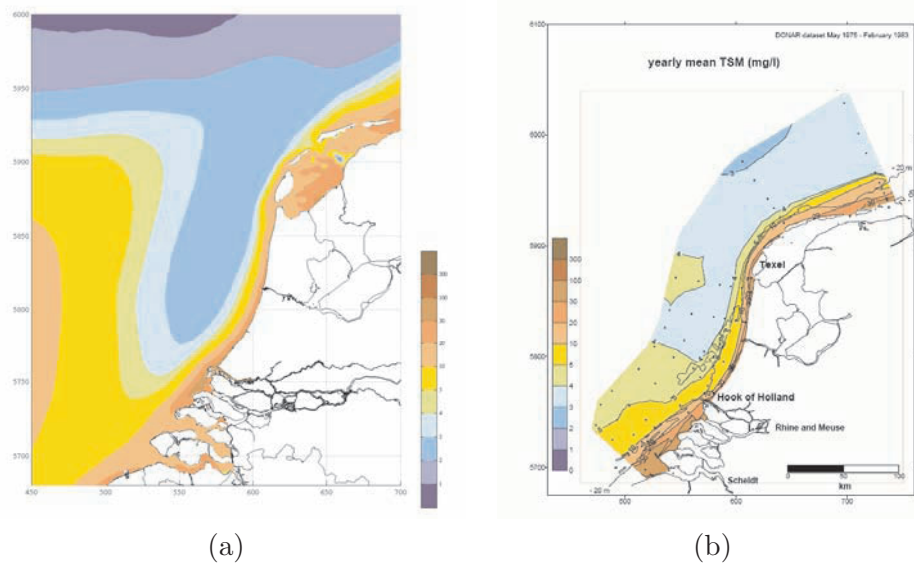


Figure 3.21: *Computed (a) and observed (b) yearly mean suspended solids concentration, source: van Prooijen et al. [71]*

Figure 3.20 shows the computational mesh of the North Sea which consists of about 25,000 nodes. Note that the spatial resolution is relatively fine along the Dutch west coast, which is the area of interest for these simulations, where the element size h_e is about 1000 m. The simulations were performed using a time step of 1800 seconds. For typical tidal current velocities up to 1 m/s velocities the resulting maximum Courant number is about 2. A horizontal diffusivity $\kappa = 15 \text{ m}^2/\text{s}$ is used to model the dispersion induced by the unresolved spatial variations of the total transport.

This yields a maximum Péclet number of about 60. The total simulation period was seven years.

The computed yearly averaged sediment distribution in the North Sea is shown in Figure 3.21, together with observed average suspended sediment concentrations. Considering the high degree of uncertainty of the sediment transport parameters, the correspondence between the computed results and the field observations is very good. It should be mentioned however that to a large extent the quality of the computed results is directly related to a proper choice for the sediment transport formulation and the corresponding parameters. Nevertheless, the results show that the interface stabilization method can be applied successfully in a typical transport problem encountered in hydraulic engineering.

3.6 Conclusion

In this chapter a stabilized finite element method has been formulated for the advection-diffusion problem. The method is based on

- DG -type flux approximation at interior element interfaces,
- static condensation yielding the computational structure of a CG method.

The general discontinuous Galerkin variational form is supplemented with basis functions defined on element interfaces. The interface field provides the weak boundary condition for a local problem on each element. The associated flux on the element boundary is expressed in terms of the interface variable and terms particular to the element. Upwinding of this flux guarantees that the local solution can be expressed entirely in terms of the interface variable. By imposing a global continuity constraint for the interface flux, elimination of the local solution at the element level leads to a formulation with the same number of degrees of freedom as for a continuous Galerkin method on the same mesh.

For linear finite element basis functions the ensuing Galerkin interface stabilization (GIS) method is easily implemented via element wise multiplication of the advection and source terms with an element stabilization matrix. The computation of this matrix involves integration over element boundaries. For the stationary advection-diffusion problem the stabilization terms closely resemble those of the SUPG method and in one-dimension the link to the SUPG stabilization parameter can be demonstrated. In effect, optimal stabilization evolves naturally from the formulation without recourse to flow dependent parameters.

The performance of the method has been demonstrated for steady and unsteady advection-diffusion problems highlighting the role of the Péclet

number and the Courant number, respectively. The computed results demonstrate accuracy, stability and at the same time minimal dissipation. A practical example of the North Sea shows that the method is well suited to be incorporated in a hydraulic engineering tool.

Chapter 4

Incompressible flow

In this chapter the flow of an incompressible fluid in a fixed domain is considered as a first step towards the more complex free-surface flow problem. It will be shown that the GIS method, developed in the previous chapter, simultaneously stabilizes advective instabilities through upwinding of the advective flux and circumvents the instability due to the continuity constraint for incompressible flows¹.

4.1 Mathematical formulation

4.1.1 Governing equations

The motion of an incompressible fluid in a domain $\Omega \subset \mathbb{R}^d$, where d is the number of spatial dimensions, is described by balance equations for mass and momentum, see the derivation in Chapter 1. To this end, a fluid with a uniform density is modelled by its velocity $\mathbf{u} : \Omega \times I \rightarrow \mathbb{R}^d$ and the normalized pressure $p : \Omega \times I \rightarrow \mathbb{R}$, where $I = (t_0, t_N)$ is the considered time interval. The incompressible Navier-Stokes problem can then be stated as: given a forcing term $\mathbf{f} : \Omega \times I \rightarrow \mathbb{R}^d$ and kinematic viscosity ν , find the velocity \mathbf{u} and the normalized pressure p such that

$$\frac{\partial \mathbf{u}}{\partial t} + \nabla \cdot \boldsymbol{\sigma} = \mathbf{f} \quad \text{in } \Omega \times I, \quad (4.1)$$

$$\boldsymbol{\sigma} = \mathbf{u} \otimes \mathbf{u} + p\mathbf{I} - 2\nu\nabla^s \mathbf{v} \quad \text{in } \Omega \times I, \quad (4.2)$$

$$\nabla \cdot \mathbf{u} = 0 \quad \text{in } \Omega \times I, \quad (4.3)$$

where \mathbf{I} is the second-order identity tensor, $\boldsymbol{\sigma}$ is the momentum flux tensor, $(\mathbf{u} \otimes \mathbf{u})_{ij} = u_i u_j$ is the advective flux and $\nabla^s(\cdot) = \frac{1}{2}\nabla(\cdot) + \frac{1}{2}\nabla(\cdot)^T$ is the

¹This chapter is partly based on: ‘A Galerkin interface stabilisation method for the advection-diffusion and Navier-Stokes equations’, Robert Jan Labeur and Garth N. Wells. In: *Computer Methods in Applied Mechanics and Engineering*, **196**, 4985-5000, 2007.

symmetric gradient. The normalized pressure p , which is the pressure divided by the fluid density, is implicitly determined by the incompressibility constraint, Equation (4.3). The forcing term usually represents gravitation, in which case it may be written as $\mathbf{f} = \nabla\Phi$, where Φ is the gravitational potential. The flow can then be modelled by setting $\mathbf{f} = \mathbf{0}$ and replacing the normalized pressure p in the flux Equation (4.2) with the non-hydrostatic pressure $p_d = p - \Phi$. In a stratified environment relative density differences may also contribute to the forcing term, see Appendix A.

The solution of Equations (4.1) to (4.3) requires initial conditions

$$\mathbf{u}(\mathbf{x}, t_0) = \mathbf{u}_0 \quad \text{in } \Omega, \quad (4.4)$$

where the initial velocity \mathbf{u}_0 should be divergence free. The initial pressure must not be specified but follows directly from the evolution of the initial flow field.

On $\Gamma \subset \partial\Omega$ boundary conditions have to be specified for all $t \in I$. It is assumed that the boundary is sufficiently smooth, and the outward unit normal vector to Γ is denoted \mathbf{n} . The boundary is partitioned into Γ_g and Γ_h such that $\Gamma_g \cup \Gamma_h = \Gamma$ and $\Gamma_g \cap \Gamma_h = \emptyset$. Dirichlet and Neumann boundary conditions on Γ_g and Γ_h are then given by, respectively,

$$\mathbf{u} = \mathbf{g} \quad \text{on } \Gamma_g \times I, \quad (4.5)$$

$$(\gamma\mathbf{u} \otimes \mathbf{u} + p\mathbf{I} - 2\nu\nabla^s\mathbf{u})\mathbf{n} = \mathbf{h} \quad \text{on } \Gamma_h \times I, \quad (4.6)$$

in which \mathbf{g} and \mathbf{h} are the imposed Dirichlet and Neumann boundary conditions, respectively, and $\gamma = 1$ on inflow boundaries ($\mathbf{u} \cdot \mathbf{n} \leq 0$) and $\gamma = 0$ on outflow boundaries ($\mathbf{u} \cdot \mathbf{n} > 0$). The Neumann boundary condition \mathbf{h} therefore specifies the total flux on inflow portions of the Neumann boundary and the diffusive flux on outflow Neumann boundaries [51].

The Dirichlet and Neumann conditions may also be imposed in a combined fashion, for instance by prescribing the normal velocity and the tangential stress. For instance, an impermeable wall boundary, denoted $\Gamma_w \subset \Gamma$, is modelled by setting the normal velocity to zero while imposing a tangential wall shear stress $\boldsymbol{\tau}_w$, according to

$$\left. \begin{array}{l} \mathbf{u} \cdot \mathbf{n} = 0 \\ \mathbf{n} \times (\gamma\mathbf{u} \otimes \mathbf{u} - 2\nu\nabla^s\mathbf{u})\mathbf{n} = \mathbf{n} \times \boldsymbol{\tau}_w \end{array} \right\} \quad \text{on } \Gamma_w \times I. \quad (4.7)$$

The wall shear stress is related to the tangential velocity via a ‘law of the wall’

$$\boldsymbol{\tau}_w = c_f |\mathbf{u}| \mathbf{u} \quad \text{on } \Gamma_w, \quad (4.8)$$

where c_f is a dimensionless friction factor, which depends on the wall roughness and the kinematic (turbulence) viscosity, see Appendix B.1. On open

boundaries, denoted $\Gamma_o \subset \Gamma$, the normal velocity may be prescribed with the tangential stress being set to zero, which yields

$$\left. \begin{aligned} \mathbf{u} \cdot \mathbf{n} &= u_n \\ \mathbf{n} \times (\gamma \mathbf{u} \otimes \mathbf{u} - 2\nu \nabla^s \mathbf{u}) \mathbf{n} &= \mathbf{0} \end{aligned} \right\} \text{ on } \Gamma_o \times I, \quad (4.9)$$

where u_n is the normal velocity boundary condition. A detailed discussion of other possible combinations of boundary conditions and their implementation is given in Gunzburger [30].

4.1.2 Variational formulation

The spatial domain Ω is partitioned into disjoint subdomains Ω_e having boundaries $\partial\Omega_e$, to which \mathbf{n} is the outward unit normal vector. This defines the unions

$$\tilde{\Omega} = \bigcup_e \Omega_e, \quad (4.10)$$

$$\tilde{\Gamma} = \bigcup_i \Gamma_i = \bigcup_e \partial\Omega_e, \quad (4.11)$$

where $\tilde{\Omega}$ is the union of element interiors, $\tilde{\Gamma}$ is the union of element boundaries and Γ_i are element interfaces.

The velocity \mathbf{u} and the pressure p may be approximated in discontinuous function spaces \mathbf{V} and Q , respectively, which are defined by

$$\mathbf{V} = \left\{ \mathbf{v} \in \mathbf{L}^2(\tilde{\Omega}) : \mathbf{v} \in \mathbf{H}^1(\Omega_e) \ \forall e \right\}, \quad (4.12)$$

$$Q = \left\{ q \in L^2(\tilde{\Omega}) : q \in H^1(\Omega_e) \ \forall e \right\}. \quad (4.13)$$

The format of the momentum balance Equations (4.1) and (4.2) is similar to that of the advection-diffusion problem given by Equations (3.1) and (3.2), and the derivation of the discontinuous weak form of the Navier-Stokes problem may proceed in a way similar to that for the transport problem in Section 3.1.2. Introducing interface variables $\tilde{\mathbf{u}} : \tilde{\Gamma} \times I \rightarrow \mathbb{R}^d$ and $\tilde{\boldsymbol{\sigma}} : \tilde{\Gamma} \times I \rightarrow \mathbb{R}^d \times \mathbb{R}^d$ and after partial integration of the continuity constraint, the resulting variational problem reads: at a given time t , find $\mathbf{u} \in \mathbf{V}$ and $p \in Q$ such that

$$\begin{aligned} \int_{\tilde{\Omega}} \frac{\partial \mathbf{u}}{\partial t} \cdot \mathbf{v} \, d\Omega - \int_{\tilde{\Omega}} \boldsymbol{\sigma} : \nabla \mathbf{v} \, d\Omega + \sum_e \int_{\partial\Omega_e} \tilde{\boldsymbol{\sigma}} \mathbf{n} \cdot \mathbf{v} \, d\Gamma \\ + \sum_e \int_{\partial\Omega_e} 2\nu (\tilde{\mathbf{u}} - \mathbf{u}) \cdot \nabla^s \mathbf{v} \, \mathbf{n} \, d\Gamma - \int_{\tilde{\Omega}} \mathbf{u} \cdot \nabla q \, d\Omega \\ + \sum_e \int_{\partial\Omega_e} \tilde{\mathbf{u}} \cdot \mathbf{n} q \, d\Gamma = \int_{\tilde{\Omega}} \mathbf{f} \cdot \mathbf{v} \, d\Omega \quad \forall \mathbf{v} \in \mathbf{V}, \quad \forall q \in Q, \end{aligned} \quad (4.14)$$

where it has been assumed that the interface terms $\bar{\boldsymbol{\sigma}}$ and $\bar{\mathbf{u}}$ satisfy the respective boundary conditions. The operator $:$ denotes the Frobenius inner product $\mathbf{A}:\mathbf{B} = \sum_{i,j} A^{ij}B^{ij}$, where \mathbf{A} and \mathbf{B} are given matrices and $\sum_{i,j}$ denotes summation over matrix elements.

For a proper choice of the spaces \mathbf{V} and Q Equation (4.14) is consistent with the strong form of the Navier-Stokes problem if the interface terms are defined consistently. The latter requires that $\bar{\mathbf{u}}$ and $\bar{\boldsymbol{\sigma}}$ approach the continuous limits if the jumps $[[\mathbf{u}]]$ and $[[\boldsymbol{\sigma}]]$ tend to zero [1]. For stability, the spaces \mathbf{V} and Q may not be chosen independently but have to satisfy the LBB condition given by Equation (2.27). In the next section, a particular choice for the spaces \mathbf{V} and Q , and the interface terms $\bar{\mathbf{u}}$ and $\bar{\boldsymbol{\sigma}}$ will be proposed which is reminiscent of the GIS method for the advection-diffusion problem and also has similar stability properties.

4.1.3 Dimensional scaling

This section examines the momentum equations in some more detail. For an incompressible flow and spatially constant viscosity ν , the gradient of the diffusive stress can be replaced by the Laplacian operator. Substitution of the flux Equation (4.2) into the momentum balance Equation (4.1) then leads to

$$\frac{\partial \mathbf{u}}{\partial t} + \nabla \cdot (\mathbf{u} \otimes \mathbf{u}) + \nabla p_d = \nu \nabla^2 \mathbf{u}, \quad (4.15)$$

in which the (gravitational) forcing term has been eliminated using the non-hydrostatic pressure p_d . In order to investigate the relative importance of each term in Equation (4.15), consider a flow with a reference velocity scale U_{ref} in a domain having a length scale L_{ref} . An appropriate intrinsic time-scale is then given by $T_{\text{ref}} = L_{\text{ref}}/U_{\text{ref}}$, which is the characteristic time for a fluid particle to travel through the domain. Introducing non-dimensional variables $\mathbf{u}^* = \mathbf{u}/U_{\text{ref}}$, $\mathbf{x}^* = \mathbf{x}/L_{\text{ref}}$ and $t^* = t/T_{\text{ref}}$, the momentum equations can be written in non-dimensional form as

$$\frac{\partial \mathbf{u}^*}{\partial t^*} + \tilde{\nabla} \cdot (\mathbf{u}^* \otimes \mathbf{u}^*) + \frac{P_{\text{ref}}}{U_{\text{ref}}^2} \tilde{\nabla} p_d^* = \frac{1}{Re} \tilde{\nabla}^2 \mathbf{u}^*, \quad (4.16)$$

where $\tilde{\nabla}$ is the scaled gradient operator, P_{ref} is the pressure scale, p_d^* is the non-dimensional pressure and $Re = U_{\text{ref}}L_{\text{ref}}/\nu$ is the Reynolds-number. The pressure may be eliminated from Equation (4.16) by taking the curl which gives the vorticity equation

$$\frac{\partial \boldsymbol{\omega}^*}{\partial t^*} + \mathbf{u}^* \cdot \tilde{\nabla} \boldsymbol{\omega}^* - \boldsymbol{\omega}^* \cdot \tilde{\nabla} \mathbf{u}^* = \frac{1}{Re} \tilde{\nabla}^2 \boldsymbol{\omega}^*, \quad (4.17)$$

where $\boldsymbol{\omega}^* = \tilde{\nabla} \times \mathbf{u}^*$ is the non-dimensional vorticity vector.

The Reynolds number to a large extent determines the behaviour of solutions of the Navier-Stokes equations. If $Re \gg 1$ the right hand side

of Equation (4.17) can be neglected and the vorticity merely changes due to advection and stretching by the velocity shear. Small perturbations of the vorticity are enhanced due to the non-linearity of the advection and stretching terms which ultimately renders the fluid motion turbulent. For $Re \ll 1$ viscous damping dominates which will prevent the onset of these instabilities. In environmental fluid mechanics, due to the small viscosity of water and the large length scales involved, the flow will be turbulent in most cases. Exceptions are fine scale processes as for example the settling of sand or silt particles or the flow through porous media, which are however not considered here. A turbulent flow is often modelled in terms of its mean, large scale flow field by means of the Reynolds averaged Navier-Stokes (RANS) equations [61]. The net influence of the small-scale fluctuations on the large scale mean flow is taken into account by adding an artificial turbulence viscosity to the fluid viscosity. The mathematical behaviour of the model will then depend on the Reynolds number resulting from the virtual turbulence viscosity, see Appendix B.

Considering that the pressure gradient in momentum Equation (4.16) balances all other terms, the reference pressure scale P_{ref} is given by

$$P_{\text{ref}} = \begin{cases} U_{\text{ref}}^2 & \text{if } Re \gg 1, \\ \nu U_{\text{ref}}/L_{\text{ref}} & \text{if } Re \ll 1. \end{cases} \quad (4.18)$$

In a numerical model, non-dimensionalization of the Navier-Stokes equations, using the above scaling parameters, will guarantee that the degrees of freedom \mathbf{u} and p have the same order of magnitude. Otherwise, numerical solution procedures may fail to converge. This especially concerns the velocity-pressure coupling where improper scaling may cause violation of the discrete incompressibility constraint, even when direct solution procedures are used, which is demonstrated in the lucid paper by Pelletier et al. [65]. For this reason, the non-dimensional form of the Navier-Stokes equations will be used in this thesis. In order to avoid notational clutter, the asterisks are dropped from the formulations and the non-dimensional form is assumed implicit throughout.

4.2 Galerkin interface stabilization method

4.2.1 Introduction

Numerical modelling of the incompressible Navier-Stokes problem requires the suppression, in a consistent way, of: (1) instabilities due to the advection terms, which is related to the Péclet number, and (2) instabilities due to the incompressibility constraint, which is related to the LBB condition, see Section 2.1.2. Heuristically, both type of instabilities are associated with incompatible velocity fields on elements, that is if the interpolated velocity

is inconsistent with the pressure gradient term or the velocity assumed on the outflow part of the element boundary. The problem may be by-passed in several ways:

- By taking different polynomial spaces for the velocity and pressure basis functions, respectively, yielding the class of Taylor-Hood elements or Raviart-Thomas elements [30]. A practical impediment with this approach is that the nodal structuring of the pressure and velocity unknowns becomes mutually different which is inconvenient when handling large systems of sparse matrix equations. In the high Péclet-number range, the advection terms still need upwind stabilization which may cause artificial dissipation.
- By using local bubble degrees of freedom for the velocity. Static condensation of the bubble velocities algebraically leads to a Laplacian operator for the pressure which stabilizes the incompressibility constraint [8]. The reduced system of equations is easier to handle and for the MINI element a global system results with the pressure and velocity degrees of freedom residing in the same nodes [7]. The stabilization may be non-optimal however or even insufficient in advection-dominated cases Simo et al. [81].
- By modifying the momentum flux using SUPG-like correction terms which depend on the local residual of the momentum transport equation. Besides stabilizing the momentum equations, using the modified velocity in the incompressibility constraint will effectively introduce a consistent Laplacian pressure stabilization term [38]. The resulting Pressure Stabilized Petrov-Galerkin (PSPG) method is algebraically equivalent to the MINI element. A user defined stabilization parameter is involved [87], the definition of which is non-trivial if different flow regimes reign within the same domain.

The proposed GIS method uses the same principle of modifying the local velocity field in a different way. By defining global velocity degrees of freedom on the element interfaces, a locally discontinuous velocity field may be eliminated from the momentum equation by static condensation. By leaving the pressure field continuous, substitution of the discontinuous velocities simultaneously stabilizes the global incompressibility constraint in a similar, consistent way as for the PSPG method. A schematic of the GIS pressure-velocity finite element pair is given in Figure 4.1. The stabilization naturally arises from the flux definition at element interfaces and does not involve flow dependent stabilization parameters. As for the MINI element the local velocity field is obtained from a back substitution step after the global equation has been solved. Obviously, the procedure has the advantage that the discrete velocity field may be used directly in the evaluation of

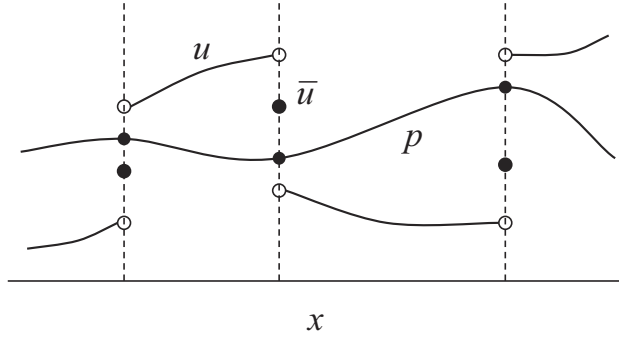


Figure 4.1: *Schematic of the GIS pressure-velocity discretization.*

the momentum advection terms without violating consistency [37]. Through the definition of the interface flux and the interface ‘frame function’ \bar{u} , in this respect the GIS method bears some similarities to hybrid finite element methods [8, 16, 17] and Trefftz-type methods [99].

4.2.2 General formulation

The starting point for the GIS variational form of the Navier-Stokes equations is the general discontinuous weak form given by Equation (4.14) with the spaces \mathbf{V} and Q given by, respectively,

$$\mathbf{V} = \left\{ \mathbf{v} \in \mathbf{L}^2(\tilde{\Omega}) : \mathbf{v} \in \mathbf{P}^k(\Omega_e) \forall e \right\}, \quad (4.19)$$

$$Q = \left\{ q \in H^1(\tilde{\Omega}) : q \in P^l(\Omega_e) \forall e \right\}, \quad (4.20)$$

where \mathbf{P}^k and P^l are sets of Lagrange polynomial basis functions with polynomial orders $k \geq 0$ and $l \geq 1$, respectively. Anticipating a global problem for the pressure, the pressure space Q is chosen continuous. Discontinuous pressure may have some interesting features, see for instance [16, 17], but is not pursued here. Reminiscent of the advection-diffusion problem, the interface velocity \bar{u} is defined as an independent field on the union of element interfaces. To this end a trace space $\bar{\mathbf{V}}$ and a related space $\bar{\mathbf{V}}_g$ are defined by, respectively,

$$\bar{\mathbf{V}} = \left\{ \bar{\mathbf{v}} \in \mathbf{H}^{1/2}(\tilde{\Gamma}) : \bar{\mathbf{v}} \in \mathbf{P}^m(\Gamma_i) \forall i \right\}, \quad (4.21)$$

$$\bar{\mathbf{V}}_g = \left\{ \bar{\mathbf{v}} \in \mathbf{H}^{1/2}(\tilde{\Gamma}) : \bar{\mathbf{v}} \in \mathbf{P}^m(\Gamma_i) \forall i, \bar{\mathbf{v}} = \mathbf{g} \text{ on } \Gamma_g \right\}, \quad (4.22)$$

where the fractional space $\mathbf{H}^{1/2}$ is the trace of $\mathbf{H}^1(\Omega)$ on $\tilde{\Gamma}$ and \mathbf{P}^m is a set of Lagrange polynomial basis functions with polynomial order $m \geq 1$ defined on interfaces Γ_i . Functions in $\bar{\mathbf{V}}_g$ only differ from functions in $\bar{\mathbf{V}}$ in that the Dirichlet boundary conditions on Γ_g are satisfied.

The above definitions for $\bar{\mathbf{u}}$ and p reduce the DG variational form Equation (4.14) to a global problem. Due to the continuity of $\bar{\mathbf{u}}$ and q on $\tilde{\Gamma}$, the interface terms from the incompressibility constraint, which is embedded in Equation (4.14), can be written as

$$\sum_e \int_{\partial\Omega_e} \bar{\mathbf{u}} \cdot \mathbf{n} q \, d\Gamma = \int_{\Gamma} \bar{\mathbf{u}} \cdot \mathbf{n} q \, d\Gamma \quad \forall q \in Q, \quad (4.23)$$

since the integrals on the left hand side vanish pairwise on interior element boundaries. For the interface terms in the momentum equations, a similar reduction is not possible because functions \mathbf{v} and the interface flux $\bar{\boldsymbol{\sigma}}$ are discontinuous across element interfaces. Instead, continuity of $\bar{\boldsymbol{\sigma}}$ is imposed weakly, which requires that

$$\begin{aligned} \sum_e \int_{\partial\Omega_e} \bar{\boldsymbol{\sigma}} \mathbf{n} \cdot \bar{\mathbf{v}} \, d\Gamma &= \int_{\Gamma_h} (1 - \gamma) (\bar{\mathbf{u}} \otimes \mathbf{u}) \mathbf{n} \cdot \bar{\mathbf{v}} \, d\Gamma \\ &\quad + \int_{\Gamma_h} \mathbf{h} \cdot \bar{\mathbf{v}} \, d\Gamma \quad \forall \bar{\mathbf{v}} \in \bar{\mathbf{V}}, \end{aligned} \quad (4.24)$$

where the Neumann boundary condition specifies the total momentum flux or the diffusive flux at inflow or outflow boundaries, respectively. The interface flux $\bar{\boldsymbol{\sigma}}$ in Equation (4.24) is yet undefined other than stating that it depends on the interface field $\bar{\mathbf{u}}$ and terms local to an element. It may not depend on quantities from neighbouring elements. Equation (4.24) thus provides a condition for $\bar{\mathbf{u}}$ and this variable may be interpreted as a Lagrange-multiplier enforcing flux continuity on $\tilde{\Gamma}$.

Using Equations (4.23) and (4.24), the general GIS variational form for the incompressible Navier-Stokes problem becomes: at time t , given the forcing term \mathbf{f} and boundary condition \mathbf{h} , find $\mathbf{u} \in \mathbf{V}$, $p \in Q$ and $\bar{\mathbf{u}} \in \bar{\mathbf{V}}_g$ such that

$$\begin{aligned} \int_{\tilde{\Omega}} \frac{\partial \mathbf{u}}{\partial t} \cdot \mathbf{v} \, d\Omega - \int_{\tilde{\Omega}} \boldsymbol{\sigma} : \nabla \mathbf{v} \, d\Omega - \sum_e \int_{\partial\Omega_e} \bar{\boldsymbol{\sigma}} \mathbf{n} \cdot (\bar{\mathbf{v}} - \mathbf{v}) \, d\Gamma \\ + \sum_e \int_{\partial\Omega_e} 2\nu (\bar{\mathbf{u}} - \mathbf{u}) \cdot \nabla^s \mathbf{v} \, \mathbf{n} \, d\Gamma + \int_{\Gamma_h} (1 - \gamma) (\bar{\mathbf{u}} \otimes \mathbf{u}) \mathbf{n} \cdot \bar{\mathbf{v}} \, d\Gamma \\ - \int_{\tilde{\Omega}} \mathbf{u} \cdot \nabla q \, d\Omega + \int_{\Gamma} \bar{\mathbf{u}} \cdot \mathbf{n} q \, d\Gamma = \int_{\tilde{\Omega}} \mathbf{f} \cdot \mathbf{v} \, d\Omega - \int_{\Gamma_h} \mathbf{h} \cdot \bar{\mathbf{v}} \, d\Gamma \\ \forall \mathbf{v} \in \mathbf{V}, \quad \forall \bar{\mathbf{v}} \in \bar{\mathbf{V}}, \quad \forall q \in P. \end{aligned} \quad (4.25)$$

Setting $\bar{\mathbf{v}} = \mathbf{0}$ and $q = 0$ in Equation (4.25) leads to a local problem on each element, from which \mathbf{u} may be expressed locally as a function of the global fields $\bar{\mathbf{u}}$ and p . This is possible since $\bar{\boldsymbol{\sigma}}$ depends on $\bar{\mathbf{u}}$ and terms local to an element. Setting then $\mathbf{v} = \mathbf{0}$ and eliminating \mathbf{u} leads to a problem for the global variables $\bar{\mathbf{u}}$ and p . After solution of the global problem the

local velocity field \mathbf{u} is found via element-wise back substitution. The entire solution procedure is essentially similar to the static condensation of bubble functions [81] and, as will be demonstrated, leads to favourable stability properties.

4.2.3 Interface flux

A particular choice for $\bar{\sigma}$ is presented having the requires properties and which enables interface stabilization by means of upwinding. To this end the numerical flux $\bar{\sigma}$ is decomposed additively into an advective component $\bar{\sigma}^a$ and a diffusive component $\bar{\sigma}^d$, the determination of which requires a different approach.

The advective flux $\bar{\sigma}^a$ is formulated as

$$\bar{\sigma}^a = \mathbf{u} \otimes \mathbf{u} + \gamma(\bar{\mathbf{u}} - \mathbf{u}) \otimes \tilde{\mathbf{u}}, \quad (4.26)$$

where $\tilde{\mathbf{u}}$ is an advective interface velocity, the parameter $\gamma = 1$ on inflow element boundaries and $\gamma = 0$ on outflow element boundaries, thereby upwinding the interface flux. Considering a typical problem where $\tilde{\mathbf{u}} = \mathbf{u}$, the advective flux on the downwind side of an element facet reads

$$\bar{\sigma}^a = \mathbf{u} \otimes \tilde{\mathbf{u}}, \quad (4.27)$$

whereas on the upwind side it reads

$$\bar{\sigma}^a = \bar{\mathbf{u}} \otimes \tilde{\mathbf{u}}, \quad (4.28)$$

which highlights the upwinding mechanism. The velocity \mathbf{u} is discontinuous at element interfaces which requires a careful formulation of $\tilde{\mathbf{u}}$ in order to obtain a correct behaviour of shocks [56]. In particular, the entropy condition should be satisfied which implies that the energy can not increase across a shock in the direction of the flow. A range of flux splitting schemes has been proposed, such as for example the HLLC scheme [33] or the Roe scheme [33]. Similar to the advection-diffusion problem, the following formulation is adopted

$$\tilde{\mathbf{u}} = \min(\mathbf{u}^+ \cdot \mathbf{n}, \mathbf{u}^- \cdot \mathbf{n}) \mathbf{n}, \quad (4.29)$$

where \mathbf{u}^+ and \mathbf{u}^- are the traces of the velocity \mathbf{u} on an element boundary. The formulation avoids problems with sink interfaces and also guarantees entropy conservation at rarefactions (source interfaces). In combination with the flux continuity constraint, Equation (4.24), the above expression for the flux resembles the definition of the interface state in flux splitting methods in a weak sense, see for instance Toro [89] or LeVeque [56]. The diffusive part of the flux $\bar{\sigma}^d$ is reminiscent of the IP method

$$\bar{\sigma}^d = p\mathbf{I} - 2\nu\nabla^s\mathbf{u} - \frac{\alpha}{h_e}\nu(\bar{\mathbf{u}} - \mathbf{u}) \otimes \mathbf{n}, \quad (4.30)$$

where h_e is a measure of the local element size and α is a penalty term which is required for stability of IP methods, see Arnold et al. [1]. The part of the diffusive flux involving $(\bar{\mathbf{u}} - \mathbf{u}) \otimes \mathbf{n}$ is not symmetric, which is permitted as the task of this term is to provide control over the term $|\bar{\mathbf{u}} - \mathbf{u}|_{\partial\Omega_e}$. It is not required for consistency. Combining Equations (4.26) and (4.30), the total numerical interface flux may be written compactly as

$$\bar{\boldsymbol{\sigma}} = \boldsymbol{\sigma} + (\bar{\mathbf{u}} - \mathbf{u}) \otimes \boldsymbol{\beta}, \quad (4.31)$$

where

$$\boldsymbol{\beta} = \gamma \tilde{\mathbf{u}} - \frac{\alpha}{h_e} \nu \mathbf{n}. \quad (4.32)$$

The quantity $\boldsymbol{\beta} \cdot \mathbf{n}$ is always negative at element boundaries from which the ensuing GIS method obtains its stabilization.

Substituting Equation (4.31) for the interface flux and setting $\bar{\mathbf{v}} = \mathbf{0}$ and $q = 0$ in Equation (4.25) gives the following local problem: at given time t , given the forcing term \mathbf{f} , find $\mathbf{u} \in \mathbf{V}$ such that

$$\begin{aligned} \int_{\tilde{\Omega}} \frac{\partial \mathbf{u}}{\partial t} \cdot \mathbf{v} \, d\Omega + \int_{\tilde{\Omega}} \nabla \cdot (\mathbf{u} \otimes \mathbf{u}) \cdot \mathbf{v} \, d\Omega + \int_{\tilde{\Omega}} \nabla p \cdot \mathbf{v} \, d\Omega \\ - \int_{\tilde{\Omega}} 2 \nabla \cdot (\nu \nabla^s \mathbf{u}) \cdot \mathbf{v} \, d\Omega + \sum_e \int_{\partial\Omega_e} \boldsymbol{\beta} \cdot \mathbf{n} (\bar{\mathbf{u}} - \mathbf{u}) \cdot \mathbf{v} \, d\Gamma \\ + \sum_e \int_{\partial\Omega_e} 2\nu (\bar{\mathbf{u}} - \mathbf{u}) \cdot \nabla^s \mathbf{v} \, \mathbf{n} \, d\Gamma = \int_{\tilde{\Omega}} \mathbf{f} \cdot \mathbf{v} \, d\Omega \quad \forall \mathbf{v} \in \mathbf{V}, \end{aligned} \quad (4.33)$$

where the regular part of the element flux has been integrated by parts. Equation (4.33) solves the momentum equations element wise with weakly imposed Dirichlet boundary conditions $\bar{\mathbf{u}}$ on $\partial\Omega_e$. Setting $\bar{\mathbf{v}} = \mathbf{0}$ in Equation (4.25) and using Equation (4.31) for the interface flux leads to the following global problem: at given time t , given the boundary condition \mathbf{h} , find $\bar{\mathbf{u}} \in \bar{\mathbf{V}}_g$ and $p \in Q$ such that

$$\begin{aligned} \sum_e \int_{\partial\Omega_e} (\mathbf{u} \otimes \mathbf{u} - 2\nu \nabla^s \mathbf{u}) \mathbf{n} \cdot \bar{\mathbf{v}} \, d\Gamma + \sum_e \int_{\partial\Omega_e} \boldsymbol{\beta} \cdot \mathbf{n} (\bar{\mathbf{u}} - \mathbf{u}) \cdot \bar{\mathbf{v}} \, d\Gamma \\ + \int_{\tilde{\Omega}} \mathbf{u} \cdot \nabla q \, d\Omega - \int_{\Gamma_h} (1 - \gamma) (\mathbf{u} \cdot \mathbf{n}) \bar{\mathbf{u}} \cdot \bar{\mathbf{v}} \, d\Gamma + \int_{\Gamma} p \mathbf{n} \cdot \bar{\mathbf{v}} \, d\Gamma \\ - \int_{\Gamma} \bar{\mathbf{u}} \cdot \mathbf{n} q \, d\Gamma = \int_{\Gamma_h} \mathbf{h} \cdot \bar{\mathbf{v}} \, d\Gamma \quad \forall \bar{\mathbf{v}} \in \bar{\mathbf{V}}, \quad \forall q \in Q, \end{aligned} \quad (4.34)$$

where the pressure terms at interior element boundaries have vanished due to the continuity of p and $\bar{\mathbf{v}}$ on $\tilde{\Gamma}$. After the elimination of \mathbf{u} via the ‘local’ problem, Equation (4.34) reduces to an equation for the global variables $\bar{\mathbf{u}}$ and p that can be readily solved.

The variational method discussed so far is still general in the sense that the polynomial orders of the involved function spaces are not yet defined specifically. Section 4.3 will consider in detail the obvious choice $k = l = m = 1$ which leads to a particularly simple and efficient implementation.

4.2.4 Properties

For a stabilized method it is crucial to verify whether the addition of the stabilization terms renders the modified variational form consistent and conservative. To this end the general form of the GIS method for the Navier-Stokes problem is considered which is given by Equation (4.25) with the interface flux according to Equation (4.31).

4.2.4.1 Consistency

For sufficiently smooth functions \mathbf{u} and p , setting $\bar{\mathbf{v}} = \mathbf{0}$ and $q = 0$ in Equation (4.25) gives, after integration by parts

$$\begin{aligned} \int_{\tilde{\Omega}} \left(\frac{\partial \mathbf{u}}{\partial t} + \nabla \cdot \boldsymbol{\sigma} - \mathbf{f} \right) \cdot \mathbf{v} \, d\Omega + \sum_e \int_{\partial\Omega_e} \boldsymbol{\beta} \cdot \mathbf{n} (\bar{\mathbf{u}} - \mathbf{u}) \mathbf{v} \cdot \mathbf{n} \, d\Gamma \\ + \sum_e \int_{\partial\Omega_e} 2\nu (\bar{\mathbf{u}} - \mathbf{u}) \cdot \nabla^s \mathbf{v} \mathbf{n} \, d\Gamma = 0 \quad \forall \mathbf{v} \in V, \end{aligned} \quad (4.35)$$

which is consistent with the strong form of the Navier-Stokes problem, given by Equation (4.1), and the enforcement of $\bar{\mathbf{u}} = \mathbf{u}$ on $\tilde{\Gamma}$. Setting then $\mathbf{v} = \mathbf{0}$, $q = 0$ and using $\bar{\mathbf{u}} = \mathbf{u}$ on $\tilde{\Gamma}$ in Equation (4.25) gives

$$\begin{aligned} \sum_e \int_{\partial\Omega_e \setminus \Gamma_h} \boldsymbol{\sigma} \mathbf{n} \cdot \bar{\mathbf{v}} \, d\Gamma + \int_{\Gamma_h} (\gamma \mathbf{u} \otimes \mathbf{u} + p \mathbf{I} - 2\nu \nabla^s \mathbf{u}) \mathbf{n} \cdot \bar{\mathbf{v}} \, d\Gamma \\ = \int_{\Gamma_h} \mathbf{h} \cdot \bar{\mathbf{v}} \, d\Gamma \quad \forall \bar{\mathbf{v}} \in \bar{\mathbf{V}}, \end{aligned} \quad (4.36)$$

which implies continuity of the flux between subdomains and satisfaction of the Neumann boundary condition given by Equation (4.6). For $\mathbf{v} = \mathbf{0}$, $\bar{\mathbf{v}} = \mathbf{0}$ and smooth functions \mathbf{u} Equation (4.25) yields, after partial integration,

$$\int_{\tilde{\Omega}} \nabla \cdot \mathbf{u} \, q \, d\Omega + \int_{\Gamma} (\bar{\mathbf{u}} - \mathbf{u}) \cdot \mathbf{n} q \, d\Gamma = 0 \quad \forall q \in Q, \quad (4.37)$$

which demonstrates consistency with the continuity constraint Equation (4.3) and also enforces $\mathbf{u} \cdot \mathbf{n} = \bar{\mathbf{u}} \cdot \mathbf{n}$ on Γ .

4.2.4.2 Volume conservation

Setting $\mathbf{v} = \mathbf{0}$, $\bar{\mathbf{v}} = \mathbf{0}$ and $q = 1$ in Equation (4.25) proves that

$$\int_{\Gamma} \bar{\mathbf{u}} \cdot \mathbf{n} \, d\Gamma = 0, \quad (4.38)$$

which is a statement of volume conservation in that the net inflow along the boundary Γ equals zero.

4.2.4.3 Momentum conservation

Setting $q = 0$, $\mathbf{v} = \mathbf{e}_j$ and $\bar{\mathbf{v}} = \mathbf{e}_j$ in Equation (4.25), with \mathbf{e}_j being the unit vector in Cartesian direction j , gives for the pure Neumann problem

$$\begin{aligned} \frac{d}{dt} \int_{\tilde{\Omega}} \mathbf{u} \cdot \mathbf{e}_j \, d\Omega &= \int_{\tilde{\Omega}} \mathbf{f} \cdot \mathbf{e}_j \, d\Omega \\ &\quad - \int_{\Gamma_h} (1 - \gamma) (\mathbf{u} \cdot \mathbf{n}) \bar{\mathbf{u}} \cdot \mathbf{e}_j \, d\Gamma - \int_{\Gamma_h} \mathbf{h} \cdot \mathbf{e}_j \, d\Gamma, \end{aligned} \quad (4.39)$$

which states that the total increase of momentum in Ω equals the body force plus the net inward momentum flux over the boundary Γ_h . For the case with Dirichlet boundary conditions proving momentum conservation is less obvious since $\bar{\mathbf{v}}$ can not be set to \mathbf{e}_j on Γ_g . The difficulty can however be circumvented by introducing an auxiliary flux on the Dirichlet boundary [37]. Considering Equation (4.25) with $q = 0$, $\bar{\mathbf{v}} = \mathbf{0}$, $\mathbf{v} = \mathbf{e}_j$ on Ω_e and $\mathbf{v} = \mathbf{0}$ elsewhere, leads to

$$\frac{d}{dt} \int_{\Omega_e} \mathbf{u} \cdot \mathbf{e}_j \, d\Omega = \int_{\Omega_e} \mathbf{f} \cdot \mathbf{e}_j \, d\Omega - \int_{\partial\Omega_e} \bar{\boldsymbol{\sigma}} \mathbf{n} \cdot \mathbf{e}_j \, d\Gamma, \quad (4.40)$$

which proves local conservation on element e in terms of the numerical flux $\bar{\boldsymbol{\sigma}}$ along the element boundary. Due to the formulation of the global flux continuity constraint, Equation (4.24), this flux is not point-wise continuous between elements.

4.2.4.4 Energy conservation

In the viscous limit, setting $\mathbf{v} = \mathbf{u}$, $\bar{\mathbf{v}} = \bar{\mathbf{u}}$ and $q = p$ in Equation (4.25) gives, after partial integration and re-arrangement,

$$\begin{aligned} \frac{d}{dt} \int_{\tilde{\Omega}} \frac{1}{2} |\mathbf{u}|^2 \, d\Omega &+ \int_{\tilde{\Omega}} 2\nu |\nabla^s \mathbf{u}|^2 \, d\Omega + \sum_e \int_{\partial\Omega_e} \frac{\alpha}{h_e} \nu |\bar{\mathbf{u}} - \mathbf{u}|^2 \, d\Gamma \\ &+ 2 \sum_e \int_{\partial\Omega_e} 2\nu (\bar{\mathbf{u}} - \mathbf{u}) \cdot \nabla^s \mathbf{u} \mathbf{n} \, d\Gamma = \int_{\tilde{\Omega}} \mathbf{f} \cdot \mathbf{u} \, d\Omega - \int_{\Gamma_h} \mathbf{h} \cdot \bar{\mathbf{u}} \, d\Gamma. \end{aligned} \quad (4.41)$$

The first term in Equation (4.41) concerns the time derivative of the total kinetic energy. In the absence of external forcing terms, i.e. the case where $\mathbf{f} = \mathbf{0}$ and $\mathbf{h} = \mathbf{0}$, the total kinetic energy should decrease monotonically. Obviously, this is not the case for Equation (4.41) as the last term on the left hand side may become negative. This deficiency can be repaired by making the penalty term α sufficiently large [1]. The problem may be circumvented altogether by changing the sign of the corresponding interface term in

Equation (4.33), leading to the skew symmetric form of the IP method which however lacks consistency [35].

For the advective limit, a similar exercise yields

$$\begin{aligned} & \frac{d}{dt} \int_{\tilde{\Omega}} \frac{1}{2} |\mathbf{u}|^2 d\Omega + \int_{\tilde{\Omega}} \frac{1}{2} |\mathbf{u}|^2 \nabla \cdot \mathbf{u} d\Omega - \sum_e \int_{\partial\Omega_e \setminus \Gamma_h} \frac{1}{2} |\bar{\mathbf{u}}|^2 \mathbf{u} \cdot \mathbf{n} d\Gamma \\ & + \sum_e \int_{\partial\Omega_e} \frac{1}{2} |\tilde{\mathbf{u}} \cdot \mathbf{n}| |\bar{\mathbf{u}} - \mathbf{u}|^2 d\Gamma + \sum_e \int_{\partial\Omega_e} \frac{1}{2} (\mathbf{u} - \tilde{\mathbf{u}}) \cdot \mathbf{n} |\bar{\mathbf{u}} - \mathbf{u}|^2 d\Gamma \\ & + \int_{\Gamma_h} \frac{1}{2} |\bar{\mathbf{u}}|^2 |\mathbf{u} \cdot \mathbf{n}| d\Gamma = \int_{\tilde{\Omega}} \mathbf{f} \cdot \mathbf{u} d\Omega - \int_{\Gamma_h} \mathbf{h} \cdot \bar{\mathbf{u}} d\Gamma, \quad (4.42) \end{aligned}$$

where the advective flux has been integrated by parts using $\nabla(\mathbf{u} \otimes \mathbf{u}) = \mathbf{u} \cdot \nabla \mathbf{u} + (\nabla \mathbf{u}) \mathbf{u}$. Without external forcing, the energy should remain constant. Inspection of Equation (4.42) reveals that the second and third terms on the left hand side may become negative. Due to the definition of $\tilde{\mathbf{u}}$, given in Equation (4.29), the remaining advection terms are strictly positive. The associated dissipative mechanism stems from the upwinding of the momentum flux at element interfaces and is partly determined by the difference between the velocity field \mathbf{u} and the interface function $\bar{\mathbf{u}}$, and partly by the advective velocity $\tilde{\mathbf{u}}$ at element facets. The energy may increase if the flow field \mathbf{u} is not divergence free. As the discrete velocity field \mathbf{u} is weakly non-divergent only, energy stability is not guaranteed in practice. Sacrificing momentum conservation, the problem may be by-passed by rendering the advection operator skew-symmetric, see for instance Gresho et al. [28]. The difficulty to simultaneously satisfy linear and quadratic conservation is a fundamental issue in numerical flow modelling. Fortunately, the differences between alternate forms of the advection operator are usually small and should not be over-emphasized, moreover if viscous terms are present [30].

Since the pressure does not appear in Equations (4.41) and (4.42) the stabilization of the incompressibility constraint does not imply artificial dissipation. Therefore, in the case of zero viscosity and negligible advection the total energy will be conserved. This does not yet mean that the pressure-velocity coupling in the proposed formulation of the incompressible Navier-Stokes problem is stable as stability requires the satisfaction of an inf – sup condition, given by Equation (2.27). Proving inf – sup stability for Equation (4.25) is not trivial and is not pursued here. As will be demonstrated in Section 4.3.4 the GIS formulation inherits a stabilization mechanism that is closely related to that of pressure stabilized Petrov-Galerkin (PSPG) methods [38].

4.3 Implementation

4.3.1 Time stepping

For time integration, the time interval I is partitioned in N sub-intervals using a sequence of discrete time levels $I = (t_0, t_1, \dots, t_{N-1}, t_N)$ and associated sub-intervals $I_n = (t_n, t_{n+1})$. On each sub-interval the flow problem is solved using a linear interpolation in time. The solution from the previous time step is used as an initial condition which, in contrast to space-time methods, is imposed strongly. The non-linearity of the momentum terms is dealt with using a Picard linearization ('frozen coefficient') where the advective field is determined explicitly by the flow state at time level t_n .

The procedure yields the following discrete local problem: given the velocity \mathbf{u}_n and the forcing term $\mathbf{f}_{n+\theta}$, find $\mathbf{u}_{n+\theta} \in \mathbf{V}$ such that

$$\begin{aligned} & \int_{\tilde{\Omega}} \frac{\mathbf{u}_{n+\theta} - \mathbf{u}_n}{\theta \Delta t} \cdot \mathbf{v} \, d\Omega + \int_{\tilde{\Omega}} \nabla \cdot (\mathbf{u}_{n+\theta} \otimes \mathbf{u}_n) \cdot \mathbf{v} \, d\Omega + \int_{\tilde{\Omega}} \nabla p_{n+\theta} \cdot \mathbf{v} \, d\Omega \\ & - \int_{\tilde{\Omega}} 2\nabla \cdot (\nu \nabla^s \mathbf{u}_{n+\theta}) \cdot \mathbf{v} \, d\Omega + \sum_e \int_{\partial\Omega_e} \beta_n \cdot \mathbf{n} (\bar{\mathbf{u}}_{n+\theta} - \mathbf{u}_{n+\theta}) \cdot \mathbf{v} \, d\Gamma \\ & + \sum_e \int_{\partial\Omega_e} 2\nu (\bar{\mathbf{u}}_{n+\theta} - \mathbf{u}_{n+\theta}) \cdot \nabla^s \mathbf{v} \, \mathbf{n} \, d\Gamma = \int_{\tilde{\Omega}} \mathbf{f}_{n+\theta} \cdot \mathbf{v} \, d\Omega \quad \forall \mathbf{v} \in \mathbf{V}, \end{aligned} \quad (4.43)$$

in which Δt denotes the time step size, $\theta \in [\frac{1}{2}, 1]$ is a time stepping parameter and the velocity $\mathbf{u}_{n+\theta}$ is given by

$$\mathbf{u}_{n+\theta} = (1 - \theta) \mathbf{u}_n + \theta \mathbf{u}_{n+1}. \quad (4.44)$$

The format of Equation (4.43) has the practical convenience that all unknowns are expressed at the same time level. The discrete global flux continuity constraint reads: given the boundary condition $\mathbf{h}_{n+\theta}$, find $\bar{\mathbf{u}}_{n+\theta} \in \bar{\mathbf{V}}_g$ such that

$$\begin{aligned} & \sum_e \int_{\partial\Omega_e} (\mathbf{u}_n \cdot \mathbf{n}) \mathbf{u}_{n+\theta} \cdot \bar{\mathbf{v}} \, d\Gamma - \sum_e \int_{\partial\Omega_e} 2\nu (\nabla^s \mathbf{u}_{n+\theta} \mathbf{n}) \cdot \bar{\mathbf{v}} \, d\Gamma \\ & + \sum_e \int_{\partial\Omega_e} \beta_n \cdot \mathbf{n} (\bar{\mathbf{u}}_{n+\theta} - \mathbf{u}_{n+\theta}) \cdot \bar{\mathbf{v}} \, d\Gamma \\ & - \int_{\Gamma_h} (1 - \gamma) (\mathbf{u}_n \cdot \mathbf{n}) \bar{\mathbf{u}}_{n+\theta} \cdot \bar{\mathbf{v}} \, d\Gamma = \int_{\Gamma_h} \tilde{\mathbf{h}}_{n+\theta} \cdot \bar{\mathbf{v}} \, d\Gamma \quad \forall \bar{\mathbf{v}} \in \bar{\mathbf{V}}, \end{aligned} \quad (4.45)$$

where the pressure terms on interior element boundaries have vanished pairwise, due to the continuity of p and $\bar{\mathbf{v}}$ on $\tilde{\Gamma}$, leading to the modified Neumann boundary condition $\tilde{\mathbf{h}}$ defined by

$$\tilde{\mathbf{h}} = \mathbf{h} - p\mathbf{n}. \quad (4.46)$$

This modification is convenient in practice since a homogeneous modified Neumann boundary condition can then be imposed at a closed wall where the fluid pressure balances the normal stress on the boundary. If $\tilde{\mathbf{h}}$ includes quadratic friction terms, as in Equation (4.8), these are discretized in time according to

$$c_f |\mathbf{u}| \mathbf{u} \approx c_f |\mathbf{u}_n| \mathbf{u}_{n+1}, \quad (4.47)$$

which will exactly solve the corresponding part of the momentum equations. Finally, the discrete global incompressibility constraint reads: find $p_{n+\theta} \in Q$ such that

$$\int_{\tilde{\Omega}} \mathbf{u}_{n+\theta} \cdot \nabla q \, d\Omega - \int_{\Gamma} \bar{\mathbf{u}}_{n+\theta} \cdot \mathbf{n} q \, d\Gamma = 0 \quad \forall q \in Q, \quad (4.48)$$

in which the pressure appears implicitly as $\mathbf{u}_{n+\theta}$ will be expressed in terms of $\bar{\mathbf{u}}_n$, $\bar{\mathbf{u}}_{n+\theta}$ and $p_{n+\theta}$ using local Equation (4.43).

The above time-discrete equations preserve a uniform flow state satisfying the boundary conditions. This assertion reflects consistency of the discrete method. The linear conservation properties, proven in Section 4.2.4, carry over unaltered to the discrete equations for any value of θ , which is easily asserted by taking $\mathbf{v} = \mathbf{e}_j$, $\bar{\mathbf{v}} = \mathbf{e}_j$ and $q = 1$ in Equations (4.43), (4.45) and (4.48), respectively. For volume conservation, the initial field \mathbf{u}_0 should be weakly non-divergent, which will yield discrete satisfaction of the incompressibility constraint at all time levels t_n . Proving quadratic conservation is more elaborate. Setting $\mathbf{v} = \mathbf{u}_{n+\theta}$, $\bar{\mathbf{v}} = \bar{\mathbf{u}}_{n+\theta}$ and $q = p_{n+\theta}$ in Equations (4.43), (4.45) and (4.48), respectively, it can be shown that in the absence of forcings and using skew-symmetric advection-diffusion operators, see Section 4.2.4, the following equation holds

$$\begin{aligned} \int_{\tilde{\Omega}} \frac{\mathbf{u}_{n+1} - \mathbf{u}_n}{\Delta t} \cdot \mathbf{u}_{n+\theta} \, d\Omega + \sum_e \int_{\partial\Omega_e} \left(\frac{1}{2} \mathbf{u}_n - \beta_n \right) \cdot \mathbf{n} |\bar{\mathbf{u}}_{n+\theta} - \mathbf{u}_{n+\theta}|^2 \, d\Gamma \\ + \int_{\tilde{\Omega}} 2\nu |\nabla^s \mathbf{u}_{n+\theta}|^2 \, d\Omega + \int_{\Gamma_h} \frac{1}{2} |\mathbf{u}_n \cdot \mathbf{n}| |\bar{\mathbf{u}}_{n+\theta}|^2 \, d\Gamma = 0. \end{aligned} \quad (4.49)$$

Due to the formulation of the interface flux the term $(\frac{1}{2} \mathbf{u} - \beta) \cdot \mathbf{n}$ is strictly positive, and the \mathcal{L}^2 norm of the velocity will decrease monotonically for $\theta > \frac{1}{2}$. Alternatively, the FS scheme is used here to render the time integration of the momentum equations strongly-stable.

4.3.2 $P^1 - P^1$ discretization

For linear function spaces, the discrete equations can be rendered in a particularly convenient form as the second derivative terms in Equations (4.43) and (4.45) vanish. Furthermore, for the case of spatially constant viscosity, the divergence of the stress term in the Navier-Stokes momentum equation

can be replaced by the Laplacian operator. Changing all symmetric gradient operators to the gradient operator and removing all appearances of the common factor ‘2’ in the variational equations leads to the formulation that would result from the direct consideration of a spatially constant viscosity. In combination with the Picard iteration for the advection terms, the Laplacian form of the viscous terms is convenient as it decouples the equations for the respective velocity components.

The local Equation (4.43) is now restated as: given \mathbf{u}_n and $\mathbf{f}_{n+\theta}$, find $\mathbf{u}_{n+\theta} \in \mathbf{V}$ such that

$$\begin{aligned} \int_{\tilde{\Omega}} \frac{\mathbf{u}_{n+\theta} - \mathbf{u}_n}{\theta \Delta t} \cdot \mathbf{v} \, d\Omega + \int_{\tilde{\Omega}} \nabla \cdot (\mathbf{u}_{n+\theta} \otimes \mathbf{u}_n) \cdot \mathbf{v} \, d\Omega + \int_{\tilde{\Omega}} \nabla p_{n+\theta} \cdot \mathbf{v} \, d\Omega \\ + \sum_e \int_{\partial\Omega_e} \beta_n \cdot \mathbf{n} (\bar{\mathbf{u}}_{n+\theta} - \mathbf{u}_{n+\theta}) \cdot \mathbf{v} \, d\Gamma \\ + \sum_e \int_{\partial\Omega_e} \nu \nabla (\bar{\mathbf{u}}_{n+\theta} - \mathbf{u}_{n+\theta}) \cdot \nabla \mathbf{v} \, \mathbf{n} \, d\Gamma = \int_{\tilde{\Omega}} \mathbf{f}_{n+\theta} \cdot \mathbf{v} \, d\Omega \quad \forall \mathbf{v} \in \mathbf{V}. \end{aligned} \quad (4.50)$$

The global flux continuity constraint Equation (4.45) becomes: given $\tilde{\mathbf{h}}_{n+\theta}$, find $\bar{\mathbf{u}}_{n+\theta} \in \bar{\mathbf{V}}_g$ such that

$$\begin{aligned} \sum_e \int_{\partial\Omega_e} (\mathbf{u}_n \cdot \mathbf{n}) \mathbf{u}_{n+\theta} \cdot \bar{\mathbf{v}} \, d\Gamma - \sum_e \int_{\partial\Omega_e} (\nu \nabla \mathbf{u}_{n+\theta} \mathbf{n}) \cdot \bar{\mathbf{v}} \, d\Gamma \\ + \sum_e \int_{\partial\Omega_e} \beta_n \cdot \mathbf{n} (\bar{\mathbf{u}}_{n+\theta} - \mathbf{u}_{n+\theta}) \cdot \bar{\mathbf{v}} \, d\Gamma \\ - \int_{\Gamma_h} (1 - \gamma) (\mathbf{u}_n \cdot \mathbf{n}) \bar{\mathbf{u}}_{n+\theta} \cdot \bar{\mathbf{v}} \, d\Gamma = \int_{\Gamma_h} \tilde{\mathbf{h}}_{n+\theta} \cdot \bar{\mathbf{v}} \, d\Gamma \quad \forall \bar{\mathbf{v}} \in \bar{\mathbf{V}}. \end{aligned} \quad (4.51)$$

The incompressibility constraint, Equation (4.48), is left unaltered for the case of linear basis functions.

The functions \mathbf{u}_n , $\bar{\mathbf{u}}_n$ and p_n at time t_n are expressed in terms of a finite element basis as

$$\mathbf{u}_n(\mathbf{x}) = \sum_i N^i(\mathbf{x}) \mathbf{u}_n^i, \quad (4.52)$$

$$p_n(\mathbf{x}) = \sum_j \tilde{N}^j(\mathbf{x}) p_n^j, \quad (4.53)$$

$$\bar{\mathbf{u}}_n(\mathbf{x}) = \sum_j \bar{N}^j(\mathbf{x}) \bar{\mathbf{u}}_n^j, \quad (4.54)$$

where N^i , \tilde{N}^j and \bar{N}^j are linear basis functions consistent with the definitions in Section 4.2 and \mathbf{u}_n^i , p_n^j and $\bar{\mathbf{u}}_n^j$ are nodal degrees of freedom. For a single element, the local numbering of the basis functions may be chosen

such that $i = j$ on corresponding nodes, dropping the distinction between N^j , \tilde{N}^j and \bar{N}^j on element boundaries.

As the equations for the respective components of the velocity vector are decoupled, the format of the discrete momentum Equations (4.50) and (4.51) is similar to the format of the discrete transport equations in Chapter 3. The algebraic treatment of the problem proceeds in a similar way as for the advection-diffusion problem, the only difference being the inclusion of the pressure gradient which appears as a source term. The matrix format of local Equation (4.50) thus becomes

$$\frac{1}{\theta\Delta t} \mathbf{M} \left(\mathbf{U}_{n+\theta}^k - \mathbf{U}_n^k \right) + \mathbf{A} \mathbf{U}_{n+\theta}^k + (\mathbf{K} + \mathbf{Q}) \left(\bar{\mathbf{U}}_{n+\theta}^k - \mathbf{U}_{n+\theta}^k \right) + \mathbf{G}_k \mathbf{p}_{n+\theta} = \mathbf{F} \mathbf{e}_k, \quad (4.55)$$

where \mathbf{U}^k , with $k = 1, \dots, d$, is the vector of unknowns of the k^{th} velocity component and \mathbf{p} is the vector of pressure unknowns. The element matrices \mathbf{M} , \mathbf{A} , \mathbf{G}_k , \mathbf{K} and \mathbf{Q} are given by, respectively,

$$M^{ij} = \int_{\Omega_e} N^i N^j d\Omega, \quad (4.56)$$

$$A^{ij} = \int_{\Omega_e} N^i \nabla \cdot (\mathbf{u}_n N^j) d\Omega, \quad (4.57)$$

$$G_k^{ij} = \int_{\Omega_e} N^i (\nabla N^j \cdot \mathbf{e}_k) d\Omega, \quad (4.58)$$

$$K^{ij} = \int_{\partial\Omega_e} N^j (\nu \mathbf{n}) \cdot \nabla N^i d\Gamma, \quad (4.59)$$

$$Q^{ij} = \int_{\partial\Omega_e} (\beta_n \cdot \mathbf{n}) N^i N^j d\Gamma, \quad (4.60)$$

and the matrix \mathbf{F} is given by

$$F^{ij} = \int_{\Omega_e} N^i \mathbf{f}_{n+\theta} \cdot \mathbf{e}_j d\Omega. \quad (4.61)$$

The matrices \mathbf{A} , \mathbf{K} and \mathbf{Q} are independent of the considered component k which has the practical convenience that the matrices have to be computed only once in each time step. For linear elements, and piecewise constant ν , the matrix \mathbf{K} is equal to the standard CG element diffusion matrix. The global momentum Equation (4.51), leads to the algebraic equation

$$\sum_e \left[\left(\tilde{\mathbf{A}} - \mathbf{K}^T \right) \mathbf{U}_{n+\theta}^k + \mathbf{Q} \left(\bar{\mathbf{U}}_{n+\theta}^k - \mathbf{U}_{n+\theta}^k \right) - \mathbf{P} \bar{\mathbf{U}}_{n+\theta}^k \right] = \sum_e \mathbf{H} \mathbf{e}_k, \quad (4.62)$$

where \sum_e represents assembly of the element matrices into a global matrix.

The matrices $\tilde{\mathbf{A}}$ and \mathbf{P} are given by, respectively,

$$\tilde{A}^{ij} = \int_{\partial\Omega_e} (\mathbf{u}_n \cdot \mathbf{n}) N^i N^j d\Omega, \quad (4.63)$$

$$P^{ij} = \int_{\partial\Omega_e \cap \Gamma_h} (1 - \gamma) (\mathbf{u}_n \cdot \mathbf{n}) N^i N^j d\Gamma, \quad (4.64)$$

and the matrix \mathbf{H} is given by

$$H^{ij} = \int_{\partial\Omega_e \cap \Gamma_h} N^i \tilde{\mathbf{h}}_{n+\theta} \cdot \mathbf{e}_j d\Gamma. \quad (4.65)$$

For piecewise constant ν and linear elements, the matrix \mathbf{K}^T equals \mathbf{K} . The pressure unknowns \mathbf{p} are determined through the simultaneous solution of the discrete continuity Equation (4.48), which in matrix form reads

$$\sum_e \left(\mathbf{D}_k \mathbf{U}_{n+\theta}^k - \mathbf{E}_k \bar{\mathbf{U}}_{n+\theta}^k \right) = \mathbf{0}, \quad (4.66)$$

where repeated indices denote summation, and the matrices \mathbf{D}_k and \mathbf{E}_k are given by, respectively,

$$D_k^{ij} = \int_{\Omega_e} (\mathbf{e}_k \cdot \nabla N^i) N^j d\Omega, \quad (4.67)$$

$$E_k^{ij} = \int_{\partial\Omega_e \cap \Gamma_h} (\mathbf{e}_k \cdot \mathbf{n}) N^i N^j d\Gamma. \quad (4.68)$$

The divergence matrix \mathbf{D}_k is the transpose of the gradient matrix \mathbf{G}_k given by Equation (4.58). Elimination of the velocity degrees of freedom $\mathbf{U}_{n+\theta}^k$ from Equation (4.66) using local momentum Equation (4.55) yields the global form of the continuity equation. The resulting solution procedure of the coupled system for $(\bar{\mathbf{U}}^1, \dots, \bar{\mathbf{U}}^d, \mathbf{p})$ is outlined in the next section.

4.3.3 Solution procedure

The solution procedure proceeds in a similar way as for the advection-diffusion equation, see Section 3.4.2, but is more complicated due to the pressure gradient terms and the incompressibility constraint.

4.3.3.1 Condensation

The first step is to express $\mathbf{U}_{n+\theta}^k$ implicitly in terms of $\bar{\mathbf{U}}_{n+\theta}^k$ and $\mathbf{p}_{n+\theta}$ on each element using local Equation (4.50) which, after some algebraic manipulation, can be rewritten as

$$\begin{aligned} \mathbf{U}_{n+\theta}^k &= \bar{\mathbf{U}}_{n+\theta}^k \\ &- \mathbf{T} \left[\frac{1}{\theta \Delta t} \mathbf{M} \left(\bar{\mathbf{U}}_{n+\theta}^k - \mathbf{U}_n^k \right) + \mathbf{A} \bar{\mathbf{U}}_{n+\theta}^k + \mathbf{G}_k \mathbf{p}_{n+\theta} - \mathbf{F} \mathbf{e}_k \right] \end{aligned} \quad (4.69)$$

in which the matrix \mathbf{T} is given by

$$\mathbf{T} = \left(\frac{1}{\theta\Delta t} \mathbf{M} + \mathbf{A} - \mathbf{K} - \mathbf{Q} \right)^{-1}. \quad (4.70)$$

Equation (4.69) states that the local velocity field is found by ‘correcting’ the global velocity field with terms proportional to element-wise ‘residual’ of the material derivative, pressure and forcing terms. Referring to Section 3.4.2 for the details of the derivation, substitution of Equation (4.69) into the global momentum Equation (4.62) finally results in the following global matrix system

$$\begin{aligned} \sum_e \mathbf{W}_1 \left[\frac{1}{\theta\Delta t} \mathbf{M} \left(\bar{\mathbf{U}}_{n+\theta}^k - \mathbf{U}_n^k \right) + \mathbf{A} \bar{\mathbf{U}}_{n+\theta}^k + \mathbf{G}_k \mathbf{p}_{n+\theta} - \mathbf{F} e_k \right] \\ + \sum_e \left(\mathbf{K} + \mathbf{P} - \tilde{\mathbf{A}} \right) \bar{\mathbf{U}}_{n+\theta}^k + \sum_e \mathbf{H} e_k = \mathbf{0}, \end{aligned} \quad (4.71)$$

where the ‘weighting’ matrix \mathbf{W}_1 is given by

$$\mathbf{W}_1 = \mathbf{I} - \left(\frac{1}{\theta\Delta t} \mathbf{M} + \mathbf{A} - \tilde{\mathbf{A}} \right) \mathbf{T}, \quad (4.72)$$

Equation (4.71) is similar to the global system of equations that would arise from the standard Galerkin method, the only difference being the appearance of the weighting matrix \mathbf{W}_1 which for the CG method would be equal to the unit matrix. The only non-standard term that must be evaluated to compute the weighting matrix is the boundary matrix \mathbf{Q} .

In a similar way, local Equation (4.69) may be substituted into the discrete global continuity equation (4.48), which yields

$$\begin{aligned} \sum_e \mathbf{D}_k \bar{\mathbf{U}}_{n+\theta}^k - \sum_e \mathbf{D}_k \mathbf{T} \left[\frac{1}{\theta\Delta t} \mathbf{M} \left(\bar{\mathbf{U}}_{n+\theta}^k - \mathbf{U}_n^k \right) + \mathbf{A} \bar{\mathbf{U}}_{n+\theta}^k + \mathbf{G}_k \mathbf{p}_{n+\theta} - \mathbf{F} e_k \right] \\ - \sum_e \mathbf{E}_k \bar{\mathbf{U}}_{n+\theta}^k = \mathbf{0}. \end{aligned} \quad (4.73)$$

Rewriting and collecting terms this can be re-arranged into

$$\begin{aligned} \sum_e \left[\left(\mathbf{D}_k \mathbf{W}_2 - \mathbf{E}_k \right) \bar{\mathbf{U}}_{n+\theta}^k \right] - \sum_e \mathbf{D}_k \mathbf{T} \mathbf{G}_k \mathbf{p}_{n+\theta} \\ + \sum_e \mathbf{D}_k \mathbf{T} \left(\frac{1}{\theta\Delta t} \mathbf{M} \mathbf{U}_n^k + \mathbf{F} e_k \right) = \mathbf{0}, \end{aligned} \quad (4.74)$$

which features a second weighting matrix \mathbf{W}_2 which is given by

$$\mathbf{W}_2 = \mathbf{I} - \mathbf{T} \left(\frac{1}{\theta\Delta t} \mathbf{M} + \mathbf{A} \right). \quad (4.75)$$

In elements where \mathbf{u} and ν are zero the above expressions remain non-singular yielding matrices \mathbf{W}_1 and \mathbf{W}_2 equal to zero. The elimination procedure leads to a modification of the CG divergence matrix, the addition of a pseudo-Laplacian operator for the pressure, and a few additional explicit terms. The structure of this system, and the stabilization properties it inherits, are discussed in Section 4.3.4.

4.3.3.2 Iteration

The discrete global momentum and continuity equations constitute a coupled system which can be written in symbolic form as

$$\begin{pmatrix} \mathcal{A} & \mathcal{G}_k \\ \mathcal{D}_k & \mathcal{B} \end{pmatrix} \begin{pmatrix} \bar{\mathbf{U}}^k \\ \mathbf{p} \end{pmatrix} \Big|_{n+\theta} = \begin{pmatrix} \mathbf{V}^k \\ \mathbf{q} \end{pmatrix} \Big|_n, \quad (4.76)$$

where $k = 1, \dots, d$, \mathcal{A} is a $d \times d$ block-diagonal matrix representing the stabilized advection-diffusion operator, \mathcal{D}_k and \mathcal{G}_k are block-row and block-column matrices for the modified divergence and gradient operators, respectively, \mathcal{B} is a Laplacian matrix and the vectors \mathbf{V}^k and \mathbf{q} on the right-hand side denote the explicit contributions from time level n . All block matrices in Equation (4.76) have the same sparse matrix structure as the degrees of freedom $\bar{\mathbf{U}}^k$ and \mathbf{p} reside in the same nodes of the finite element mesh. This not only facilitates the storage and handling of the system but may also be exploited to obtain an efficient iterative solution procedure.

For a mesh of N nodes, Equation (4.76) involves a set of $N \times N$ sparse matrices to be stored in memory for which the Block Sparse Row (BSR) storage scheme may be used. All contributions to row i from the degrees of freedom in node j are wrapped up in a single matrix A^{ij} given by

$$A^{ij} = \begin{pmatrix} \mathcal{A}^{ij} & \mathcal{G}_k^{ij} \\ \mathcal{D}_k^{ij} & \mathcal{B}^{ij} \end{pmatrix}, \quad (4.77)$$

which is easily stored as an ordered set of matrices in the same way as the Compressed Sparse Row (CSR) format stores scalar valued matrix elements. The BSR storage scheme only requires one set of pointer arrays *col*, *beg* and *di* while the elements in the array *row* are ordered matrices A^{ij} . See also Chapter 2 for the corresponding CSR format of a scalar sparse matrix. Accordingly, the right hand side vector may be stored as an ordered set of nodal vectors $[\bar{u}^1, \dots, \bar{u}^d, p]_i^T$. Matrix-vector multiplication and upper-lower inversions can now be performed efficiently, replacing the scalar operations in conventional algorithms by matrix-vector operations.

Iterative solution of block systems like Equation (4.76) by the BICGSTAB algorithm is complicated by the construction of a proper preconditioner, which is non-trivial. Basically, one may a) incorporate the block structure

into the BICGSTAB algorithm, as in Liu et al. [57], or b) construct an approximate LU block-decomposition of the system as follows, using the summation convention,

$$\begin{pmatrix} \mathcal{A} & \mathcal{G}_k \\ \mathcal{D}_k & \mathcal{B} \end{pmatrix} \approx \begin{pmatrix} \mathcal{I} & 0 \\ \mathcal{D}_k \mathcal{A}^{-1} & \mathcal{I} \end{pmatrix} \begin{pmatrix} \mathcal{A} & \mathcal{G}_k \\ 0 & \mathcal{B} - \mathcal{D}_k \mathcal{A}^{-1} \mathcal{G}_k \end{pmatrix}, \quad (4.78)$$

whose inversion requires ILU decompositions of the matrix \mathcal{A} and of the Schur-complement $\mathcal{B} - \mathcal{D}_k \mathcal{A}^{-1} \mathcal{G}_k$ only, as in van der Ploeg [69]. Although good results have been obtained with both approaches [49], this thesis proceeds in another direction. As the block systems encountered here are stored as an ordered series of matrices A^{ij} , a straightforward ILU decomposition may be performed where the operations on the scalar elements of *row* from a regular ILU preconditioner are replaced by the corresponding matrix operations. Provided that the system rows are scaled with the inverses of the diagonal elements A^{ii} , the resulting preconditioner proved efficient in all numerical examples given in this chapter.

In time dependent problems, the local solution vectors \mathbf{U}^k are obtained from a back-substitution step using Equation (4.69) and stored in memory. To do this efficiently, the matrix \mathbf{T} given by Equation (4.70) is also stored in memory during the assembly process.

4.3.4 Stabilization mechanism

In order to sketch the stabilization mechanism introduced by the interface terms, the stationary case with homogeneous Dirichlet boundary conditions and without forcing terms is considered. This simplification mainly serves to focus on the relevant aspects. Extension to the general case is straightforward but involves more lengthy notation.

For this simplified case, the local momentum equation reads, after inversion

$$\mathbf{U}^k = \bar{\mathbf{U}}^k - \mathbf{T} \left(\mathbf{A} \bar{\mathbf{U}}^k + \mathbf{G}_k \mathbf{p} \right). \quad (4.79)$$

The corresponding global momentum equation reads, after condensation

$$\sum_e \left[\left(\mathbf{A} - \tilde{\mathbf{A}} + \mathbf{K} \right) \bar{\mathbf{U}}^k + \mathbf{G}_k \mathbf{p} - \left(\mathbf{A} - \tilde{\mathbf{A}} \right) \mathbf{T} \left(\mathbf{A} \bar{\mathbf{U}}^k + \mathbf{G}_k \mathbf{p} \right) \right] = \mathbf{0}. \quad (4.80)$$

Noting that for a divergence-free velocity field $\mathbf{A} - \tilde{\mathbf{A}} = -\mathbf{A}^T$, this equation is similar to that obtained for the GIS stabilized advection-diffusion problem, Equation (3.67) in Section 3.4.3. The standard Galerkin terms are augmented with terms proportional to the element ‘residuals’ $\mathbf{R}^k = \mathbf{A} \bar{\mathbf{U}}^k + \mathbf{G}_k \mathbf{p}$, which results in a SUPG-like stabilization mechanism for the advective part of the momentum equation, as shown in Section 3.4.3. For a penalty parameter $\alpha = 4$ the stabilization is near-optimal and almost identical to that

obtained from the SUPG method, with the pressure gradient consistently retained in the stabilization terms.

At this point all of this is too familiar to be very exciting. More interesting is that the condensation procedure simultaneously stabilizes the incompressibility constraint. To this end, for homogeneous Dirichlet boundary conditions, the condensed global continuity equation reads

$$\sum_e \left[\mathbf{D}_k \bar{\mathbf{U}}^k - \mathbf{D}_k \mathbf{T} \left(\mathbf{A} \bar{\mathbf{U}}^k + \mathbf{G}_k \mathbf{p} \right) \right] = \mathbf{0}, \quad (4.81)$$

using the summation convention. Combination of the global momentum equation (4.80) and the global incompressibility constraint, Equation (4.81), yields the following block-matrix system

$$\sum_e \begin{pmatrix} -\mathbf{A}^T + \mathbf{A}^T \mathbf{T} \mathbf{A} + \mathbf{K} & \mathbf{G}_k + \mathbf{A}^T \mathbf{T} \mathbf{G}_k \\ \mathbf{D}_k - \mathbf{D}_k \mathbf{T} \mathbf{A} & -\mathbf{D}_k \mathbf{T} \mathbf{G}_k \end{pmatrix} \begin{pmatrix} \bar{\mathbf{U}}^k \\ \mathbf{p} \end{pmatrix} = \mathbf{0}. \quad (4.82)$$

For linear basis functions, the element matrices associated with the operators \mathbf{D}_k and \mathbf{G}_k are column-wise and row-wise constant, respectively, in which case it may be shown that the lower diagonal in Equation (4.82) represents a Laplacian term which stabilizes the pressure field. The stabilizing effect of the pressure Laplacian was already recognized in Johnson [42] and analyzed more fundamentally by Brezzi and Fortin [8]. The associated stability parameter is equal to the stability parameter τ'_e of the momentum equation. The additional terms in the divergence operator keep the stabilization consistent.

The above form of the global continuity constraint closely resembles that of the Pressure Stabilized Petrov-Galerkin (PSPG) method which was initially conceived in a series of papers by Hughes et al. [38]. In contrast to the PSPG method, the stabilization terms in Equation (4.82) are not added explicitly but inherited from the formulation of the interface flux in Equation (4.32) and the associated flux continuity constraint given by Equation (4.24). The back substitution by Equation (4.79) also guarantees weak zero divergence of the discrete velocity field \mathbf{u} . Hence, in time stepping problems, the advection operator is constructed naturally from a weakly zero divergent advective transport field, without recourse to correction terms as for instance in Hughes and Wells [37]. The MINI element also features this nice property but has the disadvantage that the stabilization parameter of the resulting Laplacian is non-optimal [81]. Noteworthy to mention is that discontinuous Galerkin methods with equal-order discontinuous velocity/continuous pressure are stable for Stokes flow [15].

4.4 Numerical examples

For all numerical examples a penalty parameter $\alpha = 4$ is used, unless stated otherwise. The solutions are obtained using the monolithic iterative solution

procedure outlined in Section 4.3.3. Time dependent problems use the FS time stepping scheme and time steps given denote the average value of the three substeps of this scheme. All meshes were constructed using the mesh generator from the SEPRAN package [80].

4.4.1 Stokes flow

The linear Stokes problem is obtained trivially from the Navier-Stokes problem by ignoring the advection terms. For a constant viscosity ν this yields

$$\frac{\partial \mathbf{u}}{\partial t} + \nabla p - \nu \nabla^2 \mathbf{u} = \mathbf{f}, \quad (4.83)$$

$$\nabla \cdot \mathbf{u} = 0. \quad (4.84)$$

The next two examples consider the convergence rate of the Stokes problem and the acceleration of a laminar flow in a pipe, respectively.

4.4.1.1 Stokes flow with source

This example, taken from Donea and Huerta [19], has a closed form analytical solution which is used to determine the convergence rate. The computational domain is given by the unit square $\Omega = (0, 1) \times (0, 1)$. A constant viscosity $\nu = 1$ is used, Dirichlet boundary conditions $\mathbf{g} = \mathbf{0}$ on $\partial\Omega$ and a source function $\mathbf{f} = (f_x, f_y)$ given by

$$\begin{aligned} f_x &= (12 - 24y)x^4 + (24 - 48y)x^3 - (48y - 72y^2 + 48y^3 - 12)x^2 \\ &\quad - (2 - 24y + 72y^2 - 48y^3)x + 1 - 4y + 12y^2 - 8y^3, \\ f_y &= (8 - 48y + 48y^2)x^3 - (12 - 72y + 72y^2)x^2 \\ &\quad (4 - 24y + 48y^2 - 48y^3 + 24y^4)x - 12y^2 + 24y^3 - 12y^4. \end{aligned} \quad (4.85)$$

The exact solution to this problem is, see Donea and Huerta [19],

$$\begin{aligned} u_x &= x^2(1-x)^2(2y-6y^2+4y^3), \\ u_y &= -y^2(1-y)^2(2x-6x^2+4x^3), \\ p &= x(1-x). \end{aligned} \quad (4.86)$$

The problem is solved on five different uniform meshes with element sizes h_e ranging from 1/10 to 1/160. The elements are approximately equilateral. As the pressure is only determined up to a constant, the pressure is fixed at one point.

Figure 4.2 shows the computed flow and pressure fields for $h_e = 1/40$. The computed pressure and velocity fields are reasonably smooth. The \mathcal{L}^2 error norms for the pressure and the velocity are shown in Figure 4.3. A convergence rate of order two is observed for the velocity field, while the

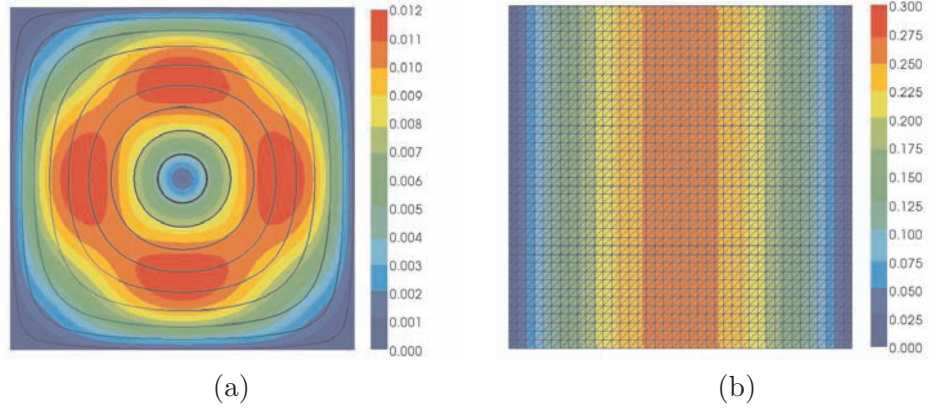


Figure 4.2: Stokes flow with source: computed flow field (a) and pressure field (b); results for $h_e = 1/40$.

pressure converges at a rate slightly better than one. Varying the penalty parameter α between 1 and 10 gives similar convergence results. Significantly larger or smaller values of α however result in a loss of accuracy.

4.4.1.2 Accelerating pipe flow

Consider a circular pipe with radius R and length L . The fluid in the pipe is initially at rest. For $t > 0$ a constant pressure difference Δp is imposed between both pipe ends causing the fluid to accelerate. For a constant viscosity ν and a no-slip boundary condition along the pipe wall, the solution for the axial velocity u_a is a function of the radial distance r and time t given by, see for instance Strauss [86],

$$u_a = \sum_j J_0(\alpha_j r) \beta_j [1 - \exp(-\alpha_j^2 \nu t)], \quad (4.87)$$

where J_0 is the Bessel function of the first kind and order zero, the coefficients α_j are determined from $J_0(\alpha_j R) = 0$ and the coefficients β_j are determined from

$$\beta_j = \frac{\int_0^R u_\infty(r) J_0(\alpha_j r) r dr}{\int_0^R J_0^2(\alpha_j r) r dr}, \quad (4.88)$$

in which u_∞ is the equilibrium axial velocity at $t = \infty$,

$$u_\infty = \frac{\Delta p}{4\nu L} (R^2 - r^2). \quad (4.89)$$

The flow problem has an intrinsic time scale $\tau_s = 1/\alpha_1^2 \nu$ and for $t > 5\tau_s$ the flow will be approximately stationary with the total wall shear stress balancing the applied pressure force.

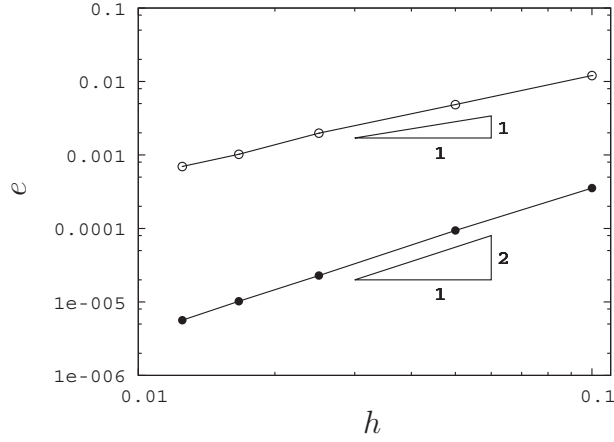


Figure 4.3: Stokes flow with source: errors in the \mathcal{L}^2 -norm of the velocity (dots) and the pressure (circles).

The numerical test concerns a pipe with a radius $R = 2$ and a length $L = 20$. The pressure drop over the pipe amounts 10 which results in an equilibrium velocity in the center of the pipe of one. A tetrahedral mesh is used with eight elements over the width and thirty elements over the length of the pipe, respectively. The viscosity is set to $\nu = 0.5$ giving an intrinsic time scale $\tau_s \approx 1.4$. For time stepping the FS scheme is used with an average time step size $\Delta t = 0.1$ giving a diffusion number $\nu\Delta t/h_e^2 = 0.8$. The end time for the simulation $T = 10$.

Figure 4.4 shows the computed and analytical solution for the velocity. Considering that the mesh is relatively coarse and the time step is relatively large compared to the intrinsic time scale of the problem, the results are good. Importantly, the final velocity profile is reproduced accurately which implies that for a prescribed discharge the pressure drop over the pipe will also be computed correctly.

4.4.2 Burgers' equation

The formulation for the Navier-Stokes equations can be modified trivially to solve the one-dimensional viscous Burger's equation

$$\frac{\partial u}{\partial t} + \frac{\partial}{\partial x} \left(\frac{u^2}{2} \right) - \nu \frac{\partial^2 u}{\partial x^2} = 0. \quad (4.90)$$

For the case $\nu = 0$ this non-linear equation admits shocks as solutions while for $\nu > 0$ shocks will have a finite width. The Burgers' equation is used to assess the numerical behaviour of the non-linear flux terms and the associated choice for the interface flux function given by Equation (4.32). In

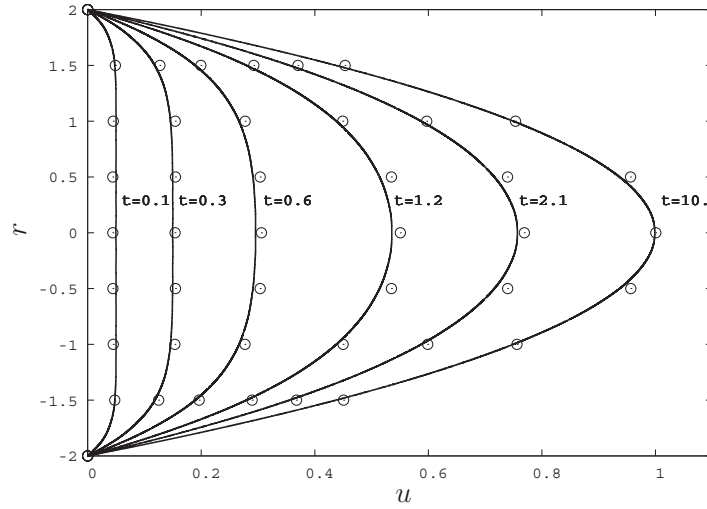


Figure 4.4: *Accelerating pipe flow: analytical solution (solid) and numerical solution (circles) of the velocity magnitude at different time steps.*

particular, shock propagation, conservation and combined non-linear advection and diffusion will be considered. To this end two cases are considered, a stationary shock and N -wave rarefaction.

4.4.2.1 Stationary compression shock

The stationary solution to the one-dimensional viscous Burgers' equation with boundary conditions $u(\pm\infty) = \mp u_0$, where $u_0 > 0$, is given by

$$u = -u_0 \arctan\left(Pe \frac{x}{h_e}\right), \quad (4.91)$$

where the Péclet number is defined as $Pe = u_0 h_e / \nu$. The numerical solution is calculated on the domain $\Omega = (-10, 10)$, which is partitioned into twenty linear elements with a uniform element size $h_e = 1$. The viscosity ν is adjusted in order to obtain Péclet numbers of 0.1, 1, 10 and 100, respectively. The solution is obtained from the non-stationary model using the initial condition $u(x, 0) = 0$ and Dirichlet boundary conditions provided by Equation (4.91) until steady state is reached.

Figure 4.5 shows that the numerical results are in good agreement with the analytical solution, giving correct positions and slopes of the shocks. The solutions for \bar{u} do not exhibit overshoot. For Péclet-numbers 10 and 100, the solution of u has some overshoot, but this remains localized to a limited region around the shock only. These results confirm that for arbitrary Péclet numbers, the combination of non-linear advection and diffusion is handled well by the GIS method without requiring additional shock capturing or limiting procedures.

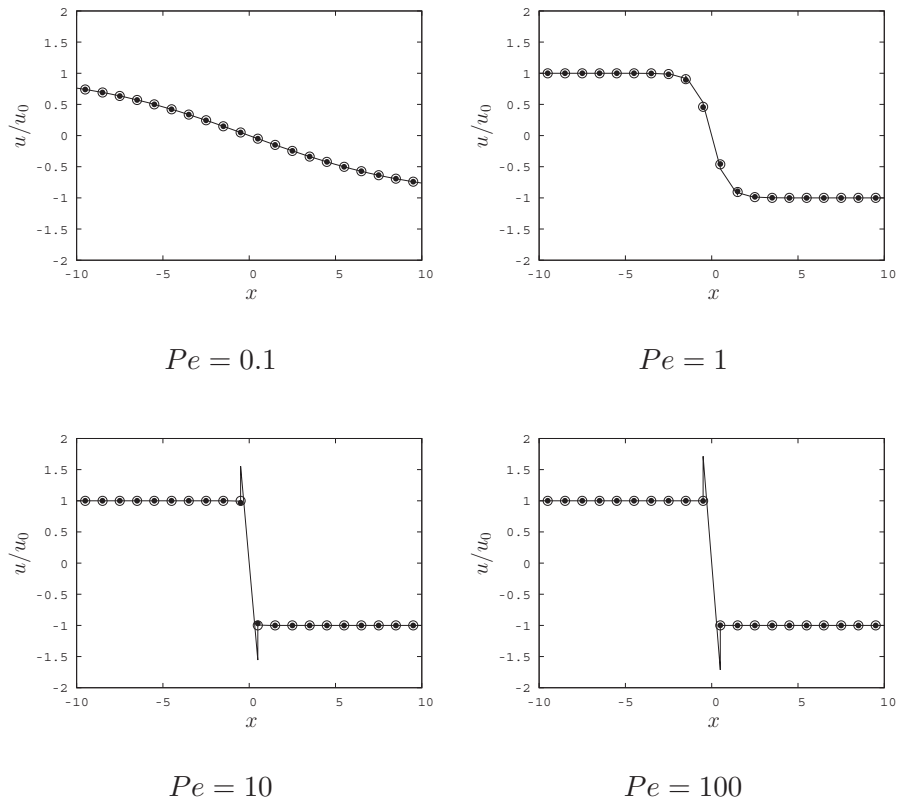


Figure 4.5: *Stationary compression shock: solution for various Péclet numbers; showing \bar{u} (dots), u (solid) and exact solution (circles).*

4.4.2.2 N -wave rarefaction

This example considers time dependent solutions of the non-viscous Burgers equation. If the initial condition u_0 has an ‘ N ’-shape given by

$$u(x, 0) = \begin{cases} u_0 x/x_0 & \text{for } |x| \leq x_0, \\ 0 & \text{elsewhere,} \end{cases} \quad (4.92)$$

the solution for the unbounded domains $\Omega = (-\infty, \infty)$ and $t > 0$ is of the form

$$u = \begin{cases} u_0 x / (x_0 + u_0 t) & \text{for } |x| < x_0 \sqrt{1 + u_0 t/x_0}, \\ u = 0 & \text{elsewhere.} \end{cases} \quad (4.93)$$

The solution has right and left propagating compression shocks on the respective sides of the N , which are separated by a rarefaction shock at the center ($x = 0$). The numerical example uses a uniform mesh of 40 linear elements and $h_e = 1$. The initial conditions are specified by setting $u_0 = 1$

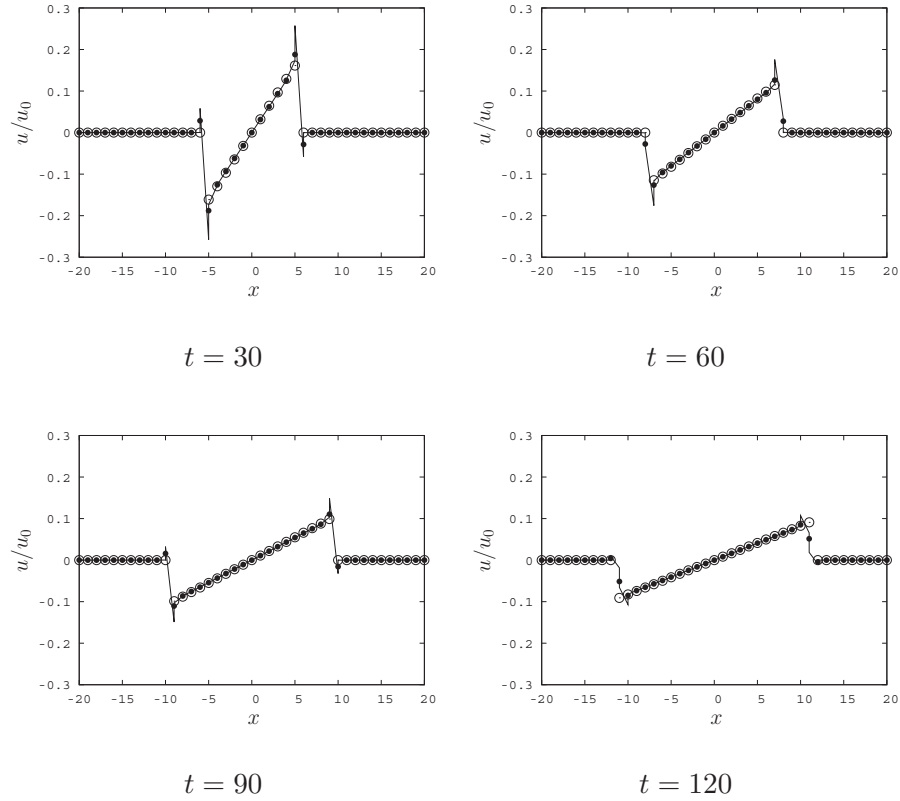


Figure 4.6: *N*-wave rarefaction: computed and analytical solution at different time steps for an initial Courant number $u_0\Delta t/h_e = 0.5$; shown are \bar{u} (dots), u (solid) and the exact solution (circles).

and $x_0 = 1$, which represents an initial *N* profile captured by just two elements. Using the FS scheme with average time step $\Delta t = 0.5$ gives a Courant number $u_0\Delta t/h_e = 0.5$.

Figure 4.6 shows the numerical and analytical solutions at different time steps. The numerical solution reproduces the analytical shock positions and shock heights well with minimal overshoot at shocks in \bar{u} . The rarefaction in the center at $x = 0$ is smoothly resolved without kink or other local irregularities in the solution. It was also confirmed that the total mass given by $\int_{\Omega} u d\Omega$ remains zero to within machine accuracy.

The examples for the Burgers' equation show that the GIS method is capable to treat the non-linearity in the problem without additional limiting or shock capturing, provided that the proper expressions for the fluxes at the interfaces and within the elements are used. Especially the behaviour of the scheme around shocks is encouraging.

4.4.3 Driven cavity flow

This test considers the incompressible Navier-Stokes problem on the square domain $\Omega = (0, 1) \times (0, 1)$ with pure Dirichlet boundary conditions, imposing $\bar{\mathbf{u}} = (1, 0)$ on the upper boundary at $y = 1$, and $\bar{\mathbf{u}} = \mathbf{0}$ elsewhere on $\partial\Omega$. The flow field has a primary vortex near the center of the domain. Smaller vortices may appear in the corners of the domain which is dependent on the Reynolds number. Defining length- and velocity scales $L_{\text{ref}} = 1$ and $U_{\text{ref}} = 1$, respectively, the viscosity ν is adjusted in order to obtain Reynolds numbers of 100, 400, 1000 and 5000, respectively.

The computational domain is discretized by approximately uniform and equilateral triangles with mesh size $h_e \approx 1/64$. The boundary conditions $\bar{\mathbf{u}}$ are discontinuous at the upper left and right corners of the domain. To bypass this singularity, the velocity is imposed via a penalty formulation with penalty parameter 10^6 . As the pressure is only determined up to a constant, the pressure is fixed at one point. The Péclet number ranges from $Pe \approx 3$ for $Re = 400$, to $Pe \approx 40$ for $Re = 5000$.

Figure 4.7 shows the computed flow fields in terms of the velocity magnitude and the corresponding streamlines. The solution involves a primary vortex, while for the higher Reynolds numbers secondary vortices appear in the lower corners of the domain. The $Re = 5000$ case also has a secondary vortex in the upper left corner. Qualitatively, the results are similar to reference solutions [19, 23] although the mesh used here is too coarse to resolve the finer details of the secondary vortices. Table 4.1 summarizes some properties of the computed main vortex together with corresponding values from reference solutions. Given the relatively coarse mesh that is used, a good agreement is observed.

4.4.4 Borda mouthpiece

This example concerns the quasi-steady, turbulent exchange flow between two reservoirs connected by a so-called Borda mouthpiece. This discharge structure, devised by de Borda², consists of a short tube with constant diameter which protrudes into the upstream reservoir. The energy loss and the contraction of the streamlines in the tube can be determined analytically by applying basic fluid mechanics principles [62]. The flow contraction coefficient, defined as the ratio of the cross-sectional area of the *vena contracta* to that of the mouthpiece, is theoretically given by $\mu = \frac{1}{2}$ and the corresponding normalized pressure drop over the mouthpiece amounts $\Delta p = \frac{1}{2}U^2$, where U is the mean flow velocity at the transect of maximum contraction.

²Jean-Charles de Borda, who lived from 1733 to 1799, was a French mathematician, physicist and political scientist. Besides the mouthpiece bearing his name he also proposed a political voting system.

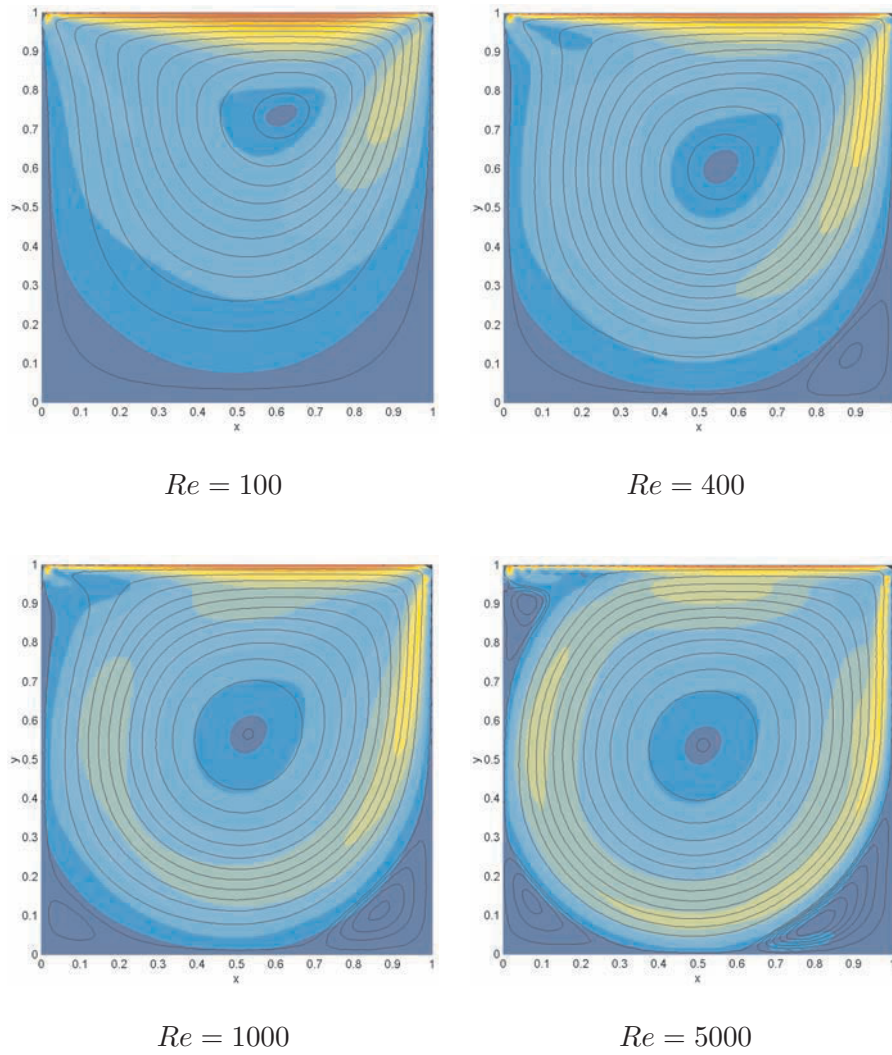


Figure 4.7: *Driven cavity flow: velocity (colour) and streamlines (isolines) for Reynolds numbers of 100, 400, 1000 and 5000; streamline intervals 10^{-2} (primary vortex) and $5 \cdot 10^{-4}$ (secondary vortices); colour interval 0.1; element size $h_e \approx 1/64$.*

Re		x	y	stream function
100	present simulation	0.608	0.737	0.104
	Donea and Huerta [19]	0.62	0.74	0.103
400	present simulation	0.557	0.611	0.115
	Donea and Huerta [19]	0.568	0.606	0.110
1000	present simulation	0.524	0.560	0.121
	Donea and Huerta [19]	0.540	0.573	0.110
	Erturk et al. [23]	0.530	0.565	0.119
5000	present simulation	0.515	0.546	0.131
	Erturk et al. [23]	0.515	0.535	0.121

Table 4.1: *Driven cavity flow: primary vortex position and stream function value; present simulation, $h_e \approx 1/64$; Donea and Huerta [19], $h_e = 1/30$; Erturk et al. [23], $h_e = 1/400$.*

The computational domain has a length of 20 m and a width of 6 m. In the middle of the domain ($x = 0$) a vertical wall is present, separating both reservoirs. The mouthpiece is situated halfway the wall ($y = 0$) and has a width of 0.5 m and a total length of 0.6 m of which 0.5 m protrudes into the upstream (left) reservoir and 0.1 m into the downstream (right) reservoir, see also Figure 4.8. The adopted mesh size ranges from 0.025 m in the vicinity of the mouthpiece to 0.15 m towards the outer boundaries. All boundaries are closed, except for the left and right boundaries where a discharge of 1 m²/s and a zero Neumann boundary condition $\tilde{\mathbf{h}} = \mathbf{0}$ are specified, respectively. The turbulent fluid motion is modelled by defining the turbulence momentum flux $\boldsymbol{\sigma}_t$ (Reynolds stress) according to

$$\boldsymbol{\sigma}_t = - (C_s h_e)^2 (\nabla^s \mathbf{u} : \nabla^s \mathbf{u})^{1/2} \nabla \mathbf{u}, \quad (4.94)$$

where C_s is the Smagorinsky parameter, see also Appendix B. The turbulent motion is initiated by prescribing a randomly perturbed inflow velocity. The turbulent wall shear stress is modelled according to Equation (4.8). In this example C_s is set to 0.15 and the random inflow perturbation amounts 15% of the inflow velocity magnitude. The wall friction coefficient c_f is calculated using a Nikuradse wall-roughness height $k_N = 1$ mm. It was confirmed that the results were not very sensitive to the precise values of C_s and c_f , nor the magnitude of the inflow perturbations. For time stepping, the FS scheme is used with a time step $\Delta t = 0.01$ s. Being strongly stable, this scheme is ultimately suited to compute high frequency turbulent fluctuations in large

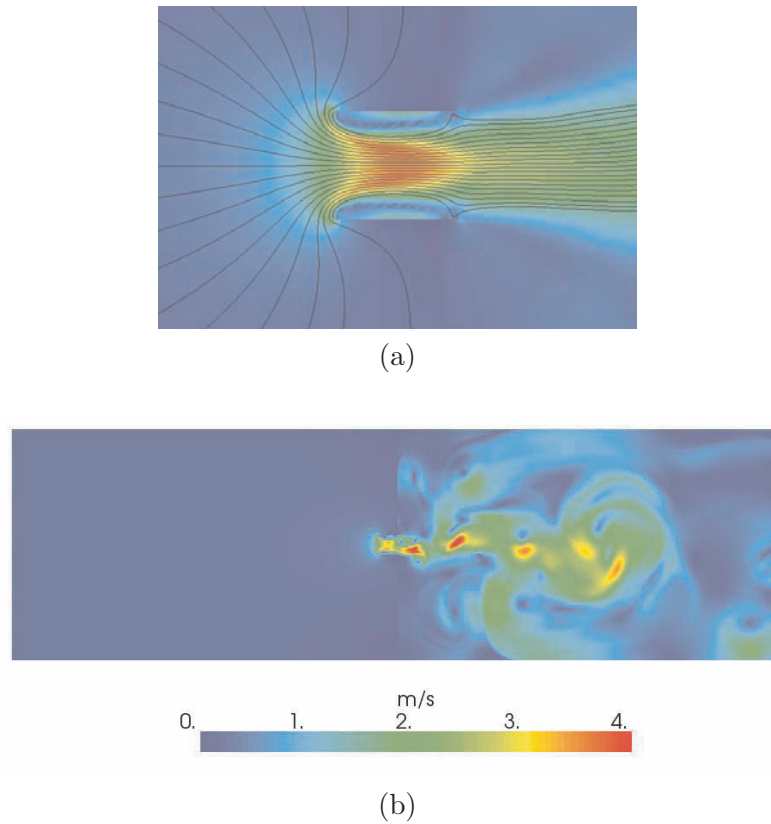


Figure 4.8: *Borda mouthpiece: (a) mean velocity magnitude and streamlines in the ‘vena contracta’ and (b) velocity magnitude instantaneous flow field.*

eddy simulations (LES) while rendering the solution stable [72]. The total simulation time is 150 s.

The computed flow fields are shown in Figure 4.8 while Figure 4.9 shows the computed mean velocity and mean pressure profiles in the mouthpiece. The mean quantities are obtained by averaging over 6000 time steps or, equivalently, 60 s. The computed maximum velocity in the *vena contracta* amounts 3.61 m/s corresponding to a contraction coefficient $\mu \approx 0.55$ which is close to the theoretical value $\mu = \frac{1}{2}$ while observed values of μ in experiments [31] range between 0.51 and 0.56. The computed normalized pressure drop over the mouthpiece corresponds to the theoretical value, see Figure 4.9b. Taking into account the actual velocity profile in the *vena contracta*, by integrating the computed momentum flux, the computed pressure drop satisfies the theoretical value $\Delta p = A^{-1} \int_A U^2 dA$, exactly. The computed pressure minimum at $x \approx 5$ m is due to a large eddy residing in the downstream reservoir, in front of the mouthpiece, see also Figure 4.8b.

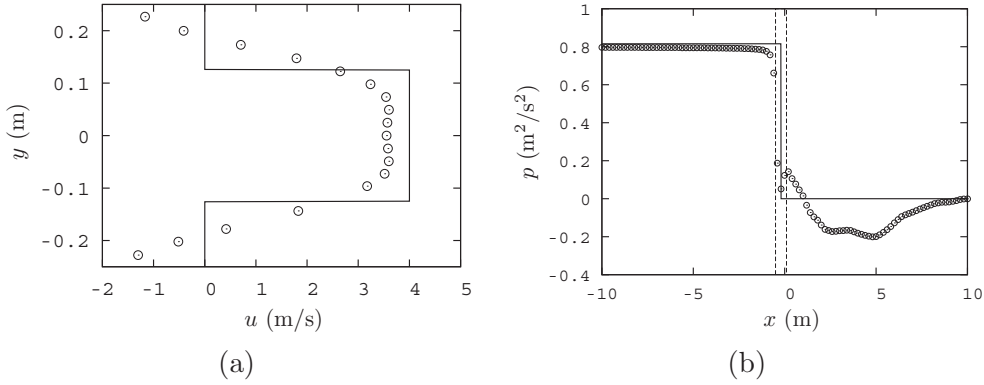


Figure 4.9: *Borda mouthpiece: (a) computed mean velocity profile in the ‘vena contracta’, $x = -0.25$ m, (circles) and corresponding theoretical velocity profile (solid); (b) computed mean normalized pressure (circles) and theoretical normalized pressure (solid) in center line $y = 0$, vertical transects indicate position mouthpiece.*

4.4.5 Internal waves

If the flow transports constituents of inhomogeneous density, the flow field and the advected density field will interact. This can be modelled by coupling the GIS transport model from Section 3.4 and the GIS model for the Navier-Stokes problem, the details of which are described in Appendix A.

Assuming small density deviations from a constant ‘reference’ density ρ_0 (Boussinesq approximation) and a uniform background velocity U , periodic, small-amplitude solutions of the vertical velocity component w satisfy the Taylor-Goldstein equation,

$$(U - c)^2 \frac{d^2 \tilde{w}}{dz^2} - \left(g \frac{d\rho^*}{dz} + \omega_r^2 \right) \tilde{w} = 0, \quad (4.95)$$

where z is the vertical coordinate, \tilde{w} is the complex amplitude of the vertical velocity component, g is gravitation, $\rho^* = (\rho - \rho_0) / \rho_0$ is the dimensionless relative density difference, c is the wave celerity and ω_r is the relative frequency as observed when moving with the velocity U [66]. Two cases will be considered, a standing wave in a closed basin and a stationary trapped wave.

4.4.5.1 Standing interfacial wave

Consider a two-layered fluid in a closed rectangular basin with vertical side walls, constant depth d and background velocity $U = 0$. At rest, the upper layer has a depth d_1 and relative density difference ρ_1^* and the lower layer has a depth $d_2 = d - d_1$ and relative density difference $\rho_2^* > \rho_1^*$. The two layers are separated by a thin interfacial layer of which the vertical elevation

is denoted ζ . The homogeneous solution of Equation (4.95) leads to the following expression for the interface elevation

$$\zeta_{mn} = A_{mn} \cos(k_m x) \cos(k_n y) \cos(\omega_{mn} t), \quad (4.96)$$

where $m, n = 0, 1, 2, \dots$, A_{mn} is the amplitude of the wave motion, k_m and k_n are horizontal wave numbers in x - and y -direction, respectively, and ω_{mn} is the corresponding radian frequency. The horizontal wave numbers are given by $k_m = m\pi/l_x$ and $k_n = n\pi/l_y$, where l_x and l_y are the horizontal dimensions of the basin in x - and y -direction, respectively. The frequency ω_{mn} is related to the wave number $k_{mn} = (k_m^2 + k_n^2)^{1/2}$ via the dispersion relation

$$\omega_{mn}^2 = (\rho_2^* - \rho_1^*) g k_{mn} \frac{\tanh(k_{mn} d_1) \tanh(k_{mn} d_2)}{\tanh(k_{mn} d_1) + \tanh(k_{mn} d_2)}. \quad (4.97)$$

The numerical example concerns a basin with $l_x = l_y = 20$ m, depths $d_1 = d_2 = 5$ m and relative density differences of $\rho_1^* = -0.01$ and $\rho_2^* = 0.01$. For $m = n = 1$ the eigen frequency $\omega_{11} = 0.1324$ rad/s which corresponds to an eigen period of $T_{11} = 47.46$ s. The initial position of the interface, denoted ζ_0 , is computed from Equation (4.96) setting $t = 0$ and $A_{11} = 0.75$ m. The initial relative density is prescribed according to

$$\rho^* = \frac{1}{2}(\rho_1^* + \rho_2^*) + \frac{1}{2}(\rho_1^* - \rho_2^*) \tanh\left(\frac{z - \zeta_0}{\Delta_i}\right), \quad (4.98)$$

where z is the vertical position and Δ_i is a measure of the interface width which in this simulation is set to 0.5 m. For the corresponding density profile an eigenmode analysis reveals that the eigenperiod equals $T_{11} = 50.78$ s. The domain is partitioned using regular tetrahedral elements with 30 elements in both horizontal directions and also 30 elements over the depth of the basin, see Figure 4.10. This gives 60 elements over one wavelength while the interface is captured in about 3 elements. The FS method is used for time stepping. The average time step size $\Delta t = 0.5$ s giving 95 time steps per wave period.

The computed position of the interface at time $t = 51.5$ s (maximum elevation) is shown in Figure 4.10. The configuration of the interface is resolved smoothly and corresponds to the exact solution given by Equation (4.96). Time series of the computed and analytical interface elevation at $(x, y) = (0, 0)$ are shown in Figure 4.11. The computed solution shows negligible amplitude damping. Initially, the phase error is small but the computed wave period gradually increases due to diffusion of the interface layer by the upwind mechanism. This artifact could be reduced by increasing the resolution in vertical direction which would however become prohibitive in most engineering applications. In this respect, the accurate computation of non-hydrostatic internal waves is far more demanding than the computation of non-hydrostatic free-surface waves, with a comparable water depth to wave length ratio, see also the examples in Section 5.5.1.

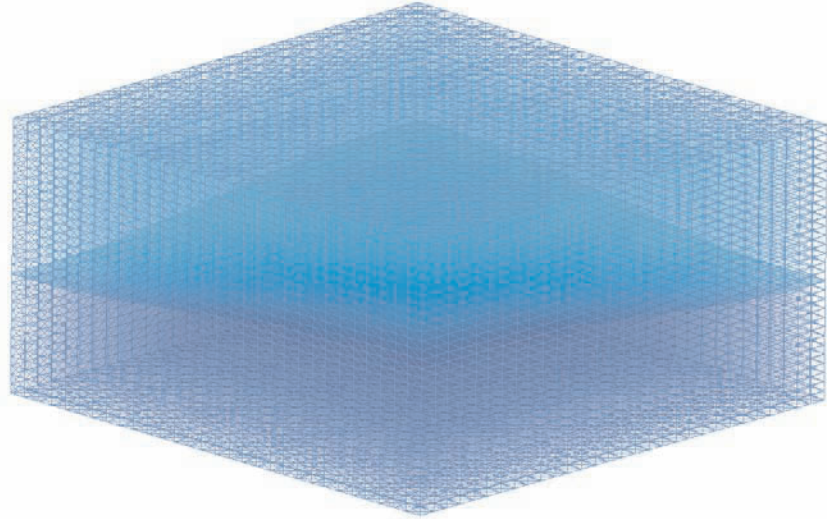


Figure 4.10: *Internal standing wave: mesh and computed interface position at $t = 51.5$ s (maximum elevation).*

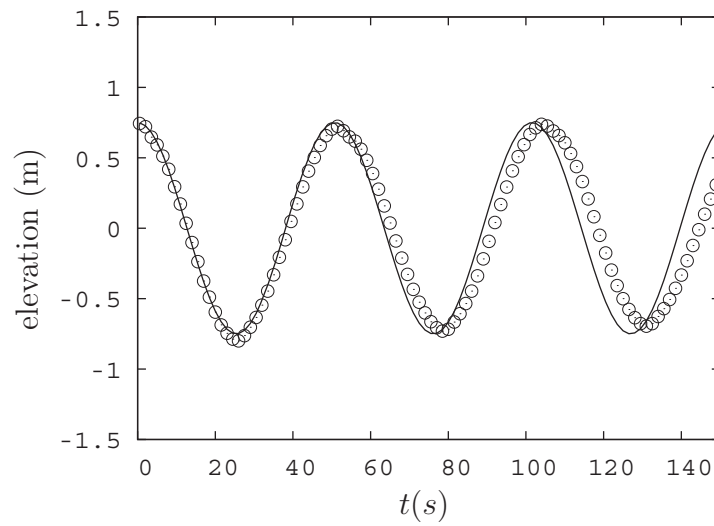


Figure 4.11: *Internal standing wave: interface elevation at $(x, y) = (0, 0)$, numerical solution (circles) and theoretical solution (solid).*

4.4.5.2 Trapped internal wave

A stably stratified flow over a non-uniform sea bed may feature stationary ‘trapped’ internal waves due to the vertical displacement of the fluid by the bed topography and the buoyant restoring forces. For a sinusoidal shape of the sea bed with amplitude a and wave number k_t , and assuming a linear density stratification, small-amplitude trapped-wave solutions for the vertical velocity component w are of the form

$$w = U k_t a \frac{\sin(\lambda z)}{\sin(\lambda d)} \sin(k_t x), \quad (4.99)$$

in which z is the vertical position with respect to the surface level, d is the undisturbed water depth and λ is defined by

$$\lambda^2 = -k^2 - \frac{g}{U^2} \frac{\partial \rho^*}{\partial z}, \quad (4.100)$$

where k is the wave number of the trapped internal wave [48]. Importantly, for cases where $\lambda = n\pi/d$, with $n = 0, 1, 2, \dots$, the solution for w given by Equation (4.99) becomes singular which is associated with resonance of the trapped waves. In an estuarine environment, with varying tidal flow velocities, the resonance conditions change during the tide leading to continuous generation and dispersion of trapped waves over the topography, the details of which are explained in Pietrzak and Labeur [66].

The numerical example concerns trapped waves having the same wave number as the topography, that is $k = k_t$. The computational domain has an undisturbed depth $d = 15$ m and a length of 800 m. In the center of the domain a series of 10 bed waves is present, with a wave length of 50 m and an amplitude of 0.15 m. The initial density field is uniform in the horizontal direction and linear in the vertical direction with a relative density difference $\Delta\rho^* = 0.01$ over the vertical. The domain is partitioned using regular triangular elements with an average horizontal element size of 2 m, which amounts to 25 elements per wave length, while the vertical element size is 0.5 m. At the bottom and at $z = 0$ a zero normal velocity and zero tangential stress are imposed. At the lateral boundaries the background velocity U is prescribed using values of 0.40 m/s, 0.15 m/s and 0.085 m/s, respectively, in order to obtain a range of trapped-wave modes. Reflection of travelling internal waves from the boundaries is suppressed by applying a flow relaxation scheme (sponge layer) over a 100 m wide section at both ends of the domain. A relaxation parameter of 0.1 s^{-1} is used. As the transient solution damps very slowly the horizontal viscosity and horizontal diffusivity are increased to $0.01 \text{ m}^2/\text{s}$ to accelerate convergence towards steady state which, using the backward Euler method and a time step size $\Delta t = 2$ s, requires about 5000 time steps.

The theoretical and computed fields of the vertical velocity are shown in Figure 4.12 for a 50 m wide section (one wave length) in the middle of

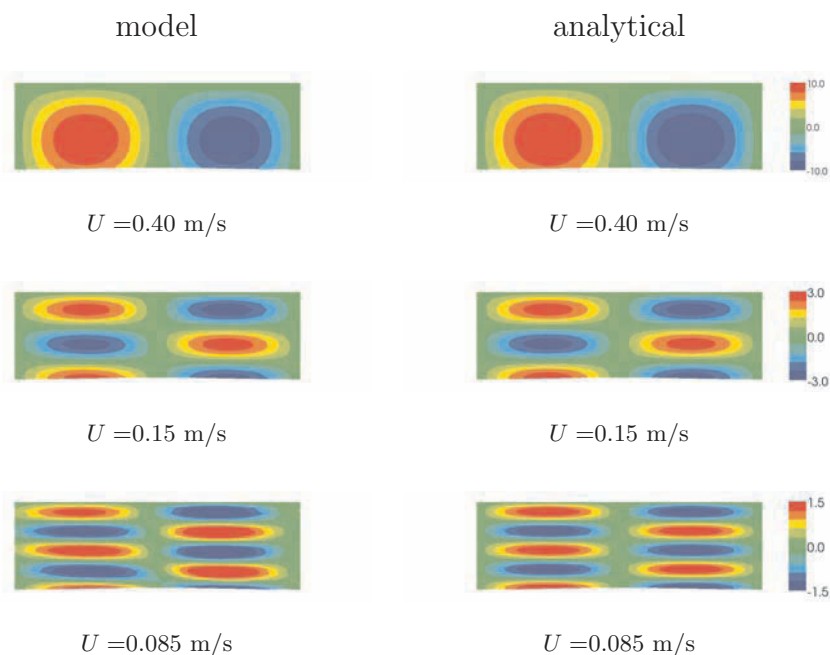


Figure 4.12: *Trapped internal wave: computed (left) and theoretical (right) solutions of the vertical velocity w (mm/s).*

the domain. The model results are in good agreement with the theoretical solution obtained from Equation (4.99). The effect of the added horizontal diffusivity is minimal in the sense that conventional upwinding of the fluxes would cause a much larger distortion of the solution, in particular of the higher wave-modes, which is demonstrated in Labeur and Pietrzak [49]. Practical situations primarily concern low mode internal waves and the example shows that a vertical resolution of 30 elements is generally sufficient in this case.

4.4.6 Practical application: current load on VLCC

Ships, when moored at an open jetty, at anchor or while slowly manoeuvring, may experience drag forces from ambient currents. For very large crude carriers (VLCC's) these current loads are difficult to handle by a fender system or by tugs. The Oil Companies International Marine Forum (OCIMF) has conducted experimental work to investigate these loads [64]. More specifically, the influence of the angle of the current and the influence of the keel-clearance were considered. Most relevant in this respect are the longitudinal and lateral drag forces F_x and F_y , respectively, and the yaw current

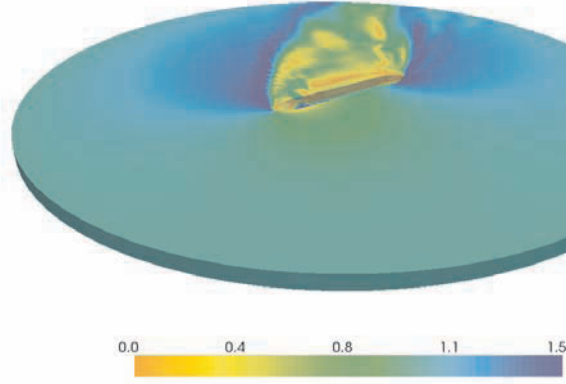


Figure 4.13: *Current load on VLCC: computed current velocity magnitude $|\bar{\mathbf{u}}|$ in m/s for $\varphi = 50^\circ$.*

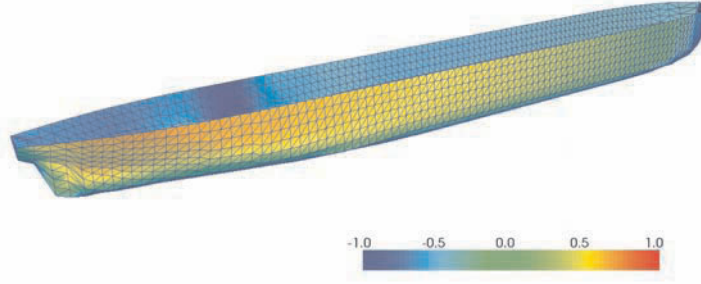


Figure 4.14: *Current load on VLCC: computed dimensionless non-hydrostatic pressure p_d/U^2 at ships' hull for $\varphi = 50^\circ$.*

moment M_{xy} which depend on the ambient current velocity U according to

$$F_x = \frac{1}{2} C_x \rho U^2 L_{BP} T, \quad (4.101)$$

$$F_y = \frac{1}{2} C_y \rho U^2 L_{BP} T, \quad (4.102)$$

$$M_{xy} = \frac{1}{2} C_{xy} \rho U^2 L_{BP}^2 T, \quad (4.103)$$

where ρ is the density of water, L_{BP} is the length of the vessel between perpendiculars, T is the draft of the vessel and C_x , C_y and C_{xy} are the drag and yaw moment coefficients, respectively [64]. The horizontal forces and the yaw moment are highly dependent on the keel-clearance factor $k = d/T$, where d is the water depth. The associated current load coefficients generally increase if k decreases due to the enhanced blockage by the ship which causes

the water to flow around rather than beneath the hull.

The computational example concerns a fully loaded VLCC without bulb and length $L_{BP} = 310$ m, width $B = 45$ m and draft $T = 20$ m. The water depth $d = 24$ m which yields a keel-clearance factor $k = 1.2$. The computations involve an ambient current velocity magnitude $U = 1$ m/s and current angles φ of 10° , 50° , 90° , 130° and 170° , respectively, using the OCIMF convention where a zero angle denotes a stern-on current. A three-dimensional mesh with a circular boundary of radius 600 m is used with the VLCC situated in the center, see Figure 4.13. The average element size $h_e \approx 3$ m near the hull and gradually increases towards the lateral boundary, yielding about 36,000 nodes and 240,000 tetrahedral elements. At the lateral boundary the ambient current velocity is specified, at the bottom and the surface a zero Neumann boundary condition is applied and at the ships' hull the tangential shear stress is imposed using a Nikuradse roughness-height $k_N = 0.02$ m, see Appendix B.1. The turbulence viscosity is modelled using a Smagorinsky-type formulation setting $C_s = 0.15$. It was confirmed that the computed results are not very sensitive to the precise value of the wall-roughness height nor the viscosity formulation. Using the backward Euler time stepping scheme with time step $\Delta t = 1$ s the simulation is run until quasi-steady state which takes approximately 2000 s.

Figures 4.13 and 4.14 show the computed velocity magnitudes around the VLCC and the pressure distribution on the hull for $\varphi = 50^\circ$. In accordance with theory, the maximum non-hydrostatic pressure on the hull equals the stagnation pressure $\Delta p_s = \frac{1}{2}U^2$. Table 4.2 summarizes the computed current load coefficients and measured values given in [39]. The coefficients are obtained from the model results by integrating the computed pressure force and momentum over the hull of the ship. Overall, the computed longitudinal and lateral drag force coefficients are in good agreement with the experimental results. The good correspondence of the yaw momentum coefficient indicates that the pressure distribution along the hull is computed accurately. In practice these results were used to predict current loads on slowly manoeuvring VLCC's in the Port of Rotterdam, also in situations with density stratification [46]. It was concluded that stratification may increase considerably the current drag coefficients.

4.5 Conclusion

In this chapter the interface stabilized finite element method has been extended to the incompressible Navier-Stokes problem. Analogous to the advection-diffusion problem, by using velocity basis functions which are discontinuous across element boundaries and interface velocity functions connecting elements, natural upwinding is incorporated into the formulation which stabilizes the advective-diffusive part of the momentum equa-

$\varphi :$		10°	50°	90°	130°	170°
C_x	model	0.00	0.11	0.04	0.07	0.01
	MARIN	0.01	0.08	0.04	0.10	0.01
C_y	model	0.23	1.36	2.05	1.50	0.27
	MARIN	0.35	1.51	2.02	1.47	0.41
C_{xy}	model	-0.10	-0.22	-0.01	0.19	0.10
	MARIN	-0.10	-0.32	-0.09	0.15	0.08

Table 4.2: *Current load on VLCC: comparison of computed and measured [39] longitudinal current force coefficient C_x , transverse current force coefficient C_y and current yaw moment coefficient C_{xy} ; zero angle denotes current stern-on; keel-clearance $k = 1.20$.*

tions. Moreover, by choosing a continuous pressure space, the formulation invokes a PSPG like pressure stabilization term without introducing double-degrees of freedom on element boundaries. Since functions on each element communicate only via the interface function the local degrees of freedom can be eliminated at the element level. This leads to a formulation with the same number of degrees of freedom as a regular continuous Galerkin method on the same mesh when using equal-order elements.

The performance of the method for the $P^1 - P^1$ element is demonstrated for steady and unsteady Stokes flow, Burgers' equations and for the steady and unsteady Navier-Stokes equations. The computed results demonstrate that the method provides stability, has good convergence properties and at the same time introduces minimal dissipation. In particular, the performance of the method near shocks is promising.

Chapter 5

Free-surface flow

Free-surface flow is basically governed by the Navier-Stokes equations treated in Chapter 4. It may be anticipated that the GIS method can be used as a solution procedure for problems with a free surface as well. However, the unconstrained movement of the free surface introduces some additional numerical issues. These mainly concern the formulation of free-surface boundary conditions, the adaptation of the mesh to the movement of the free surface and the representation of the momentum and continuity equations in a moving reference frame. Hence, the extension of the model to the case with moving free surfaces is not as straightforward as may seem in first instance. The developments of this chapter are presented in an arbitrary Lagrangian-Eulerian (ALE) framework which is a convenient way to describe fluid motion on deforming meshes¹.

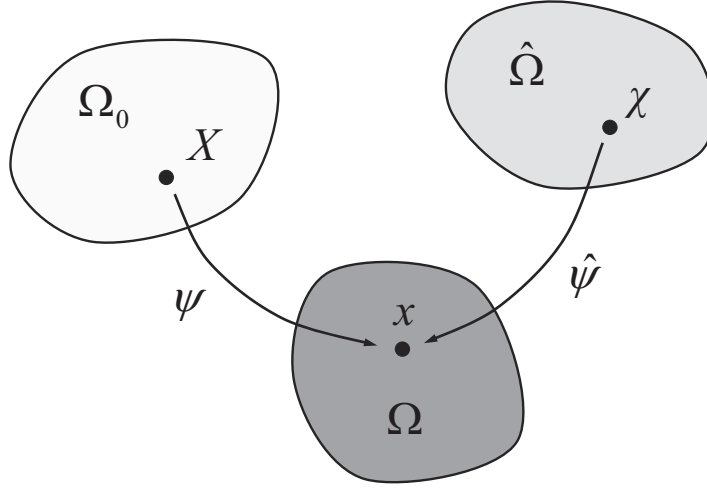
5.1 Moving domains

This section introduces some notation to describe the movement of the domain of interest Ω while it deforms under the action of the moving boundaries and free-surface dynamics. Of special concern is the description of functions defined in a reference domain $\hat{\Omega}$ associated with ‘the mesh’, and the transformation of conservation laws from the spatial domain onto the referential domain.

5.1.1 Kinematics

A fluid dynamics problem may be described in the spatial domain $\Omega \subset \mathbb{R}^d$, in the material domain $\Omega_0 \subset \mathbb{R}^d$, or in a reference domain $\hat{\Omega} \subset \mathbb{R}^d$. Points $\mathbf{x} \in \Omega$ are fixed in space and posing the flow problem in Ω leads to the

¹This chapter is partly based on: ‘Interface stabilised finite element method for moving domains and free surface flows’, Robert Jan Labeur and Garth N. Wells. In: *Computer Methods in Applied Mechanics and Engineering*, **198**, 615-630, 2009.

Figure 5.1: *Schematic illustration of mappings.*

Eulerian formulation of fluid dynamics. Points $\mathbf{X} \in \Omega_0$ are attached to fluid particles which leads to a Lagrangian description of the flow. Points $\boldsymbol{\chi} \in \hat{\Omega}$ finally, are labels connected to an arbitrary reference frame and the resulting formulation of the fluid flow is coined the arbitrary Eulerian-Lagrangian (ALE) method. The reference frame is associated with a finite element mesh which partially follows the fluid motion. In practice points \mathbf{X} and points $\boldsymbol{\chi}$ are chosen such that $\mathbf{X} = \boldsymbol{\chi} = \mathbf{x}$ at the initial time $t = t_0$. For arbitrary t material points \mathbf{X} are mapped to points \mathbf{x} via the transformation $\boldsymbol{\psi}$ which is defined by

$$\boldsymbol{\psi}: \mathbf{X} \rightarrow \mathbf{x} = \boldsymbol{\psi}(\mathbf{X}, t) \quad \forall \mathbf{X} \in \Omega_0, t \geq t_0, \quad (5.1)$$

and the mapping of a reference point $\boldsymbol{\chi}$ to a point \mathbf{x} is defined via the transformation $\hat{\boldsymbol{\psi}}$ defined by

$$\hat{\boldsymbol{\psi}}: \boldsymbol{\chi} \rightarrow \mathbf{x} = \hat{\boldsymbol{\psi}}(\boldsymbol{\chi}, t) \quad \forall \boldsymbol{\chi} \in \hat{\Omega}, t \geq t_0. \quad (5.2)$$

It will be assumed throughout that the maps $\boldsymbol{\psi}$ and $\hat{\boldsymbol{\psi}}$ are continuous and invertible. A schematic illustration of the various domains and the mappings $\boldsymbol{\psi}$ and $\hat{\boldsymbol{\psi}}$ is given in Figure 5.1.

The Jacobian \mathbf{F} of the transformation $\hat{\boldsymbol{\psi}}$ reads

$$\mathbf{F} = \nabla_{\boldsymbol{\chi}} \hat{\boldsymbol{\psi}} = \frac{\partial x_i}{\partial \chi_j}, \quad (5.3)$$

and the determinant of the Jacobian is denoted by J ,

$$J = \det(\mathbf{F}). \quad (5.4)$$

Infinitesimal volume elements $d\Omega$ and $d\hat{\Omega}$ on the spatial and reference domains, respectively, are related via

$$d\Omega = Jd\hat{\Omega}. \quad (5.5)$$

Infinitesimal surface elements $\mathbf{n} d\Gamma$ and $\hat{\mathbf{n}} d\hat{\Gamma}$ on the spatial and reference domains, respectively, are related via Nanson's relationship,

$$\mathbf{n} d\Gamma = J\mathbf{F}^{-T} \hat{\mathbf{n}} d\hat{\Gamma}, \quad (5.6)$$

where \mathbf{n} and $\hat{\mathbf{n}}$ are unit vectors normal to the respective surface elements and \mathbf{F}^{-T} denotes the inverse transpose of the Jacobian \mathbf{F} .

The Eulerian velocity \mathbf{u} of a material point \mathbf{X} is given by

$$\mathbf{u}(\mathbf{X}, t) = \frac{\partial \psi}{\partial t}, \quad (5.7)$$

and the Eulerian velocity $\hat{\mathbf{u}}$ of a reference point $\boldsymbol{\chi}$ is given by

$$\hat{\mathbf{u}}(\boldsymbol{\chi}, t) = \frac{\partial \hat{\psi}}{\partial t}. \quad (5.8)$$

In the context of finite element methods, $\hat{\mathbf{u}}$ is referred to as the 'mesh velocity'. The velocity \mathbf{c} of a material point relative to the mesh, which is the 'convective velocity', is defined as

$$\mathbf{c}(\mathbf{x}, t) = \mathbf{u} - \hat{\mathbf{u}}. \quad (5.9)$$

The 'referential material velocity' \mathbf{w} , is then defined by the following transformation

$$w_i = \frac{\partial x_i}{\partial \chi_j} c_j \quad \Rightarrow \quad \mathbf{w} = \mathbf{F}^{-1} \mathbf{c}, \quad (5.10)$$

which expresses the convective velocity in terms of the reference coordinates. When the reference domain coincides with the material domain $\mathbf{c} = \mathbf{w} = \mathbf{0}$, which is the Lagrangian limit, and when the reference domain is fixed in space $\mathbf{c} = \mathbf{w} = \mathbf{u}$ giving the Eulerian limit.

At the boundary the material velocity may be constrained by the presence of the boundary. At moving boundaries, denoted $\Gamma_s \subseteq \partial\Omega$, material points cannot cross the boundary, which is formally expressed by

$$\mathbf{u} \cdot \mathbf{n} = \hat{\mathbf{u}} \cdot \mathbf{n} \quad \text{on } \Gamma_s, \quad (5.11)$$

where \mathbf{n} is the outward unit normal vector to $\partial\Omega$. The expression 'moving boundary' will be used to describe both free surfaces and moving impermeable boundaries. From the definition of the convective velocity \mathbf{c} in Equation (5.9) the moving-boundary condition requires that

$$\mathbf{c} \cdot \mathbf{n} = 0 \quad \text{on } \Gamma_s. \quad (5.12)$$

Using Nanson's relationship, Equation (5.6), this condition may be equivalently restated as

$$\mathbf{w} \cdot \hat{\mathbf{n}} = 0 \quad \text{on } \hat{\Gamma}_s. \quad (5.13)$$

Equation (5.12) leads to a coupling between the material velocity and the mesh velocity. Yet, this leaves undetermined the motion of reference points parallel to the spatial boundary and the displacement of interior points. See also Section 5.1.3.

5.1.2 Transport theorem

The transformation of the Navier-Stokes equations onto the reference domain requires a reformulation of the transport equation in terms of referential quantities. From Equation (5.3), the spatial and referential gradients of a scalar function f are related by

$$\frac{\partial f}{\partial \chi_i} = \frac{\partial x_j}{\partial \chi_i} \frac{\partial f}{\partial x_j} \quad \Rightarrow \quad \nabla_\chi f = \mathbf{F}^T \nabla_x f, \quad (5.14)$$

where ∇_x and ∇_χ denote the gradient operators in the spatial and reference domains, respectively. From Equation (5.14) the following identities for spatial derivatives can be derived:

$$\nabla_x f = \mathbf{F}^{-T} \nabla_\chi f, \quad (5.15)$$

$$\nabla_x \mathbf{a} = (\nabla_\chi \mathbf{a}) \mathbf{F}^{-1}, \quad (5.16)$$

$$\nabla_x \cdot \boldsymbol{\sigma} = J^{-1} \nabla_\chi \cdot (J \boldsymbol{\sigma} \mathbf{F}^{-T}), \quad (5.17)$$

where \mathbf{a} is a vector and $\boldsymbol{\sigma}$ is a second-order tensor, see also Chadwick [13].

The relation between the referential and spatial time derivatives of a scalar function f is given by

$$\left. \frac{\partial f}{\partial t} \right|_\chi = \left. \frac{\partial f}{\partial t} \right|_x + \frac{\partial \hat{\psi}_j}{\partial t} \frac{\partial f}{\partial x_j}, \quad (5.18)$$

and the material and spatial time derivatives of f are related by

$$\left. \frac{\partial f}{\partial t} \right|_X = \left. \frac{\partial f}{\partial t} \right|_x + \frac{\partial \psi_j}{\partial t} \frac{\partial f}{\partial x_j}. \quad (5.19)$$

Subtraction and using Equation (5.15) to rewrite the spatial gradient and using the definition of \mathbf{w} in Equation (5.10), the Lagrangian (material) time derivative of f may be written as

$$\left. \frac{\partial f}{\partial t} \right|_X = \left. \frac{\partial f}{\partial t} \right|_\chi + \mathbf{w} \cdot \nabla_\chi f. \quad (5.20)$$

Equation (5.20) is the non-conservative form of the transport equation in the reference frame with the left hand side constituting the source term.

To obtain the conservative form of the transport equation, consider a control volume C which moves with the mesh velocity $\hat{\mathbf{u}}$. Applying Leibniz' rule of integration to the time derivative of the volume integral of f gives

$$\frac{d}{dt} \int_C f \, d\Omega = \int_C \left. \frac{\partial f}{\partial t} \right|_x d\Omega + \int_{\partial C} f \hat{\mathbf{u}} \cdot \mathbf{n} \, d\Gamma. \quad (5.21)$$

For a referential control volume \hat{C} moving with velocity $\hat{\mathbf{u}}$, Leibniz' rule yields

$$\frac{d}{dt} \int_{\hat{C}} Jf \, d\hat{\Omega} = \int_{\hat{C}} \left. \frac{\partial (Jf)}{\partial t} \right|_x d\hat{\Omega}. \quad (5.22)$$

Combining Equations (5.21) and (5.22) and using the divergence theorem, it can be deduced that

$$\left. \frac{\partial f}{\partial t} \right|_x = J^{-1} \left. \frac{\partial (Jf)}{\partial t} \right|_x - \nabla_x \cdot (f\hat{\mathbf{u}}). \quad (5.23)$$

Setting $f = 1$ in Equation (5.23) leads to an important identity,

$$\left. \frac{\partial J}{\partial t} \right|_x = J \nabla_x \cdot \hat{\mathbf{u}}, \quad (5.24)$$

which is the 'geometric' conservation law. Equation (5.23) may be regarded as the conservative form of Equation (5.18) since the volumetric changes induced by the transformation $\hat{\boldsymbol{\psi}}$ are preserved. In a similar way, for a control volume moving with the material velocity \mathbf{u} ,

$$\left. \frac{\partial f}{\partial t} \right|_x = J_0^{-1} \left. \frac{\partial (J_0 f)}{\partial t} \right|_X - \nabla_x \cdot (f\mathbf{u}), \quad (5.25)$$

in which J_0 denotes the Jacobian determinant of the map $\boldsymbol{\psi}$. Subtraction of Equation (5.23) from Equation (5.25), using the divergence theorem and Nanson's relation, the conservative form of the transport equation on the reference domain $\hat{\Omega}$ is obtained,

$$\frac{J}{J_0} \left. \frac{\partial (J_0 f)}{\partial t} \right|_X = \left. \frac{\partial (Jf)}{\partial t} \right|_x + \nabla_x \cdot (Jf\mathbf{w}). \quad (5.26)$$

Without loss of generality J_0 can be taken equal to the specific volume ρ^{-1} after which Equation (5.26) may be used to restate the Navier-Stokes problem on the reference domain. As an example, for $f = \rho$, the resulting mass balance equation reads

$$\left. \frac{\partial (J\rho)}{\partial t} \right|_x + \nabla_x \cdot (J\rho\mathbf{w}) = 0. \quad (5.27)$$

See also Scovazzi [79] for a detailed derivation of balance laws on reference configurations.

5.1.3 Construction of mappings

The mapping $\hat{\psi}$ involves the reconstruction of the position \mathbf{x} of interior points χ given the time dependent Eulerian position of the boundaries. Equivalently, the mesh velocity $\hat{\mathbf{u}}$ may be determined after which the nodal positions follow from Equation (5.8). It will be assumed here that the normal component of the mesh velocity at the boundary is specified, although finding the boundary movement is often a part of the solution process.

The determination of the interior mesh velocity from the boundary conditions requires interpolation techniques such as affine mapping or a simple smoothing procedure where $\hat{\mathbf{u}}$ is averaged, in some way, from the mesh velocities in surrounding points. Alternatively, a pseudo-elasticity problem may be solved in which the mesh movement is controlled by imposing stresses along the boundary Γ , see for instance Duarte et al. [21]. The problem is complicated by the fact that at moving boundaries, due to Equation (5.12), only the normal displacements are known while the tangential displacements can not be specified directly. This problem may be by-passed by releasing the tangential stress at the boundaries that would result from the deformation of the mesh. In general terms, the mapping problem can then be stated as: given the boundary condition $\hat{\mathbf{v}} \cdot \mathbf{n}$ on $\Gamma_s \times I$, where $I = (t_0, t_N)$ is the time interval of interest, find the mesh velocity $\hat{\mathbf{u}}$ such that

$$\nabla \cdot (\nabla \hat{\mathbf{u}} + \lambda \mathbf{I} \nabla \cdot \hat{\mathbf{u}}) = \mathbf{0} \quad \text{in } \Omega \times I, \quad (5.28)$$

$$\mathbf{n} \times (\nabla \hat{\mathbf{u}} + \lambda \mathbf{I} \nabla \cdot \hat{\mathbf{u}}) \mathbf{n} = \mathbf{0} \quad \text{on } \Gamma \times I, \quad (5.29)$$

$$\hat{\mathbf{u}} \cdot \mathbf{n} = \hat{\mathbf{v}} \cdot \mathbf{n} \quad \text{on } \Gamma_s \times I, \quad (5.30)$$

where \mathbf{I} is the second-order identity tensor and $\lambda \geq 0$ is a parameter to control the compression of the mesh. For cases with free surfaces, the mapping problem needs to be solved in conjunction with the flow problem as the latter provides the boundary condition $\hat{\mathbf{v}} \cdot \mathbf{n}$ on the free surface via the kinematic condition given by Equation (5.12).

The pseudo-elastic mesh deformation allows the nodes to move in all directions which renders the equations for the different components of $\hat{\mathbf{u}}$ fully coupled. Obviously, this complicates the ensuing discrete mapping problem. However, for flow problems involving truly multi-directional free-surface movement the coupled approach is necessary to prevent severe mesh distortion [21]. For the free-surface flows encountered here moderate, non-overturning surface displacements will be assumed, which allows a simplified approach where the mesh is moved in the vertical direction only. This will yield a significant reduction of Equations (5.28) and (5.29).

5.2 Incompressible flow on moving domains

The incompressible Navier-Stokes equations on a fixed spatial domain Ω have been given in Section 4.1. The problem is extended here to moving domains

with geophysical free-surface flows as a special class. The developments are presented on the reference domain, instead of on the more familiar and intuitive spatial domain. Since the reference domain is constant in time this avoids ambiguities with respect to the precise form of the time stepping scheme to be introduced later on.

5.2.1 General formulation

The Navier-Stokes equations can be formulated in the reference domain $\hat{\Omega}$ using the transformed transport equation given by Equation (5.26). For an incompressible flow the procedure simplifies considerably since the density ρ of a fluid particle remains constant. The continuity equation is then easily obtained by setting $f = 1$ in Equation (5.26). Setting $f = \mathbf{u}$ yields the momentum equations where the left hand side of Equation (5.26) constitutes the body force plus the divergence of the Cauchy stress tensor which is transformed using the identity given in Equation (5.17).

For a domain of interest $\hat{\Omega} \subset \mathbb{R}^d$, having a boundary $\partial\hat{\Omega}$ which is partitioned such that $\hat{\Gamma}_g \cup \hat{\Gamma}_h = \partial\hat{\Omega}$ and $\hat{\Gamma}_g \cap \hat{\Gamma}_h = \emptyset$, the resulting problem on the time interval $I = (t_0, t_N)$ reads: given the map $\hat{\psi} : \hat{\Omega} \times I \rightarrow \mathbb{R}^d$, a forcing term $\mathbf{f} : \hat{\Omega} \times I \rightarrow \mathbb{R}^d$, the boundary conditions $\mathbf{g} : \hat{\Gamma}_g \times I \rightarrow \mathbb{R}^d$ and $\hat{\mathbf{h}} : \hat{\Gamma}_h \times I \rightarrow \mathbb{R}^d$, and the initial velocity $\mathbf{u}_0 : \hat{\Omega} \rightarrow \mathbb{R}^d$, find the velocity \mathbf{u} and the normalized pressure p such that

$$\frac{\partial(J\mathbf{u})}{\partial t} + \nabla_{\chi} \cdot \hat{\boldsymbol{\sigma}} = \hat{\mathbf{f}} \quad \text{in } \hat{\Omega} \times I, \quad (5.31)$$

$$\hat{\boldsymbol{\sigma}} = J\mathbf{u} \otimes \mathbf{w} + \mathbf{P} \quad \text{in } \hat{\Omega} \times I, \quad (5.32)$$

$$\frac{\partial J}{\partial t} + \nabla_{\chi} \cdot (J\mathbf{w}) = 0 \quad \text{in } \hat{\Omega} \times I, \quad (5.33)$$

$$\mathbf{u} = \mathbf{g} \quad \text{on } \hat{\Gamma}_g \times I, \quad (5.34)$$

$$(\gamma J\mathbf{u} \otimes \mathbf{w} + \mathbf{P}) \hat{\mathbf{n}} = \hat{\mathbf{h}} \quad \text{on } \hat{\Gamma}_h \times I \quad (5.35)$$

$$\mathbf{w} \cdot \hat{\mathbf{n}} = 0 \quad \text{on } \hat{\Gamma}_s \times I, \quad (5.36)$$

$$\mathbf{u}(\chi, 0) = \mathbf{u}_0 \quad \text{in } \hat{\Omega}, \quad (5.37)$$

where the body force $\hat{\mathbf{f}} = J\mathbf{f}$, $\hat{\boldsymbol{\sigma}}$ is the total referential momentum flux, the product tensor $(\mathbf{u} \otimes \mathbf{w})_{ij} = u_i w_j$ and \mathbf{P} is analogous to the first Piola-Kirchhoff stress. It is assumed throughout that the forcing terms and boundary conditions possess sufficient regularity. The stress tensor \mathbf{P} is given by

$$\mathbf{P} = J\boldsymbol{\tau}\mathbf{F}^{-T}, \quad (5.38)$$

where $\boldsymbol{\tau}$ is the Cauchy stress,

$$\boldsymbol{\tau} = p\mathbf{I} - 2\nu\nabla_x^s \mathbf{u}, \quad (5.39)$$

in which \mathbf{I} is the second-order identity tensor, ν is the kinematic viscosity and $\nabla_x^s(\cdot)$ is the symmetric spatial gradient operator. On inflow boundaries, that is where $\mathbf{w} \cdot \hat{\mathbf{n}} < 0$, $\gamma = 1$ and on outflow boundaries, where $\mathbf{w} \cdot \hat{\mathbf{n}} \geq 0$, $\gamma = 0$. The use of the function γ implies that the total flux is prescribed on inflow portions of $\hat{\Gamma}_h$, and only the diffusive flux is prescribed on outflow portions of $\hat{\Gamma}_h$ [37]. More complex combinations of Dirichlet and Neumann boundary conditions can be specified in which different components of the velocity are subject to different boundary condition types [30]. Frequently, Dirichlet and Neumann boundary conditions are specified for the normal velocity and tangential stress, respectively, see also Section 4.1.

For simplicity, it is stated that the map $\hat{\psi}$ is explicitly given, although in many cases, such as free-surface flows, finding the map is part of the solution process.

5.2.2 Geophysical free-surface flows

Under certain conditions, which are typical for geophysical flows, the incompressible Navier-Stokes equations can be reformulated in terms of the piezometric level in place of the pressure. Such a reformulation is particularly convenient when employing a moving mesh as it will turn out that the location of the free surface is defined naturally then.

For a fluid of uniform density under the action of gravity in the $-\mathbf{e}_z$ direction, the body force due to gravity is of the form

$$\mathbf{f} = -g\mathbf{e}_z, \quad (5.40)$$

where g is the gravitational constant. The piezometric level η is related to the normalized pressure p via

$$p = p_a + g(\eta - z), \quad (5.41)$$

where p_a is the normalized atmospheric pressure. Physically, η is the height to which the pressure causes the fluid to rise in a column. For a spatially constant atmospheric pressure, the gravity body force and the pressure can be eliminated from the Navier-Stokes equations in favour of the piezometric level since after taking the gradient of Equation (5.41) and using Equation (5.40) the pressure gradient may be rewritten as

$$\nabla_x p = g\nabla_x \eta + \mathbf{f}. \quad (5.42)$$

Formulating a problem in terms of the piezometric level leads to an alternative expression for the Cauchy stress,

$$\boldsymbol{\tau} = g\eta\mathbf{I} - 2\nu\nabla_x^s \mathbf{u}. \quad (5.43)$$

Therefore, setting the source term $\mathbf{f} = \mathbf{0}$ and using Equation (5.43) in the definition of the flux and the flux boundary condition leads to a form

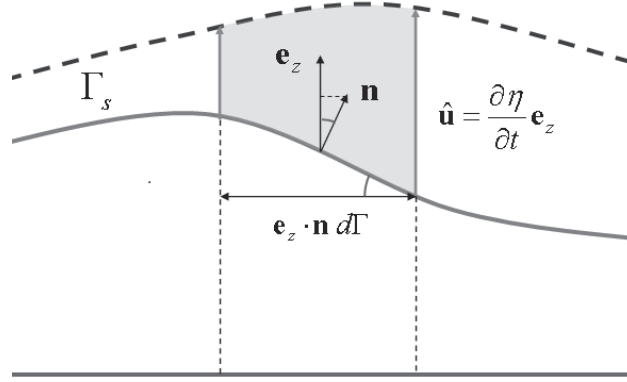


Figure 5.2: *Kinematic free-surface condition for vertical mesh motion.*

of the Navier-Stokes equations which is applicable for various geophysical free-surface flows. Other body forces, such as the Coriolis force, can still be considered in which case only the gravity effects are excluded from the source term \mathbf{f} while all other forcing terms are retained.

The normalized pressure at the free surface equals the atmospheric pressure p_a , which from Equation (5.41) leads to

$$\eta = z \quad \text{on } \Gamma_s. \quad (5.44)$$

The mesh velocity in the \mathbf{e}_z direction at the free surface is then given by

$$\hat{\mathbf{u}} \cdot \mathbf{e}_z = \left. \frac{\partial \eta}{\partial t} \right|_{\chi} \quad \text{on } \Gamma_s. \quad (5.45)$$

The motion of the free surface is therefore expressed compactly in terms of the piezometric head. If the mesh motion is restricted to the \mathbf{e}_z direction only, the free surface condition in Equation (5.11) can be rewritten as

$$\mathbf{u} \cdot \mathbf{n} = \left. \frac{\partial \eta}{\partial t} \right|_{\chi} \mathbf{e}_z \cdot \mathbf{n} \quad \text{on } \Gamma_s, \quad (5.46)$$

where the term $\mathbf{e}_z \cdot \mathbf{n}$ is the projection of a unit surface element onto the horizontal plane, see also Figure 5.2. For strictly vertical mesh motion this quantity remains constant in time and is hence determined by the initial configuration of the domain.

5.2.3 Dimensional scaling

This section considers the continuity equation in some more detail, in particular the free-surface boundary condition given by Equation (5.46). In

Section 4.1.3 it was shown that a flow problem with a reference length scale L_{ref} and a velocity scale U_{ref} , has a pressure scale P_{ref} given by

$$P_{\text{ref}} = U_{\text{ref}}^2 (1 + Re^{-1}), \quad (5.47)$$

where $Re = U_{\text{ref}}L_{\text{ref}}/\nu$ is the Reynolds number. Using Equation (5.41), which relates the pressure to the piezometric level, the corresponding scale of the piezometric level, denoted H_{ref} , is given by

$$H_{\text{ref}} = \frac{U_{\text{ref}}^2}{g} (1 + Re^{-1}), \quad (5.48)$$

from which the non-dimensional form of the momentum equations, given by Equations (5.31) and (5.32) can be obtained. Non-dimensionalization guarantees that all variables in the coupled set of equations have the same order of magnitude which, for the fully discrete problem, is a prerequisite to obtain convergence of the resulting algebraic solution across all Reynolds numbers [65].

The free-surface dynamics, introduced by the boundary condition for the continuity equation, leads to additional scaling arguments. To this end, non-dimensionalization of the free-surface boundary condition, Equation (5.46), gives

$$\frac{H_{\text{ref}}}{T_{\text{ref}}} \frac{\partial \eta^*}{\partial t^*} \Big|_{\chi} = U_{\text{ref}} \mathbf{u}^* \cdot \mathbf{n} \quad \text{on } \Gamma_s, \quad (5.49)$$

where the asterisks denote dimensionless quantities. Setting the reference time scale $T_{\text{ref}} = L_{\text{ref}}/U_{\text{ref}}$ and using Equation (5.48) for H_{ref} , this can be written as

$$Fr^2 (1 + Re^{-1}) \frac{\partial \eta^*}{\partial t^*} \Big|_{\chi} = \mathbf{u}^* \cdot \mathbf{n} \quad \text{on } \Gamma_s, \quad (5.50)$$

where $Fr = U_{\text{ref}}/\sqrt{gL_{\text{ref}}}$ denotes the Froude number. The length scale L_{ref} , used in the definition of Fr , can be related to the length of an object in the flow field or, in case of gravity-wave propagation, to the water depth. According to the dimensionless free-surface condition, the Froude number determines the order of magnitude of the surface movement relative to the remaining terms of the continuity equation. In this respect, for $Re \gg 1$ and $Fr \ll 1$, the surface movement is relatively weak and the dynamics associated with the mesh motion may be neglected. If on the other hand $Fr \geq \mathcal{O}(10^{-1})$ the surface dynamics will be appreciable and the full formulation of the moving domain problem is required.

Consideration of the Froude number is important when applying the boundary conditions. For surface-wave propagation, the condition $Fr < 1$ yields a sub-critical flow regime in which long, infinitely small perturbations of the free-surface will propagate in every direction. As a consequence, boundary conditions must be specified on the inflow as well as on the outflow boundaries of the domain. For $Fr > 1$ the flow is super-critical and

the disturbances propagate in downstream direction only. In this case, the boundary conditions can only be specified on the inflow portion of Γ .

5.3 Galerkin interface stabilization method

The developments in this section proceed along similar lines as for the incompressible Navier-Stokes equations of Chapter 4. New aspects are the moving domain and the associated free-surface boundary condition, which only require minor modifications to fit into the GIS systematic given in the previous chapter. Using the referential form of the Navier-Stokes equations, the resulting variational formulation naturally lends itself to a GIS treatment. Obviously, the referential form involves a constant domain of integration which is particularly appropriate when considering semi-discrete variational formulations.

5.3.1 General formulation

The reference domain $\hat{\Omega}$ is partitioned into disjoint elements $\hat{\Omega}_e$ having boundaries $\partial\hat{\Omega}_e$ on which $\hat{\mathbf{n}}$ denotes the outward unit normal vector. The elements intersect pairwise in interfaces $\hat{\Gamma}_i$. This defines the following unions

$$\tilde{\Omega} = \bigcup_e \hat{\Omega}_e, \quad (5.51)$$

$$\tilde{\Gamma} = \bigcup_i \hat{\Gamma}_i = \bigcup_e \partial\hat{\Omega}_e, \quad (5.52)$$

where $\tilde{\Gamma}$ is the union of element boundaries. In order to avoid notational clutter, $\tilde{\Omega}$ denotes the union of all elements, excluding element facets, and in the remainder integration over $\tilde{\Omega}$ implies the summation of all integrals over elements. On $\tilde{\Omega}$ a discontinuous velocity space \mathbf{V} and a continuous pressure space Q are defined by, respectively,

$$\mathbf{V} = \left\{ \mathbf{v} \in \mathbf{L}^2(\tilde{\Omega}), \quad \mathbf{v} \in \mathbf{P}^k(\hat{\Omega}_e) \quad \forall e \right\}, \quad (5.53)$$

$$Q = \left\{ q \in H^1(\tilde{\Omega}), \quad q \in P^l(\hat{\Omega}_e) \quad \forall e \right\}, \quad (5.54)$$

where \mathbf{P}^k and P^l denote the standard Lagrangian polynomial spaces on elements of degrees k and l , respectively, where $l > k \geq 0$. The spaces \mathbf{V} and Q are similar to the corresponding spaces from Section 4.2.2, except for the domains in which they are defined. Interestingly, on moving domains, switching from the spatial domain Ω to the reference domain $\hat{\Omega}$ leads to the convenient property that for any basis function the time derivative equals zero.

The general discontinuous weak formulation of the Navier-Stokes problem posed on $\tilde{\Omega}$, can be obtained directly from Equations (5.31) to (5.33).

Introducing, as before, an interface velocity $\bar{\mathbf{u}}: \tilde{\Gamma} \times I \rightarrow \mathbb{R}^d$ and a referential interface flux $\hat{\boldsymbol{\sigma}}: \tilde{\Gamma} \times I \rightarrow \mathbb{R}^d \times \mathbb{R}^d$, the procedure is essentially similar to that for the Navier-Stokes problem on the fixed spatial domain. Assuming that $\bar{\mathbf{u}}$ and $\hat{\boldsymbol{\sigma}}$ satisfy the Dirichlet and Neumann boundary conditions on $\hat{\Gamma}_g$ and $\hat{\Gamma}_h$, respectively, the resulting DG method reads: at time t , given the map $\hat{\boldsymbol{\psi}}: \tilde{\Omega} \times I \rightarrow \mathbb{R}^d$ and the source term $\mathbf{f}: \tilde{\Omega} \times I \rightarrow \mathbb{R}^d$, find $\mathbf{u} \in \mathbf{V}$ and $p \in Q$ such that

$$\begin{aligned} & \int_{\tilde{\Omega}} \frac{\partial(J\mathbf{u})}{\partial t} \cdot \mathbf{v} \, d\hat{\Omega} - \int_{\tilde{\Omega}} \hat{\boldsymbol{\sigma}}: \nabla_{\chi} \mathbf{v} \, d\hat{\Omega} + \sum_e \int_{\partial\hat{\Omega}_e} \hat{\boldsymbol{\sigma}} \hat{\mathbf{n}} \cdot \mathbf{v} \, d\hat{\Gamma} \\ & + \sum_e \int_{\partial\hat{\Omega}_e} 2\nu (\bar{\mathbf{u}} - \mathbf{u}) \cdot \mathbf{S}(\mathbf{v}) \hat{\mathbf{n}} \, d\hat{\Gamma} + \int_{\tilde{\Omega}} \frac{\partial J}{\partial t} q \, d\hat{\Omega} - \int_{\tilde{\Omega}} J \mathbf{w} \cdot \nabla_{\chi} q \, d\hat{\Omega} \\ & + \sum_e \int_{\partial\hat{\Omega}_e} J \bar{\mathbf{w}} \cdot \hat{\mathbf{n}} q \, d\hat{\Gamma} = \int_{\tilde{\Omega}} \hat{\mathbf{f}} \cdot \mathbf{v} \, d\hat{\Omega} \quad \forall \mathbf{v} \in \mathbf{V}, \forall q \in Q, \end{aligned} \quad (5.55)$$

where

$$\mathbf{S}(\mathbf{v}) = \frac{J}{2} \left[(\nabla_{\chi} \mathbf{v}) \mathbf{F}^{-1} + \mathbf{F}^{-T} (\nabla_{\chi} \mathbf{v})^T \right] \mathbf{F}^{-T} = J \nabla_x^s \mathbf{v} \mathbf{F}^{-T}. \quad (5.56)$$

The form of the referential flux $\hat{\boldsymbol{\sigma}}$ follows from Equation (5.32) and $\bar{\mathbf{w}} = \mathbf{F}^{-1} \bar{\mathbf{c}} = \mathbf{F}^{-1} (\bar{\mathbf{u}} - \hat{\mathbf{u}})$ is the referential material velocity on element interfaces. In standard DG methods the interface velocity $\bar{\mathbf{u}}$ and the interface flux $\hat{\boldsymbol{\sigma}}$ depend on the traces of \mathbf{u} and $\hat{\boldsymbol{\sigma}}$ on $\partial\hat{\Omega}_e$, respectively [1].

Following the general GIS procedure, the interface field $\bar{\mathbf{u}}$ is rendered an independent global variable, which is defined in a space $\bar{\mathbf{V}}$ on $\tilde{\Gamma}$ given by

$$\bar{\mathbf{V}} = \left\{ \bar{\mathbf{v}} \in \mathbf{H}^{1/2}(\tilde{\Gamma}), \quad \bar{\mathbf{v}} \in \mathbf{P}^m(\hat{\Gamma}_i) \quad \forall i \right\}, \quad (5.57)$$

where the fractional space $\mathbf{H}^{1/2}$ is the trace of $\mathbf{H}^1(\tilde{\Omega})$ on $\tilde{\Gamma}$ and \mathbf{P}^m is a set of Lagrange polynomial basis functions with polynomial order $m > 1$ defined on element interfaces. An associated subspace $\bar{\mathbf{V}}_g$ contains all functions in $\bar{\mathbf{V}}$ satisfying the Dirichlet boundary condition $\bar{\mathbf{v}} = \mathbf{g}$ on $\hat{\Gamma}_g$. The definition of $\bar{\mathbf{u}}$ renders the interface velocity $\bar{\mathbf{w}}$ single-valued on an element facet. As functions $q \in Q$ are also single-valued on a facet, terms containing $\bar{\mathbf{w}}$ in Equation (5.55) vanish on interior element interfaces. The continuity of $\bar{\mathbf{u}}$ does not yet imply that the interface flux is also single-valued at element facets since $\hat{\boldsymbol{\sigma}}$ not only depends on $\bar{\mathbf{u}}$ but also depends on the velocity \mathbf{u} in the adjacent element. Instead, continuity of $\hat{\boldsymbol{\sigma}}$ is imposed weakly in $\bar{\mathbf{V}}$ which is formally expressed as

$$\begin{aligned} \sum_e \int_{\partial\hat{\Omega}_e} \hat{\boldsymbol{\sigma}} \hat{\mathbf{n}} \cdot \bar{\mathbf{v}} \, d\hat{\Gamma} &= \int_{\hat{\Gamma}_h} (1 - \gamma) J (\bar{\mathbf{u}} \otimes \mathbf{w}) \hat{\mathbf{n}} \cdot \bar{\mathbf{v}} \, d\hat{\Gamma} + \int_{\hat{\Gamma}_h} \hat{\mathbf{h}} \cdot \bar{\mathbf{v}} \, d\hat{\Gamma} \\ &\quad \forall \bar{\mathbf{v}} \in \bar{\mathbf{V}}, \end{aligned} \quad (5.58)$$

where $\gamma = 1$ on inflow Neumann boundaries, that is where $\mathbf{w} \cdot \hat{\mathbf{n}} < 0$, and $\gamma = 0$ on outflow Neumann boundaries where $\mathbf{w} \cdot \hat{\mathbf{n}} \geq 0$.

Subtracting Equation (5.58) from Equation (5.55), and using the continuity of $\bar{\mathbf{w}}$ and q across element facets, the variational problem can be restated as: at time t , given the map $\hat{\psi}$, the source term \mathbf{f} , the boundary conditions $\mathbf{g} : \hat{\Gamma}_g \times I \rightarrow \mathbb{R}^d$ and $\hat{\mathbf{h}} : \hat{\Gamma}_h \times I \rightarrow \mathbb{R}^d$, find $\mathbf{u} \in \mathbf{V}$, $\bar{\mathbf{u}} \in \bar{\mathbf{V}}_g$ and $p \in Q$ such that

$$\begin{aligned} & \int_{\hat{\Omega}} \frac{\partial(J\mathbf{u})}{\partial t} \cdot \mathbf{v} \, d\hat{\Omega} - \int_{\hat{\Omega}} \hat{\boldsymbol{\sigma}} : \nabla_{\mathbf{x}} \mathbf{v} \, d\hat{\Omega} - \sum_e \int_{\partial\hat{\Omega}_e} \hat{\boldsymbol{\sigma}} \hat{\mathbf{n}} \cdot (\bar{\mathbf{v}} - \mathbf{v}) \, d\hat{\Gamma} \\ & + \sum_e \int_{\partial\hat{\Omega}_e} 2\nu (\bar{\mathbf{u}} - \mathbf{u}) \cdot \mathbf{S}(\mathbf{v}) \cdot \hat{\mathbf{n}} \, d\hat{\Gamma} + \int_{\hat{\Gamma}_h} (1 - \gamma) J(\bar{\mathbf{u}} \otimes \mathbf{w}) \hat{\mathbf{n}} \cdot \bar{\mathbf{v}} \, d\hat{\Gamma} \\ & \quad + \int_{\hat{\Omega}} \frac{\partial J}{\partial t} q \, d\hat{\Omega} - \int_{\hat{\Omega}} J \mathbf{w} \cdot \nabla_{\mathbf{x}} q \, d\hat{\Omega} + \int_{\hat{\Gamma}} J \bar{\mathbf{w}} \cdot \hat{\mathbf{n}} q \, d\hat{\Gamma} \\ & = \int_{\hat{\Omega}} \hat{\mathbf{f}} \cdot \mathbf{v} \, d\hat{\Omega} - \int_{\hat{\Gamma}_h} \hat{\mathbf{h}} \cdot \bar{\mathbf{v}} \, d\hat{\Gamma} \quad \forall \mathbf{v} \in \mathbf{V}, \forall \bar{\mathbf{v}} \in \bar{\mathbf{V}}, \forall q \in Q. \end{aligned} \quad (5.59)$$

It is useful to remind at this point some aspects of the above variational formulation. If the interface flux $\hat{\boldsymbol{\sigma}}$ is chosen such that its value on one side of an element facet does not depend on terms from the other side of the facet, the ‘local’ velocity field \mathbf{u} on an element is not linked directly to the velocity field on neighbouring elements. The velocities \mathbf{u} on neighbouring elements are linked via the ‘global’ interface function $\bar{\mathbf{u}}$ only. In practice, it is therefore possible to eliminate degrees of freedom corresponding to \mathbf{u} locally in the same way as the degrees of freedom associated with bubble functions are eliminated locally via static condensation. Only degrees of freedom corresponding to $\bar{\mathbf{u}}$ and p will therefore appear in a global system of equations. This avoids the common criticism of DG methods, compared to CG methods, that the double degrees of freedom at element facets lead to a dramatic increase in the computational cost, yet the momentum flux on element facets can be specially formulated, as is typical for DG methods.

The equivalence of variational Equation (5.59) with the GIS method for the Navier-Stokes equations on the spatial domain, given by Equation (4.25), can be shown by pushing Equation (5.59) forward to the spatial configuration. In the Eulerian limit ($\hat{\mathbf{u}} = \mathbf{0}$) the spatial equations are identical to those presented in Section 4.2. See also Labour and Wells [52].

5.3.2 Interface flux

It remains to complete the variational problem by defining the interface flux $\hat{\boldsymbol{\sigma}}$. Proceeding in a similar way as in Section 4.2.3, using the transformation rules for second-order tensors, the referential interface flux is defined

as

$$\hat{\boldsymbol{\sigma}} = \hat{\boldsymbol{\sigma}} + J \left[\gamma (\bar{\mathbf{u}} - \mathbf{u}) \otimes \tilde{\mathbf{c}} - \frac{\alpha}{h_e} \nu (\bar{\mathbf{u}} - \mathbf{u}) \otimes \mathbf{n} \right] \mathbf{F}^{-T} \quad \text{on } \partial\hat{\Omega}_e. \quad (5.60)$$

The interface velocity $\tilde{\mathbf{c}}$ is given by

$$\tilde{\mathbf{c}} = \min(\mathbf{c}^+ \cdot \mathbf{n}, \mathbf{c}^- \cdot \mathbf{n}) \mathbf{n}, \quad (5.61)$$

where \mathbf{c}^+ and \mathbf{c}^- are traces of the convective velocities on either side of an interface, α is a dimensionless penalty parameter and h_e is a measure of the element size in the spatial configuration. The term $\gamma = 1$ on inflow element facets, that is where $\tilde{\mathbf{c}} \cdot \mathbf{n} < 0$, and $\gamma = 0$ elsewhere, thereby upwinding the interface flux. The formulation for $\tilde{\mathbf{c}}$ in Equation (5.61) prevents singularities in case of source interfaces, that is where $\mathbf{c} \cdot \mathbf{n}^- < 0 < \mathbf{c}^+ \cdot \mathbf{n}$, or in case of sink interfaces, where $\mathbf{c}^- \cdot \mathbf{n} > 0 > \mathbf{c}^+ \cdot \mathbf{n}$. The diffusive part of the interface flux is constructed such that it reduces to an interior penalty-type term on the spatial domain [1]. The interface flux as a whole coincides with the interface flux on the spatial domain defined in Section 4.2.3. Defining a term $\hat{\boldsymbol{\beta}}$ according to

$$\hat{\boldsymbol{\beta}} = \mathbf{F}^{-1} \left(\gamma \tilde{\mathbf{c}} - \frac{\alpha}{h_e} \nu \mathbf{n} \right) = \gamma \tilde{\mathbf{w}} - \frac{\alpha}{h_e} \nu \mathbf{F}^{-1} \mathbf{n}, \quad (5.62)$$

where $\tilde{\mathbf{w}} = \mathbf{F}^{-1} \tilde{\mathbf{c}}$, the interface flux may be written compactly as

$$\hat{\boldsymbol{\sigma}} = \hat{\boldsymbol{\sigma}} + J (\bar{\mathbf{u}} - \mathbf{u}) \otimes \hat{\boldsymbol{\beta}} \quad \text{on } \partial\hat{\Omega}_e. \quad (5.63)$$

Owing to its definition, the quantity $\hat{\boldsymbol{\beta}} \cdot \hat{\mathbf{n}}$ is always negative at element boundaries.

Supplementing Equation (5.59) with the above definition of the flux, and setting $\bar{\mathbf{v}} = \mathbf{0}$ and $q = 0$, the GIS method leads to the following local problem: at time t , given the mapping $\hat{\boldsymbol{\psi}}$ and the forcing term $\hat{\mathbf{f}}$, find $\mathbf{u} \in \mathbf{V}$ such that

$$\begin{aligned} & \int_{\hat{\Omega}} \frac{\partial(J\mathbf{u})}{\partial t} \cdot \mathbf{v} \, d\hat{\Omega} + \int_{\hat{\Omega}} \nabla_{\chi} \cdot (J\mathbf{u} \otimes \mathbf{w}) \cdot \mathbf{v} \, d\hat{\Omega} + \int_{\hat{\Omega}} J\mathbf{F}^{-T} \nabla_{\chi} p \cdot \mathbf{v} \, d\hat{\Omega} \\ & - \int_{\hat{\Omega}} 2 \nabla_{\chi} \cdot [\nu \mathbf{S}(\mathbf{u})] \cdot \mathbf{v} \, d\hat{\Omega} + \sum_e \int_{\partial\hat{\Omega}_e} J \hat{\boldsymbol{\beta}} \cdot \hat{\mathbf{n}} (\bar{\mathbf{u}} - \mathbf{u}) \cdot \mathbf{v} \, d\hat{\Gamma} \\ & + \sum_e \int_{\partial\hat{\Omega}_e} 2\nu (\bar{\mathbf{u}} - \mathbf{u}) \cdot \mathbf{S}(\mathbf{v}) \hat{\mathbf{n}} \, d\hat{\Gamma} = \int_{\hat{\Omega}} \hat{\mathbf{f}} \cdot \mathbf{v} \, d\hat{\Omega} \quad \forall \mathbf{v} \in \mathbf{V}. \end{aligned} \quad (5.64)$$

With a view to later manipulations the regular flux term has been integrated by parts. The associated global problem is obtained by setting $\mathbf{v} = \mathbf{0}$

in Equation (5.59) and substituting the referential interface flux from Equation (5.63). The procedure yields: at time t , given the mapping $\hat{\boldsymbol{\psi}}$, find $\bar{\mathbf{u}} \in \bar{\mathbf{V}}_g$ and $q \in Q$, such that

$$\begin{aligned} & \sum_e \int_{\partial\hat{\Omega}_e} [J\mathbf{u} \otimes \mathbf{w} - 2\nu\mathbf{S}(\mathbf{u})] \hat{\mathbf{n}} \cdot \bar{\mathbf{v}} d\hat{\Gamma} + \sum_e \int_{\partial\hat{\Omega}_e} J\hat{\boldsymbol{\beta}} \cdot \hat{\mathbf{n}} (\bar{\mathbf{u}} - \mathbf{u}) \cdot \bar{\mathbf{v}} d\hat{\Gamma} \\ & - \int_{\hat{\Omega}} \frac{\partial J}{\partial t} q d\hat{\Omega} + \int_{\hat{\Omega}} J\mathbf{w} \cdot \nabla_{\chi} q d\hat{\Omega} - \int_{\hat{\Gamma}} J\bar{\mathbf{w}} \cdot \hat{\mathbf{n}} q d\hat{\Gamma} + \int_{\hat{\Gamma}} Jp\mathbf{F}^{-T} \hat{\mathbf{n}} \cdot \bar{\mathbf{v}} d\hat{\Gamma} \\ & - \int_{\hat{\Gamma}_h} (1 - \gamma) J(\mathbf{w} \cdot \hat{\mathbf{n}}) \bar{\mathbf{u}} \cdot \bar{\mathbf{v}} d\hat{\Gamma} = \int_{\hat{\Gamma}_h} \hat{\mathbf{h}} \cdot \bar{\mathbf{v}} d\hat{\Gamma} \quad \forall \bar{\mathbf{v}} \in \bar{\mathbf{V}}, \forall q \in Q. \end{aligned} \quad (5.65)$$

Due to the continuity of p and $\bar{\mathbf{v}}$ the pressure terms have canceled at interior element interfaces. Noteworthy to mention is the correspondence of the above referential format of the GIS method to the formulation on the fixed spatial domain described in the previous chapter.

For a geophysical free-surface flow the corresponding equations are obtained by setting $p = g\eta$ and $\mathbf{f} = \mathbf{0}$ in Equations (5.64) and (5.65), respectively. In particular, on free surfaces the kinematic boundary condition which is embedded in Equation (5.65) will read

$$\int_{\hat{\Gamma}_s} J\bar{\mathbf{w}} \cdot \hat{\mathbf{n}} q d\hat{\Gamma} = \int_{\hat{\Gamma}_s} J\mathbf{F}^{-1} \left(\frac{\partial \eta}{\partial t} \mathbf{e}_z - \hat{\mathbf{u}} \right) \cdot \hat{\mathbf{n}} q d\hat{\Gamma}, \quad (5.66)$$

using the free-surface kinematic boundary condition for vertical mesh motion, Equation (5.46).

5.3.3 Properties

This section considers various properties of the GIS variational formulation of free-surface Navier-Stokes flow given by Equation (5.59) with the interface flux according to Equation (5.63). A similar exercise has been performed in Chapter 4 for the fixed spatial domain and the analysis is continued here by considering the moving domain and free-surface issues.

5.3.3.1 Consistency

For sufficiently smooth functions, setting $\bar{\mathbf{v}} = \mathbf{0}$ and $q = 0$ in Equation (5.59) gives, after integration by parts,

$$\begin{aligned} & \int_{\hat{\Omega}} \left[\frac{\partial (J\mathbf{u})}{\partial t} + \nabla_{\chi} \cdot \hat{\boldsymbol{\sigma}} - \hat{\mathbf{f}} \right] \cdot \mathbf{v} d\hat{\Omega} + \sum_e \int_{\partial\hat{\Omega}_e} J\hat{\boldsymbol{\beta}} \cdot \hat{\mathbf{n}} (\bar{\mathbf{u}} - \mathbf{u}) \cdot \mathbf{v} d\hat{\Gamma} \\ & + \sum_e \int_{\partial\hat{\Omega}_e} 2\nu (\bar{\mathbf{u}} - \mathbf{u}) \cdot \mathbf{S}(\mathbf{v}) \hat{\mathbf{n}} d\hat{\Gamma} = 0 \quad \forall \mathbf{v} \in \mathbf{V}, \end{aligned} \quad (5.67)$$

which demonstrates consistency with the referential form of the momentum equation posed on a moving domain, given in Equation (5.31), and the

enforcement of $\bar{\mathbf{u}} = \mathbf{u}$ on $\hat{\Gamma}$. Setting then $\mathbf{v} = \mathbf{0}$, $q = 0$ and using $\bar{\mathbf{u}} = \mathbf{u}$ on $\hat{\Gamma}$ in Equation (5.59) gives

$$\begin{aligned} \int_{\partial\hat{\Omega}_e \setminus \hat{\Gamma}_h} \hat{\boldsymbol{\sigma}} \hat{\mathbf{n}} \cdot \bar{\mathbf{v}} \, d\hat{\Gamma} + \int_{\hat{\Gamma}_h} (\gamma J \mathbf{u} \otimes \mathbf{w} + \mathbf{P}) \hat{\mathbf{n}} \cdot \bar{\mathbf{v}} \, d\hat{\Gamma} \\ = \int_{\hat{\Gamma}_h} \hat{\mathbf{h}} \cdot \bar{\mathbf{v}} \, d\hat{\Gamma} \quad \forall \bar{\mathbf{v}} \in \bar{\mathbf{V}}, \end{aligned} \quad (5.68)$$

which implies continuity of the referential flux between subdomains and satisfaction of the Neumann boundary condition given by Equation (5.35).

For $\mathbf{v} = \mathbf{0}$, $\bar{\mathbf{v}} = \mathbf{0}$ and smooth functions \mathbf{u} , partial integration of Equation (5.59) leads to

$$\int_{\hat{\Omega}} \left[\frac{\partial J}{\partial t} + \nabla_{\chi} \cdot (J \mathbf{w}) \right] q \, d\hat{\Omega} = \int_{\hat{\Gamma}} J (\mathbf{w} - \bar{\mathbf{w}}) \cdot \hat{\mathbf{n}} q \, d\hat{\Gamma} \quad \forall q \in Q, \quad (5.69)$$

which is consistent with the strong form of the continuity constraint posed on the reference domain, given in Equation (5.33), and the enforcement of $\mathbf{w} = \bar{\mathbf{w}}$ on $\hat{\Gamma}$. Setting $\bar{\mathbf{w}} = \mathbf{w}$ on $\hat{\Gamma}_s$ in the surface boundary condition Equation (5.66) leads to

$$\int_{\hat{\Gamma}_s} J \mathbf{F}^{-1} \left(\frac{\partial \eta}{\partial t} \mathbf{e}_z - \mathbf{u} \right) \cdot \hat{\mathbf{n}} q \, d\hat{\Gamma} = 0 \quad \forall q \in Q, \quad (5.70)$$

which, by Nanson's relation, implies the strong form of the kinematic free-surface boundary condition for vertical mesh movement, Equation (5.46).

5.3.3.2 Volume conservation

Setting $\mathbf{v} = \mathbf{0}$, $\bar{\mathbf{v}} = \mathbf{0}$ and $q = 1$ in the general GIS formulation given by Equation (5.59) leads to

$$\int_{\hat{\Omega}} \frac{\partial J}{\partial t} \, d\hat{\Omega} + \int_{\hat{\Gamma}} J \bar{\mathbf{w}} \cdot \hat{\mathbf{n}} \, d\hat{\Gamma} = 0. \quad (5.71)$$

Pushing forward to Ω ,

$$\frac{d}{dt} \int_{\Omega} d\Omega + \int_{\Gamma} (\bar{\mathbf{u}} - \hat{\mathbf{u}}) \cdot \mathbf{n} \, d\Gamma = 0, \quad (5.72)$$

reveals that the total volume change equals the net inward convective flow over the boundary, thereby proving volume conservation. The replacement of $\bar{\mathbf{w}}$ on $\hat{\Gamma}_s$ in Equation (5.71), by using the kinematic free-surface condition for vertical mesh motion from Equation (5.66), and applying the divergence theorem on the boundary terms containing $\hat{\mathbf{u}}$ leads to

$$\begin{aligned} \int_{\hat{\Omega}} \left[\frac{\partial J}{\partial t} - J \nabla_x \cdot \hat{\mathbf{u}} \right] \, d\hat{\Omega} + \int_{\hat{\Gamma} \setminus \hat{\Gamma}_s} J \mathbf{F}^{-1} \bar{\mathbf{u}} \cdot \hat{\mathbf{n}} \, d\hat{\Gamma} \\ + \int_{\hat{\Gamma}_s} J \mathbf{F}^{-1} \frac{\partial \eta}{\partial t} \mathbf{e}_z \cdot \hat{\mathbf{n}} \, d\hat{\Gamma} = 0. \end{aligned} \quad (5.73)$$

By virtue of the geometric conservation law, Equation (5.24), the first integral in Equation (5.73) vanishes and the push-forward to the spatial domain Ω gives

$$\int_{\Gamma \setminus \Gamma_s} \bar{\mathbf{u}} \cdot \mathbf{n} \, d\Gamma + \frac{d}{dt} \int_{\Gamma_s} \eta(\mathbf{e}_z \cdot \mathbf{n}) \, d\Gamma = 0. \quad (5.74)$$

The term $\mathbf{e}_z \cdot \mathbf{n} \, d\Gamma$ projects a free-surface element onto the horizontal plane. This projection remains constant for strictly vertical mesh motion. The associated surface integral then gives the volumetric change due to the surface displacement which, as stated by Equation (5.74), equals the net inflow over the remaining part of the boundary. Obviously, for the case where $\Gamma_s = \emptyset$, Equation (5.74) shows that the net inward flow velocity over the boundary equals zero which is an equivalent statement of volume conservation.

5.3.3.3 Momentum conservation

For the pure Neumann problem, i.e. $\hat{\Gamma}_g = \emptyset$, global conservation of linear momentum can be proven by setting $\mathbf{v} = \mathbf{e}_j$, $\bar{\mathbf{v}} = \mathbf{e}_j$ and $q = 0$ in Equation (5.59) which yields

$$\begin{aligned} \frac{d}{dt} \int_{\hat{\Omega}} J \mathbf{u} \cdot \mathbf{e}_j \, d\hat{\Omega} &= \int_{\hat{\Omega}} \hat{\mathbf{f}} \cdot \mathbf{e}_j \, d\hat{\Omega} \\ &\quad - \int_{\hat{\Gamma}_h} (1 - \gamma) J(\mathbf{w} \cdot \hat{\mathbf{n}}) \bar{\mathbf{u}} \cdot \mathbf{e}_j \, d\hat{\Gamma} - \int_{\hat{\Gamma}_h} \hat{\mathbf{h}} \cdot \mathbf{e}_j \, d\hat{\Gamma}. \end{aligned} \quad (5.75)$$

Pushing forward to Ω ,

$$\begin{aligned} \frac{d}{dt} \int_{\Omega} \mathbf{u} \cdot \mathbf{e}_j \, d\Omega &= \int_{\Omega} \mathbf{f} \cdot \mathbf{e}_j \, d\Omega \\ &\quad - \int_{\Gamma_h} (1 - \gamma) (\mathbf{c} \cdot \mathbf{n}) \bar{\mathbf{u}} \cdot \mathbf{e}_j \, d\Gamma - \int_{\Gamma_h} \mathbf{h} \cdot \mathbf{e}_j \, d\Gamma, \end{aligned} \quad (5.76)$$

reveals that the global change of momentum is balanced by the net inward momentum flux over the boundary and the total body force. For Dirichlet boundary conditions, the proof is more complicated as it is not possible to set $\bar{\mathbf{v}} = \mathbf{e}_j$ on $\hat{\Gamma}_g$. By defining an auxiliary flux on $\hat{\Gamma}_g$ the problem can be circumvented and global conservation can be demonstrated [37].

For local conservation, considering Equation (5.59) with $q = 0$, $\bar{\mathbf{v}} = \mathbf{0}$, $\mathbf{v} = \mathbf{e}_j$ on $\hat{\Omega}_e$ and $\mathbf{v} = \mathbf{0}$ on $\hat{\Omega} \setminus \hat{\Omega}_e$ results in

$$\frac{d}{dt} \int_{\hat{\Omega}_e} J \mathbf{u} \cdot \mathbf{e}_j \, d\hat{\Omega} = \int_{\hat{\Omega}_e} \hat{\mathbf{f}} \cdot \mathbf{e}_j \, d\hat{\Omega} - \int_{\partial \hat{\Omega}_e} \hat{\boldsymbol{\sigma}} \hat{\mathbf{n}} \cdot \mathbf{e}_j \, d\hat{\Gamma}. \quad (5.77)$$

The push-forward to the spatial domain Ω ,

$$\frac{d}{dt} \int_{\Omega_e} \mathbf{u} \cdot \mathbf{e}_j \, d\Omega = \int_{\Omega_e} \mathbf{f} \cdot \mathbf{e}_j \, d\Omega - \int_{\partial \Omega_e} \bar{\boldsymbol{\sigma}} \mathbf{n} \cdot \mathbf{e}_j \, d\Gamma, \quad (5.78)$$

proves local conservation of linear momentum in terms of the numerical flux $\bar{\sigma}$ on $\partial\Omega_e$. Yet, it has to be reminded that this flux is only weakly continuous across element boundaries.

5.3.3.4 Energy conservation

Next, energy conservation is considered for the inviscid case which highlights the stabilizing mechanism for advection dominated problems. In the diffusive limit the analysis is similar to that on the fixed spatial domain and a reference is made to Section 4.2.4. For a pure Neumann problem and in the absence of body forces, subtracting Equations (5.65) from Equation (5.64), setting $\nu = 0$, $\mathbf{v} = \mathbf{u}$, $\bar{\mathbf{v}} = \bar{\mathbf{u}}$ and $q = p$ results in

$$\begin{aligned} & \int_{\hat{\Omega}} \frac{\partial(J\mathbf{u})}{\partial t} \cdot \mathbf{u} d\hat{\Omega} + \int_{\hat{\Omega}} \nabla_{\chi} \cdot (J\mathbf{u} \otimes \mathbf{w}) \cdot \mathbf{u} d\hat{\Omega} \\ & - \sum_e \int_{\partial\hat{\Omega}_e} J(\mathbf{w} \cdot \hat{\mathbf{n}}) \mathbf{u} \cdot \bar{\mathbf{u}} d\hat{\Gamma} - \sum_e \int_{\partial\hat{\Omega}_e} \gamma J(\tilde{\mathbf{w}} \cdot \hat{\mathbf{n}}) |\bar{\mathbf{u}} - \mathbf{u}|^2 d\hat{\Gamma} \\ & + \int_{\hat{\Gamma}_h} (1 - \gamma) J(\mathbf{w} \cdot \hat{\mathbf{n}}) |\bar{\mathbf{u}}|^2 d\hat{\Gamma} = - \int_{\hat{\Gamma}_h} \hat{\mathbf{h}} \cdot \bar{\mathbf{u}} d\hat{\Gamma}, \quad (5.79) \end{aligned}$$

where $\tilde{\mathbf{w}} = \mathbf{F}^{-1}\tilde{\mathbf{c}}$ and strict geometric conservation has been assumed. Applying integration by parts to the advection term over $\hat{\Omega}$ and reformulating the time derivative leads to

$$\begin{aligned} & \frac{d}{dt} \int_{\hat{\Omega}} \frac{1}{2} J |\mathbf{u}|^2 d\hat{\Omega} + \int_{\hat{\Omega}} \frac{1}{2} |\mathbf{u}|^2 \left[\frac{\partial J}{\partial t} + \nabla_{\chi} \cdot (J\mathbf{w}) \right] d\hat{\Omega} \\ & - \sum_e \int_{\partial\hat{\Omega}_e \setminus \hat{\Gamma}_h} \frac{1}{2} J |\bar{\mathbf{u}}|^2 \mathbf{w} \cdot \hat{\mathbf{n}} d\hat{\Gamma} + \sum_e \int_{\partial\hat{\Omega}_e} J |\bar{\mathbf{u}} - \mathbf{u}|^2 \left(\frac{1}{2} \mathbf{w} - \gamma \tilde{\mathbf{w}} \right) \cdot \hat{\mathbf{n}} d\hat{\Gamma} \\ & + \int_{\hat{\Gamma}_h} \frac{1}{2} J |\bar{\mathbf{u}}|^2 |\mathbf{w} \cdot \hat{\mathbf{n}}| d\hat{\Gamma} = - \int_{\hat{\Gamma}_h} \hat{\mathbf{h}} \cdot \bar{\mathbf{u}} d\hat{\Gamma}. \quad (5.80) \end{aligned}$$

The first term in Equation (5.80) is the time derivative of the total kinetic energy. If the vector field \mathbf{w} satisfies the continuity constraint Equation (5.33) point-wise, all remaining integrals in Equation (5.80) are non-negative in which case the total kinetic energy cannot increase and will generally decrease. The dissipative mechanism stems from the upwinding of the momentum flux at the element facets and is determined partly by the difference between the velocity field \mathbf{u} and the interface function $\bar{\mathbf{u}}$, and partly by the referential velocity \mathbf{w} at element facets. As the discrete field \mathbf{w} satisfies the continuity equation only in a weak sense, monotonic energy decay is not guaranteed for the homogeneous Neumann problem. This deficiency may be circumvented by adding correction terms rendering the discrete advection operator skew-symmetric [28]. A monotonic energy decay does not yet prove stability of the GIS method as stability requires

the satisfaction of an inf – sup condition, the proof of which is not pursued here. For the $P^1 - P^1$ element a stabilizing mechanism is present which is closely related to that of the PSPG method and the MINI-element, see also Section 4.3.4.

For a free-surface problem in which the pressure is replaced by the piezometric head, the Neumann boundary condition on the free surface reads $\hat{\mathbf{h}} = Jg\eta\mathbf{F}^{-T}\hat{\mathbf{n}}$. Setting $\hat{\mathbf{h}} = \mathbf{0}$ on $\hat{\Gamma}_h \setminus \hat{\Gamma}_s$, the surface integral on the right hand side of Equation (5.80) reads

$$\int_{\hat{\Gamma}_h} \hat{\mathbf{h}} \cdot \bar{\mathbf{u}} \, d\hat{\Gamma} = \int_{\hat{\Gamma}_s} Jg\eta\mathbf{F}^{-T}\hat{\mathbf{n}} \cdot \bar{\mathbf{u}} \, d\hat{\Gamma}. \quad (5.81)$$

Pushing forward to the spatial domain, using the free-surface boundary condition for vertical mesh movement given by Equation (5.46) and Nanson's relation, gives

$$\int_{\hat{\Gamma}_s} Jg\eta\mathbf{F}^{-T}\hat{\mathbf{n}} \cdot \bar{\mathbf{u}} \, d\hat{\Gamma} = \int_{\Gamma_s} g\eta \frac{\partial \eta}{\partial t} (\mathbf{n} \cdot \mathbf{e}_z) \, d\Gamma. \quad (5.82)$$

Since the term $\mathbf{n} \cdot \mathbf{e}_z \, d\Gamma$ remains constant for strictly vertical mesh motion, Equation (5.81) may finally be restated as

$$\int_{\hat{\Gamma}_h} \hat{\mathbf{h}} \cdot \bar{\mathbf{u}} \, d\hat{\Gamma} = \frac{d}{dt} \int_{\Gamma_s} \frac{1}{2} g\eta^2 (\mathbf{n} \cdot \mathbf{e}_z) \, d\Gamma, \quad (5.83)$$

which represents the time derivative of the global potential energy. Therefore, in the case of free-surface flows, the sum of the global kinetic and potential energy will decrease monotonically for point-wise satisfaction of the continuity constraint and in the absence of forcing terms. For small-amplitude wave motion, the advection terms in Equation (5.80) are negligible and the sum of the total kinetic and potential energy is conserved, as will be demonstrated by an example in Section 5.5.1.

5.4 The fully-discrete problem

Rather than solving for all unknown fields simultaneously, a fractional-step algorithm is formulated to decouple the momentum and continuity equations. Problems are considered for which the domain update is either given or is computed explicitly using known data.

5.4.1 Fractional-step formulation

For time stepping a partitioning $I = (t_0, t_1, \dots, t_{N-1}, t_N)$ is used which defines the sub-intervals $I_n = (t_n, t_{n+1})$ and time step sizes $\Delta t = t_{n+1} - t_n$. The domain motion is often dependent on the flow field which complicates

the solution procedure. This difficulty is by-passed by solving first the discrete flow problem on sub-interval I_n with the required mapping $\hat{\psi}_n \rightarrow \hat{\psi}_{n+1}$ determined explicitly from the known mesh velocity at time t_n ,

$$\hat{\psi}_{n+1} = \hat{\psi}_n + \hat{\mathbf{u}}_n \Delta t. \quad (5.84)$$

The above definition implies that $\hat{\mathbf{u}}$ is piecewise constant in time. Once $\hat{\psi}_{n+1}$ has been computed, J_{n+1} and \mathbf{F}_{n+1} can be evaluated. Also, a term J_{n+1}^* is defined which is computed ‘consistently’ with the mesh velocity,

$$J_{n+1}^* = J_n + \Delta t \nabla_\chi \cdot (J_n \mathbf{F}_n^{-1} \hat{\mathbf{u}}_n) = J_n + \Delta t J_n \nabla_x \cdot \hat{\mathbf{u}}_n. \quad (5.85)$$

The use of this term will prove crucial in satisfying particular conservation principles. It is assumed that $\hat{\psi}_{n+1}$ is affine on elements, implying linear triangles or tetrahedral elements for defining the mesh displacement.

Next, the discrete flow problem can be solved on I_n for which the fully-coupled scheme from Section 4.3.3 could be used. In case of a moving domain it is however more convenient to solve the momentum equations and the continuity constraint separately in two consecutive steps. An advantage of this so-called predictor-corrector scheme is the reduced computational effort relative to the fully-coupled scheme. In the first step an intermediate flow field \mathbf{u}_{n+1}^* is computed from Equations (5.64) and (5.65) using the explicitly known pressure p_n . The resulting predictor step reads: given the mapping $\hat{\psi}_n \rightarrow \hat{\psi}_{n+1}$, the forcing term $\mathbf{f}_{n+\theta}$, the boundary condition $\mathbf{h}_{n+\theta}$, the velocities $\mathbf{u}_n \in \mathbf{V}$ and $\bar{\mathbf{u}}_n \in \bar{\mathbf{V}}_g$, and the pressure $p_n \in Q$, find the intermediate velocity $\mathbf{u}_{n+1}^* \in \mathbf{V}$ and the velocity $\bar{\mathbf{u}}_{n+1} \in \bar{\mathbf{V}}_g$ such that

$$\begin{aligned} & \int_{\hat{\Omega}} \frac{J_{n+1}^* \mathbf{u}_{n+1}^* - J_n \mathbf{u}_n}{\Delta t} \cdot \mathbf{v} \, d\hat{\Omega} + \int_{\hat{\Omega}} \nabla_\chi (J_n \mathbf{u}_{n+\theta} \otimes \mathbf{w}_n) \cdot \mathbf{v} \, d\hat{\Omega} \\ & \quad + \int_{\hat{\Omega}} J_n \mathbf{F}_n^{-T} \nabla_\chi p_n \cdot \mathbf{v} \, d\hat{\Omega} - \int_{\hat{\Omega}} 2 \nabla_\chi [\nu \mathbf{S}_n(\mathbf{u}_{n+\theta})] \cdot \mathbf{v} \, d\hat{\Omega} \\ & \quad + \sum_e \int_{\partial \hat{\Omega}_e} J_n \hat{\boldsymbol{\beta}}_n \cdot \hat{\mathbf{n}} (\bar{\mathbf{u}}_{n+\theta} - \mathbf{u}_{n+\theta}) \cdot \mathbf{v} \, d\hat{\Gamma} \\ & \quad + \sum_e \int_{\partial \hat{\Omega}_e} 2\nu (\bar{\mathbf{u}}_{n+\theta} - \mathbf{u}_{n+\theta}) \cdot \mathbf{S}_n(\mathbf{v}) \hat{\mathbf{n}} \, d\hat{\Gamma} = \int_{\hat{\Omega}} \hat{\mathbf{f}}_{n+\theta} \cdot \mathbf{v} \, d\hat{\Omega} \quad \forall \mathbf{v} \in \mathbf{V}. \end{aligned} \quad (5.86)$$

and

$$\begin{aligned} & \sum_e \int_{\partial \hat{\Omega}_e} [J_n \mathbf{u}_{n+\theta} \otimes \mathbf{w}_n - 2\nu \mathbf{S}_n(\mathbf{u}_{n+\theta})] \hat{\mathbf{n}} \cdot \bar{\mathbf{v}} \, d\hat{\Gamma} \\ & \quad + \sum_e \int_{\partial \hat{\Omega}_e} J_n \hat{\boldsymbol{\beta}}_n \cdot \hat{\mathbf{n}} (\bar{\mathbf{u}}_{n+\theta} - \mathbf{u}_{n+\theta}) \cdot \bar{\mathbf{v}} \, d\hat{\Gamma} + \int_{\hat{\Gamma}_h} J_n p_n \mathbf{F}_n^{-T} \hat{\mathbf{n}} \cdot \bar{\mathbf{v}} \, d\hat{\Gamma} \\ & \quad - \int_{\hat{\Gamma}_h} (1 - \gamma) J_n (\mathbf{w}_n \cdot \hat{\mathbf{n}}) \bar{\mathbf{u}}_{n+\theta} \cdot \bar{\mathbf{v}} \, d\hat{\Gamma} = \int_{\hat{\Gamma}_h} \hat{\mathbf{h}}_{n+\theta} \cdot \bar{\mathbf{v}} \, d\hat{\Gamma} \quad \forall \bar{\mathbf{v}} \in \bar{\mathbf{V}}, \end{aligned} \quad (5.87)$$

where $\theta \in [1/2, 1]$ is a time stepping parameter and

$$\mathbf{u}_{n+\theta} = (1 - \theta) \mathbf{u}_n + \theta \mathbf{u}_{n+1}^*, \quad (5.88)$$

$$\bar{\mathbf{u}}_{n+\theta} = (1 - \theta) \bar{\mathbf{u}}_n + \theta \bar{\mathbf{u}}_{n+1}, \quad (5.89)$$

and

$$\mathbf{S}_n(\mathbf{v}) = \frac{J_n}{2} \left[\nabla_\chi \mathbf{v} \mathbf{F}_n^{-1} + \mathbf{F}_n^{-T} (\nabla_\chi \mathbf{v})^T \right] \mathbf{F}_n^{-T}. \quad (5.90)$$

The non-linear advection terms have been linearized by using the advective velocity at t_n . For simplicity, various domain-dependent terms are also evaluated at time t_n . The solution procedure involves the static condensation of the internal degrees of freedom \mathbf{u}_{n+1}^* from Equation (5.86) after which Equation (5.87) yields a global system of equations for the global degrees of freedom $\bar{\mathbf{u}}_{n+1}$ only. The details for linear elements are explained in Section 5.4.3.

In the subsequent corrector step, the velocity \mathbf{u}_{n+1}^* is modified using the increment of the pressure $\Delta p_n = p_{n+1} - p_n$ in Equation (5.64) such that \mathbf{u}_{n+1} satisfies the weak continuity constraint at time t_{n+1} . However, rather than using the weak form of the continuity equation in Equation (5.65), the pull-back of the weak incompressibility constraint $\nabla_x \cdot \mathbf{u} = 0$ is used. The ensuing corrector step reads: given the map $\hat{\psi}_{n+1}$, the boundary condition $\bar{\mathbf{u}}'_{n+1}$ and the velocity \mathbf{u}_{n+1}^* , find the velocity $\mathbf{u}_{n+1} \in \mathbf{V}$ and the pressure increment $\Delta p_n \in Q$ such that

$$\int_{\hat{\Omega}} J_{n+1} \frac{\mathbf{u}_{n+1} - \mathbf{u}_{n+1}^*}{\Delta t} \cdot \mathbf{v} \, d\hat{\Omega} + \int_{\hat{\Omega}} J_{n+1} \mathbf{F}_{n+1}^{-T} \nabla_\chi (\theta \Delta p_n) \cdot \mathbf{v} \, d\hat{\Omega} = 0 \quad \forall \mathbf{v} \in \mathbf{V}, \quad (5.91)$$

and

$$\int_{\hat{\Omega}} J_{n+1} \mathbf{F}_{n+1}^{-1} \mathbf{u}_{n+1} \cdot \nabla_\chi q \, d\hat{\Omega} - \int_{\hat{\Gamma}} J_{n+1} \mathbf{F}_{n+1}^{-1} \bar{\mathbf{u}}'_{n+1} \cdot \hat{\mathbf{n}} q \, d\hat{\Gamma} = 0 \quad \forall q \in Q, \quad (5.92)$$

where $\bar{\mathbf{u}}'_{n+1}$ is either the computed $\bar{\mathbf{u}}_{n+1}$ or is supplied by the boundary conditions which are given or are consistent with the impermeability condition $\bar{\mathbf{w}}_{n+1} \cdot \hat{\mathbf{n}} = 0$ on $\hat{\Gamma}_s$. The values of Δt and θ are the same as in the preceding predictor step. Since $\nabla_\chi Q \subseteq \mathbf{V}$ and $\hat{\psi}$ is affine on elements, Equation (5.91) can be rewritten as

$$\int_{\hat{\Omega}} J_{n+1} \mathbf{F}_{n+1}^{-1} \mathbf{u}_{n+1} \cdot \nabla_\chi q \, d\hat{\Omega} = \int_{\hat{\Omega}} J_{n+1} \mathbf{F}_{n+1}^{-1} \mathbf{u}_{n+1}^* \cdot \nabla_\chi q \, d\hat{\Omega} - \theta \Delta t \int_{\hat{\Omega}} J_{n+1} \mathbf{F}_{n+1}^{-1} \mathbf{F}_{n+1}^{-T} \nabla_\chi (\Delta p_n) \cdot \nabla_\chi q \, d\hat{\Omega} \quad \forall q \in Q. \quad (5.93)$$

This result can be used to eliminate \mathbf{u}_{n+1} from Equation (5.92) leading to an equation for computing the pressure which reads: given $\hat{\psi}_{n+1}$, \mathbf{u}_{n+1}^* and $\bar{\mathbf{u}}'_{n+1}$, find $\Delta p_n \in Q$ such that

$$\theta \Delta t \int_{\hat{\Omega}} J_{n+1} \mathbf{F}_{n+1}^{-1} \mathbf{F}_{n+1}^{-T} \nabla_{\chi} (\Delta p_n) \cdot \nabla_{\chi} q \, d\hat{\Omega} = \int_{\hat{\Omega}} J_{n+1} \mathbf{F}_{n+1}^{-1} \mathbf{u}_{n+1}^* \cdot \nabla_{\chi} q \, d\hat{\Omega} - \int_{\hat{\Gamma}} J_{n+1} \mathbf{F}_{n+1}^{-1} \bar{\mathbf{u}}'_{n+1} \cdot \hat{\mathbf{n}} q \, d\hat{\Gamma} \quad \forall q \in Q. \quad (5.94)$$

Depending on the form of $\bar{\mathbf{u}}'_{n+1}$ it may be necessary to provide boundary conditions for Δp_n , see also Section 5.4.3. Once Δp_n has been computed, the velocity \mathbf{u}_{n+1} can be easily evaluated from Equation (5.91), a step which is particularly economical since \mathbf{u}_{n+1} is discontinuous across element facets and can be computed element wise.

The solution at time t_{n+1} is used to update the domain for the next time interval I_{n+1} . The process is repeated alternately until the solution on the time interval I is found. Summarizing, the time stepping procedure evolves as follows:

1. Given the mesh velocity $\hat{\mathbf{u}}_n$, the domain at t_{n+1} is found using Equation (5.84).
2. From the data at time t_n compute the intermediate velocity \mathbf{u}_{n+1}^* and the interface velocity $\bar{\mathbf{u}}_{n+1}$ using Equations (5.86) and (5.87).
3. Compute the pressure increment Δp_n using Equation (5.94).
4. Compute the corrected velocity \mathbf{u}_{n+1} using Equation (5.91).
5. If $t_{n+1} < t_N$ the sequence is repeated from Step (1).

For $\theta = 1/2$ (Crank-Nicolson scheme) the resulting time integration scheme yields second order accuracy but is weakly stable only [72]. By using the FS fractional-step θ scheme strong stability can be achieved while retaining second order accuracy [9]. For the special case of free-surface flow the details of the solution process are outlined in Section 5.4.3.

5.4.2 Discrete conservation

The alternating sequence of mesh update and flow computation, using the predictor-corrector method for the latter, warrants a closer inspection of the conservation properties as these do not carry over automatically to the fully-discrete case. Of primary concern in this respect is the satisfaction of the discrete geometric conservation law, coined D-GCL, which guarantees that a uniform flow state can be preserved irrespective of the mesh motion [29].

For a constant velocity field, Equation (5.87) implies that $\bar{\mathbf{u}}$ is equal to \mathbf{u} on element facets. Insertion of constant fields \mathbf{u} and $\bar{\mathbf{u}}$ into the predictor Equation (5.86) and setting $\hat{\mathbf{f}} = \mathbf{0}$ leads to

$$\int_{\hat{\Omega}} \frac{J_{n+1}^* - J_n}{\Delta t} \mathbf{u} \cdot \mathbf{v} d\hat{\Omega} + \int_{\hat{\Omega}} \nabla_{\chi} \cdot (J_n \mathbf{w}_n) \mathbf{u} \cdot \mathbf{v} d\hat{\Omega} = 0 \quad \forall \mathbf{v} \in \mathbf{V}. \quad (5.95)$$

Using the expression for \mathbf{w} given by Equation (5.10) and taking into account that \mathbf{u} is constant, the satisfaction of Equation (5.95) requires that the following form of the D-GCL holds

$$\int_{\hat{\Omega}} (J_{n+1}^* - J_n) \mathbf{u} \cdot \mathbf{v} d\hat{\Omega} = \Delta t \int_{\hat{\Omega}} \nabla_{\chi} \cdot (J_n \mathbf{F}_n^{-1} \hat{\mathbf{u}}_n) \mathbf{u} \cdot \mathbf{v} d\hat{\Omega} \quad \forall \mathbf{v} \in \mathbf{V}, \quad (5.96)$$

which states that the net volumetric change of an element (left hand side) should equal the divergence of the ALE mesh displacement. After consideration of the expression for J_{n+1}^* in Equation (5.85), the above condition is obviously satisfied. The corrector step (5.91) is formulated such that it will not modify the velocity for this case, therefore, a constant velocity can be represented irrespective of the mesh movement. Using J^* in the predictor Equation (5.86) is pivotal in satisfying discrete geometric conservation.

The D-GCL has an interesting link to discrete volume conservation and to conservative and advective forms of the momentum equation. For discrete volume conservation, consideration of continuity Equation (5.92) in combination with the definition of J^* given in Equation (5.85) gives, after partial integration,

$$\int_{\hat{\Omega}} \frac{J_{n+1}^* - J_n}{\Delta t} q d\hat{\Omega} - \int_{\hat{\Omega}} J_n \mathbf{w}_n \cdot \nabla_{\chi} q d\hat{\Omega} = \int_{\hat{\Gamma}} J_n \bar{\mathbf{w}}_n \cdot \hat{\mathbf{n}} q d\hat{\Gamma} \quad \forall q \in Q. \quad (5.97)$$

Therefore, at time level n the advective field \mathbf{w}_n which is used in the next predictor step satisfies a weak form of continuity Equation (5.33). For discrete momentum conservation, subtracting Equation (5.87) from Equation (5.86), adding Equation (5.91) and setting $\mathbf{v} = \mathbf{e}_j$ and $\bar{\mathbf{v}} = \mathbf{e}_j$ yields, after summation and re-arrangement,

$$\begin{aligned} \int_{\hat{\Omega}} \frac{J_{n+1} \mathbf{u}_{n+1} - J_n \mathbf{u}_n}{\Delta t} \cdot \mathbf{e}_j d\hat{\Omega} + \int_{\hat{\Omega}} \frac{J_{n+1} - J_{n+1}^*}{\Delta t} \mathbf{u}_{n+1}^* \cdot \mathbf{e}_j d\hat{\Omega} \\ = \int_{\hat{\Omega}} \hat{\mathbf{f}}_{n+\theta} \cdot \mathbf{e}_j d\hat{\Omega} \\ - \int_{\hat{\Gamma}_h} (1 - \gamma) J_n (\mathbf{w}_n \cdot \hat{\mathbf{n}}) \bar{\mathbf{u}}_{n+\theta} \cdot \mathbf{e}_j d\hat{\Gamma} - \int_{\hat{\Gamma}_h} \hat{\mathbf{h}}_{n+\theta} \cdot \mathbf{e}_j d\hat{\Gamma}, \end{aligned} \quad (5.98)$$

where the pressure has been fixed on $\hat{\Gamma}_h$ in the corrector step. For cases where $J_{n+1} = J_{n+1}^*$ discrete volume and momentum are conserved in terms

of the numerical fluxes at the boundary in Equations (5.97) and (5.98), respectively. The formulations remain consistent with the strong form of the incompressible Navier-Stokes problem, irrespective of the mesh motion.

Considering now an affine mapping with mesh movement in direction j only, the determinant of the Jacobian is computed from

$$J = \frac{\partial \hat{\psi}_j}{\partial \chi_j} \quad (\text{no summation}), \quad (5.99)$$

which, after insertion in Equation (5.85) proves that for uni-directional mesh motion $J_{n+1} = J_{n+1}^*$. Therefore, from Equation (5.98), global momentum conservation is implied if the mesh moves in one direction. Setting $J_{n+1} = J_{n+1}^*$ and $q = 1$ in Equation (5.97) shows that the volumetric increase of the spatial domain in the time interval (t_n, t_{n+1}) equals the net inflow over the boundary at time t_n , thereby proving volume conservation. Importantly, Equation (5.99) and the implied discrete conservation properties will hold for the vertical mesh displacement assumed earlier for geophysical free-surface flows.

5.4.3 Implementation for geophysical flows

For the GIS method, combining the previous time stepping scheme with linear function spaces for all variables in the finite element space definitions of Section 5.3.1, that is $k = l = m = 1$, leads to a particularly simple implementation. The velocities \mathbf{u}_n and $\bar{\mathbf{u}}_n$, the piezometric level η_n and the map $\hat{\psi}_n$ on the reference domain $\tilde{\Omega}$ at time t_n are expressed in terms of the basis functions and nodal values as

$$\mathbf{u}_n(\boldsymbol{\chi}) = \sum_i N^i(\boldsymbol{\chi}) \mathbf{u}_n^i, \quad (5.100)$$

$$\bar{\mathbf{u}}_n(\boldsymbol{\chi}) = \sum_j \bar{N}^j(\boldsymbol{\chi}) \bar{\mathbf{u}}_n^j, \quad (5.101)$$

$$\eta_n(\boldsymbol{\chi}) = \sum_j \tilde{N}^j(\boldsymbol{\chi}) \eta_n^j, \quad (5.102)$$

$$\hat{\psi}_n(\boldsymbol{\chi}) = \sum_j \tilde{N}^j(\boldsymbol{\chi}) \hat{\psi}_n^j, \quad (5.103)$$

where N^i , \bar{N}^j and \tilde{N}^j are finite element shape functions consistent with the definitions of the spaces in Section 5.3.1, and \mathbf{u}_n^i , $\bar{\mathbf{u}}_n^j$, η_n^j and $\hat{\psi}_n^j$ are nodal degrees of freedom. On each reference element $\tilde{\Omega}_e$, the local index i and global index j may be chosen such that they become locally equivalent. The distinction can therefore be dropped in the resulting algebraic systems. The piecewise linear mapping $\hat{\psi}$ implies piecewise constant Jacobian matrices \mathbf{F} and piecewise constant Jacobian determinants J . Importantly, linear

functions remain linear under the action of the mapping $\hat{\psi}$ which also implies that elements preserve their geometrical shape when transformed to the spatial domain Ω .

5.4.3.1 Domain update

The computational sequence starts by determining the mapping $\psi^n \rightarrow \psi^{n+1}$ on the considered time interval I_n . Assuming mesh movement in the vertical direction only, the mesh velocity $\hat{\mathbf{u}}_n$ at the free surface is determined by

$$\hat{\mathbf{u}}_n = \left. \frac{\partial \eta}{\partial t} \right|_{\chi, n} \mathbf{e}_z \quad \text{on } \Gamma_s, \quad (5.104)$$

which is used to update the free surface position via Equation (5.84). The time derivative of the piezometric level is computed from

$$\left. \frac{\partial \eta}{\partial t} \right|_{\chi, n} = \frac{1}{\theta} \frac{\eta_n - \eta_{n-1}}{\Delta t} - \frac{1 - \theta}{\theta} \left. \frac{\partial \eta}{\partial t} \right|_{\chi, n-1}, \quad (5.105)$$

where the value of θ is the same as that used in the predictor-corrector scheme. All quantities that are required to compute $\partial \eta / \partial t|_{\chi, n}$ are available from the previous time step.

Once the new position of the free surface has been determined, the mesh velocity in the vertical direction, denoted by $\hat{u}_z = \hat{\mathbf{u}} \cdot \mathbf{e}_z$, is computed at all points in the domain by solving the following Poisson problem: find $\hat{u}_z \in Q_g$ such that

$$\int_{\tilde{\Omega}} \nabla_{\chi} \hat{u}_z \cdot \nabla_{\chi} q \, d\tilde{\Omega} = 0, \quad \forall \quad q \in Q, \quad (5.106)$$

where Q_g satisfies the necessary boundary conditions such as on the free-surface boundary $\hat{\Gamma}_s$ and on solid boundaries such as a sea bed. The unconstrained movement of nodes along vertical walls is imposed by means of the homogeneous Neumann boundary condition which is implicit in Equation (5.106). For a proper partitioning $\tilde{\Omega}$, Equation (5.106) satisfies a discrete maximum principle implying that the mapping $\hat{\psi}$ is monotonic and that $J > 0$, provided that the free surface remains located above the bottom level. The restriction to vertical mesh displacement excludes the movement of boundary nodes along inclined walls. In order to compute the run-up of surface waves on a beach for example, one therefore has to resort to other techniques such as flooding and drying of individual elements which is not considered here.

5.4.3.2 Predictor step

The predictor-corrector scheme for free-surface flows follows directly from Equations (5.86) and (5.87) by setting $p_n = g\eta_n$ and $\hat{\mathbf{f}}_n = \mathbf{0}$. For the case of spatially constant viscosity, the terms involving the symmetric gradient

can simply be replaced with the regular gradient which has the convenience that the equations for the respective velocity components become decoupled. Noting that any term involving second derivatives with respect to space will vanish due to the choice of P^1 functions, and setting $J_{n+1}^* = J_{n+1}$ (which is the case for vertical mesh motion), this leads to

$$\begin{aligned} & \int_{\tilde{\Omega}} \frac{J_{n+1} \mathbf{u}_{n+1}^* - J_n \mathbf{u}_n}{\Delta t} \cdot \mathbf{v} d\hat{\Omega} + \int_{\tilde{\Omega}} \nabla_{\chi} \cdot (J_n \mathbf{u}_{n+\theta} \otimes \mathbf{w}_n) \cdot \mathbf{v} d\hat{\Omega} \\ & + \int_{\tilde{\Omega}} \nabla_{\chi} \cdot (J_n g \eta_n \mathbf{F}_n^{-T}) \cdot \mathbf{v} d\hat{\Omega} + \sum_e \int_{\partial \hat{\Omega}_e} J_n \nu (\bar{\mathbf{u}}_{n+\theta} - \mathbf{u}_{n+\theta}) \nabla_{\chi} \mathbf{v} \mathbf{F}_n^{-1} \mathbf{F}_n^{-T} \hat{\mathbf{n}} d\hat{\Gamma} \\ & + \sum_e \int_{\partial \hat{\Omega}_e} J_n \hat{\boldsymbol{\beta}}_n \cdot \hat{\mathbf{n}} (\bar{\mathbf{u}}_{n+\theta} - \mathbf{u}_{n+\theta}) \cdot \mathbf{v} d\hat{\Gamma} = \mathbf{0} \quad \forall \mathbf{v} \in V, \end{aligned} \quad (5.107)$$

and

$$\begin{aligned} & \sum_e \int_{\partial \hat{\Omega}_e} J_n (\mathbf{w}_n \cdot \hat{\mathbf{n}}) \mathbf{u}_{n+\theta} \cdot \bar{\mathbf{v}} d\hat{\Gamma} - \sum_e \int_{\partial \hat{\Omega}_e} J_n \nu \nabla_{\chi} \mathbf{u}_{n+\theta} \mathbf{F}_n^{-1} \mathbf{F}_n^{-T} \hat{\mathbf{n}} \cdot \bar{\mathbf{v}} d\hat{\Gamma} \\ & + \sum_e \int_{\partial \hat{\Omega}_e} J_n \hat{\boldsymbol{\beta}}_n \cdot \hat{\mathbf{n}} (\bar{\mathbf{u}}_{n+\theta} - \mathbf{u}_{n+\theta}) \cdot \bar{\mathbf{v}} d\hat{\Gamma} - \int_{\hat{\Gamma}_h} (1 - \gamma) J_n (\mathbf{w}_n \cdot \hat{\mathbf{n}}) \bar{\mathbf{u}}_{n+\theta} \cdot \bar{\mathbf{v}} d\hat{\Gamma} \\ & = \int_{\hat{\Gamma}_h} (\hat{\mathbf{h}}_{n+\theta} - J_n g \eta_n \mathbf{F}_n^{-T} \hat{\mathbf{n}}) \cdot \bar{\mathbf{v}} d\hat{\Gamma} \quad \forall \bar{\mathbf{v}} \in \bar{V}. \end{aligned} \quad (5.108)$$

Equations (5.107) and (5.108) are very similar, component wise, to the discrete scalar transport problem from Section 3.4.2.

The solution proceeds with the elimination of \mathbf{u}_{n+1}^* , element wise, from Equation (5.107). To this end, the matrix format of Equation (5.107) reads

$$\begin{aligned} & \frac{1}{\Delta t} \left(\mathbf{M}_{n+1} \mathbf{U}_{n+1}^{k,*} - \mathbf{M}_n \mathbf{U}_n^k \right) + \mathbf{A} \mathbf{U}_{n+\theta}^k + \mathbf{G}_k \boldsymbol{\eta}_n \\ & + (\mathbf{K} + \mathbf{Q}) \left(\bar{\mathbf{U}}_{n+\theta}^k - \mathbf{U}_{n+\theta}^k \right) = \mathbf{0}, \end{aligned} \quad (5.109)$$

where \mathbf{U}_n^k is a vector containing the local unknowns of velocity component k at time t_n , $\boldsymbol{\eta}_n$ is the vector of nodal piezometric levels at t_n . The element matrices $\mathbf{M}_{n,n+1}$, \mathbf{A} , \mathbf{G}_k , \mathbf{K} and \mathbf{Q} are given by, respectively,

$$M_{n,n+1}^{ij} = \int_{\hat{\Omega}_e} J_{n,n+1} N^i N^j d\hat{\Omega}, \quad (5.110)$$

$$A^{ij} = \int_{\hat{\Omega}_e} N^i \nabla_{\chi} \cdot (J_n \mathbf{w}_n N^j) d\hat{\Omega}, \quad (5.111)$$

$$G_k^{ij} = \int_{\hat{\Omega}_e} J_n N^i \nabla_{\chi} \cdot (g N^j \mathbf{F}_n^{-T}) \cdot \mathbf{e}_k d\hat{\Omega}, \quad (5.112)$$

$$K^{ij} = \int_{\partial \hat{\Omega}_e} J_n \nu N^j \nabla_{\chi} N^i \cdot \mathbf{F}_n^{-1} \mathbf{F}_n^{-T} \hat{\mathbf{n}} d\hat{\Gamma}, \quad (5.113)$$

$$Q^{ij} = \int_{\partial \hat{\Omega}_e} J_n (\hat{\boldsymbol{\beta}}_n \cdot \hat{\mathbf{n}}) N^i N^j d\hat{\Gamma}. \quad (5.114)$$

The matrix \mathbf{K} is algebraically equivalent to the standard element diffusion matrix of a linear CG method. Replacing $\mathbf{U}_{n+1}^{k,*} = \mathbf{U}_n^k + (\mathbf{U}_{n+\theta}^k - \mathbf{U}_n^k)/\theta$ in Equation (5.109), following some re-arrangement, an expression for $\mathbf{U}_{n+\theta}^k$ in terms of the global degrees of freedom $\bar{\mathbf{U}}_{n+\theta}^k$ reads

$$\begin{aligned} \mathbf{U}_{n+\theta}^k &= \bar{\mathbf{U}}_{n+\theta}^k \\ &- \mathbf{T} \left[\frac{1}{\theta \Delta t} \left(\mathbf{M}_{n+1} \bar{\mathbf{U}}_{n+\theta}^k - \mathbf{M}_{n+1-\theta} \mathbf{U}_n^k \right) + \mathbf{A} \bar{\mathbf{U}}_{n+\theta}^k + \mathbf{G}_k \boldsymbol{\eta}_n \right], \end{aligned} \quad (5.115)$$

where

$$\mathbf{T} = \left(\frac{1}{\theta \Delta t} \mathbf{M}_{n+1} + \mathbf{A} - \mathbf{K} - \mathbf{Q} \right)^{-1}, \quad (5.116)$$

and $\mathbf{M}_{n+1-\theta} = \theta \mathbf{M}_n + (1 - \theta) \mathbf{M}_{n+1}$. Global Equation (5.108) leads to the algebraic equation

$$\sum_e \left[\left(\tilde{\mathbf{A}} - \mathbf{K}^T \right) \mathbf{U}_{n+\theta}^k + \mathbf{Q} \left(\bar{\mathbf{U}}_{n+\theta}^k - \mathbf{U}_{n+\theta}^k \right) - \mathbf{P} \bar{\mathbf{U}}_{n+\theta}^k \right] = \sum_e \mathbf{H} \mathbf{e}_k, \quad (5.117)$$

where \sum_e denotes assembly of the element matrices into a global matrix. The element matrices in the above equation are given by

$$\tilde{A}^{ij} = \int_{\partial \hat{\Omega}_e} J_n(\mathbf{w}_n \cdot \hat{\mathbf{n}}) N^i N^j d\hat{\Gamma}, \quad (5.118)$$

$$P^{ij} = \int_{\partial \hat{\Omega}_e \cap \hat{\Gamma}_h} (1 - \gamma) J_n(\mathbf{w}_n \cdot \hat{\mathbf{n}}) N^i N^j d\hat{\Gamma}, \quad (5.119)$$

and the vector \mathbf{H} is given by

$$H^{ij} = \int_{\partial \hat{\Omega}_e \cap \hat{\Gamma}_h} N^i \left(\hat{\mathbf{h}}_{n+\theta} - J_n g \boldsymbol{\eta}_n \mathbf{F}_n^{-T} \hat{\mathbf{n}} \right) \cdot \mathbf{e}_j d\hat{\Gamma}. \quad (5.120)$$

As the basis functions are piecewise linear and ν is piecewise constant, the matrix \mathbf{K}^T equals the matrix \mathbf{K} in Equation (5.113). The format of the above matrix equations is similar to that of the Navier-Stokes problem on a fixed domain, with only a slight redefinition of the mass matrices due to the mesh movement.

Static condensation using Equation (5.117) leads to a global equation for $\bar{\mathbf{U}}_{n+\theta}^k$ which after some algebraic manipulation, see also Section 4.3.3, can be written compactly as

$$\begin{aligned} \sum_e \mathbf{W} \left[\frac{1}{\theta \Delta t} \left(\mathbf{M}_{n+1} \bar{\mathbf{U}}_{n+\theta}^k - \mathbf{M}_{n+1-\theta} \mathbf{U}_n^k \right) + \mathbf{A} \bar{\mathbf{U}}_{n+\theta}^k + \mathbf{G}_k \boldsymbol{\eta}_n \right] \\ + \sum_e \left(\mathbf{K} + \mathbf{P} - \tilde{\mathbf{A}} \right) \bar{\mathbf{U}}_{n+\theta}^k + \sum_e \mathbf{H} \mathbf{e}_k = \mathbf{0}, \end{aligned} \quad (5.121)$$

where the element ‘weighting matrix’ \mathbf{W} is given by

$$\mathbf{W} = \mathbf{I} - \left(\frac{1}{\theta \Delta t} \mathbf{M}_{n+1} + \mathbf{A} - \tilde{\mathbf{A}} \right) \mathbf{T}. \quad (5.122)$$

After solving for $\bar{\mathbf{U}}_{n+\theta}^k$, the local degrees of freedom $\mathbf{U}_{n+\theta}^k$ are obtained from a back-substitution step using Equation (5.115). To do this efficiently the matrix \mathbf{T} in Equation (5.116) is stored in memory during assembly. The unknowns $\mathbf{U}_{n+1}^{k,*}$ are determined by extrapolation, using Equation (5.88), and stored in memory.

5.4.3.3 Corrector step

Next, the increment of the piezometric level is computed from Equation (5.94), setting $\Delta p_n = g \Delta \eta_n$, and using Equations (5.104) and (5.105) for the free-surface boundary condition,

$$\begin{aligned} & \theta \Delta t \int_{\hat{\Omega}} J_{n+1} g \mathbf{F}_{n+1}^{-1} \mathbf{F}_{n+1}^{-T} \nabla_{\chi} \Delta \eta_n \cdot \nabla_{\chi} q \, d\hat{\Omega} + \frac{1}{\theta \Delta t} \int_{\hat{\Gamma}_s} J_{n+1} \mathbf{F}_{n+1}^{-1} \Delta \eta_n \mathbf{e}_z \cdot \hat{\mathbf{n}} q \, d\hat{\Gamma} \\ &= \int_{\hat{\Omega}} J_{n+1} \mathbf{F}_{n+1}^{-1} \mathbf{u}_{n+1}^* \cdot \nabla_{\chi} q \, d\hat{\Omega} - \int_{\hat{\Gamma} \setminus \hat{\Gamma}_s} J_{n+1} \mathbf{F}_{n+1}^{-1} \bar{\mathbf{u}}'_{n+1} \cdot \hat{\mathbf{n}} q \, d\hat{\Gamma} \\ & \quad + \frac{1-\theta}{\theta} \int_{\hat{\Gamma}_s} J_{n+1} \mathbf{F}_{n+1}^{-1} \left. \frac{\partial \eta}{\partial t} \right|_n \mathbf{e}_z \cdot \hat{\mathbf{n}} q \, d\hat{\Gamma} \quad \forall q \in Q. \end{aligned} \quad (5.123)$$

The matrix format of this equation reads

$$\sum_e \left(\theta \Delta t \mathbf{S} + \frac{1}{\theta \Delta t} \mathbf{M}_s \right) \Delta \eta_n = \sum_e (\mathbf{D} - \mathbf{E} + \mathbf{F}), \quad (5.124)$$

where $\Delta \eta_n$ is a vector of unknowns containing the nodal piezometric level increments. The element matrices \mathbf{S} and \mathbf{M}_s are given by, respectively,

$$S^{ij} = \int_{\hat{\Omega}_e} J_{n+1} g \mathbf{F}_{n+1}^{-1} \mathbf{F}_{n+1}^{-T} \nabla_{\chi} N^i \cdot \nabla_{\chi} N^j \, d\hat{\Omega}, \quad (5.125)$$

$$M_s^{ij} = \int_{\partial \hat{\Omega}_e \cap \hat{\Gamma}_s} J_{n+1} N^i N^j \mathbf{F}_{n+1}^{-1} \mathbf{e}_z \cdot \hat{\mathbf{n}} \, d\hat{\Gamma}, \quad (5.126)$$

and the right-hand side terms in (5.124) are given by

$$D^{ij} = \int_{\hat{\Omega}_e} J_{n+1} N^j \mathbf{u}_{n+1}^{*,j} \cdot \mathbf{F}_{n+1}^{-T} \nabla_{\chi} N^i \, d\hat{\Omega}, \quad (5.127)$$

$$E^{ij} = \int_{\partial \hat{\Omega}_e \cap (\hat{\Gamma} \setminus \hat{\Gamma}_s)} J_{n+1} N^i N^j \mathbf{F}_{n+1}^{-1} \bar{\mathbf{u}}'^{j} \cdot \hat{\mathbf{n}} \, d\hat{\Gamma}, \quad (5.128)$$

$$F^{ij} = \frac{1-\theta}{\theta} \int_{\partial \hat{\Omega}_s \cap \hat{\Gamma}_s} J_{n+1} N^i N^j \mathbf{F}_{n+1}^{-1} \left. \frac{\partial \eta}{\partial t} \right|_n^j \mathbf{e}_z \cdot \hat{\mathbf{n}} \, d\hat{\Gamma}. \quad (5.129)$$

After solving Equation (5.124) for $\Delta\boldsymbol{\eta}_n$ the corrected velocity unknowns \mathbf{U}_{n+1}^k are obtained via a back-substitution step from

$$\mathbf{U}_{n+1}^k = \mathbf{U}_{n+1}^{k,*} - \theta\Delta t g \left(\mathbf{F}_{n+1}^{-T} \nabla_{\chi} N^j \cdot \mathbf{e}_k \right) \Delta\eta_n^j, \quad (5.130)$$

which is a local procedure on elements which for linear functions does not involve the inversion of a global mass matrix. Finally, the time derivative $\partial\eta/\partial t$ on $\hat{\Gamma}_s$ is updated using Equation (5.105) which is a point-wise operation.

The overall predictor-corrector solution procedure is very economical since only the solution of $d + 1$ simple scalar sparse matrix systems is involved, each having the sparsity structure of the corresponding CG method on the same mesh. The procedure requires the assembly of two global matrices, one for the predictor step and one for the corrector step, and the construction of two corresponding ILU preconditioners. The approach as a whole is facilitated by the ‘splitting’ of the velocity field in two complementary fields, on element interiors and on element interfaces, respectively.

5.4.4 Normal mode analysis

To analyze the numerical behaviour of the $P^1 - P^1$ -implementation of the GIS scheme in combination with the FS time stepping scheme, periodic small-amplitude waves are considered. For a regular finite element mesh, as depicted in Figure 5.3, the associated algebraic system from Equations (5.107) and (5.123) can be solved analytically to yield the vertical modes of the numerical solution as a function of the horizontal wave number, defined as $k = 2\pi/L$, where L is the wave length. Choosing the undisturbed water level at $z = 0$ and the bottom level at $z = -d$, the theoretical solution for the complex valued piezometric level of a linear small-amplitude wave is given by

$$\eta = \tilde{A} \frac{\cosh [k(z+d)]}{\cosh(kd)} e^{i(\omega t - kx)}, \quad (5.131)$$

where \tilde{A} is the complex amplitude of the free-surface elevation and the radian frequency ω is related to the wave number k through the dispersion relation

$$\omega^2 = gk \tanh(kd). \quad (5.132)$$

Next, the numerical and analytical solutions are compared for different wave length to water depth ratios. In particular, the celerity and amplitude errors are determined as a function of the number of elements per wave length $N_L = L/h_H$, the number of horizontal layers $N_z = d/h_V$ and the Courant number $CFL = c\Delta t/h_H$, where c is the wave celerity and h_H and h_V are the element sizes in horizontal and vertical direction, respectively. The results of the normal mode analysis are shown in Figures 5.4 and 5.5 giving, in respective order, the relative celerity error and the relative amplitude error after one wave period as a function of the number of nodes per wave length.

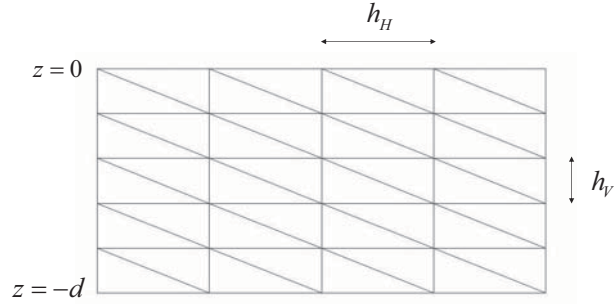


Figure 5.3: *Regular mesh configuration used for the normal mode analysis.*

5.4.4.1 Dispersion

A relative celerity error $|1 - c_{model}/c_{exact}| < 10^{-2}$ is considered sufficiently accurate for most practical purposes. Figure 5.4 shows that this requirement is usually satisfied for more than 20 nodes per wave length, provided that the number of layers is sufficient. Obviously, the required vertical resolution depends on the wave length to depth ratio. For highly dispersive waves the element size in vertical direction h_V should be approximately equal to the horizontal mesh size h_H . Longer waves require considerably fewer vertical nodes. As shown in Figure 5.4 for $L > 10d$ two layers are generally sufficient. Comparing the magnitudes of the partial derivatives of η in the horizontal and vertical direction, respectively, yields the following expression for the optimal ratio of the vertical to horizontal element size

$$\frac{h_V}{h_H} \approx \coth(kd). \quad (5.133)$$

Having selected the element sizes h_V and h_H , the time step Δt should be chosen such that the Courant number is not larger than $1 \sim 2$. The Courant number may be increased provided that the number of nodes per wave length increases accordingly. For example, Figure 5.4 shows that taking $CFL = 4$ would require about 80 elements per wave length in order to have an acceptable celerity error.

5.4.4.2 Damping

While, theoretically, the CN time stepping scheme has no amplitude damping, the smoothing property of the FS scheme involves some attenuation of high wave number components. This motivates a closer look at the damping properties of this scheme. Theoretical amplitude errors of the regular $P^1 - P^1$ element with FS time stepping are shown in Figure 5.5. The amplitude error $|1 - \rho_r|$ is defined as the relative error of the wave amplitude after one wave period.

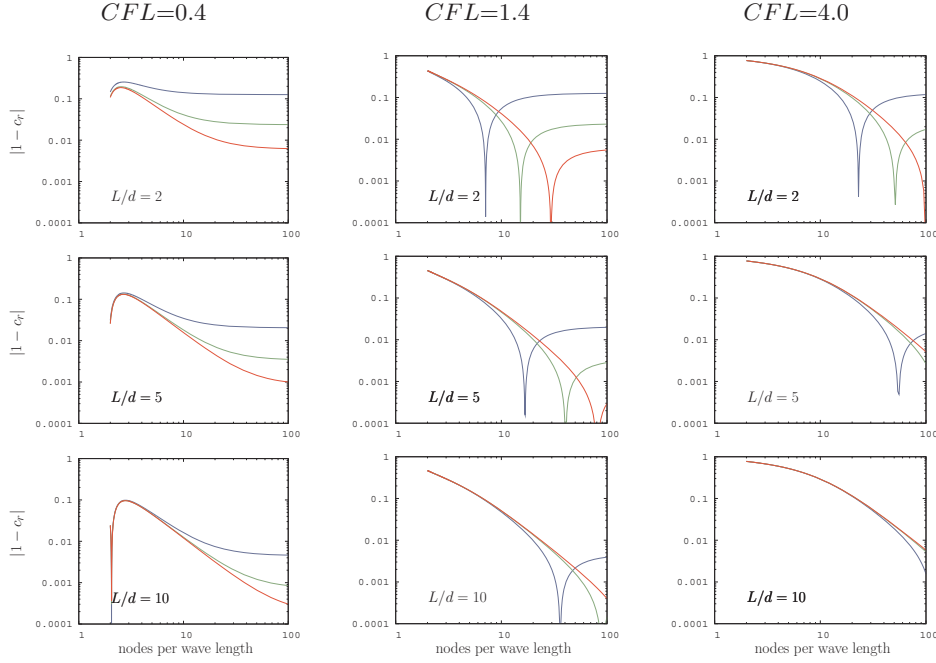


Figure 5.4: *Relative celerity error $|1 - c_r|$ for various wave length to depth ratios L/d , Courant numbers and number of vertical layers: $N_z = 2$ (blue), $N_z = 5$ (green) and $N_z = 10$ (red).*

Figure 5.5 shows that the amplitude error generally decreases when increasing the number of nodes per wave length while it is hardly influenced by the vertical resolution of the mesh and the wave length to depth ratio. For appropriate Courant numbers and a minimum of 20 nodes per wave length the damping will cause a 0.1% to 1% amplitude decrease after one wave period. This implies that the smoothing of the FS scheme is negligible if the mesh sizes and time step are chosen such that also the phase is sufficiently accurate. Higher wave number components however gradually extinct loosing about 10% of their amplitude per wave period which explains the excellent smoothing behaviour of the scheme. Interestingly, the damping error is hardly dependent on the number of elements over the vertical.

5.5 Numerical examples

The moving free-surface GIS method is illustrated by means of a few examples representing a range of situations encountered in environmental hydraulics, including sophisticated lab experiments. All examples use a gravitational acceleration $g = 9.81 \text{ m/s}^2$, the interface penalty parameter $\alpha = 4$ and, unless otherwise stated, $\nu = 10^{-6} \text{ m}^2/\text{s}$, which is the natural kinematic viscosity of water. All problems use P^1 basis functions on simplexes for all

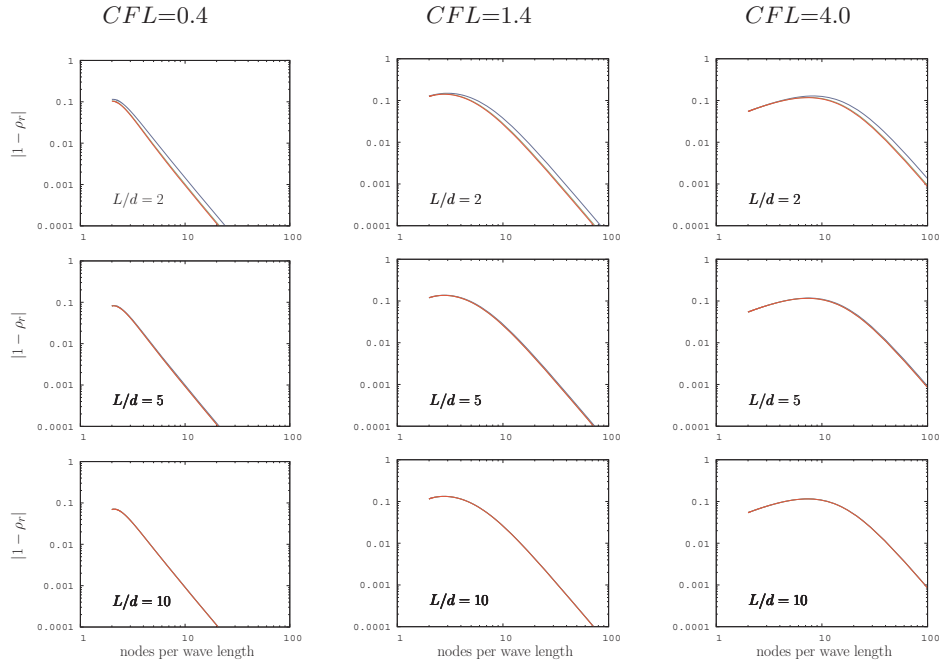


Figure 5.5: *Relative amplitude error $|1 - \rho_r|$ after one wave period for various wave length to depth ratios L/d , Courant numbers and number of vertical layers: $N_z = 2$ (blue), $N_z = 5$ (green) and $N_z = 10$ (red).*

unknowns. The FS time stepping scheme is used throughout and reported time steps are the averages of the three substeps of the scheme as described in Section 2.3.2.

5.5.1 Linear waves

The series of tests presented first consider natural linear-wave modes in basins with a horizontal bottom and closed vertical walls. For the inviscid case, these linear waves exhibit zero damping and the tests are thus particularly suited to detect dissipative mechanisms of the model. In particular the treatment of the kinematic free-surface boundary condition is tested. In practice, the occurrence of natural wave modes in enclosed basins is often the result of near-resonant forcing [18]. Accurate numerical simulation of these phenomena therefore hinges on minimal artificial dissipation.

5.5.1.1 Narrow channel

Consider a closed basin $\Omega: (x, z) \in (0, l) \times (-d, 0)$ with vertical side walls in $x = 0$ and $x = l$ and the undisturbed free surface Γ_s at $z = 0$. Natural wave

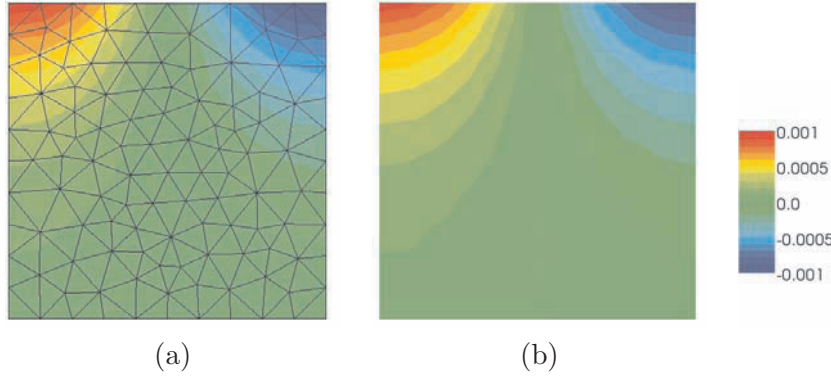


Figure 5.6: *Narrow channel: computational mesh and computed solution (a), and exact solution (b) for η at $t = 17.8$ s (maximum elevation), units in m .*

modes in the basin have the following solution for the piezometric level

$$\eta_m = A_m \frac{\cosh [k_m (z + d)]}{\cosh (k_m d)} \cos (k_m x) \cos (\omega_m t), \quad (5.134)$$

where $m = 1, 2, 3 \dots$ denotes the wave mode, $k_m = m\pi/l$ is the associated wave number, ω_m is the eigen frequency and A_m is the maximum surface elevation, see for instance Mei et al. [60]. The frequency is related to the wave number via the dispersion relation

$$\omega_m^2 = g k_m \tanh (k_m d). \quad (5.135)$$

The solution represents a standing wave with constant amplitude. The problem is frequently used as a test example in literature [41, 84].

This example concerns a mode $m = 1$ standing wave in a basin of depth $d = 10$ m and length $l = 10$ m for which the wave number $k_1 = 0.314$ rad/m and the natural frequency $\omega_1 = 1.751$ rad/s. The amplitude A_1 is set to 0.001 m. The computational domain Ω is partitioned by equilateral triangles with approximately uniform element size $h_e \approx 1$ m. The mesh used in the computation is depicted in Figure 5.6. The nodes are not aligned in the vertical direction. The time step $\Delta t = 0.1$ s which involves approximately 35 time steps per wave period and a Courant number of 0.55 .

Figure 5.6 shows the computed and exact fields of the piezometric level at $t = 17.8$ s. Considering that the mesh size and the time step are relatively large compared to the wave length and the wave period, respectively, the result is very accurate. Time series of the computed and analytical piezometric level at $(x, y) = (0, 0)$ are shown in Figure 5.7. The computed solution shows negligible damping while the phase error amounts approximately 1% which corresponds to the results of the normal mode analysis. For larger wave amplitudes the advective velocity will be larger which ultimately introduces numerical damping due to the upwind mechanism at element interfaces.

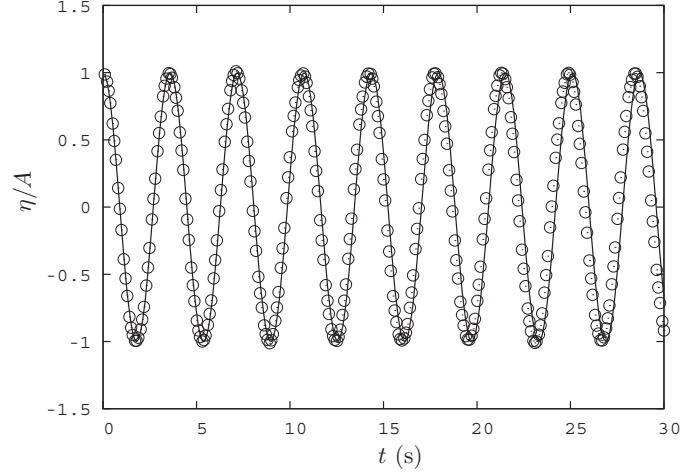


Figure 5.7: *Narrow channel: time series of piezometric level η/A at $(x, y) = (0, 0)$, exact (solid) and numerical (circles) solutions.*

5.5.1.2 Cylindrical basin

A cylindrical basin of radius a with a horizontal bottom at $z = -d$ is considered. Using polar coordinates (r, θ) , the solution for the piezometric level of small-amplitude natural wave modes in the basin is given by

$$\eta_{mn} = A_{mn} J_m(k_{mn}r) \cos(m\theta) \frac{\cosh[k_{mn}(z+d)]}{\cosh(k_{mn}d)} \cos(\omega_{mn}t) \quad (5.136)$$

where $n = 1, 2, 3, \dots$ and $m = 0, 1, 2, 3, \dots$ denote the wave mode, J_m is the Bessel function of order m , A_{mn} is the maximum surface elevation, k_{mn} is the wave number and ω_{mn} is the corresponding frequency, see Mei et al. [60]. Letting j_{mn} denote the n^{th} zero of J'_m , the wave number k_{mn} is determined by the relation $k_{mn}a = j_{mn}$. The natural frequency ω_{mn} is related to k_{mn} via the dispersion relationship

$$\omega_{mn}^2 = gk_{mn} \tanh(k_{mn}d). \quad (5.137)$$

The simulated case concerns a basin of radius $a = 10$ m and depth $d = 10$ m, with $m = 2$ and $n = 1$. The initial condition for η is obtained from Equation (5.136) by setting $A_{21} = 0.05$ m and $t = 0$ while the initial velocity is zero. The wave number k_{21} and frequency ω_{21} are 0.3054 rad/m and 1.7271 rad/s, respectively. For the adopted element size $h_e \approx 1$ m, there are 10 elements over the depth of the basin and approximately 20 elements per wave length. The computational domain and mesh is shown in Figure 5.8a. A time step $\Delta t = 0.1$ s is used, which results in approximately 35 time steps per oscillation.

Contours of the computed surface level at $t = 10.9$ s are shown in Figure 5.8b, together with the corresponding analytical solution. Considering

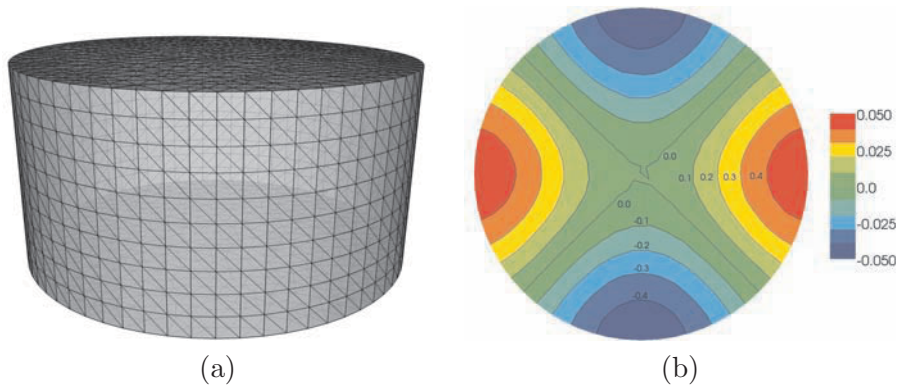


Figure 5.8: *Cylindrical basin: (a) Computational domain and mesh; and (b) exact (solid) and computed (colour) surface level contours (m) at $t = 10.9$ s.*

that the element size is relatively large compared to the wave length, the computed result is particularly accurate. Figure 5.9 shows the computed time history of the surface elevation at $(x, y) = (a, 0)$. Compared to the analytical result, the computed elevation reveals a relative phase error of approximately 1% and a damping error of approximately 0.5% per wave period. These results confirm that for linear waves the interface stabilization method introduces negligible energy dissipation.

5.5.2 Large amplitudes

In contrast to the previous linearized results, larger wave amplitudes involve higher velocities which activate the upwind mechanism at element interfaces. For higher waves, the associated dissipation may therefore result in some decay of the wave energy. It is therefore interesting to take a closer look at some problems with considerable amplitudes.

5.5.2.1 Periodic oscillations in a U-tube

This example concerns the oscillatory motion of a fluid in a U-shaped tube with vertical open ends. For an inviscid fluid, and if the tube diameter is small with respect to the radius of the bend of the tube, the free-surface elevation ζ on the sides of the tube is described by

$$\zeta = \pm A \sin(\omega t), \quad (5.138)$$

where A is the amplitude of the free-surface oscillation and $\omega = \sqrt{2g/l}$ is the frequency of the motion, where l is the total length of the fluid column in the tube [62]. The corresponding axial fluid velocity is nearly-uniform.

The numerical example involves a tube of diameter 0.1 m, bend-radius $1/\pi$ m and total fluid column length $l = 3$ m, measured along the axis

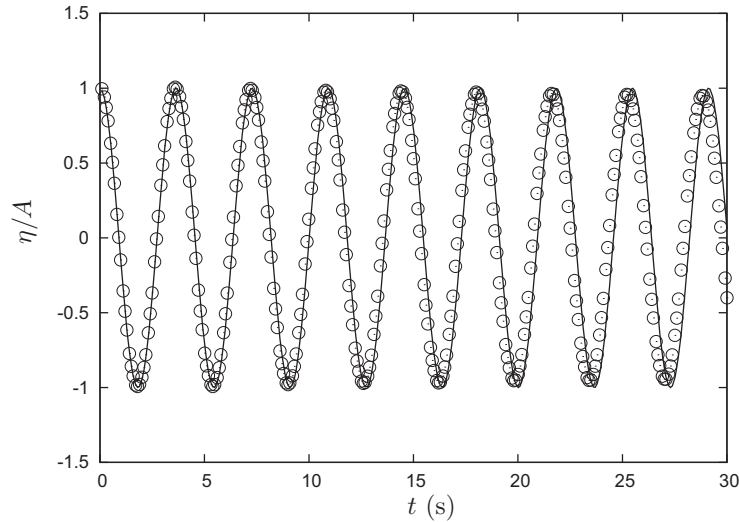


Figure 5.9: *Cylindrical basin: time histories of the analytical (solid) and computed (circles) normalized piezometric level at $(x, y, z) = (10, 0, 0)$.*

of the tube. The resulting analytical frequency is $\omega = 2.56$ rad/s. The adopted tetrahedral mesh of the tube has approximately six elements across the diameter and 50 elements along the fluid column. The initial elevations in the vertical pipe ends are set to $\zeta_0 = \pm 0.3$ m. The initial velocity is zero and the initial piezometric level at time $t = 0$ is obtained by solving a Laplace equation with the Dirichlet boundary conditions $\eta = \zeta_0$ at the free surface and homogeneous Neumann boundary conditions along the pipe wall. This procedure guarantees that the initial condition satisfies balance of momentum. A time step size of $\Delta t = 0.05$ s is used, giving 50 time steps per period of oscillation.

The computed configuration of the mesh at maximum elevation is shown in Figure 5.10, and Figure 5.11 shows the computed vertical elevation on one side of the tube as a function of time, together with the corresponding analytical solution. The computed and analytical results in Figure 5.11 are barely distinguishable, showing that negligible damping is present in the model if the velocity gradients are small.

5.5.2.2 Soliton propagation

A soliton is a non-linear solitary wave which, in the absence of dissipation and on a horizontal bottom, propagates without changing height and form due to a subtle balance between dispersive and non-linear terms [60]. In a (x, z) – reference frame, with the undisturbed surface at $z = 0$ and the



Figure 5.10: *Spatial mesh configuration for U-shaped tube problem at maximum surface elevation.*

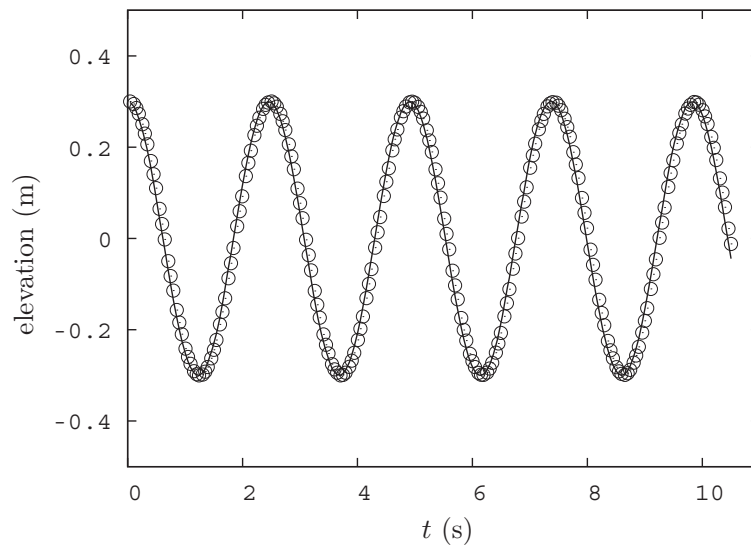


Figure 5.11: *U-shaped tube problem: time histories of the analytical (solid) and computed (circles) surface elevations.*

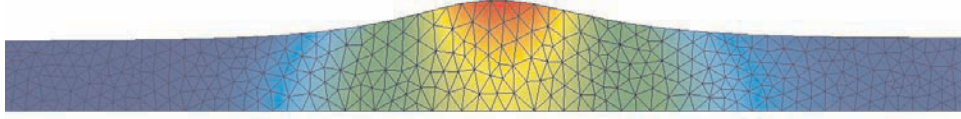


Figure 5.12: *Soliton: snapshot of mesh configuration for $H/d = 0.60$ at $t = 30$ s, colour shading indicates piezometric level.*

bottom at $z = -d$, the free-surface elevation ζ can be approximated by

$$\zeta = H \operatorname{sech}^2 \left[\sqrt{\frac{3H}{4d^3}} (x - ct) \right] \quad (5.139)$$

in which H is the wave height, d is the undisturbed water depth and $c = \sqrt{g(d+H)}$ is the wave celerity. The horizontal velocity u , which is vertically uniform, and the vertical velocity w are given by, respectively,

$$\begin{aligned} u &= c \frac{\zeta}{\zeta + d}, \\ w &= -(z + d) \frac{\partial u}{\partial x}. \end{aligned} \quad (5.140)$$

The above approximate solution is accurate to the order $(H/d)^2$, see for instance Mei et al. [60].

The numerical simulation concerns a horizontal channel with depth $d = 10$ m and a horizontal length of 600 m. The initial condition is that of a soliton having its crest at $x = 100$ m where the initial velocity field is specified according to Equation (5.140). The relative wave height H/d ranges from 0.15 to 0.60 giving corresponding wave lengths between 180 m and 90 m. The element size $h_e \approx 2$ m yielding 5 vertical layers of triangular elements and, depending on the relative wave height, 45 to 90 elements per wave length. A snapshot of the deformed mesh for the case $H/d = 0.60$ is depicted in Figure 5.12 showing the vertical stretching of the unstructured elements. The time step size Δt is set to 0.1 s giving a Courant number $CFL = c_0 \Delta t / h_H \approx 0.55$, where $c_0 = \sqrt{gd}$ is the linear shallow water wave celerity. The computation proceeds for 30 seconds during which the solitons travel over a distance of about 300 m.

Figure 5.13 shows the computed relative surface elevations ζ/d at $t = 30$ s and the corresponding theoretical solutions. The computed results are in good agreement with theory as the shape and height of the solitons are nicely preserved. The higher solitons reveal a celerity error which increases with the wave height up to about 4% for $H/d = 0.60$. Presumably this is

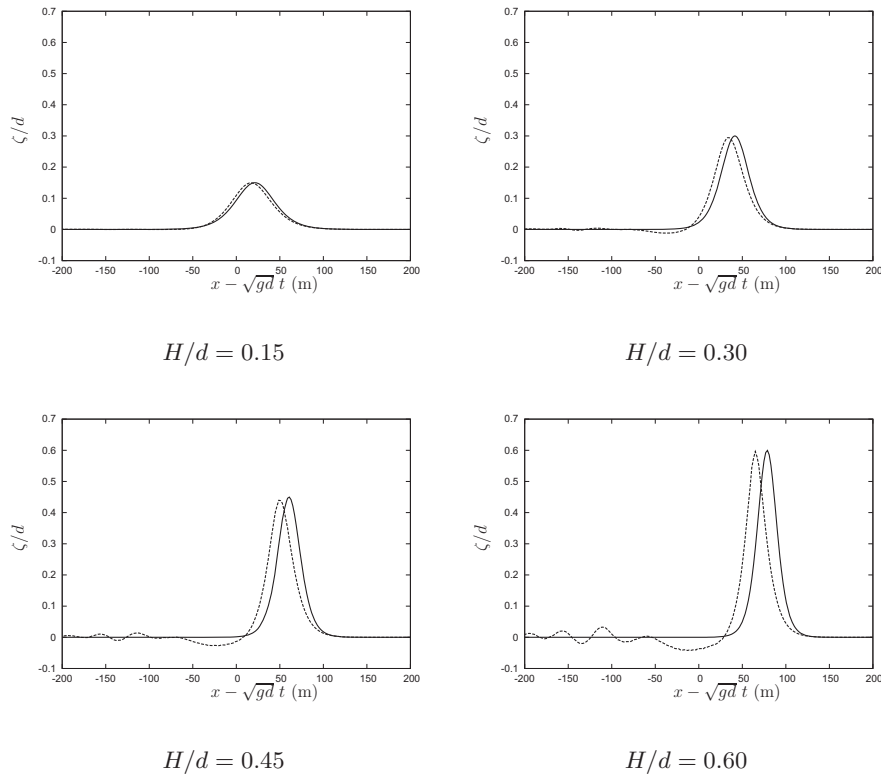


Figure 5.13: *Soliton: theoretical (solid) versus computed (dashed) surface elevation at $t = 30$ s for varying relative wave heights H/d .*

related to the non-linear advection terms and the associated dissipation by the upwind mechanism at the element interfaces. It should be mentioned however that Equation (5.139) is exact to second order of the relative wave height which may also partly explain this discrepancy.

5.5.3 Wave propagation over a submerged bar

The propagation of regular waves over a submerged bar has been investigated by Beji and Battjes [5] in a series of laboratory experiments. The wave flume used in the experiments has a still water depth of 0.40 m, and a trapezoidal bar was placed in the flume, with a minimum still water depth of 0.10 m above the bar. The length of the flume is 30 m. Waves are generated by a piston-type wave maker situated on the left-hand end of the flume (see Figure 5.14). The slope at the opposite end of the flume absorbs the waves, thereby avoiding reflections.

In the experiment considered here, referred to as Experiment A in Beji and Battjes [5], the imposed wave height at the left-hand end is 0.02 m and the wave period is 2.02 s. At the bar, bound higher harmonics are generated

which become free as soon as the waves leave the bar. The simulation of these higher harmonics is numerically demanding, and this problem has become a frequently used example test case for non-hydrostatic wave models [43, 84].

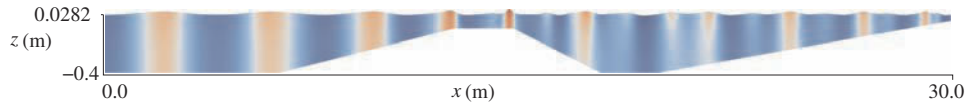


Figure 5.14: *Waves over a submerged bar: configuration of the experimental flume with snapshot of computed free surface and piezometric level (colour) at $t = 40$ s.*

The computational mesh of the flume uses triangular elements with an element size $h_e = 0.05$ m in the deeper part of the flume, yielding eight elements across the depth. Towards the shoal, the element size gradually decreases to $h_e = 0.025$ m, with the intention to accommodate the decreasing wave length and the emergence of higher harmonics at the shoal. The time step size Δt is set to 0.01 s. At the left-hand boundary, a harmonic normal velocity is imposed with an amplitude of 0.045 m/s. The right boundary has a weakly reflective boundary condition prescribing the normal velocity as $\mathbf{u} \cdot \mathbf{n} = \sqrt{g/d} \eta$, where $d = 0.05$ m is the local water depth. This treatment suppresses the reflection of waves back into the domain, as in the laboratory experiments.

Figure 5.15 shows measured and computed water levels at several stations along the flume. Shoaling and steepening of the waves in front of the bar (station 4) are reproduced well, and the computed bound higher harmonics at the bar (stations 5, 6 and 7) match the experimental measurements closely. The free propagation of the higher harmonic waves on the downward slope of the bar (stations 8 and 9) is computed reasonably accurately, but less well further from the bar (stations 10 and 11). Considering that the mesh is relatively coarse, the results are particularly encouraging.

5.5.4 Undulating flow downstream of a weir

The stationary flow over a weir features many interesting free-surface phenomena which are determined, in particular, by the Froude number at the crest of the weir. The Froude number is defined as ratio of the local fluid velocity to the celerity of surface waves. For Froude numbers slightly below one, undulating flows develop downstream of the weir. This phenomena has been investigated experimentally in a series of laboratory experiments by Wols et al. [98]. The experiment considered here concerns a horizontal flume having a width of 0.40 m and an upstream water depth of 0.31 m. The weir has a height of 0.15 m, relative to the bottom of the flume, and a length of 0.97 m. The weir has a rounded leading edge and a steep trai-

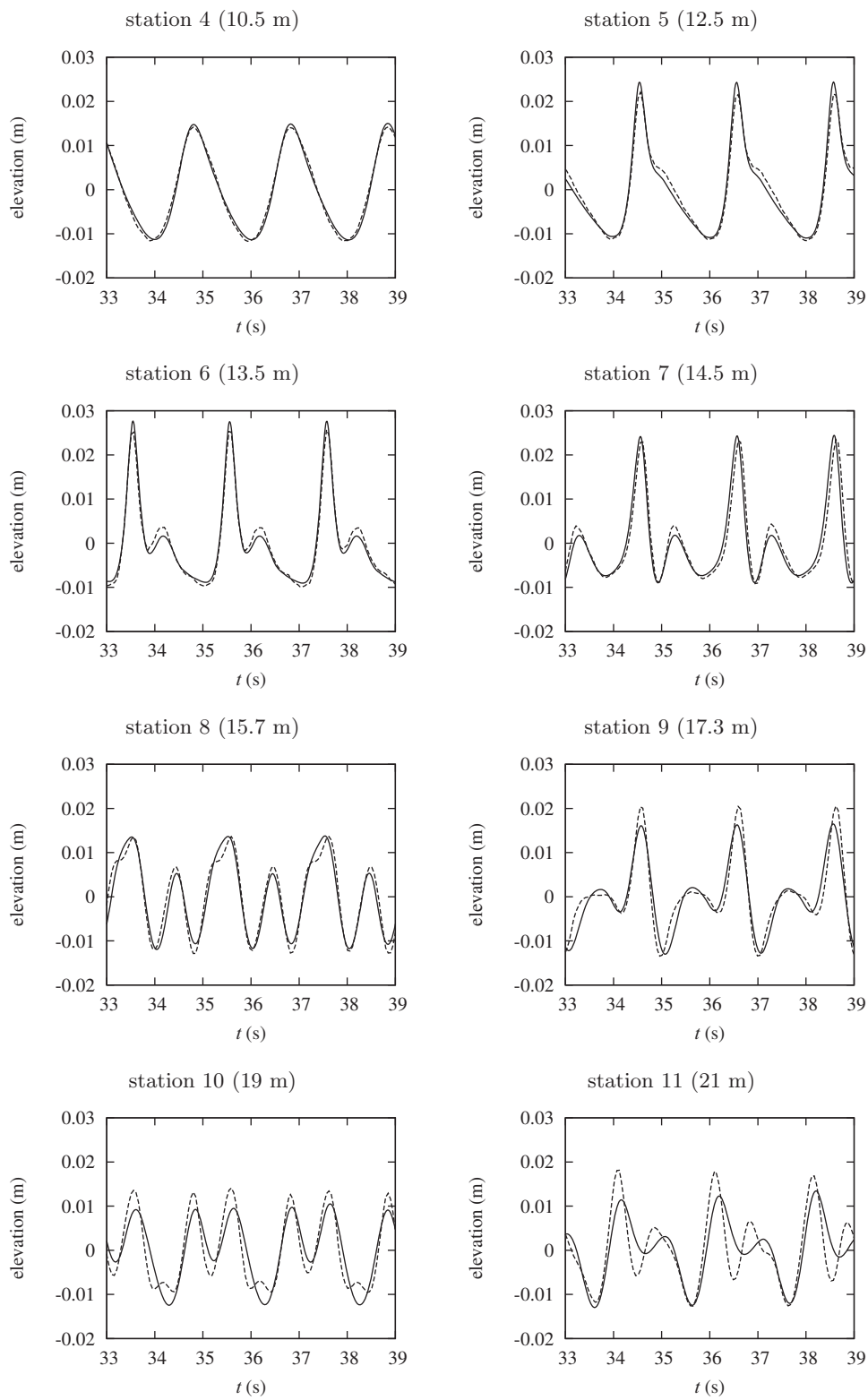


Figure 5.15: Waves over a submerged bar: time series of measured (dashed) and computed (solid) surface elevations.

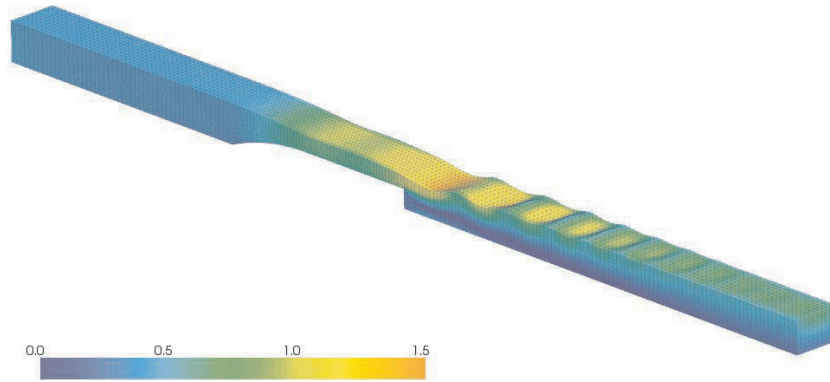


Figure 5.16: *Undulating flow: computed flow velocity magnitude (m/s).*

ling edge (see Figure 5.16). The discharge rate is 45 l/s. Water levels were measured visually by taking photographs from the glass side walls, while velocities were measured at the center line of the flume using laser Doppler anemometer probes.

The computational mesh consists of tetrahedral elements with an element size of $h_e \approx 0.025$ m. On the inflow boundary, a normal velocity of 0.36 m/s is specified, while at the outflow boundary the piezometric level is set to 0.26 m, in accordance with the experiment. The time step size Δt is set to 0.005 s. Flow separation at the trailing edge of the weir induces a turbulent mixing layer. The resulting momentum transport due to turbulent fluctuations is modelled by using a simple turbulence viscosity ν_t which is computed as

$$\nu_t = l_m^2 (\nabla^s \mathbf{u} : \nabla^s \mathbf{u})^{1/2}, \quad (5.141)$$

where l_m is the so-called mixing length, which is set to 0.01 m. The tangential shear stress at the vertical sides and the bottom of the flume is modelled by a quadratic friction law,

$$\mathbf{h} = c_f |\mathbf{u}| \mathbf{u}, \quad (5.142)$$

where c_f is a dimensionless friction parameter which is computed via a logarithmic wall-law. The form of c_f can be found in Appendix B.1. The wall-roughness height is set to $k_N = 0.1$ mm, which is a parameter used in computing c_f . Resolving the turbulent flow field sufficiently accurately is important as it determines the characteristics of the lee wave. The total simulation time is set to 75 s, during which time the surface profile has reached a stationary state.

The computed free-surface waves downstream from the weir are evident from the deformed mesh in Figure 5.16. Figure 5.17 shows the computed

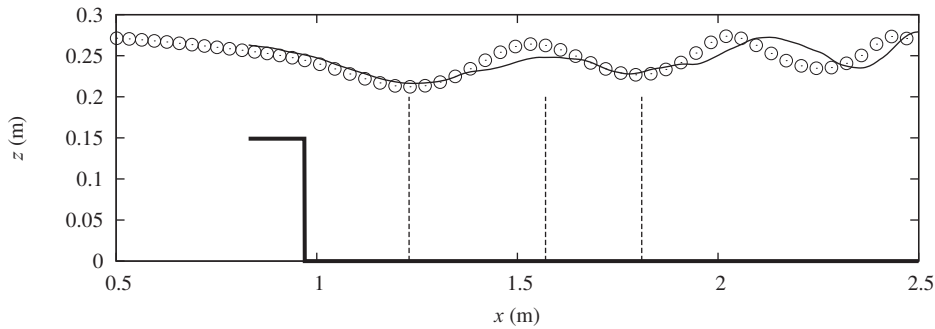


Figure 5.17: *Undulating flow: measured (solid) versus computed (circles) surface elevation behind weir, also showing the transects along which velocity measurements are made (dashed lines).*

and measured surface heights of the undulating flow along the side wall on the lee side of the weir. The computed wave amplitude and wave length agree well with the measurements, although the computed wave crests have a slight offset in the upstream direction. Figure 5.18 shows measured and computed velocity profiles at three transects at the center line downstream of the weir. Considering the relatively simple turbulence model that is used, the agreement is good. However, the mesh provides insufficient resolution and the mixing length model is too simple to model the details of the circulation zone which is situated directly behind the weir (station $x = 1.23$ m). Importantly, the drop in the piezometric level over the weir is computed accurately. The measured and computed values are 5.20 cm and 5.22 cm, respectively.

5.5.5 Sub-marine landslide

Motivated by studies predicting the generation of catastrophic waves should the Cumbre Vieja volcano at La Palma, Gran Canaria collapse [97], tsunamis generated by sub-marine landslides have been investigated experimentally in van Nieuwkoop [63]. The experiment involved a semi-ellipsoidal object which was dragged along a sloped bottom, creating outward radiating free-surface waves and waves bound to the moving object. The experimental set-up consisted of a 15 m wide and 24 m long basin in which the undisturbed water depth d varies with longitudinal position x , and is given by

$$d = \begin{cases} x/20 \text{ m} & 0 \leq x \leq 8 \text{ m}, \\ 0.4 \text{ m} & 8 \text{ m} < x \leq 24 \text{ m}. \end{cases} \quad (5.143)$$

The semi-ellipsoidal object of length 0.7 m, width 0.3 m and height 0.12 m, was moved along the bottom of the basin along the center line $y = 0$ at a constant speed. In the experiments, various starting positions of the object

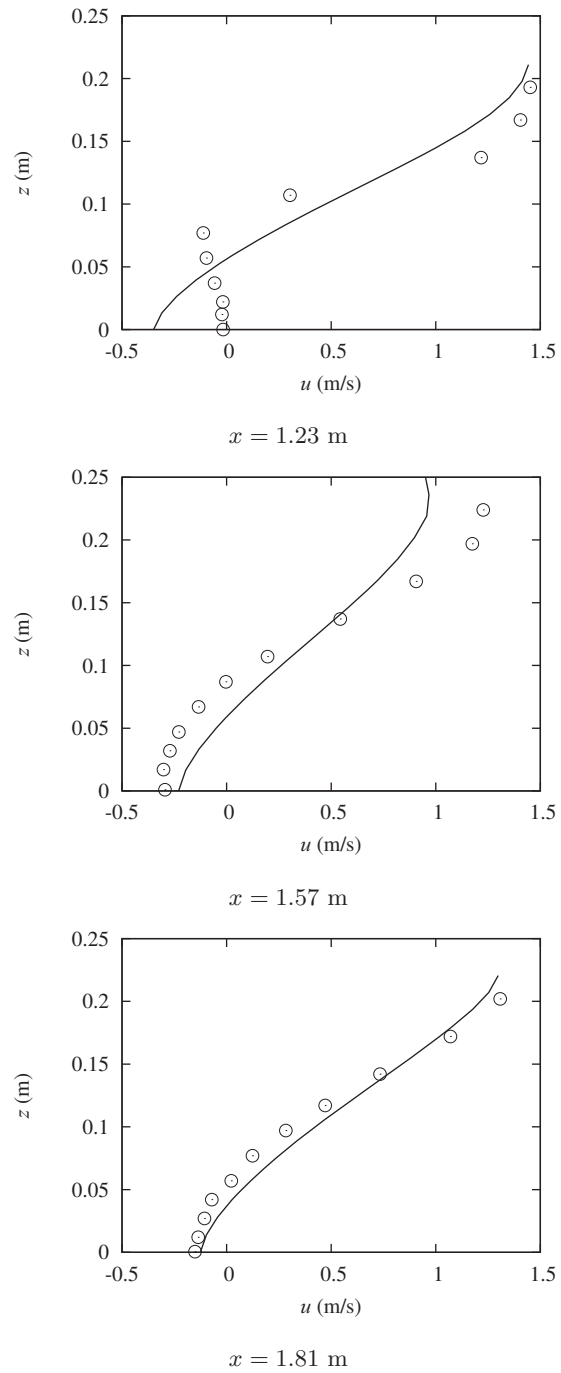


Figure 5.18: *Undulating flow: computed (solid) versus measured (circles) flow velocities in several transects behind weir (see also Figure 5.17).*



Figure 5.19: *Sub-marine landslide experiment [63].*

and speeds were used. A photograph of the experimental set-up is shown in Figure 5.19, which also illustrates the generated waves. At several locations, listed Table 5.1, the surface elevation was measured. Acoustic probes were placed at ‘g’ stations and capacitance gauges were placed at ‘a’ stations to measure the water height. A sampling frequency of 100 Hz was used.

The numerical simulation concerns a case with an initial position of the

station	g26	g27	g11	a1	a2	a3
x (m)	5.10	8.13	5.20	6.53	7.53	6.04
y (m)	0.51	0.52	3.52	0	0	4.22

Table 5.1: *Locations of surface elevation measurement stations for the sub-marine landslide experiments (object slides along the line $y = 0$).*

trailing end of the object of $x = 4.2$ m, $y = 0$ m and a constant speed of 1.3 m/s, measured along the slope, over a time interval of 2.3 s, after which the object is stopped abruptly. The effect of the moving object is modelled by deforming the mesh around the object by specifying a vertical mesh velocity at the bottom of the basin. Therefore, not only does the mesh move to accommodate the free surface, but also to model the solid object moving along the bottom of the basin. The problem is symmetric about the x -axis, hence it suffices to consider the region $y \geq 0$. The horizontal distance over which the waves radiate during the experiment is limited and the numerical domain may be taken smaller than the actual size of the wave basin. Therefore, the computational domain has a length, along the center

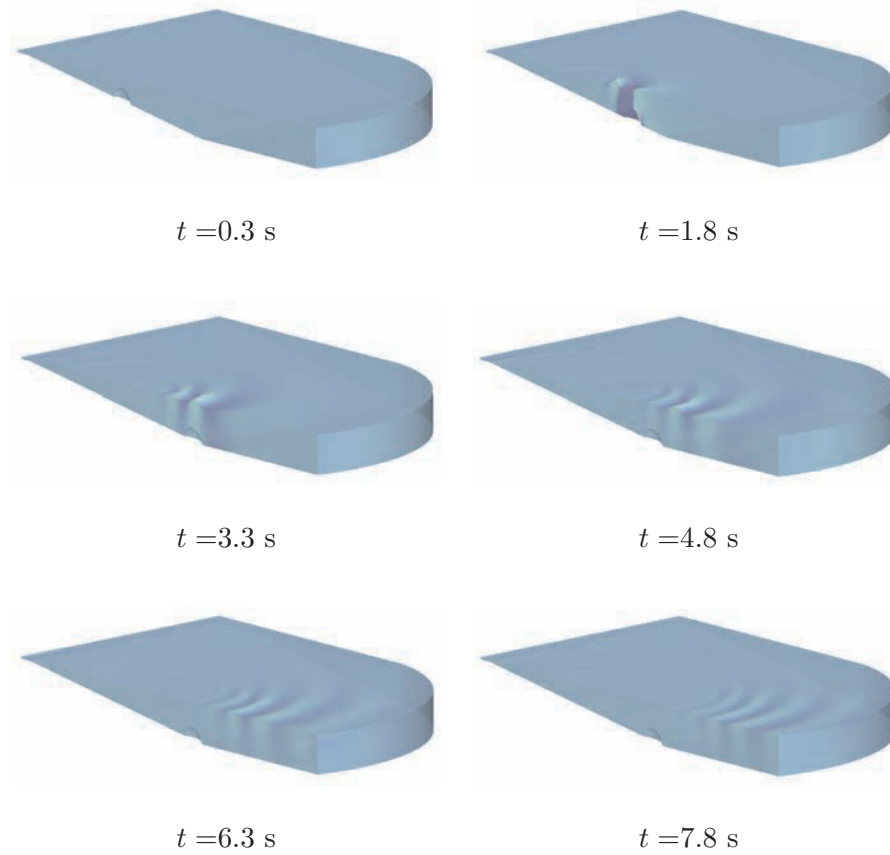


Figure 5.20: *Snapshots at increasing times for the sub-marine landslide problem showing the displacement of the free surface and the displacement of the bottom due to the slider. The figures have been stretched by a factor of three in the depth direction.*

line, of 13.2 m, a width of 7.5 m, while the side boundary has a straight section of 8 m, and an arc joins the side boundary and the center line. The element size h_e is approximately 0.04 m in the region around the path of the object and the measuring stations. Towards the lateral boundary, the element size on the horizontal plane increases to approximately 0.08 m. The time step size Δt is set to 0.01 s.

Snapshots showing the computed surface elevation and position of the moving object are shown in Figure 5.20. The basin is relatively shallow, so the figure has been stretched by a factor of three in the depth direction for illustrative purposes. The computations feature a low leading wave, a surface depression above the object and a high trailing wave, which is in accordance with the experimental observations. Figure 5.21 shows the computed surface elevations as a function of time at the different measuring

stations. The computed elevations are in good agreement with the experimental measurements, both in terms of the wave height and the wave-phase. The correspondence is generally better at the ‘a’ stations.

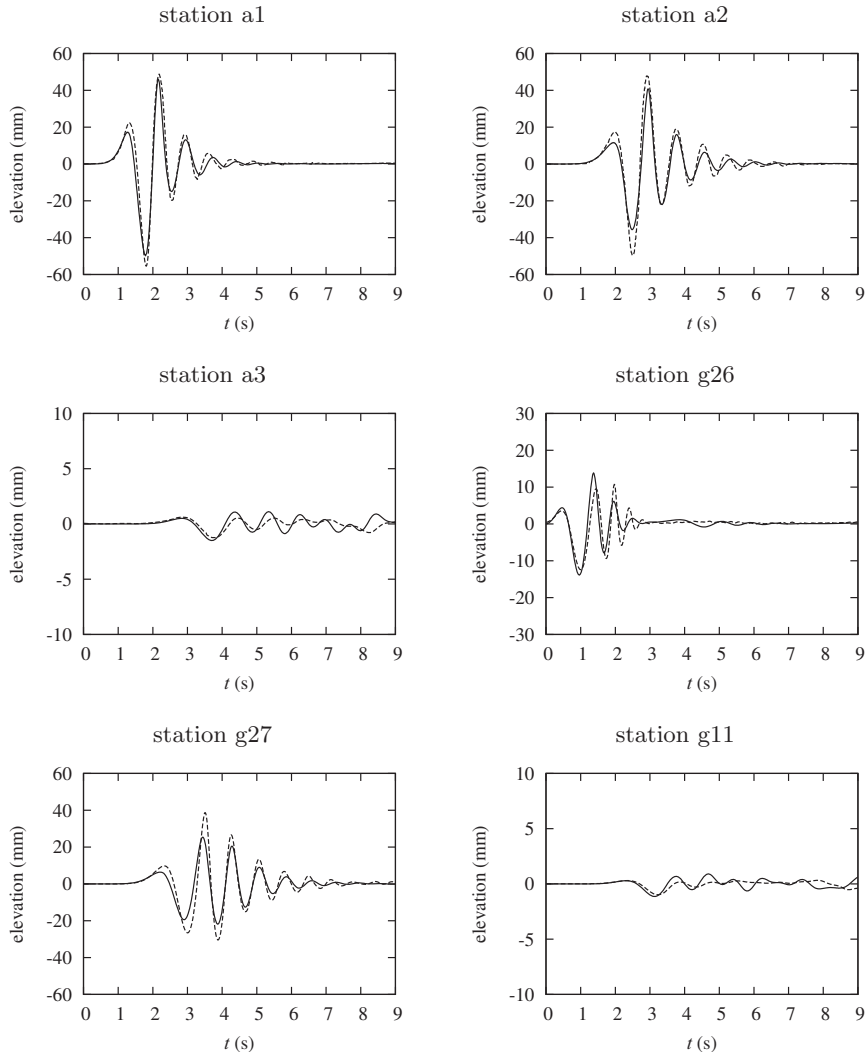


Figure 5.21: Measured (dashed) and computed (solid) time series of the surface elevation for the sub-marine landslide problem at various measuring stations as given in Table 5.1.

The physics of the landslide generated tsunami is essentially different from that of tsunamis following a large mega thrust earthquake, see Pietrzak et al. [67]. The shorter length scale and longer time scale of the former leads to the formation of relatively much lower waves, see also the classical paper by Hammack [32]. This fundamental difference has caused considerable



Figure 5.22: *Haringvliet barrier during construction.*

confusion in literature and in public discussion.

5.5.6 Practical application: storm surge barrier

The barrier in the Haringvliet estuary, the Netherlands, is one of the major construction works that were completed as a part of the ‘Delta Plan’ after the catastrophic flood of 1953. The barrier consists of a series of long-crested weirs with circular shaped ‘sector’ gates which are closed during high tide and partly opened during low tide in order to discharge the river water, see Figure (5.22). The resulting change of the tidal regime in the area has affected the ecological condition of the Haringvliet delta. Restoring the tidal motion, by opening a few gates permanently and to close the barrier only in case of a storm surge, should mitigate these effects. The consequence of the inflow of sea water has been the subject of many investigations, as part of which some gates were opened for five days in March 1997 while measuring, amongst others, the flow velocities and salinity distribution in the vicinity of the barrier [40].

The numerical example concerns a maximum flood situation as observed on March 12th, 1997, at 4:50 am with a gate elevation of 2 m. The employed finite element mesh is shown in Figure 5.23. Each discharge sluice has a crest height of 5.5 m below mean sea level, a total width of 58.5 m and a cross-sectional width between the pillars of 53 m. The domain of interest extends over 200 m towards the river and the sea sides, respectively. As the situation is symmetric about the center line of the barrier it suffices to consider one half of its cross section. The tetrahedral elements have an average size of

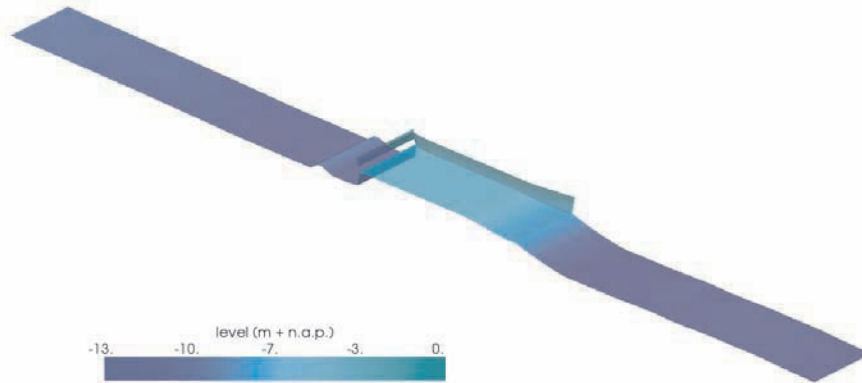


Figure 5.23: *Mesh configuration Haringvliet barrier showing crest, stilling basin, side walls and gate (with sea side on the left).*

0.5 m near the gate increasing to 3 m towards the sea and river boundaries, respectively. At both open ends a Neumann boundary condition is specified, imposing a zero tangential stress and piezometric levels of 1.49 m and 0.39 m on the sea and river side, respectively, as observed during the measurements [50]. At the bottom and side walls a partial slip boundary condition is specified, using a Nikuradse roughness height $k_N = 0.05$ m to compute the friction parameter c_f while the turbulence viscosity is computed from the mixing length model with a mixing length $l_m = 0.5$ m, see Appendix B. The numerical results were not very sensitive to the precise value of k_N nor l_m . At maximum flood, the density difference between sea and river hardly influences the flow field due to the intense mixing within the sluice, which is also confirmed by field observations [40]. The present computations are therefore performed with the density coupling terms switched off. Density effects may however become important further away from the barrier or during situations with smaller flow velocities and/or smaller gate openings.

The computed flow field is shown in Figure 5.24. The flow accelerates towards the gate from which a jet-like flow structure emerges. Due to flow stagnation and contraction at the leading edge of the pillar the flow velocities are relatively high near the side wall of the pillar. The jet gradually diffuses across the depth and the width of the barrier. Near the trailing edge of the pillar a small recirculation zone persists close to the side walls. The computed piezometric level along the center line of the barrier is shown in Figures 5.24a. The piezometric level is minimum at the maximum contraction point and gradually increases in several stages while the cross-sectional profile increases. Figure 5.24b shows computed and measured velocity profiles in a vertical transect positioned at a distance of 67 m from the heart of the barrier, measured in downstream direction. The observed velocity

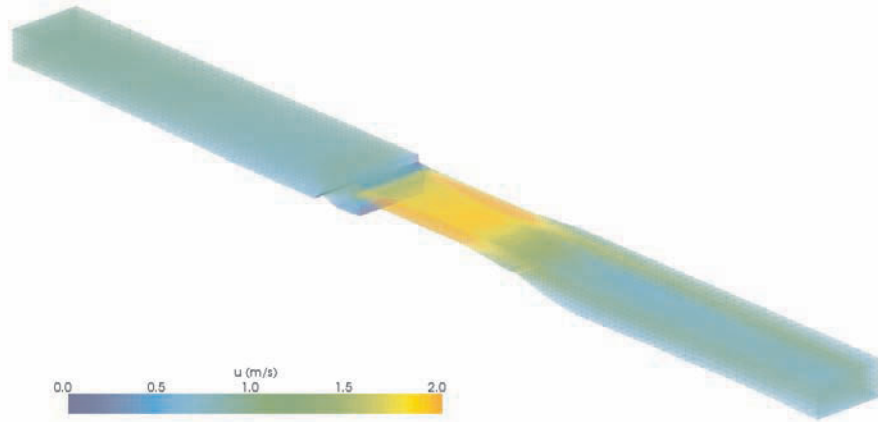


Figure 5.24: *Haringvliet barrier: computed velocity field during flood.*

profile reveals a recirculation zone near the bottom. The computed velocity profile matches the measured (ADCP) profile closely. The good results are remarkable given the simple turbulence model that is used. As shown in Figure 5.24b the more sophisticated $k - \epsilon$ model, the implementation of which is described in Appendix B, is less convincing in this particular application.

5.6 Conclusion

In this chapter the GIS finite element method has been generalized to the incompressible Navier-Stokes equations on moving domains with free surfaces. The formulation has been specialized for a class of geophysical flow problems in which the pressure can be replaced by the piezometric head, which leads to an elegant description of the free-surface dynamics. The stabilization mechanism due to the upwinding has been elucidated by examining the kinetic and potential energy balance implied by the model. Particular attention has been paid to the details of a predictor-corrector method used to advance the model in time in the context of a moving domain. The continuity constraint has been reformulated such that the convective velocity field on the new mesh satisfies a discrete form of the geometric conservation law. It was demonstrated that discrete mass and momentum are conserved in terms of the numerical fluxes.

As for the Navier-Stokes problem on the fixed domain, the GIS approach leads to stable results with minimal numerical dissipation. This is particularly important for the target application of geophysical flows, and free-surface waves in particular, in which advective effects often dominate and excessive numerical dissipation can alter the fundamental physics of a problem. It has been demonstrated via numerous complicated examples that

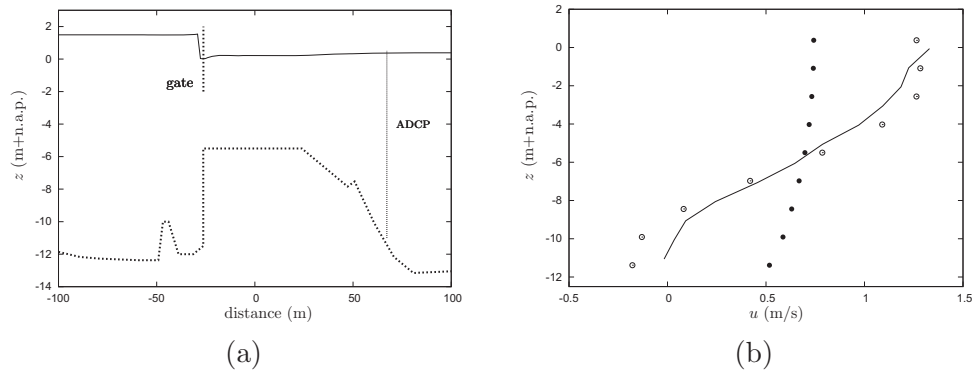


Figure 5.25: *Haringvliet barrier: computed surface level along center line also showing vertical transect velocity measurements (a); measured (solid) and computed velocity profiles in transect (b), mixing length model (circles) and standard $k - \epsilon$ model (dots); n.a.p. refers to Dutch reference level.*

the approach is robust, and indeed negligible artificial dissipation is introduced, which is particularly evident in the numerical examples which involve periodic free-surface motion.

Chapter 6

General discussion and outlook

6.1 General discussion

Evidently, there is a trend in environmental hydraulics focusing on small-scale flow and transport phenomena, varying from the breaking of waves on a beach to complex flows in the vicinity of man made objects such as weirs, barriers, sluices and outfalls. The finite element method may be adopted as a numerical tool for these problems as it allows complex geometries to be modelled accurately and efficiently. Chapter 1 gives some examples which clearly demonstrate the convenience of finite element methods in practical applications.

Finite element modelling is generally complicated by the unstructured topology of the underlying computational mesh. Problems involving a large number of unknowns therefore result in large sparse matrix systems whose solution typically relies on iterative solution procedures [69]. To minimize the computational burden the associated sparse matrix structure should be kept as simple as possible. This requirement is partially met by continuous Galerkin (CG) methods which, given a certain polynomial order, lead to a minimum number of floating point operations per iteration step, which is demonstrated in Chapter 2. However, in the context of environmental flow problems, continuous methods generally suffer from instabilities arising from either dominant advection terms or from the incompressibility constraint. The suppression of these instabilities, without violating consistency, has been the topic of many investigations starting with the pioneering work of Brooks and Hughes [10]. Typically, the numerical fluxes are modified using residual based terms which automatically guarantees consistency. Since the discrete flux differs from the modified flux conservation may be violated, especially when an advective field is obtained from a stabilized formulation [37]. Discontinuous Galerkin (DG) methods are superior to CG methods in

that upwind fluxes on element interfaces are naturally defined such that advective instabilities are avoided. Satisfaction of the inf – sup condition, which guarantees stable pressure-velocity coupling, is easily accomplished by expanding the velocity in a discontinuous space which includes the gradient of the pressure space. An impediment for using DG models is the proliferation of degrees of freedom which renders the solution of implicit problems time consuming. Explicit time stepping poses a strong limitation on the allowable time step size, given the target applications of small scale, advection dominated flow problems.

In this thesis a computational framework has been developed which combines the unique properties of DG methods and the computational structure of CG methods. Crucial in this respect is the use of continuous functions that are defined on element interfaces and that are left undefined on element interiors. In this way a particular field v is spanned by a discontinuous space V defined on element interiors and a continuous space \bar{V} defined on interfaces, such that $v \in V \oplus \bar{V}$. The decomposition is unique since $V \cap \bar{V} = \emptyset$ which avoids ambiguities that would arise when choosing \bar{V} as a continuous sub space of V [35]. The states in two adjacent cells interact via the interface function. To this end the interface fluxes, which appear in the general DG formulation, are written in terms of the interface variable and the traces of element functions on element boundaries. This procedure is similar to the determination of an intermediate flux in a particular class of Riemann solvers except that flux continuity is imposed weakly in \bar{V} [33, 56]. For a proper choice of the flux formulation, this leads to a set of local problems on elements for which the interface variable provides a weak Dirichlet boundary condition. The local degrees of freedom can be eliminated yielding a global problem for the interface degrees of freedom which has the same structure as that of the corresponding CG method. After solving the global problem, the local solution is obtained via element wise back substitution. This final step guarantees conservation in terms of the discrete flux, in contrast to residual based stabilization methods [87]. This feature is also shared with methods employing bubble degrees of freedom such as the MINI element [7]. A marked difference with the former is the use of discontinuous functions which involves the construction of discrete operators acting on the jump discontinuities at element boundaries. Being slightly more complicated, this also gives near-optimal stability. The proposed Galerkin Interface Stabilization (GIS) method is consistent and conservative. A stability and *a priori* error analysis is not trivial since GIS has the mathematical structure of a mixed problem. In fact, the interface variable plays the role of a Lagrange multiplier enforcing weak flux continuity across element interfaces. This requires the satisfaction of an inf – sup condition, the proof of which is not pursued in his thesis. Various examples, ranging from simple advection-diffusion problems to advanced non-linear surface wave propagation, have however revealed remarkable stability properties for linear elements.

In Chapter 3 the GIS method is explored for the scalar advection-diffusion problem. Using linear elements, the algebraic format of the resulting equations is similar to that of the Streamline Upwind Petrov-Galerkin (SUPG) method. In the linear case the GIS procedure requires nothing but the standard CG element matrices and an element wise stabilization matrix which involves integration over element boundaries. Hence, the GIS method can be implemented efficiently in existing CG codes. A potential drawback is the computation of the stabilization matrix which endures a matrix inversion on each element. While the matrix to be inverted can never become singular, due to the formulation of the local problem, this operation may somewhat reduce the computational speed compared to conventional CG methods. For a simple one-dimensional problem optimal behaviour is established across all Péclet numbers for a fixed value of the penalty parameter α , which appears in the computation of the interface flux in order to suppress a potential instability associated with the diffusive terms [1]. This robustness is an advantage over residual based methods where the stabilization parameters must be adjusted to the flow regime. Bubble elements face similar difficulties as the optimal ‘bubble’ is also a function of the flow condition in an element [75, 81]. In two and three dimensions optimal values for α can not be established analytically but good results are obtained using the optimal value from the one-dimensional analysis. Multi-dimensional solutions are not monotone which becomes especially manifest at outflow Dirichlet boundaries. The value of the interface function imposed at the outflow boundary affects the flux towards all elements connected to the associated boundary nodes which therefore loses its upwind nature. Although this overshoot remains localized, a better option is to use Neumann boundary conditions at such boundaries. At characteristic boundary layers over/undershoot is less pronounced, typically a few percent of the jump. Altogether, the method is perfectly suited for practical transport problems as demonstrated by an example concerning long term sediment dispersal in the North Sea [71].

In Chapter 4 the GIS method is applied to the incompressible Navier-Stokes problem, focusing on small-scale advection dominated problems. The advection-diffusion part of the momentum equations can be treated in a similar way as the scalar transport problem using a discontinuous velocity space on elements in combination with $H^{1/2}$ continuous interface velocity spaces on element interfaces. The non-linearity of the advective fluxes requires a careful formulation of the associated interface terms and the time stepping scheme. Numerical examples of the one dimensional Burgers’ equation show that non-linear shocks and rarefactions can be reproduced accurately with a minimum of over/undershoot. The pressure gradient, which appears as a source term in the momentum equations, can be included consistently if the pressure space is H^1 continuous. If the associated gradient space lies within the discontinuous velocity space, the inf – sup stability condition is satisfied automatically. This suggests using equal-order spaces for the pressure and

the velocity, respectively, where the linear $P^1 - P^1$ element pair is obviously the simplest choice. The practical implementation of this element pair is particularly elegant due to the cancellation of various second order terms. The resulting elimination procedure for the momentum equations leads to a global equation for the velocity and pressure unknowns which reside in the same nodes. The system can be solved efficiently using compressed Block Sparse Row (BSR) techniques, after which the velocity field on elements is obtained in an explicit back substitution step. Due to the formulation of the incompressibility constraint the discrete velocity field is weakly divergence free. This guarantees that the velocity-pressure coupling does not introduce artificial dissipation, in contrast to pressure stabilized Petrov-Galerkin methods [87]. Quantities defined in a subspace of the pressure space can be advected stably while avoiding stability problems when a conservative formulation is chosen [37]. Similar properties hold for the discrete Navier-Stokes problem if a Picard linearization is used with the discrete velocity from the previous time step as the advective field. The minimal damping, and stable momentum advection of the $P^1 - P^1$ GIS model enables large eddy simulations, as confirmed for an example with Borda's mouthpiece. Besides, consistent inclusion of the forcing terms, inherited from the GIS procedure, significantly improves the numerical behaviour of internal waves compared to methods using conventional upwinding for the advection of the density field [49]. The Navier-Stokes and density transport equations are coupled in a semi-implicit fashion, outlined in Appendix A, which imposes no serious constraints on the allowable time step size given the relatively small celerity of internal waves.

The extension to free-surface flows, an important class of problems in environmental fluid mechanics, is not as straightforward as may seem in first instance. In Chapter 5 the arbitrary Lagrangian-Eulerian (ALE) framework is used to reformulate the Navier-Stokes equations in terms of quantities defined on a constant reference domain. For a given motion of the spatial domain, the resulting system of equations has the same format as on the fixed domain and can be readily solved using the GIS approach with a Picard linearization of the advective velocity. Unlike cases with a fixed domain, momentum is not conserved for arbitrary mesh motion due a discrepancy between discrete volume changes and the divergence of the mesh displacement [29]. For free-surface flows the domain motion is not known beforehand but follows from the surface position which is obtained naturally by expressing the pressure variable in terms of the piezometric level. The mesh is advanced in time using an estimate of the new free-surface position which is obtained from a second order accurate extrapolation in time. The explicit nature of the mesh update procedure may induce instable free surface behaviour in near-critical flow conditions. The underlying mechanism is not yet fully understood but can be avoided by taking the Courant number smaller than one. For free-surface problems the domain motion is restricted to the ver-

tical direction only. In combination with the chosen time stepping scheme this leads to discrete geometric conservation. For the $P^1 - P^1$ element pair a predictor - corrector scheme has been implemented which satisfies mass and momentum conservation for vertically moving surfaces. An additional advantage is that one time step involves the solution of independent systems for each separate velocity component and the piezometric level, respectively, which is an obvious advantage over the fully coupled scheme developed in Chapter 4. As a consequence the tangential velocity can not be imposed on inflow Neumann boundaries which may lead to instabilities. Linear wave test cases reveal negligible damping. Non-linear waves are however attenuated, depending on the mesh size and time step relative to the wavelength and wave period, respectively. As shown by theoretical analysis this dissipation is attributed to the upwind mechanism at the interfaces rather than to the deformation of the mesh, which is confirmed by an example of large amplitude surface oscillation in a U-shaped tube. For moderate wave amplitudes, the associated flow velocities introduce only a small amount of upwind dissipation and excellent results are obtained for a number of tests involving advanced laboratory experiments. From examples concerning a long crested weir and the Haringvliet storm surge barrier, respectively, it is evident that the flow separation downstream of discharge structures requires reliable turbulence modelling. The performance of the standard $k - \epsilon$ model, the implementation of which is outlined in Appendix B, is still questionable in this respect.

Concluding, GIS is a promising finite element method which can be used to simulate a wide range of flow and transport problems in environmental hydraulics. The general variational framework can be applied to a much wider class of problems including structural mechanics and notably the shallow water equations, for which the corresponding GIS variational form is given in Appendix C. Various favourable properties of the method enable accurate simulation of many interesting, detailed flow phenomena. In terms of computational speed, GIS may not be as efficient as methods employing structured grids. Yet, practically relevant flow problems can be handled successfully with reasonable computational effort.

6.2 Outlook

Motivated by its transparent structure and the numerical examples given in this thesis the GIS method warrants further analysis and development. This section gives some suggestions for topics which are worthwhile exploring in more detail.

While this thesis primarily considers linear basis functions a rigorous error analysis for arbitrary polynomial orders could reveal other, possibly interesting, combinations of local and interface function spaces. In particular,

the approximation of local fields by higher order polynomials is interesting as this would increase the accuracy of the method while retaining the same number of global degrees of freedom. The required theoretical analysis is however non-trivial since the method has the structure of a mixed formulation which for stability requires the satisfaction of an inf – sup stability condition.

The GIS method has revealed near optimal behaviour for advection- diffusion problems. Yet, results are not monotone in the high Péclet number range if the solution involves steep gradients. Although numerical solutions of Burgers’ equation have shown stable non-linear shock propagation, non-monotone behaviour may become problematic when dealing with strongly non-linear transport problems, for instance sediment transport. Given the correspondence of the scheme with the SUPG method ‘discontinuity capturing’ flux formulations may be pursued to obtain crisp solutions of problems with discontinuities. For the scalar transport equation, GIS stabilization is not strictly necessary if explicit time stepping schemes are used. In this case the problem can be stabilized efficiently by using the interfacial DG fluxes directly. Schemes may be developed that exploit this property by switching automatically to implicit GIS stabilization, where dictated by the local Courant number, while the more efficient explicit DG scheme is used elsewhere.

While continuous pressure fields are employed to discretize the Navier-Stokes equations, discontinuous pressures could pose certain advantages. Most importantly, the incompressibility constraint can be satisfied element wise, although efficient solution of the resulting elliptic pressure equation would require an interface pressure field. Various alternative discrete forms of the momentum advection and diffusion terms have different energy and momentum conservation properties. By adapting the scheme locally to the prevailing flow conditions, subgrid dissipation may be captured accurately which will guarantee energy conservation in contracting flows and momentum conservation where the flow diverges. Turbulence modelling requires special attention. As the GIS method can be given a variational multi-scale interpretation, alternative LES strategies can be pursued using the difference between local and global velocity fields to define the turbulence closure terms. Lagrangian averaging of the Navier-Stokes equations is an interesting new approach that would fit seamlessly into the GIS framework. The present results of the standard $k - \epsilon$ model are not yet convincing in cases with flow separation. The discretization of the source and boundary terms involves certain numerical ‘tricks’ which must be addressed more carefully to improve the performance in these situations.

The present implementation of the GIS procedure for free-surface flows is based on vertically moving meshes. Application is therefore limited to situations with vertical lateral boundaries. Extension to sloping or moving lateral boundaries requires an algorithm which allows for arbitrary mesh motion.

Particular attention must then be paid to discrete geometric conservation the satisfaction of which is not trivial, yet crucial for volume and momentum conservation. The surface wave problems in this thesis concern non-breaking waves. In principle, the model can resolve spilling breakers as well but further testing is needed to verify if surf-zone dynamics, including wave induced circulations, can be reproduced correctly. The precise formulation of momentum advection terms may play an important role here. Practical improvements of the free-surface model concern the efficiency when dealing with quasi two-dimensional geophysical flows. By using vertical stacks of elements instead of allowing arbitrary mesh topologies the nearly-horizontal structure of these problems can be exploited to enhance the computational performance. It is thinkable that splitting the pressure into hydrostatic and non-hydrostatic components may also reduce the computational burden. Utilization of flow models in three-dimensional situations requires parallel computing techniques for which the interface functions, inherited by the GIS formulation, may prove useful in decoupling sub domains.

Finally, the general mathematical format of the GIS method can be applied to a much wider class of problems, including compressible gas flow or solid mechanics. Of particular interest in the field of environmental fluid mechanics are the shallow water equations. The further development of a GIS shallow water model should address specific issues such as flooding and drying and non-linear breaking waves (bores). In this respect the present results for Burgers' equation are promising as stable results for non-linear shocks were obtained without any form of limiting.

Chapter 7

Summary/samenvatting

7.1 Summary

‘Finite element modelling of transport and non-hydrostatic flow in environmental fluid mechanics’

In this thesis a numerical method is designed for solving the advection-diffusion and incompressible Navier-Stokes equations on unstructured finite element meshes with moving free surfaces, although the presence of a free surface is not strictly necessary. The resulting model is applicable to a wide range of flows encountered in environmental engineering practice and is primarily aimed at situations involving complex, small-scale geometries and non-hydrostatic pressure. From the onset, no assumptions are being made concerning a ‘preferred’ direction in the mesh. More specifically, the vertical direction is treated in the same way as the horizontal directions thus allowing intrinsic three-dimensional geometries. The resulting mesh can be built of triangles or tetrahedrons having an arbitrary shape and orientation. This flexibility is particularly useful in engineering projects as it allows a quick set-up or modification of a computational mesh enabling the interactive use of the model in a design process. In Chapter 1 some practical examples are shown which clearly demonstrate these favourable properties.

At the same time, the above starting points lead to a number of practical difficulties that in some way have to be circumvented. First, the matrices evolving from the spatial discretization on unstructured meshes are inherently difficult to manipulate when performing algebraic operations, except for matrix-vector multiplications. This imposes some constraints on the solution algorithms that can be adopted. Obviously, this calls for a simple mesh topology where each node has a minimum number of direct neighbours. In Chapter 2 the continuous and discontinuous Galerkin methods are compared with particular emphasis on the resulting computational structures. For a simple elliptic problem it is demonstrated that, while yielding the

same order of convergence, the discontinuous Galerkin method is outperformed by the continuous Galerkin method in terms of work load, moreover when considering three-dimensional problems. Second, discrete flow and transport problems may suffer from: (1) instabilities associated with the advection terms and (2) instabilities due to the incompressibility constraint. Both types of instabilities become particularly manifest when using continuous methods. Advective instabilities may be suppressed by modifying the advective fluxes using stabilization terms which must be judiciously formulated. Instabilities due to the incompressibility constraint are more difficult to avoid in that different function spaces have to be chosen for the continuous pressure and velocity fields where the latter generally requires a higher order approximation. This leads to an even more complex data structure requiring different mesh topologies for the velocity and pressure unknowns. Alternatively, stabilization terms may be added explicitly to the formulation but ensuring sufficient stability without the introduction of excessive dissipation can become problematic. In this respect, discontinuous methods are more attractive due to the ease with which the fluxes at element interfaces can be formulated such as to gain complete control over the instabilities.

To this end a general variational framework has been developed which blends the favourable properties of continuous and discontinuous finite element methods. The formulation bears similarity with continuous Galerkin methods in that the resulting sparse matrix system has the same computational structure, involving only global degrees of freedom. All element matrices, computed during the assembly process, are standard except for a local mass matrix which involves integration over element boundaries. The similarity with discontinuous Galerkin methods stems from the use of upwind formulations at element interfaces where the local discontinuity of the solution is exploited to construct an upwind biased flux that stabilizes the formulation. However, unless classical discontinuous Galerkin methods, the proliferation of degrees of freedom is completely avoided. This is effected by rendering the interface flux dependent on an auxiliary global variable, which is defined on interfaces, and on terms local to an element. In this way, the interface variable provides a weak Dirichlet boundary condition for the local problem on each element. This feature enables the elimination of the local degrees of freedom from the system, through static condensation, in favour of the global interface variable. An equation for the interface variable is formulated by requiring weak continuity of the interface flux across element interfaces. In this way the interface variable acts as a Lagrange multiplier enforcing this constraint.

In Chapter 3 this approach, coined Galerkin Interface Stabilization (GIS) method, is explored for the linear advection-diffusion problem. The advective part of the interface flux is constructed using an upwind formulation where on an inflow element boundary the flux is determined by the interface variable whereas it is determined by the local element flux on outflow

element boundaries. The diffusive part of the interface flux contains the element diffusive flux plus a penalty term involving the jump between the interface variable and the local field on an element, in a way similar to the Interior Penalty method. The resulting semi-discrete formulation is consistent and conservative. In the advective limit, the quadratic norm can not increase if the transport velocity is divergence free. In the diffusive limit the penalty parameter has to be chosen sufficiently large in order to ensure energy stability. The fully-discrete problem is elaborated using linear basis functions for the advected field combined with θ -methods for time stepping. The matrix equations on the element level are obtained by multiplying the standard continuous Galerkin terms with an element wise ‘stabilization’ matrix. For stationary, one-dimensional problems the resulting stabilization is near-optimal for a fixed value of the penalty parameter which leads to second order convergence in the \mathcal{L}_2 error-norm. Various examples show that the method is accurate and involves minimum artificial diffusion. However, solutions are not monotone and in two or three dimensions significant overshoot may develop at outflow boundary layers.

Chapter 4 extends the GIS method to the incompressible Navier-Stokes problem on a fixed domain. The momentum equations are treated, component wise, in a similar way as for the advection-diffusion problem using a continuous pressure field to evaluate the pressure gradient on elements. The local velocity field, which can be expressed in terms of the interface velocities and the local pressure gradient, is used in the weak form of the incompressibility constraint. This procedure yields a consistent stabilization of the continuity equation due to the emergence of a Laplacian pressure stabilization term. The method contains no flow-dependent stabilization parameters and is able to model a wide range of flow conditions stably without user intervention. Moreover, as instabilities associated with the incompressibility constraint are naturally suppressed, the use of equal-order basis functions for the velocity and pressure fields is permitted. An implementation is described for the $P^1 - P^1$ element pair adopting a monolithic solution procedure using efficient Block Sparse Row (BSR) techniques. The resulting flow solver is particularly efficient since the same number of unknowns results as for linear continuous Galerkin methods on the same mesh. For a steady linear Stokes problem $\mathcal{O}(h^2)$ and $\mathcal{O}(h^1)$ convergence rates are observed for the \mathcal{L}^2 error-norms of the velocity and pressure, respectively. Numerical examples concerning internal wave propagation confirm that negligible numerical dissipation is introduced by the stabilization mechanism. In particular, the performance of the method near shocks is promising as shown by numerical tests for the Burgers’ equation. The low artificial dissipation allows large eddy simulation (LES) which is demonstrated by an example concerning Borda’s mouthpiece.

In Chapter 5 the flow and transport model is generalized to moving domains and free-surface problems. To this end the incompressible Navier-

Stokes equations are restated on a constant reference domain as this avoids ambiguities with respect to the precise form of the time integration scheme. An additional complication in free-surface problems is the dependence of the domain motion on the free-surface movement, the determination of which is part of the solution process. The kinematic free-surface boundary condition is therefore reformulated using the piezometric level, instead of the pressure, which naturally defines the position of the free surface. Particular attention has been paid to the formulation of a predictor-corrector time stepping scheme in the context of a moving domain. The fully-discrete continuity constraint has been formulated such that the convective field on the new mesh satisfies a discrete form of the geometric conservation law (D-GCL), which is pivotal in proving discrete mass and momentum conservation. It is shown that for linear free-surface waves negligible dissipation is introduced while non-linear waves are slightly damped due to the upwind terms at element interfaces. Numerical examples provide an extensive comparison with analytical solutions and experimental data. The results confirm that the approach is robust and that little artificial dissipation is introduced which is particularly evident in the tests involving periodic free-surface motion. For two examples concerning discharge structures, a long-crested weir in a laboratory flume and the Haringvliet storm surge barrier (The Netherlands), the net head losses are computed accurately.

Concluding, the GIS method reconciles the attractive upwinding possibilities of discontinuous Galerkin finite element methods and the efficiency of continuous methods. The method is elegant and exhibits superior stabilization properties compared to conventional stabilized finite element methods, especially for dominant advection and free-surface problems. As such the method is promising and warrants further understanding and analysis. Chapter 6 provides some suggestions for further research. While this thesis is primarily directed at linear basis functions, a rigorous error analysis for arbitrary polynomial orders could reveal other, possibly interesting, combinations of local and interface function spaces that are worthwhile exploring. This analysis is non-trivial since the method has the structure of a mixed formulation which for stability requires the satisfaction of an inf – sup condition. As the GIS method lacks monotonicity in multi-dimensional advection problems modifications may be pursued in order to better resolve sharp fronts and steep boundary layers. Given the resemblance of the method with SUPG stabilization it should be possible to construct a discontinuity capturing form of the interface flux. Owing to its general variational format the GIS method can be applied to a much wider class of problems, including the shallow water equations (SWE) which would entail specific issues such as flooding and drying algorithms. Practical improvements of the model concern the efficiency when dealing with quasi two-dimensional geophysical flows. By using vertical stacks of elements instead of allowing arbitrary mesh topologies the nearly-horizontal structure of these problems can be exploited

to increase the computational performance. Utilization in three-dimensional situations practically requires parallel computing techniques for which the interface functions, inherited by the GIS formulation, may also prove useful in that subdomains can be decoupled.

R.J. Labeur

7.2 Samenvatting in het Nederlands

‘Eindige elementen modellering van transport en niet-hydrostatische stroming in de waterloopkunde’

Dit proefschrift beschrijft de ontwikkeling van een eindige elementen model voor het berekenen van drie-dimensionale transportverschijnselen en niet-hydrostatische stromingen in de context van waterloopkundige stromingsproblemen. Uitgangspunt is het gebruik van ongestructureerde ruimtelijke schematisaties waarmee willekeurige geometrieën kunnen worden weergegeven waarbij in een deel van het domein een vrij oppervlak aanwezig kan zijn, al is dit laatste niet direct noodzakelijk. Het resulterende numerieke model is toepasbaar binnen een ruime klasse van stromingsproblemen maar richt zich vooral op relatief kleinschalige situaties met complexe geometrieën en niet-hydrostatische drukken. Er worden op voorhand geen aannamen gedaan betreffende de oriëntatie van het rekenrooster. Anders gezegd, de verticale richting wordt op dezelfde manier behandeld als de beide horizontale richtingen zodat intrinsiek drie-dimensionale rekenroosters kunnen worden gebruikt. Modelschematisaties worden zodoende opgebouwd uit driehoeken (in twee dimensies) of tetraeders (in drie dimensies) die betrekkelijk willekeurig van vorm en oriëntatie kunnen zijn. Deze aanpak is vooral handig bij toepassingen binnen de adviespraktijk omdat een model snel opgezet dan wel gewijzigd kan worden waardoor een directie interactie met het ontwerpproces mogelijk is. In Hoofdstuk 1 worden enkele voorbeelden aangehaald waaruit de toegevoegde waarde hiervan duidelijk blijkt.

Tegelijkertijd leiden de genoemde uitgangspunten tot een aantal specifieke moeilijkheden die omzeild moeten worden wil het een praktisch bruikbaar numeriek model opleveren. Zo zijn de matrixstelsels die worden verkregen bij discretisatie op ongestructureerde roosters in het algemeen lastig te hanteren, wat beperkingen met zich mee brengt ten aanzien van de oplosstechnieken die gebruikt kunnen worden. Het is duidelijk dat men hier gebaat is bij een zo eenvoudig mogelijke, ‘ijle’ matrixstructuur met zo min mogelijk matrixelementen ongelijk aan nul. In Hoofdstuk 2 worden continue en discontinue Galerkin methoden op dit punt met elkaar vergeleken. Zoals blijkt uit een eenvoudig elliptisch probleem leidt de discontinue Galerkin (DG) methode tot zeer omvangrijke stelsels, ten opzichte van de continue Galerkin (CG) methode op hetzelfde rooster, terwijl de orde van convergen-

tie gelijk is. Dit maakt de eerstgenoemde methode praktisch onbruikbaar voor het oplossen van impliciete problemen, vooral in drie dimensies. Een andere moeilijkheid bij discrete transport- en stromingsproblemen zijn instabiliteiten die de kop opsteken (1) als gevolg van de advectione termen in de vergelijkingen en (2) als gevolg van de onsamendrukbaarheidsvoorwaarde. De eerstgenoemde categorie kan worden onderdrukt door het gebruik van *upwind* formuleringen waarbij de advectione flux wordt bepaald aan de hand van de heersende stromingsrichting, wat echter zeer zorgvuldig dient te gebeuren. Instabiliteiten samenhangend met de onsamendrukbaarheidsvoorwaarde zijn in het algemeen moeilijker te omzeilen. Bij de continue Galerkin methode is het hiervoor nodig het snelheidsveld met hogere orde polynomen te benaderen dan het drukveld. Dit levert echter complexe stelsels vergelijkingen op omdat verschillende matrixstructuren nodig zijn voor respectievelijk de druk- en de snelheidsvariabelen. Als alternatief kunnen de stabilisatietermen rechtstreeks aan de vergelijkingen worden toegevoegd maar formuleringen hiervoor zijn meestal probleemafhankelijk, en dus niet algemeen toepasbaar, en leiden daarnaast al gauw tot te veel dissipatie. Discontinue Galerkin methoden hebben in dit opzicht het voordeel dat de fluxen op de elementranden vrij eenvoudig geformuleerd kunnen worden zodanig dat instabiliteiten onderdrukt worden.

Een algemene numerieke methode is ontwikkeld waarin de kenmerkende voordelen van continue en discontinue eindige elementen methoden gecombineerd zijn. De nieuwe methode deelt met de continue Galerkin methode de eigenschap dat er slechts ijle matrixstelsels hoeven te worden opgelost voor een set globale variabelen. De hiervoor benodigde elementmatrices zijn daarbij hetzelfde als die voor de standaard CG methode met uitzondering van een matrix waarvoor over de elementranden geïntegreerd moet worden. De overeenkomst met discontinue Galerkin methoden schuilt in het toepassen van *upwind* formuleringen voor het bepalen van de flux op de elementranden om zodoende verschillende termen in de vergelijkingen te kunnen stabiliseren. In tegenstelling tot de klassieke DG methode leidt deze aanpak hier echter niet tot een toename van het aantal onbekenden in de resulterende stelsels vergelijkingen. Dit wordt bereikt door op de elementranden een nieuwe, globale variabele te definiëren en de flux op de elementrand vervolgens afhankelijk te maken van deze nieuwe variabele en de lokale oplossing op het element. De globale variabele fungeert zo als een zwakke Dirichlet randvoorwaarde voor een lokaal probleem dat per element kan worden opgelost. De lokale, discontinue oplossing kan zodoende elementsgewijs worden uitgedrukt in een set globale vrijheidsgraden. Door eliminatie van de lokale oplossing wordt vervolgens een stelsel vergelijkingen verkregen voor alleen de globale variabelen, met dezelfde omvang als dat van de overeenkomstige CG methode. Als extra vergelijking die hiervoor nodig is wordt een zwakke formulering gebruikt die stelt dat de flux over de elementranden continu is. De globale variabele op de elementranden kan zo worden gezien als een

Lagrange multiplier die de continuïteit van de flux over de elementrand waarborgt.

In Hoofdstuk 3 wordt deze procedure, genaamd Galerkin Interface Stabilisatie methode (kortweg GIS methode), nader uitgewerkt voor het advection-diffusie probleem. Op een instroomrand van een element wordt het advectieve deel van de flux bepaald door de globale concentratieverdeling op de elementrand terwijl op een uitstroomrand de lokale waarde van de concentratie in het element bepalend is. De diffusieve flux op een elementrand is gelijk aan de diffusieve flux binnen het element vermeerderd met een ‘*penalty*’ term die evenredig is met de discontinuïteit tussen de lokale concentratie in het element en de globale concentratie op de elementrand. De resulterende semi-discrete vergelijking is consistent met het advection-diffusie probleem en bovendien massa behoudend. Daarnaast kan voor advectief transport met een divergentievrij snelheidsveld worden aangetoond dat de \mathcal{L}^2 norm van de concentratie niet kan groeien. In het diffusie-gedomineerde geval geldt dit laatste alleen als de ‘*penalty*’ term voldoende groot is. De formulering wordt verder uitgewerkt voor eerste-orde basisfuncties in combinatie met de methode der lijnen voor de tijdsintegratie. De algebraïsche vorm van de vergelijkingen wordt in dit geval verkregen door de elementmatrices van de CG methode te vermenigvuldigen met een per element te bepalen stabilisatie matrix. Voor stationaire, één-dimensionale problemen leidt dit voor een specifieke waarde van de ‘*penalty*’ parameter tot een vrijwel optimale stabilisatie. De bijbehorende \mathcal{L}^2 norm van de fout convergeert kwadratisch in de roostermaat. Zoals blijkt uit verschillende rekenvoorbeelden is de methode nauwkeurig terwijl de kunstmatige diffusie minimaal is. Oplossingen zijn echter niet monotoon waardoor met name in twee of drie dimensies te hoge en/of negatieve concentraties kunnen optreden, vooral in de nabijheid van Dirichlet uitstroomranden.

In Hoofdstuk 4 wordt de GIS methode uitgebreid naar de onsamendrukbare Navier-Stokes vergelijkingen op een vast domein. De impulsvergelijkingen worden hierbij per component op dezelfde manier gediscretiseerd als een scalar advection-diffusie probleem met als lokale bronterm de drukgradiënt volgend uit een continue drukverdeling. Het snelheidsveld binnen een element kan zo worden uitgedrukt in termen van het globale snelheidsveld op de elementranden en het globale drukveld. Dit lokale snelheidsveld is zwak divergentievrij wat na substitutie van bovengenoemde uitdrukking leidt tot een gestabiliseerde vorm van de onsamendrukbaarheidsvergelijking. De stabilisatie hangt samen met een Laplaciaan voor de druk die via de eliminatieprocedure in deze vergelijking opduikt zonder aan consistentie in te boeten. De GIS methode is bruikbaar voor verschillende typen stroming zonder dat aan stabilisatieparameters gesleuteld hoeft te worden. Dankzij de stabilisatieprocedure kunnen de druk en de snelheid benaderd worden door polynomen van gelijke orde. De methode is geïmplementeerd voor lineaire druk- en snelheidsvelden, hetgeen feitelijk resulteert in een co-lineair

rekenrooster. Het stelsel vergelijkingen wordt iteratief opgelost, gebruikmakend van efficiënte Block Sparse Row (BSR) technieken, met een gelijk aantal onbekenden als voor lineaire CG methoden op hetzelfde mesh. Uit een numeriek voorbeeld voor de stationaire, lineaire Stokes vergelijkingen blijkt dat de fout in de \mathcal{L}^2 norm convergeert volgens $\mathcal{O}(h^2)$ voor de snelheid en volgens $\mathcal{O}(h^1)$ voor de druk. Numerieke voorbeelden van interne golven bevestigen dat de stabilisatie slechts een geringe extra dissipatie geeft. Dit maakt het in principe mogelijk om Large Eddy Simulaties (LES) met het model uit te voeren, wat wordt gedemonstreerd aan de hand van het zogenaamde buisje van Borda. Het is verder opmerkelijk dat de methode de voortplanting van schokken nauwkeurig weergeeft, zonder enige vorm van *limiting*, zoals blijkt uit rekenvoorbeelden met de Burgers' vergelijking.

Stroming in een bewegend domein, in het bijzonder met een vrij oppervlak, is het onderwerp van Hoofdstuk 5. De Navier-Stokes vergelijkingen worden hiertoe getransformeerd naar een tijdsonafhankelijk referentie domein. Dit heeft als voordeel dat de tijdsintegratie eenduidig uitgevoerd kan worden. Een moeilijkheid bij vrij-oppervlaktestroming is dat het ruimtelijke domein niet vooruit bekend is maar, via de beweging van het oppervlak, afhangt van de oplossing van het probleem. De kinematische oppervlakterandvoorwaarde en de drukgradiënt zijn hiertoe geformuleerd in termen van het piëzometrisch niveau. De positie van het vrij oppervlak ligt hiermee eenduidig vast. Voor de tijdsintegratie wordt vervolgens een predictor-corrector methode gebruikt waarbij de berekeningen van het piëzometrisch niveau en van de snelheidscomponenten ontkoppeld worden. Een implementatie wordt beschreven waarbij de divergentie van het convectieve snelheidsveld overeenkomt met de volumeveranderingen als gevolg van de beweging van het rooster. Dit blijkt cruciaal voor het behoud van volume en impuls. Voor lineaire oppervlaktegolven kan vervolgens worden aangetoond dat ook de som van de kinetische en potentiële energie behouden blijft. Niet-lineaire golven worden enigszins gedempt door de stabilisatietermen. Via numerieke voorbeelden wordt de methode uitgebreid vergeleken met theoretische oplossingen en met laboratoriumexperimenten. De resultaten bevestigen dat de methode robuust is en weinig kunstmatige dissipatie aan een probleem toevoegt. Dit blijkt vooral uit de voorbeelden met vrij-oppervlaktegolven. Daarnaast wordt de stroming over en langs kunstwerken beschouwd, een modeloverlaat en de stormvloedkering in het Haringvliet, waarbij zowel het berekende snelheidsveld als het berekende verval nauwkeurig zijn.

Concluderend biedt de GIS methode de optimale stabilisatie van discontinue Galerkin methoden en de efficiëntie van continue Galerkin methoden. De formulering is helder en leidt voor lineaire basisfuncties tot betere eigenschappen dan conventionele stabilisatietechnieken. Verdere toepassing is veelbelovend maar vereist een diepgaandere analyse en ontwikkeling van de methode. In Hoofdstuk 6 worden enkele suggesties gedaan voor verder onderzoek. Dit proefschrift beperkt zich vooral tot eerste-orde basisfuncties

maar een analyse van de convergentie voor willekeurige basisfuncties zou andere interessante combinaties aan het licht kunnen brengen. Een dergelijke analyse is echter niet-triviaal door de structuur van de formulering die het karakter heeft van een *mixed* probleem en waarvoor een inf – sup stabiliteitsvoorwaarde geldt. In twee en drie dimensies voldoen GIS oplossingen van de advection-diffusie vergelijking niet aan het maximum principe, vooral bij uitstroomgrenslagen is dit duidelijk zichtbaar. Gezien de overeenkomst met SUPG methoden is het wellicht mogelijk de flux op de elementranden zodanig te herformuleren dat scherpere grenslagen en monotone oplossingen verkregen kunnen worden. Omdat de GIS methode generiek geformuleerd is kan deze worden toegepast op een ruimere klasse van problemen. Interessant in de context van dit proefschrift zijn de ondiep-watervergelijkingen, waartoe een eerste aanzet is gegeven in Appendix C.1, maar waarvoor specifieke moeilijkheden moeten worden aangepakt zoals bijvoorbeeld droogval. De praktische bruikbaarheid zou verbeterd kunnen worden door bij quasi twee-dimensionale problemen de verticale structuur van het rooster te benutten. Door de elementen verticaal te stapelen en de hydrostatische druk af te splitsen van de totale druk kan in dergelijke situaties de rekentijd sterk worden bekort. Daarnaast verdient het aanbeveling een parallelle versie van het model te ontwikkelen. De functies op de elementranden, die zo kenmerkend zijn voor de GIS methode, kunnen daarbij worden gebruikt om subdomeinen te ontkoppelen.

R.J. Labeur

Appendices

Appendix A

Internal flow

If the transport of constituents (temperature, salinity, sediments) involves inhomogeneous densities, the flow field and the advected density field will interact. Even small density variations can have a huge impact on the flow field and may thus be responsible for a wide range of internal flow phenomena in estuarine environments or around discharge structures [24, 66]. The modelling of these phenomena requires the coupling of the transport and flow models given in Chapters 3 and 4, respectively, and this section describes some aspects of the underlying procedure. Numerical examples are given in Section 4.4.5.

A.1 Boussinesq approximation

The coupling of the flow and transport equations is effected through the forcing term \mathbf{f} in the momentum balance equations, which becomes dependent on the density ρ of the fluid. Density changes caused by natural variations of salinity and temperature are usually small with respect to some reference (background) density. A constant reference density ρ_0 may then be used to define the momentum flux and the normalized pressure while density variations are retained in the forcing term. This ‘Boussinesq approximation’ effectively leads to momentum Equation (4.1) with the forcing term \mathbf{f} given by

$$\mathbf{f} = -\rho^* g \mathbf{e}_z, \tag{A.1}$$

where $\rho^* = (\rho - \rho_0) / \rho_0$ is the dimensionless relative density difference, g is the gravitational constant and \mathbf{e}_z denotes the vertical unit vector. The Boussinesq approximation is valid when $\rho^* \ll 1$. By assumption, the flow remains incompressible and the incompressibility constraint Equation (4.3) is used to determine the normalized pressure. The associated transport

equation for ρ^* reads

$$\frac{\partial \rho^*}{\partial t} + \nabla \cdot \boldsymbol{\sigma} = 0, \quad (\text{A.2})$$

$$\boldsymbol{\sigma} = \mathbf{u}\rho^* - \kappa \nabla \rho^*, \quad (\text{A.3})$$

where κ is the diffusivity. Boundary conditions for Equation (A.2) must be supplied according to the procedure outlined in Section 3.1.1.

A.2 Solution algorithm

The semi-discrete variational form of Equations (A.2) and (A.3) is given in Section (3.3). To discretize in time the θ method is used, see Section 3.4, where the transport and flow equations are solved sequentially. Starting with the transport equation, the updated values for ρ^* are used to compute the forcing term \mathbf{f} in the Navier-Stokes equations. This semi-implicit procedure is necessary because of the presence of the following subsystem in the coupled set of equations

$$\frac{\partial}{\partial t} \begin{pmatrix} \rho^* \\ w \end{pmatrix} + \begin{pmatrix} 0 & \partial \rho^* / \partial z \\ g & 0 \end{pmatrix} \begin{pmatrix} \rho^* \\ w \end{pmatrix} = \mathbf{0}, \quad (\text{A.4})$$

where w is the vertical velocity component. For stable stratification Equation (A.4) has periodic solutions with eigen frequency $N = (-g \partial \rho^* / \partial z)^{1/2}$. The semi-implicit treatment renders the time stepping scheme conditionally stable with maximum allowable time step size $\Delta t_{max} = N^{-1}$. A slightly modified version of the scheme uses an extrapolated value of ρ^* to compute the forcing term on the new time level $n + 1$,

$$\mathbf{f}_{n+1} = -[(1 + \delta) \rho_{n+1}^* - \delta \rho_n^*] g \mathbf{e}_z, \quad (\text{A.5})$$

where the damping parameter $\delta \in [0, 1]$ can be adjusted in order to smooth unphysical transients while leaving steady solutions unaltered.

Still, in flows with dominant buoyancy, unphysical velocity and density modes may emerge as the discrete forcing term in the momentum equation is generally not compatible with the gradient of the discrete pressure [65]. This can be avoided by projecting the forcing term \mathbf{f} onto the gradient of a discrete potential function $\Phi \in Q$, where Q is the discrete pressure space, which leads to

$$\int_{\hat{\Omega}} \nabla \Phi \cdot \nabla q \, d\Omega = - \int_{\hat{\Omega}} \rho^* g \frac{\partial q}{\partial z} \, d\Omega \quad \forall q \in Q. \quad (\text{A.6})$$

The gradient $\nabla \Phi$ is then used in place of the forcing term \mathbf{f} in the momentum equations. This projection removes the incompatible modes from the solution [49].

Appendix B

Turbulence modelling

Turbulence modelling involves the computation of the net contribution of turbulent fluctuations to the mean flow. To this end, the underlying momentum equations are averaged over a time interval much larger than the turbulence time-scale to yield the Reynolds averaged Navier-Stokes (RANS) equations. The averaging procedure leads to a closure problem which requires a parameterization of the wall shear stress and the turbulent stress within the fluid [61]. This section describes the numerical implementation of some standard approaches in the context of a finite element method. For notational convenience, the various equations are given on the fixed, spatial domain. The ALE form of the equations can be obtained using the transformed transport theorem of Equation (5.25).

B.1 Wall-friction coefficient

For a plane, turbulent shear flow parallel to a solid wall, the velocity u at a distance h from the wall is given by

$$u(h) = \frac{u_\star}{\kappa} \log\left(\frac{h}{h_0}\right), \quad (\text{B.1})$$

where $\kappa \approx 0.4$ is Von Karman's constant, h_0 is a length scale which is related to the wall roughness and u_\star is the shear velocity which is related to the wall shear stress τ_w and the density ρ according to

$$\tau_w = \rho u_\star^2. \quad (\text{B.2})$$

The wall shear stress should be expressed in terms of the computed velocity u_w at the wall,

$$\tau_w = \rho c_f |u_w| u_w, \quad (\text{B.3})$$

in which c_f is a dimensionless wall-friction parameter. According to the mixing-length hypothesis τ_w is also related to the velocity gradient,

$$\tau_w = \rho l_m^2 \left| \frac{\partial u}{\partial h} \right| \frac{\partial u}{\partial h}, \quad (\text{B.4})$$

in which l_m is the ‘mixing length’ [68]. In an element adjacent to the wall, Equations (B.2) and (B.4) lead to

$$u_\star = l_m \frac{|u(h_e) - u_w|}{h_e}, \quad (\text{B.5})$$

where h_e is the element size normal to the wall facet. Using Equation (B.1) to express $u(h_e)$ in terms of u_\star and setting $u_w = u_\star / \sqrt{c_f}$ yields

$$\frac{1}{\sqrt{c_f}} = \frac{1}{\kappa} \log \left(\frac{h_e}{h_0} \right) - \frac{h_e}{l_m}. \quad (\text{B.6})$$

The length scale h_0 is computed from

$$h_0 = \frac{1}{30} \left(k_N + \frac{3.3 \nu}{u_\star} \right), \quad (\text{B.7})$$

where k_N is the Nikuradse roughness height and ν is the molecular kinematic viscosity.

B.2 Turbulence viscosity

The mean turbulent stress is modelled in terms of the gradient of the resolved velocities, analogous to the representation of viscous stresses, leading to an expression for the total flux

$$\boldsymbol{\sigma} = \mathbf{u} \otimes \mathbf{u} - 2(\nu + \nu_t) \nabla^s \mathbf{u}, \quad (\text{B.8})$$

where \mathbf{u} is the mean flow velocity, ν and ν_t are the molecular and turbulence kinematic viscosities, respectively, and ∇^s is the symmetric spatial gradient operator.

Using the mixing-length hypothesis the turbulence viscosity ν_t is given by

$$\nu_t = l_m^2 S, \quad (\text{B.9})$$

where S is the \mathcal{H}^1 semi-norm of the velocity,

$$S = (\nabla^s \mathbf{u} : \nabla^s \mathbf{u})^{1/2}. \quad (\text{B.10})$$

The mixing length may be prescribed directly or computed from the element width h_e using

$$l_m = C_s h_e, \quad (\text{B.11})$$

c_μ	c_1	c_2	σ_k	σ_ϵ
0.09	1.44	1.92	1.0	1.3

Table B.1: *Empirical constants used in the standard $k - \epsilon$ model [74].*

where $C_s \approx 0.05 - 0.20$ is Smagorinsky's constant. This approach should be used if large, coherent turbulent structures are to be resolved, via large eddy simulation (LES), see the example in Section 4.4.4. Often, the mixing length is not known *a priori* as it adjusts dynamically to the flow conditions.

The $k - \epsilon$ model [74], relates the turbulence viscosity to the turbulence kinetic energy k and the turbulence dissipation rate ϵ according to

$$\nu_t = c_\mu \frac{k^2}{\epsilon}, \quad (\text{B.12})$$

where c_μ is an empirical constant, see Table B.1. The evolution of k and ϵ in time is described by the following transport equations,

$$\frac{\partial k}{\partial t} + \mathbf{u} \cdot \nabla k - \nabla \cdot \left(\frac{\nu_t}{\sigma_k} \nabla k \right) = P_k - \epsilon, \quad (\text{B.13})$$

$$\frac{\partial \epsilon}{\partial t} + \mathbf{u} \cdot \nabla \epsilon - \nabla \cdot \left(\frac{\nu_t}{\sigma_\epsilon} \nabla \epsilon \right) = \frac{\epsilon}{k} (c_1 P_k - c_2 \epsilon), \quad (\text{B.14})$$

where P_k is the kinetic energy production term which for a flow with homogeneous density is given by

$$P_k = \nu_t S^2, \quad (\text{B.15})$$

and σ_k , σ_ϵ , c_1 and c_2 are additional empirical constants listed in Table B.1. In case of buoyant flows the expression for P_k and the coefficient c_1 are modified using the vertical gradient of the density [68]. At solid, impermeable boundaries Γ_s the following Dirichlet boundary condition applies to k ,

$$k = \frac{u_\star^2}{\sqrt{c_\mu}} = c_f \frac{u_w^2}{\sqrt{c_\mu}} \quad \text{on } \Gamma_s, \quad (\text{B.16})$$

and at free surfaces a zero Neumann boundary condition holds. The wall-friction coefficient c_f is computed from Equation (B.6) using a 'near-wall' mixing length $l_m = \kappa h_e$. At impermeable walls, ϵ is a function of the distance h to the wall,

$$\epsilon(h) = \frac{u_\star^3}{\kappa h}, \quad (\text{B.17})$$

from which the following flux boundary condition is obtained

$$\frac{\nu_t}{\sigma_\epsilon} \frac{\partial \epsilon}{\partial n} = \frac{\kappa u_\star}{\sigma_\epsilon} \epsilon \quad \text{on } \Gamma_s, \quad (\text{B.18})$$

which is used either as a Robin boundary condition or as a Neumann boundary condition by specifying a representative value for ϵ in the near-wall region.

The spatial discretization of k and ϵ employs continuous piecewise linear basis functions. The advective terms in Equations (B.13) and (B.14) are stabilized by the SUPG method, see Section 3.2.1. Using the backward Euler method for time stepping, the equations for k and ϵ are solved in a decoupled fashion. To enhance numerical stability, the corresponding source terms are treated explicitly and the sink terms implicitly. This gives for Equation (B.13),

$$\frac{k_{n+1} - k_n}{\Delta t} + \mathbf{u} \cdot \nabla k_{n+1} - \nabla \cdot \left(\frac{\nu_t}{\sigma_k} \nabla k_{n+1} \right) + \frac{\epsilon_n}{k_n} k_{n+1} = P_{k,n}, \quad (\text{B.19})$$

and for Equation (B.14),

$$\frac{\epsilon_{n+1} - \epsilon_n}{\Delta t} + \mathbf{u} \cdot \nabla \epsilon_{n+1} - \nabla \cdot \left(\frac{\nu_t}{\sigma_\epsilon} \nabla \epsilon_{n+1} \right) + c_2 \frac{\epsilon_n}{k_n} \epsilon_{n+1} = c_1 \frac{\epsilon_n}{k_n} P_{k,n}. \quad (\text{B.20})$$

The turbulence viscosity and the coefficient ϵ/k are not bounded for arbitrary k and ϵ . Therefore, the turbulence viscosity is computed as

$$\nu_t = \begin{cases} c_\mu k^2 / \epsilon & \text{where } \tilde{k}^{3/2} < \epsilon l_{max}, \\ \max(\nu, l_{max} \tilde{k}^{1/2}) & \text{elsewhere,} \end{cases} \quad (\text{B.21})$$

in which $\tilde{k} = \max(k, 0)$ and l_{max} is a maximum turbulence length scale defined by for instance the size of the domain. The coefficient ϵ/k is then computed as $c_\mu \tilde{k} / \nu_t$. This strategy avoids zero division. Various details of implementing the $k - \epsilon$ model are given in Kuzmin et al. [45].

Appendix C

Shallow-water equations

The shallow-water equations (SWE) arise in the study of nearly-horizontal geophysical flows for which the ratio of the vertical and horizontal velocity magnitudes is very small. The piezometric level η is then constant in the vertical direction and the Navier-Stokes equations can be integrated over the water depth. If the horizontal velocity is nearly uniform in the vertical direction, which in many cases is a reasonable assumption, the SWE provide a good approximation of the original flow problem while offering a substantial reduction in terms of complexity and computational burden. The GIS method can be adapted to solve the SWE which only requires minor modifications to the computer implementation of the free surface Navier-Stokes problem given in Chapter 5.

C.1 Governing equations

Let $\Omega \subset \mathbb{R}^2$ denote a horizontal domain of interest having a boundary $\Gamma = \partial\Omega$ on which \mathbf{n} denotes the outward unit normal vector. The boundary is partitioned into Γ_g and Γ_h where $\Gamma = \Gamma_g \cup \Gamma_h$ and $\Gamma_g \cap \Gamma_h = \emptyset$. Denoting with $I = (t_0, t_N)$ the time interval of interest, the SWE can be stated as: given the forcing term $\mathbf{f}: \Omega \rightarrow \mathbb{R}^2$ and the boundary conditions $\mathbf{g}: \Gamma_g \rightarrow \mathbb{R}^2$ and $\mathbf{h}: \Gamma_h \rightarrow \mathbb{R}^2$, find the velocity $\mathbf{u}: \Omega \rightarrow \mathbb{R}^2$ and the piezometric level $\eta: \Omega \rightarrow \mathbb{R}$ such that

$$\frac{\partial(d\mathbf{u})}{\partial t} + \nabla \cdot \boldsymbol{\sigma} + gd\nabla\eta + \mathbf{F}\mathbf{u} = \mathbf{f}, \quad \text{on } \Omega \times I, \quad (\text{C.1})$$

$$\boldsymbol{\sigma} = d\mathbf{u} \otimes \mathbf{u} - 2d\nu\nabla^s\mathbf{u} \quad \text{on } \Omega \times I, \quad (\text{C.2})$$

$$\frac{\partial\eta}{\partial t} + \nabla \cdot (d\mathbf{u}) = 0 \quad \text{on } \Omega \times I, \quad (\text{C.3})$$

$$\mathbf{u} = \mathbf{g} \quad \text{on } \Gamma_g \times I, \quad (\text{C.4})$$

$$(\gamma d\mathbf{u} \otimes \mathbf{u} + gd\eta\mathbf{I} - 2d\nu\nabla^s\mathbf{u})\mathbf{n} = \mathbf{h} \quad \text{on } \Gamma_h \times I, \quad (\text{C.5})$$

where g denotes gravitation, d is the water depth which is given by the non-negative difference between η and the bottom level z_b , and \mathbf{I} is the second-order identity tensor. The matrix \mathbf{F} includes the effects of bottom friction and the earth's rotation and is given by

$$\mathbf{F} = \begin{pmatrix} c_f |\mathbf{u}| & f_c \\ -f_c & c_f |\mathbf{u}| \end{pmatrix}, \quad (\text{C.6})$$

where c_f is a dimensionless friction parameter and f_c is Coriolis' coefficient. On Neumann boundaries either the total flux or the diffusive flux is imposed, depending on the sign of the normal velocity component which is controlled by the parameter γ . The forcing term \mathbf{f} includes atmospheric forcings (variable pressure, wind shear stress) and wave-induced forces (radiation stress divergence). As initial conditions the velocity \mathbf{u} and piezometric level η must be prescribed at time $t = t_0$. A comparison with Equations (5.31) to (5.33) shows that the mathematical format of the SWE is nearly identical to that of the incompressible Navier-Stokes equations with a free surface.

C.2 Variational formulation

The partitioning of the domain of interest into elements Ω_e is denoted $\tilde{\Omega}$ and $\tilde{\Gamma}$ is the union of element interfaces Γ_i and the exterior boundary. Various finite element spaces are defined

$$\mathbf{V} = \left\{ \mathbf{v} \in \mathbf{L}^2(\tilde{\Omega}) : \mathbf{v} \in \mathbf{P}^k(\Omega_e) \quad \forall e \right\}, \quad (\text{C.7})$$

$$\bar{\mathbf{V}} = \left\{ \bar{\mathbf{v}} \in \mathbf{H}^{1/2}(\tilde{\Gamma}) : \bar{\mathbf{v}} \in \mathbf{P}^m(\Gamma_i) \quad \forall i \right\}, \quad (\text{C.8})$$

$$Q = \left\{ q \in H^1(\tilde{\Omega}) : q \in P^m(\Omega_e) \quad \forall e \right\}, \quad (\text{C.9})$$

where $\mathbf{H}^{1/2}$ is the trace of \mathbf{H}^1 on $\tilde{\Gamma}$, the sets P^n and \mathbf{P}^n denote the standard polynomial finite element basis functions of degree n , and $k \geq 0$ and $m \geq 1$. Furthermore, a space $\bar{\mathbf{V}}_g$ is defined which contains those functions of $\bar{\mathbf{V}}$ that satisfy the Dirichlet boundary condition.

The GIS variational problem corresponding to the equations in Section C.1 reads: at time t , given the source term \mathbf{f} and the boundary condition \mathbf{h} , find $\mathbf{u} \in \mathbf{V}$, $\bar{\mathbf{u}} \in \bar{\mathbf{V}}_g$ and $\eta \in Q$ such that

$$\begin{aligned} & \int_{\tilde{\Omega}} \frac{\partial(d\mathbf{u})}{\partial t} \cdot \mathbf{v} \, d\Omega + \int_{\tilde{\Omega}} \nabla \cdot \boldsymbol{\sigma} \cdot \mathbf{v} \, d\Omega + \int_{\tilde{\Omega}} g d\nabla\eta \cdot \mathbf{v} \, d\Omega \\ & \quad + \int_{\tilde{\Omega}} \mathbf{F}\mathbf{u} \cdot \mathbf{v} \, d\Omega + \sum_e \int_{\partial\Omega_e} d\boldsymbol{\beta} \cdot \mathbf{n} (\bar{\mathbf{u}} - \mathbf{u}) \cdot \mathbf{v} \, d\Gamma \\ & \quad + \sum_e \int_{\partial\Omega_e} 2d\nu (\bar{\mathbf{u}} - \mathbf{u}) \cdot \nabla^s \mathbf{v} \, \mathbf{n} \, d\Gamma = \int_{\tilde{\Omega}} \mathbf{f} \cdot \mathbf{v} \, d\Omega \quad \forall \mathbf{v} \in \mathbf{V}. \end{aligned} \quad (\text{C.10})$$

and

$$\begin{aligned} \sum_e \int_{\partial\Omega_e} \boldsymbol{\sigma} \mathbf{n} \cdot \bar{\mathbf{v}} \, d\Gamma + \sum_e \int_{\partial\Omega_e} d\boldsymbol{\beta} \cdot \mathbf{n} (\bar{\mathbf{u}} - \mathbf{u}) \cdot \bar{\mathbf{v}} \, d\Gamma + \int_{\Gamma} g d\eta \, \mathbf{n} \cdot \bar{\mathbf{v}} \, d\Gamma \\ - \int_{\Gamma_h} (1 - \gamma) d(\mathbf{u} \cdot \mathbf{n}) \bar{\mathbf{u}} \cdot \bar{\mathbf{v}} \, d\Gamma = \int_{\Gamma_h} \mathbf{h} \cdot \bar{\mathbf{v}} \, d\Gamma \quad \forall \bar{\mathbf{v}} \in \bar{\mathbf{V}}, \end{aligned} \quad (\text{C.11})$$

and

$$\int_{\tilde{\Omega}} \frac{\partial \eta}{\partial t} q \, d\Omega - \int_{\tilde{\Omega}} d\mathbf{u} \cdot \nabla q \, d\Omega + \int_{\Gamma} d\bar{\mathbf{u}} \cdot \mathbf{n} q \, d\Gamma = 0 \quad \forall q \in Q. \quad (\text{C.12})$$

Equation (C.10) is the local momentum balance equation, Equation (C.11) is the momentum flux continuity constraint and Equation (C.12) is the weak continuity equation. The element flux $\boldsymbol{\sigma}$ is defined by Equation (C.2). The term $\boldsymbol{\beta}$ which arises in the definition of the interface flux, see Section 5.3.2, is given by

$$\boldsymbol{\beta} = \gamma \tilde{\mathbf{u}} - \frac{\alpha}{h_e} \nu \mathbf{n}, \quad (\text{C.13})$$

where $\tilde{\mathbf{u}}$ is a suitably chosen advective velocity, the upwind parameter γ equals one on inflow element boundaries and zero elsewhere, α is an $\mathcal{O}(1)$ penalty parameter and h_e is a measure of the local element width.

The fully-discrete problem is obtained by using the θ time stepping method, taking all non-linear coefficients on the previous time level. Static condensation of the local momentum equation can be used to eliminate the variable \mathbf{u} from the global flux continuity constraint. The resulting discrete global problem for $(\bar{\mathbf{u}}, \eta)$ can be solved by either the fully coupled scheme from Chapter 4 or the predictor-corrector scheme from Chapter 5. A first application concerns LES computations for a shallow mixing-layer between two parallel streams in a river [78].

Bibliography

- [1] D. Arnold, F. Brezzi, B. Cockburn, and D. Marine. Unified analysis of discontinuous Galerkin methods for elliptic problems. *SIAM Journal on Scientific Computation*, 39:1749–1779, 2002.
- [2] Douglas N. Arnold. An interior penalty finite element method with discontinuous elements. *SIAM Journal on Numerical Analysis*, 19:742–760, 1982.
- [3] M.J. Baines. *Moving finite elements*. Oxford Clarendon, 1994.
- [4] F. Bassi and S. Rebay. A high-order accurate discontinuous finite element method for the numerical solution of the compressible Navier-Stokes equations. *Journal of Computational Physics*, 131:267–279, 1997.
- [5] S. Beji and J.A. Battjes. Experimental investigation of wave propagation over a bar. *Coastal Engineering*, 93:151–162, 1993.
- [6] J.C.W. Berkhoff. *Mathematical models for simple harmonic linear water waves; wave diffraction and refraction*. PhD thesis, Delft University of Technology, 1976.
- [7] D. Braess. *Finite elements - Theory, fast solvers and applications in solid mechanics*. Cambridge University Press, Cambridge, 1997.
- [8] F. Brezzi and M. Fortin. *Mixed and hybrid finite element methods*, volume 15 of *Springer Series in Computational Mathematics*. Springer, New York, 1991.
- [9] M.O. Bristeau, R. Glowinsky, and J. Periaux. Numerical method for the Navier-Stokes equations. Applications to the simulation of compressible and incompressible viscous flows. *Computer Physics Reports*, 6:73–187, 1987.
- [10] A. Brooks and T.J.R. Hughes. Streamline upwind/Petrov-Galerkin methods for advection dominated flows. In *3rd International Conference on Finite Element Methods in Fluid Flows*, pages 283–292, Banff, Canada, 1980.

- [11] A. Buffa, T.J.R. Hughes, and G. Sangalli. Analysis of a multiscale discontinuous Galerkin method for convection-diffusion problems. *SIAM Journal on Numerical Analysis*, 44(4):1420–1440, 2006.
- [12] V. Casulli and R. Walters. An unstructured grid three dimensional model based on the shallow water equations. *International Journal for Numerical Methods in Fluids*, 32:331–348, 2000.
- [13] P. Chadwick. *Continuum mechanics*. Dover Publications Inc., New York, 1999.
- [14] A.J. Chorin and J.E. Marsden. *A mathematical introduction to fluid mechanics*. Springer, New York, 1993.
- [15] B. Cockburn, G. Kanschat, D. Schotzau, and C. Schwab. Local discontinuous Galerkin methods for the Stokes system. *SIAM Journal on Numerical Analysis*, 40(1):319–343, 2002.
- [16] Bernardo Cockburn and Jayadeep Gopalakrishnan. Incompressible finite elements via hybridization. part I: The Stokes system in two space dimensions. *SIAM Journal on Numerical Analysis*, 43(4):1627–1650, 2005.
- [17] Bernardo Cockburn and Jayadeep Gopalakrishnan. Incompressible finite elements via hybridization. part II: The Stokes system in three space dimensions. *SIAM Journal on Numerical Analysis*, 43(4):1651–1672, 2005.
- [18] M.P.C. de Jong, M. Bottema, R.J. Labeur, J.A. Battjes, and C. Stolk. Atmospherically generated large-scale water-level fluctuations in a closed basin. In Jane McKee Smith, editor, *Coastal Engineering, Proceedings of the 30th International Conference*, volume 2, pages 1184–1196. World Scientific, 2006.
- [19] J. Donea and A. Huerta. *Finite element methods for flow problems*. Wiley, Chichester, 2002.
- [20] J.J. Dronkers. *Tidal computations in rivers and coastal waters*. North Holland Publ., Amsterdam, 1964.
- [21] Fabin Duarte, Ral Gormaz, and Srinivasan Natesan. Arbitrary Lagrangian-Eulerian method for Navier-Stokes equations with moving boundaries. *Computer Methods in Applied Mechanics and Engineering*, 193:4819–4836, 2004.
- [22] Maurits Ertsen. *Prescribing perfection. Emergence of an engineering irrigation design approach in the Netherlands East Indies and its legacy, 1830-1990*. PhD thesis, Delft University of Technology, 2005.

- [23] E. Erturk, T.C. Corke, and C. Gökçöl. Numerical solutions of 2-D steady incompressible driven cavity flow at high Reynolds numbers. *International Journal for Numerical Methods in Fluids*, 48:747–774, 2005.
- [24] H.B. Fischer. *Mixing in inland and coastal waters*. Academic Press, New York, 1979.
- [25] L.P. France, C. Farhat, M. Lesoinne, and A. Russo. Unusual stabilized finite element methods and residual free bubbles. *International Journal for Numerical Methods in Fluids*, 27:159–168, 1998.
- [26] Abdolreza Ghods, Farhad Sobouti, and Jafar Arkani-Hamed. An improved second moment method for solution of pure advection problems. *International Journal for Numerical Methods in Fluids*, 32:959–977, 2000.
- [27] E.D. de Goede. *Numerical methods for the three-dimensional shallow water equations on supercomputers*. PhD thesis, University of Amsterdam, 1992.
- [28] P.M. Gresho, R.L. Sani, and M.S. Engelman. *Incompressible flow and the finite element method: advection-diffusion and isothermal laminar flow*. John Wiley and Sons, Chichester, 1998.
- [29] Hervé Guillard and Charbel Farhat. On the significance of the geometric conservation law for flow computations on moving meshes. *Computer Methods in Applied Mechanics and Engineering*, 190:1467–1482, 2000.
- [30] M.D. Gunzburger. *Finite element methods for viscous incompressible flows*. Boston Academic Press, 1989.
- [31] Wei guo Dong and John H. Lienhard. Contraction coefficients for Borda mouthpieces. *Journal of Fluids Engineering*, 108:377–379, 1986.
- [32] Joseph L. Hammack. A note on tsunamis: their generation and propagation in an ocean of uniform depth. *Journal of Fluid Mechanics*, 60(4):769–799, 1973.
- [33] A. Harten, P.D. Lax, and Bram van Leer. On upstream differencing and Godunov-type schemes for hyperbolic conservation laws. *SIAM Review*, 25(1):35–61, 1998.
- [34] Thomas J.R. Hughes, Gerald Engel, Luca Mazzei, and Mats G. Larson. The continuous Galerkin method is locally conservative. *Journal of Computational Physics*, 163:467–488, 2000.

- [35] Thomas J.R. Hughes, Guglielmo Scovazzi, Pavel B. Bochev, and Annalisa Buffa. A multiscale discontinuous Galerkin method with the computational structure of a continuous Galerkin method. *Computer Methods in Applied Mechanics and Engineering*, 195:2761–2787, 2006.
- [36] T.J.R. Hughes. Recent progress in the development and understanding of SUPG methods with special reference to the compressible Euler and Navier-Stokes equations. *International Journal for Numerical Methods in Fluids*, 7:1261–1275, 1987.
- [37] T.J.R. Hughes and G.N. Wells. Conservation properties for the Galerkin and stabilised forms of the advection-diffusion and incompressible Navier-Stokes equations. *Computer Methods in Applied Mechanics and Engineering*, 194(9–11):1141–1159, 2005.
- [38] T.J.R. Hughes, L.P. Franca, and M. Balestra. A new finite element formulation for computational fluid dynamics: V. Circumventing the Babuška-Brezzi condition: a stable Petrov-Galerkin formulation of the Stokes problem accommodating equal-order interpolations. *Computer Methods in Applied Mechanics and Engineering*, 59:85–99, 1986.
- [39] R.H.M. Huijsmans. Current force measurements on a 200 KDWT tanker model. Technical Report 010146-2-BT, Maritime Research Institute Netherlands (MARIN), 1991.
- [40] P. Jacobs, B.P.C. Steenkamp, and S. de Goederen. Analyse zoutmetingen inlaatproef Haringvliet in maart 1997. RIZA rapport 2003.001 ISBN 90 3695 481 9, Rijkswaterstaat, 2003. in Dutch.
- [41] J.A. Jankowski. *A non-hydrostatic model for free surface flows*. PhD thesis, Institut für Strömungsmechanik und Elektron. Rechnen im Bauwesen der Universität Hannover, 1999. Bericht nr. 56.
- [42] C. Johnson. *Numerical solution of partial differential equations by the finite element method*. Cambridge University Press, 1990.
- [43] Y. Kanarska and V. Maderich. A non-hydrostatic numerical model for calculating free-surface stratified flows. *Ocean Dynamics*, 53(3): 176–185, 2003.
- [44] L. Krivodonova, J. Xin, J.-F. Remacle, N. Chevaugeon, and J.E. Flaherty. Shock detection and limiting with discontinuous Galerkin methods for hyperbolic conservation laws. *Applied Numerical Mathematics*, 48:323–338, 2004.
- [45] D. Kuzmin, O. Mierka, and S. Turek. On the implementation of the $k - \epsilon$ turbulence model in incompressible flow solvers based on a finite

- element discretization. *International Journal of Computing Science and Mathematics*, 2/3/4:193–206, 2007.
- [46] R.J. Labeur. Hydraulisch onderzoek Beerkanaal. Technical Report 01311/1166, Svašek Hydraulics b.v., 2001. in Dutch.
- [47] R.J. Labeur. Verziltingsstudie uitbreiding Kanaal Gent-Terneuzen. Technical Report 1139, Royal Haskoning, 2002. in Dutch.
- [48] R.J. Labeur and J.D. Pietrzak. Computation of non-hydrostatic internal waves over undular topography. In G.H. Jirka and W.S.J. Uijtewaai, editors, *International Symposium on Shallow flows*, volume II. Elsevier Scientific Press, 2003.
- [49] R.J. Labeur and J.D. Pietrzak. A fully three dimensional unstructured grid non-hydrostatic finite element coastal model. *Ocean Modelling*, 10:51–67, 2005.
- [50] R.J. Labeur, C. Gautier, and B.A.J. Les. 3 D berekeningen Haringvlietsluizen - fase 2. Technical Report 02050/1205, Svašek Hydraulics bv., 2002.
- [51] Robert Jan Labeur and Garth N. Wells. A Galerkin interface stabilisation method for the advection-diffusion and incompressible Navier-Stokes equations. *Computer Methods in Applied Mechanics and Engineering*, 196:4985–5000, 2007.
- [52] Robert Jan Labeur and Garth N. Wells. Interface stabilised finite element method for moving domains and free surface flows. *Computer Methods in Applied Mechanics and Engineering*, 198:615–630, 2009.
- [53] Jan J. Leendertse. *Aspects of a computational model for long-period water-wave propagation*. PhD thesis, Delft University of Technology, 1967.
- [54] Bram van Leer. Towards the ultimate conservative difference scheme. IV. A new approach to numerical convection. *Journal of Computational Physics*, 23:276–299, 1977.
- [55] B.A.J. Les, G. Dam, and R.J. Labeur. Hydraulische en morfologische studie naar herinrichting aansluiting Lek-Lekkanaal. Technical Report 99574/1141, Svašek Hydraulics b.v., 2000. in Dutch.
- [56] Randall J. LeVeque. *Numerical methods for hyperbolic conservation laws*. Birkhäuser, Basel, 1999.

- [57] Weiming Liu, Mike Ashworth, and David Emerson. Pressure correction methods based on Krylov subspace conception for solving incompressible Navier-Stokes problems. *International Journal for Numerical Methods in Fluids*, 45:1249–1268, 2004.
- [58] H.A. Lorentz. Verslag Staatscommissie Zuiderzee. Technical report, 1926. in Dutch.
- [59] D.R. Lynch, J.T.C. Ip, C.E. Namie, and F.E. Werner. Comprehensive coastal circulation model with application to the Gulf of Maine. *Continental Shelf Research*, 16:875–906, 1996.
- [60] Chiang C. Mei, Michael Stiasnie, and Dick K.-P. Yue. *Theory and applications of ocean surface waves, Part 1: Linear aspects*. World Scientific Publishing Co. Pte. Ltd., 2005.
- [61] B. Mohammadi and O. Pironneau. *Analysis of the K-Epsilon turbulence model*. John Wiley & Sons, 1994.
- [62] Bruce R. Munson, Donald F. Young, and Theodore H. Okiishi. *Fundamentals of fluid mechanics, Fifth Edition*. John Wiley & Sons Inc., 2006.
- [63] J.C.C. van Nieuwkoop. Experimental and numerical modelling of tsunami waves generated by landslides. Master’s thesis, Delft University of Technology, Faculty of Civil Engineering and Geosciences, 2007.
- [64] Oil Companies International Marine Forum (OCIMF), editor. *Prediction of wind and current loads on VLCCs*. Witherby & Co.,Ltd., London, 2nd edition, 1994.
- [65] Dominique Pelletier, Andre Fortin, and Ricardo Camarero. Are fem solutions of incompressible flows really incompressible? (or how simple flows can cause headaches!). *International Journal for Numerical Methods in Fluids*, 9:96–112, 1989.
- [66] J.D. Pietrzak and R.J. Labeur. Trapped internal waves over undular topography in a partially mixed estuary. *Ocean Dynamics*, 54:315–323, 2004.
- [67] Julie Pietrzak, Anne Socquet, David Ham, Wim Simons, Christophe Vigny, Robert Jan Labeur, Ernst Schrama, Guus Stelling, and Deepak Vatvani. Defining the source region of the Indian Ocean tsunami from GPS, altimeters, tide gauges and tsunami models. *Earth and Planetary Science Letters*, 261(1-2):49–64, 2007.
- [68] O. Pironneau. *Finite element methods for fluids*. John Wiley & Sons, Inc., 1989.

- [69] A. van der Ploeg. *Preconditioning for sparse matrices with applications*. PhD thesis, Rijksuniversiteit Groningen, 1994.
- [70] N. Praagman. *Numerical solution of the shallow water equations by a finite element method*. PhD thesis, Delft University of Technology, 1979.
- [71] B.C. van Prooijen, T. van Kessel, and M. van Ledden. Modelling of fine sediment in a sandy environment - the coastal zone of the Netherlands. In *Proceedings of the XXXII IAHR Congress*, Venice, Italy, 2007.
- [72] R. Rannacher. Finite element methods for the incompressible Navier-Stokes equations. In G. P. Galdi, J. G. Heywood, and R. Rannacher, editors, *Fundamental Directions in Mathematical Fluid Mechanics*. Birkhäuser Verlag, Basel, 2000.
- [73] W.H. Reed and T.R. Hill. Triangular mesh methods for the neutron transport equation. Technical Report LA-UR-73-479, Los Alamos Scientific Laboratory, 1973.
- [74] Wolfgang Rodi. *Turbulence models and their applications in hydraulics*. International Association for Hydraulic Research (IAHR), Delft, The Netherlands, 1980.
- [75] Alessandro Russo. Streamline-upwind Petrov-Galerkin method (SUPG) vs residual-free bubbles. *Computer Methods in Applied Mechanics and Engineering*, 195:1608–1620, 2006.
- [76] Rick Salmon. *Lectures on geophysical fluid dynamics*. Oxford University Press, New York, 1998.
- [77] Giancarlo Sangalli. A discontinuous residual-free bubble method for advection-diffusion problems. *Journal of Engineering Mathematics*, 49:149–162, 2004.
- [78] I. Schnauder, A. Sukhokolov, W.S.J. Uijttewaalt, and R.J. Labeur. Field experiments and numerical modelling on shallow mixing layers at a confluence of two parallel streams. In M.S. Altinakar, M.A. Kokpinar, I. Aydin, S. Cokgor, and S. Kirkgoz, editors, *Proceedings of the international conference on fluvial hydraulics*, pages 883–892, Izmir, Turkey, 2008.
- [79] G. Scovazzi. A discourse on galilean invariance, SUPG stabilization, and the variational multiscale framework. *Computer Methods in Applied Mechanics and Engineering*, 196:1108–1132, 2007.
- [80] G. Segal and N. Praagman. Sepran user manual. Technical report, Ingenieursbureau Sepra b.v., 2000.

- [81] J.C. Simo, F. Armero, and C.A. Taylor. Stable and time dissipative finite element methods for the incompressible Navier-Stokes equations in advection dominated flows. *International Journal for Numerical Methods in Engineering*, 38:1475–1506, 1995.
- [82] G. Stelling and M. Zijlema. An accurate and efficient finite-difference algorithm for non-hydrostatic free-surface flow with application to wave propagation. *International Journal for Numerical Methods in Fluids*, 43:1–23, 2003.
- [83] G.S. Stelling. *On the construction of computational methods for shallow water flow problems*. PhD thesis, Delft University of Technology, 1983.
- [84] G.S. Stelling and S.P.A. Duinmeijer. A staggered conservative scheme for every Froude number in rapidly varied shallow water flows. *International Journal for Numerical Methods in Fluids*, 43:1329–1354, 2003.
- [85] Theodor Storm. *Der Schimmelreiter*. 1888. novel, in German.
- [86] Walter A. Strauss. *Partial differential equations, an introduction*. John Wiley & Sons, Inc., 1992.
- [87] T.E. Tezduyar. Stabilized finite element formulations for incompressible flow computations. *Advances in applied mechanics*, 28:1–44, 1992.
- [88] J.Th. Thijsse. *Hydraulica*. Technische vraagbaak, deel W. Kluwer, Deventer, 1951.
- [89] Eleuterio F. Toro. *Riemann solvers and numerical methods for fluid dynamics; a practical introduction*. Springer Verlag, Berlin, 1997.
- [90] Shuangzhang Tu and Shahrouz Aliabadi. A slope limiting procedure for gasdynamics applications. *International Journal of Numerical Analysis and Modelling*, 2:163–178, 2005.
- [91] J. van Veen. Analogie entre marées et courants alternatifs. *La Houille Blanche*, pages 401–416, 1947.
- [92] Jacob Versteegh. *The numerical simulation of three-dimensional flow through or around hydraulic structures*. PhD thesis, Delft University of Technology, 1990.
- [93] H.A. van der Vorst. Bi-CGSTAB: A fast and smoothly converging variant of Bi-CG for the solution of non-symmetric linear systems. *SIAM Journal on Scientific and Statistical Computation*, 13:631–644, 1992.

- [94] C.B. Vreugdenhil. *Computation of gravity currents in estuaries*. PhD thesis, Delft University of Technology, 1970.
- [95] C.B. Vreugdenhil. Uncertainties and appropriate models. In *Coastal Hydro- and Morphodynamics*, 2004.
- [96] Kees Vreugdenhil, Gerard Alberts, and Pieter van Gelder. Waterloopkunde, een eeuw wiskunde en werkelijkheid. *NWA*, pages 266–276, 2003. in Dutch.
- [97] S.N. Ward and S. Day. Cumbre Vieja Volcano – Potential collapse and tsunami at La Palma, Canary Islands. *Geophysical Research Letters*, 28(17):3397–3400, 2001.
- [98] B.A. Wols, W.S.J. Uijttewaal, R.J. Labeur, and G.S. Stelling. Rapidly varying flow over oblique weirs. In M. Piasecki, editor, *The 7th International Conference on Hydroscience and Engineering*, pages 1–13, Philadelphia, 2007. Drexel University Libraries.
- [99] O.C. Zienkiewicz and R.L. Taylor. *The finite element method: Basic formulation and linear problems*, volume 1. McGraw-Hill, London, 1989.
- [100] O.C. Zienkiewicz and R.L. Taylor. *The finite element method: Solid and fluid mechanics, dynamics and non-linearity*, volume 2. McGraw-Hill, London, 1991.

List of Figures

1.1	<i>Zuiderzee flood, 1916, the Netherlands: (a) inundation of the island of Marken and (b) computational network for tidal predictions as employed by Lorentz [58].</i>	2
1.2	<i>Schematic of Eulerian control volume V.</i>	4
1.3	<i>Schematic illustration of discretization principles.</i>	7
1.4	<i>Example river optimization study (Lek - the Netherlands): finite difference shallow-water flow model (a) and finite element model (b) used to compute the horizontal circulation in modified lay-out of junction [55].</i>	8
1.5	<i>Linear two-dimensional basis functions: (a) continuous, (b) discontinuous, (c) global interface function.</i>	10
1.6	<i>Example model application (Terneuzen - the Netherlands): exchange of salt water (red) and fresh water (blue) in shipping lock, distances in m [47].</i>	12
2.1	<i>Schematic of finite element partitioning.</i>	16
2.2	<i>Schematic of broken (discontinuous) function space.</i>	16
2.3	<i>The discontinuous field ϕ and the interface function $\bar{\phi}$.</i>	22
2.4	<i>Example of finite element mesh: section of the river Lek, The Netherlands.</i>	26
2.5	<i>Linear and quadratic two- and three-dimensional continuous elements.</i>	26
2.6	<i>Linear and quadratic two- and three-dimensional discontinuous elements.</i>	27
2.7	<i>Some stable two- and three-dimensional mixed-element combinations for the potential (\bullet) and velocity (\blacksquare) degrees of freedom.</i>	28
2.8	<i>Example of a space-time mesh.</i>	29
2.9	<i>Mapping a triangular element (left) onto a standard triangle (right).</i>	31
2.10	<i>Sparsity pattern of the nodal structure underlying the mesh of the river Lek from Figure 2.4; $N_{\text{node}} = 1942$, $N_{\text{sparse}} = 12700$.</i>	33
2.11	<i>Outlet and corresponding orthonormal flow net, from Thijsse [88].</i>	36

2.12	<i>Flow in an outlet: finite element mesh (a) and computed ortho-normal flow net for the MINI element (b).</i>	37
2.13	<i>Flow in an outlet: number of floating point operations (a) and increments of the energy functional ΔJ relative to the finest mesh solution (b).</i>	38
2.14	<i>Standing wave: errors for the linear CG and GIS methods in the \mathcal{L}^2 norm (a) and in the \mathcal{H}^1 semi-norm (b).</i>	39
3.1	<i>Schematic of inflow and outflow boundaries.</i>	42
3.2	<i>The Reynolds number: (a) dominant diffusion ($Re \ll 1$) and (b) dominant advection ($Re \gg 1$).</i>	45
3.3	<i>The Péclet number: outflow boundary layer for $Pe > 1$ (a) and for $Pe < 1$ (b); analytical solution (solid) and numerical solution (circles).</i>	46
3.4	<i>SUPG method: regular weighting function N^i and modified weighting function \tilde{N}^i.</i>	48
3.5	<i>Bubble function N^e of the MINI element.</i>	49
3.6	<i>The local Riemann problem.</i>	51
3.7	<i>Nodal degrees of freedom for the linear CG method (a) and the DG method (b).</i>	52
3.8	<i>Discontinuous functions connected by a continuous interface 'frame'.</i>	53
3.9	<i>Construction of the advective flux from the local Riemann problem.</i>	56
3.10	<i>Optimal ξ (dark blue) and critical ξ (black) for the SUPG method and ξ' for the GIS method with $\alpha = 4$ (green) and $\alpha = 6$ (light blue).</i>	65
3.11	<i>Fourier analysis: advection, (a) dispersion and (b) damping; diffusion ($\alpha = 6$), dispersion (c) and damping (d); physical roots (blue), non-physical roots (red) and exact solutions (green).</i>	66
3.12	<i>Advection-diffusion with source: error in the \mathcal{L}^2 norm (a) and in the \mathcal{H}^1 semi-norm (b) for $Pe = 100$ (blue), $Pe = 1$ (green) and $Pe = 0.01$ (red).</i>	67
3.13	<i>Outflow boundary layer for various Péclet numbers; $\bar{\phi}$ (dots), ϕ (solid) and exact solution (circles).</i>	69
3.14	<i>Characteristic boundary layer: numerical solution $\bar{\phi}$ for various characteristic directions.</i>	70
3.15	<i>Advection in a box: numerical solution $\bar{\phi}$ (interpolated) for different Péclet numbers, view is in upstream direction; red indicates $\bar{\phi} > 1$.</i>	71
3.16	<i>Anisotropic diffusion: numerical solution $\bar{\phi}$ (colour) and exact solution (isolines) for different orientations of the principal axis of the diffusion tensor; contour intervals 0.02.</i>	73

3.17	<i>Translation of a Gaussian hill for various Courant numbers showing ϕ (solid), $\bar{\phi}$ (dots) and exact solution (circles).</i>	75
3.18	<i>Numerical solution $\bar{\phi}$ (colour) and exact solution (isolines) of the rotating cone problem for various Courant numbers; values isolines: 0.2, 0.4, 0.6 and 0.8.</i>	76
3.19	<i>Spiralling blob: numerical solution $\bar{\phi}$ (colour) for different Courant numbers, helical flow is from right to left.</i>	77
3.20	<i>Finite element mesh of the North Sea (a) and detail of the area around the Port of Rotterdam (b), source: van Prooijen et al. [71].</i>	78
3.21	<i>Computed (a) and observed (b) yearly mean suspended solids concentration, source: van Prooijen et al. [71]</i>	78
4.1	<i>Schematic of the GIS pressure-velocity discretization.</i>	87
4.2	<i>Stokes flow with source: computed flow field (a) and pressure field (b); results for $h_e = 1/40$.</i>	104
4.3	<i>Stokes flow with source: errors in the \mathcal{L}^2-norm of the velocity (dots) and the pressure (circles).</i>	105
4.4	<i>Accelerating pipe flow: analytical solution (solid) and numerical solution (circles) of the velocity magnitude at different time steps.</i>	106
4.5	<i>Stationary compression shock: solution for various Péclet numbers; showing \bar{u} (dots), u (solid) and exact solution (circles).</i>	107
4.6	<i>N-wave rarefaction: computed and analytical solution at different time steps for an initial Courant number $u_0\Delta t/h_e = 0.5$; shown are \bar{u} (dots), u (solid) and the exact solution (circles).</i>	108
4.7	<i>Driven cavity flow: velocity (colour) and streamlines (isolines) for Reynolds numbers of 100, 400, 1000 and 5000; streamline intervals 10^{-2} (primary vortex) and $5 \cdot 10^{-4}$ (secondary vortices); colour interval 0.1; element size $h_e \approx 1/64$.</i>	110
4.8	<i>Borda mouthpiece: (a) mean velocity magnitude and streamlines in the ‘vena contracta’ and (b) velocity magnitude instantaneous flow field.</i>	112
4.9	<i>Borda mouthpiece: (a) computed mean velocity profile in the ‘vena contracta’, $x = -0.25$ m, (circles) and corresponding theoretical velocity profile (solid); (b) computed mean normalized pressure (circles) and theoretical normalized pressure (solid) in center line $y = 0$, vertical transects indicate position mouthpiece.</i>	113
4.10	<i>Internal standing wave: mesh and computed interface position at $t = 51.5$ s (maximum elevation).</i>	115
4.11	<i>Internal standing wave: interface elevation at $(x, y) = (0, 0)$, numerical solution (circles) and theoretical solution (solid).</i>	115

4.12	<i>Trapped internal wave: computed (left) and theoretical (right) solutions of the vertical velocity w (mm/s).</i>	117
4.13	<i>Current load on VLCC: computed current velocity magnitude $\bar{\mathbf{u}}$ in m/s for $\varphi = 50^\circ$.</i>	118
4.14	<i>Current load on VLCC: computed dimensionless non-hydrostatic pressure p_d/U^2 at ships' hull for $\varphi = 50^\circ$.</i>	118
5.1	<i>Schematic illustration of mappings.</i>	122
5.2	<i>Kinematic free-surface condition for vertical mesh motion.</i>	129
5.3	<i>Regular mesh configuration used for the normal mode analysis.</i>	150
5.4	<i>Relative celerity error $1 - c_r$ for various wave length to depth ratios L/d, Courant numbers and number of vertical layers: $N_z = 2$ (blue), $N_z = 5$ (green) and $N_z = 10$ (red).</i>	151
5.5	<i>Relative amplitude error $1 - \rho_r$ after one wave period for various wave length to depth ratios L/d, Courant numbers and number of vertical layers: $N_z = 2$ (blue), $N_z = 5$ (green) and $N_z = 10$ (red).</i>	152
5.6	<i>Narrow channel: computational mesh and computed solution (a), and exact solution (b) for η at $t = 17.8$ s (maximum elevation), units in m.</i>	153
5.7	<i>Narrow channel: time series of piezometric level η/A at $(x, y) = (0, 0)$, exact (solid) and numerical (circles) solutions.</i>	154
5.8	<i>Cylindrical basin: (a) Computational domain and mesh; and (b) exact (solid) and computed (colour) surface level contours (m) at $t = 10.9$ s.</i>	155
5.9	<i>Cylindrical basin: time histories of the analytical (solid) and computed (circles) normalized piezometric level at $(x, y, z) = (10, 0, 0)$.</i>	156
5.10	<i>Spatial mesh configuration for U-shaped tube problem at maximum surface elevation.</i>	157
5.11	<i>U-shaped tube problem: time histories of the analytical (solid) and computed (circles) surface elevations.</i>	157
5.12	<i>Soliton: snapshot of mesh configuration for $H/d = 0.60$ at $t = 30$ s, colour shading indicates piezometric level.</i>	158
5.13	<i>Soliton: theoretical (solid) versus computed (dashed) surface elevation at $t = 30$ s for varying relative wave heights H/d.</i>	159
5.14	<i>Waves over a submerged bar: configuration of the experimental flume with snapshot of computed free surface and piezometric level (colour) at $t = 40$ s.</i>	160
5.15	<i>Waves over a submerged bar: time series of measured (dashed) and computed (solid) surface elevations.</i>	161
5.16	<i>Undulating flow: computed flow velocity magnitude (m/s).</i>	162

5.17	<i>Undulating flow: measured (solid) versus computed (circles) surface elevation behind weir, also showing the transects along which velocity measurements are made (dashed lines).</i>	163
5.18	<i>Undulating flow: computed (solid) versus measured (circles) flow velocities in several transects behind weir (see also Figure 5.17).</i>	164
5.19	<i>Sub-marine landslide experiment [63].</i>	165
5.20	<i>Snapshots at increasing times for the sub-marine landslide problem showing the displacement of the free surface and the displacement of the bottom due to the slider. The figures have been stretched by a factor of three in the depth direction.</i> . . .	166
5.21	<i>Measured (dashed) and computed (solid) time series of the surface elevation for the sub-marine landslide problem at various measuring stations as given in Table 5.1.</i>	167
5.22	<i>Haringuliet barrier during construction.</i>	168
5.23	<i>Mesh configuration Haringuliet barrier showing crest, stilling basin, side walls and gate (with sea side on the left).</i>	169
5.24	<i>Haringuliet barrier: computed velocity field during flood.</i> . . .	170
5.25	<i>Haringuliet barrier: computed surface level along center line also showing vertical transect velocity measurements (a); measured (solid) and computed velocity profiles in transect (b), mixing length model (circles) and standard $k-\epsilon$ model (dots); n.a.p. refers to Dutch reference level.</i>	171

List of Tables

2.1	<i>Element comparison for the potential flow problem on a mesh of N nodes.</i>	35
2.2	<i>Flow in an outlet: number of required BICGSTAB iterations.</i>	37
3.1	<i>Characteristic boundary layer: minimum and maximum values of computed ϕ and $\bar{\phi}$.</i>	70
3.2	<i>Advection in a box: minimum and maximum values of $\bar{\phi}$.</i>	72
3.3	<i>Summary simple-wave tests: minimum and maximum concentrations and relative celerity; initial distributions are Gaussian with standard deviation $2h_e$; theoretical total displacements $15h_e$.</i>	74
4.1	<i>Driven cavity flow: primary vortex position and stream function value; present simulation, $h_e \approx 1/64$; Donea and Huerta [19], $h_e = 1/30$; Erturk et al. [23], $h_e = 1/400$.</i>	111
4.2	<i>Current load on VLCC: comparison of computed and measured [39] longitudinal current force coefficient C_x, transverse current force coefficient C_y and current yaw moment coefficient C_{xy}; zero angle denotes current stern-on; keel-clearance $k = 1.20$.</i>	120
5.1	<i>Locations of surface elevation measurement stations for the sub-marine landslide experiments (object slides along the line $y = 0$).</i>	165
B.1	<i>Empirical constants used in the standard $k - \epsilon$ model [74].</i>	197

Notation

Abbreviations

Abbreviation	Description
ADCP	Acoustic Doppler Current Profiler
ALE	Arbitrary Lagrangian-Eulerian
BI-CGSTAB	Bi-Conjugate Gradient STABILized
BSR	Block Sparse Row (matrix format)
CFL	Courant-Friedrich-Lewis (number)
CG	Continuous Galerkin (method)
CN	Crank-Nicolson (method)
CSR	Compressed Sparse Row (matrix format)
DG	Discontinuous Galerkin (method)
D-GCL	Discrete Geometric Conservation Law
Fr	Froude number
FS	Fractional Step (method)
GIS	Galerkin Interface Stabilization (method)
ILU	Incomplete Lower-Upper (decomposition)
LBB	Ladyshenskaya-Babuška-Brezzi (condition)
LES	Large Eddy Simulation
NSE	Navier-Stokes Equations
Pe	Péclet number
PSPG	Pressure-Stabilized Petrov-Galerkin (method)
RANS	Reynolds-Averaged Navier-Stokes (equations)
Re	Reynolds number
SUPG	Streamline Upwind Petrov-Galerkin (method)
SWE	Shallow-Water Equations

Roman symbols

Symbol	Description	Unit
\mathbf{a}	advective velocity	[m/s]
\mathbf{c}	convective velocity	[m/s]
d	number of spatial dimensions	
d	water depth	[m]
\mathbf{e}_j	unit vector in Cartesian direction j	
f	densimetric source term	[1/s]
\mathbf{f}	specific body force	[m/s ²]
\mathbf{F}	Jacobian matrix	
g	gravitational acceleration	[m/s ²]
g, \mathbf{g}	Dirichlet boundary condition	
h, h_e	global, local element size	
h, \mathbf{h}	Neumann boundary condition	
H^1	Hilbert space of differentiable functions	
$H^{1/2}$	fractional Hilbert (trace) space	
I	time interval	
\mathbf{I}	second-order identity tensor	
J	Jacobian determinant, functional	
k	wave number	[rad/m]
k	turbulence kinetic energy	[m ² /s ²]
l_m	turbulence mixing length	[m]
L^2	space of Lebesgue-integrable functions	
\mathbf{n}	unit normal vector	
N	number of nodes, basis function	
p	normalized pressure	[m ² /s ²]
p_a	normalized atmospheric pressure	[m ² /s ²]
p_d	normalized non-hydrostatic pressure	[m ² /s ²]
P^k	Lagrange polynomial basis of order k	
\mathbf{P}	Piola-Kirchoff stress	[m ² /s ²]
S	velocity shear	[1/s]
\mathbf{S}	referential symmetric gradient operator	
t	time	[s]
\mathbf{u}	flow velocity	[m/s]
\mathbf{w}	referential material velocity	[m/s]
\mathbf{x}	spatial coordinate	[m]
\mathbf{X}	material coordinate	[m]

Greek symbols

Symbol	Description	Unit
α	penalty term	
β	interface term	[m/s]
γ	upwind parameter	
Γ, Γ_i	boundary, interface	
δ	variation, damping parameter	
Δ	increment, difference	
ϵ	turbulence dissipation rate	[m ² /s ³]
ζ	elevation	[m]
η	piezometric head	[m]
θ	time stepping parameter	
κ	diffusivity, von Karman constant	
λ	Lagrange multiplier	
μ	dynamic viscosity	[Ns/m ²]
ν	kinematic viscosity	[m ² /s]
ξ	stabilization parameter	
ρ	density	[kg/m ³]
ρ^*	relative density difference	
σ	flux	[m/s]
σ	flux tensor	[m ² /s ²]
τ_e	stabilization parameter	[s]
τ	Cauchy stress	[m ² /s ²]
φ	angle	
ϕ	densimetric concentration	
Φ	gravity potential	[m ² /s ²]
χ	reference coordinate	[m]
ψ	map	
ω	frequency	[rad/s]
ω	vorticity vector	[1/s]
Ω, Ω_e	domain, element	

Diacritical marks

Diacritic	Name	Description
$\bar{\square}$	macron	quantity is defined on element interfaces
$\hat{\square}$	circumflex	quantity is defined on the reference domain
$\tilde{\square}$	tilde	generally denotes a union
\square^*	asterisk	non-dimensional quantity

Curriculum Vitae

1964, July 25th	Born in Zaandam, The Netherlands
1976-1982	VWO, Lorentz Scholengemeenschap, Arnhem
1982-1989	Msc Civil Engineering, Delft University of Technology, Delft
1989	Researcher, Section Fluid Mechanics, Delft University of Technology, Delft
1990-2002	Project Engineer, Svašek Hydraulics B.V., Rotterdam
2001-present	Assistant Professor, Faculty of Civil Engineering and Geosciences, Section Environmental Fluid Mechanics, Delft University of Technology, Delft